

# Theory and numerics of higher gradient inelastic material behavior

vom Fachbereich Maschinenbau und  
Verfahrenstechnik der Universität Kaiserslautern  
zur Verleihung des akademischen Grades  
Doktor-Ingenieur (Dr.-Ing.)  
genehmigte Dissertation

von Dipl.-Ing. Tina Liebe  
aus Magdeburg

Hauptreferent:	Prof. Dr.-Ing. Paul Steinmann
Korreferenten:	Prof. Dr. rer. nat. B. Svendsen Prof. Dr. A. Benallal
Vorsitzender:	Prof. Dr.-Ing. H.-D. Hellmann
Dekan:	Prof. Dr.-Ing. Paul Steinmann
Tag der Einreichung:	19. Februar 2003
Tag der mündlichen Prüfung:	07. April 2003



# Preface

The work presented in this thesis has been carried out during the period 1999-2003 at the Chair of Applied Mechanics at the University of Kaiserslautern. The financial support of the DFG (Deutsche Forschungsgemeinschaft) within the project '*Theorie und Numerik von Mono- und Polykristallplastizität unter Berücksichtigung höherer Gradienten*' (STE-544/7-1-3) is gratefully acknowledged.

In the first place, I would like to thank Professor Paul Steinmann for his constant support and guidance, his never ending patience, inspiring comments and the time he put into my thesis. He motivated me to come to Kaiserslautern and take up this PhD-project and I owe him a great deal for making these last four years a successful and enjoyable stage of my life.

My sincere thanks go to Professor Bob Svendsen and Professor Ahmed Benallal, who spontaneously agreed to become correferrees for my thesis. Many scientific discussions and valuable remarks encouraged and helped me getting a deeper insight into the subject of my work, and at some stages even more enlightening were the insights they provided to the overall picture.

Special thanks go to Professor Erwin Stein who introduced me to the fascinating world of mechanics, in particular computational mechanics, already during my study at the university in Hanover. Furthermore, I would like to thank Professor Kaspar Willam for his hospitality and support during my stay at the Colorado University Boulder, where I carried out my diploma thesis. The open-minded atmosphere I encountered there raised my interest to carry on with scientific research.

I appreciated the pleasant working climate at the Chair of Applied Mechanics at the University of Kaiserslautern, which is undoubtedly due to my colleagues. In particular, I like to thank my room-mates during the period of this work: Thomas Svedberg, Ellen Kuhl and Bernd Kleuter, who made our office-life a great deal more enjoyable.

Last, but not least, I would like to express my gratitude to my parents and my brother, Jörg, for their continuous encouragement and for always standing behind me. Especially, I thank Klaus Schmitt for his support - not to forget his sometimes funny but always valuable questions and comments during the reading and re-reading of the manuscript at various stages of its development.

Kaiserslautern, in April 2003

Tina Liebe



# Contents

<b>Preface</b>	<b>i</b>
<b>Notation</b>	<b>vii</b>
<b>Introduction</b>	<b>1</b>
<b>1 Concepts of the formulation</b>	<b>9</b>
1.1 Internal degrees of freedom . . . . .	10
1.2 Internal variables . . . . .	11
<b>2 Continuum dislocation theory</b>	<b>13</b>
2.1 Kinematics of the dislocation tensor . . . . .	14
2.1.1 Incompatibility measures . . . . .	14
2.2 Exploitation of the Positive Dissipation Principle . . . . .	16
2.2.1 Simplified gradient model . . . . .	18
<b>3 Phenomenological isotropic gradient plasticity</b>	<b>21</b>
3.1 Thermodynamics of phenomenological local plasticity . . . . .	22
3.2 Thermodynamics of phenomenological gradient plasticity . . . . .	22
3.3 Isotropic local and gradient prototypes . . . . .	24
3.4 Well-posedness of the coupled problem . . . . .	25
3.5 Numerical treatment of phenomenological gradient plasticity . . . . .	27
3.5.1 Strong form of the coupled problem . . . . .	27
3.5.2 Weak form of the coupled problem . . . . .	28
3.5.3 Temporal discretization of the coupled problem . . . . .	29
3.5.4 Spatial discretization of the coupled problem . . . . .	30
3.5.5 Monolithic iterative solution . . . . .	32
3.5.5.1 Constitutive update . . . . .	33
3.5.5.2 Active set search . . . . .	33
3.6 Numerical examples of phenomenological gradient plasticity . . . . .	34
3.6.1 1D-model problem: bar under uniaxial tension . . . . .	35
3.6.1.1 Hardening . . . . .	36
3.6.1.2 Softening . . . . .	39
3.6.2 Geometrically non-linear model problem: panel under tension . . . . .	42

<b>4</b>	<b>Gradient plasticity in single and double slip</b>	<b>45</b>
4.1	Kinematics of single crystals . . . . .	46
4.2	Thermodynamics of single crystal gradient plasticity . . . . .	48
4.3	Numerical treatment of single crystal gradient plasticity . . . . .	49
4.4	Numerical examples of single crystal gradient plasticity . . . . .	51
4.4.1	Single slip model problem: simple shear of a crystalline strip . . . . .	53
4.4.2	Double slip model problem: simple shear of a crystalline strip . . . . .	55
<b>5</b>	<b>Phenomenological isotropic gradient damage</b>	<b>59</b>
5.1	Thermodynamics of phenomenological local damage . . . . .	60
5.2	Thermodynamics of phenomenological gradient damage . . . . .	61
5.3	Isotropic local and gradient prototypes . . . . .	63
5.4	Well-posedness of the coupled problem . . . . .	64
5.5	Numerical treatment of phenomenological gradient damage . . . . .	66
5.5.1	Strong form of the coupled problem . . . . .	66
5.5.2	Weak form of the coupled problem . . . . .	68
5.5.3	Temporal discretization of the coupled problem . . . . .	68
5.5.4	Spatial discretization of the coupled problem . . . . .	69
5.5.5	Monolithic iterative solution . . . . .	70
5.5.5.1	Constitutive update . . . . .	71
5.6	Numerical examples of phenomenological gradient damage . . . . .	72
5.6.1	1D-model problem: bar under uniaxial tension . . . . .	72
5.6.2	2D-model problem: panel in tension . . . . .	77
5.6.3	Geometrically non-linear model problem: bar under uniaxial tension . . . . .	78
<b>6</b>	<b>Material Force Method coupled to damage</b>	<b>81</b>
6.1	Continuum format of J-integral . . . . .	82
6.2	Spatial versus material motion problem . . . . .	83
6.3	Hyperelasticity coupled to isotropic damage . . . . .	83
6.3.1	Spatial motion problem . . . . .	84
6.3.2	Material motion problem . . . . .	85
6.4	Numerical treatment incorporating the Material Force Method . . . . .	85
6.4.1	Weak form of the coupled problem . . . . .	86
6.4.1.1	Spatial motion problem . . . . .	86
6.4.1.2	Material motion problem . . . . .	87
6.4.2	Discretization of the coupled problem . . . . .	87
6.4.2.1	Spatial motion problem . . . . .	87
6.4.2.2	Material motion problem . . . . .	89
6.4.2.3	Discretized format of J-integral: Material Force Method . . . . .	90
6.5	Numerical examples of the Material Force Method coupled to damage . . . . .	91
6.5.1	Specimen with elliptic hole . . . . .	91
6.5.2	Specimen with center crack . . . . .	96
6.5.3	MBL-specimen . . . . .	97
	<b>Summary and Outlook</b>	<b>99</b>

---

<b>A</b>	<b>A few notes about continuum mechanics</b>	<b>103</b>
A.1	Kinematics . . . . .	103
A.1.1	Spatial motion problem . . . . .	103
A.1.2	Material motion problem . . . . .	104
A.1.3	Spatial versus material motion problem . . . . .	105
A.2	Quasi-static balance of momentum . . . . .	105
A.2.1	Spatial motion problem . . . . .	105
A.2.2	Material motion problem . . . . .	106
<b>B</b>	<b>Geometrically non-linear gradient plasticity</b>	<b>107</b>
B.1	Discretization in time and space of the coupled problem . . . . .	108
B.2	Prototype isotropic gradient plasticity model . . . . .	109
B.3	Constitutive update . . . . .	110
<b>C</b>	<b>Geometrically non-linear gradient damage</b>	<b>113</b>
C.1	Discretization in time and space of the coupled problem . . . . .	113
C.2	Prototype isotropic gradient damage model . . . . .	115
C.3	Constitutive update . . . . .	116





# Notation

Throughout the thesis, scalars are denoted by small non-bold symbols  $a = a$ , vectors by small bold symbols  $\mathbf{a} = a_i \mathbf{e}_i$ , whereas second order tensors are mainly indicated by capital bold symbols  $\mathbf{A} = A_{ij} \mathbf{e}_i \otimes \mathbf{e}_j$  and fourth order tensors are recognized as calligraphic symbols  $\mathcal{A} = \mathcal{A}_{ijkl} \mathbf{e}_i \otimes \mathbf{e}_j \otimes \mathbf{e}_k \otimes \mathbf{e}_l$ . Here, reference to the Euclidean basis  $\mathbf{e}_{i,\dots,l}$  is tacitly assumed. If special distinction between material and spatial configuration is employed, capital bold symbols denote material second order tensors, while small bold symbols define spatial second order tensors. In particular, the second order unit tensor is denoted as  $\mathbf{1} = \delta_{ij} \mathbf{e}_i \otimes \mathbf{e}_j$  and the fourth order unit tensor is given by  $\mathcal{I} = \delta_{ik} \delta_{jl} \mathbf{e}_i \otimes \mathbf{e}_j \otimes \mathbf{e}_k \otimes \mathbf{e}_l$  with respect to the Kronecker delta  $\delta_{ij} = 1$  for  $i = j$  and  $\delta_{ij} = 0$  for  $i \neq j$ . Furthermore, the scalar and vector products of, e.g., vectors  $\mathbf{a}, \mathbf{b}, \mathbf{c}$  are defined in standard fashion, namely  $\mathbf{a} \cdot \mathbf{b} = \mathbf{b} \cdot \mathbf{a}$  and  $[\mathbf{a} \otimes \mathbf{c}] \cdot \mathbf{b} = [\mathbf{c} \cdot \mathbf{b}] \mathbf{a}$ , respectively, whereby each  $\cdot$  indicates one contraction. The subsequent list gives a general overview of the symbols used throughout this thesis.

$\{\bullet\}^{sym}$	symmetric part of $\{\bullet\}$ , e.g., $\mathbf{A}^{sym} := \frac{1}{2}[\mathbf{A} + \mathbf{A}^t]$
$\{\bullet\}^{skw}$	skewsymmetric part of $\{\bullet\}$ , e.g., $\mathbf{A}^{skw} := \frac{1}{2}[\mathbf{A} - \mathbf{A}^t]$
$\{\bullet\}^{vol}$	volumetric part of $\{\bullet\}$ , e.g., $\mathbf{A}^{vol} := \frac{1}{3}[\mathbf{A} : \mathbf{1}] \mathbf{1}$
$\{\bullet\}^{dev}$	deviatoric part of $\{\bullet\}$ , e.g., $\mathbf{A}^{dev} := \mathbf{A} - \mathbf{A}^{vol}$
$\delta(\bullet)$	variational form of $(\bullet)$
$[\bullet]_I$	$[\bullet]$ corresponding to slip system $I$
$[\bullet]$	time derivative
$[\bullet]_{n+1}$	temporally discretized form
$[\bullet]^t$	transpose of $[\bullet]$
$\varphi(\bullet)$	equivalent stress
$M_{KL}, \mathbf{K}_{KL}^{**}$	fundamental matrix and iteration matrices
$\mathbf{A}_e$	assembly of all elements $e$
$\mathcal{B}, \mathcal{B}_e$	global solution domain and its elementwise discretization
$\mathbb{B}, \mathbb{B}_e$	global and elementwise discretization node point sets
$\mathbb{B}_{act}$	active discretization node point set
$k, K$	elementwise numbering and global numbering
$n_{en}, n_{np}$	number of elements and number of nodal points
$N_x^k, N_u^k, N_\kappa^k, N_d^k, N_\Phi^k$	shape functions corresponding to discretization variable $\mathbf{u}, \mathbf{x}, \kappa, d, \Phi$
$\gamma$	shear number
$K, G$	bulk and shear modulus
$c$	gradient parameter

$\mathcal{B}_0, T\mathcal{B}_0$	compatible material configuration and corresponding tangent space
$\mathcal{B}_t, T\mathcal{B}_t$	compatible spatial configuration and tangent space
$\mathcal{B}_p, T\mathcal{B}_p$	incompatible, isoclinic intermediate configuration and tangent space
$t, t_0$	reference and current time
$\mathbf{X}, \mathbf{x}$	placements of a material point at time $t_0$ and $t$
$\varphi$	non-linear deformation map
$\mathbf{F}, \mathbf{f}$	direct and inverse tangent map
$\mathbf{F}^p, \mathbf{f}^p$	direct and inverse inelastic tangent map
$\mathbf{F}^e, \mathbf{f}^e$	direct and inverse elastic tangent map
$J, j$	Jacobian wrt $\mathbf{F}$ and $\mathbf{f}$
$\mathbf{M}^t$	Mandel–type second order stress tensor
$\mathbf{\Pi}^t$	first Piola–Kirchhoff second order stress tensor
$\mathbf{L}^p$	plastic ‘velocity gradient’
$\beta$	Burger’s vector
$\mathcal{C}_0, \mathcal{C}_t$	contour line in $\mathcal{B}_0, \mathcal{B}_t$
$\mathcal{A}_0, \mathcal{A}_t$	contour line area in $\mathcal{B}_0, \mathcal{B}_t$
$\mathbf{N}, \mathbf{n}$	normal vectors
$\mathbf{E}, \mathbf{e}$	material and spatial permutation tensor
$\mathbf{A}^t : T\mathcal{B}_0 \rightarrow T\mathcal{B}_p$	dislocation density tensor
$\mathbf{a}^t : T\mathcal{B}_t \rightarrow T\mathcal{B}_p$	dislocation density tensor
$\Psi_0^{mac}, \Psi_0^{dis}, \Psi_0^{har}$	free Helmholtz energy density (macroscopic, dislocation, hardening part)
$\mathcal{D}_0, \Phi$	dissipation and inelastic potential
$\mathcal{P}_0$	nonlocality residual
$\mathbf{Y}^t$	hyperstress
$\mathbf{B}_0, \mathbf{b}_0$	material and spatial distributed volume forces
$\mathcal{B}_0^p, \partial\mathcal{B}_{0int}^p, \partial\mathcal{B}_{0ext}^p$	plastic loading part of the body and boundary (internal, external)
$\mathcal{B}_0^e$	elastic loading part of the body
$\bar{\mathbf{M}}^t$	quasi-nonlocal relative stress
$\mathbf{s}_0, \mathbf{m}_0$	slip direction and slip plane normal in $\mathcal{B}_0$
$\mathbf{s}_p, \mathbf{m}_p$	slip direction and slip plane normal in $\mathcal{B}_p$
$\mathbf{s}_t, \mathbf{m}_t$	slip direction and slip plane normal in $\mathcal{B}_t$
$\mathbf{s}_I, \mathbf{m}_I$	slip direction and slip plane normal corresponding to slip system $I$
$\mathbf{K}, \mathbf{k}$	material and spatial gradient of the hardening variable
$\tau$	Kirchhoff stress
$\mathcal{V}_0$	arbitrary subdomain of $\mathcal{B}_0$
$\mathfrak{F}_{sur,s}, \mathfrak{F}_{sur,r}, \mathfrak{F}_{vol}$	singular, regular surface force and volume force
$\mathfrak{J}$	vectorial $J$ -integral
$\mathbf{a}$	general internal variable
$\Sigma^t$	material Cauchy stress
$W_0, W_t$	material and spatial energy density
$\mu, \lambda$	Lamé parameters
$\lambda_A^e$	elastic eigenvalue

$\Psi^{mac}, \Psi^{dis}, \Psi^{har}$	free Helmholtz energy density (macroscopic, dislocation, hardening part)
$\mathcal{D}, \Phi$	dissipation and inelastic potential
$\mathcal{P}$	nonlocality residual
$\epsilon, \epsilon^e, \epsilon^p$	total, elastic and plastic strains
$\sigma, \sigma^p$	macroscopic (Cauchy) stress and dissipative stress
$Y, H$	damage and hardening flux
$Y_0, Y_{0r}, Y_{0p}$	initial, initially reduced and perturbed yield stress
$H_0, \beta$	linear softening/hardening modulus, exponential parameter
$\kappa$	internal hardening/history variable
$\lambda$	plastic multiplier
$\kappa_0$	initial damage threshold
$E, E_r, \nu$	elastic and reduced elastic modulus, Poisson ratio
$Y, \bar{Y}$	local and quasi-nonlocal yield stress
$H, \bar{H}$	local and quasi-nonlocal drag stress
$W_\epsilon, W_\kappa, W_d$	local stored energy and gradient part (plasticity, damage)
$\mathcal{E}_\epsilon, \mathcal{E}_\kappa, \mathcal{E}_d$	elastic and gradient fourth order material tensor (plasticity, damage)
$\mathbf{u}$	displacement vector
$\hat{\mathbf{n}}, \hat{\mathbf{m}}, (\hat{m})$	wave propagation direction and polarization
$i, k$	imaginary and wave number
$Q_\epsilon, Q_\nu, Q_\kappa, Q_d, h$	partitions of the localization tensor
$E_\kappa^{local, crit}, E_\kappa^{crit}$	critical local and gradient hardening modulus
$\mathbf{b}$	distributed body forces per unit volume
$\mathbf{t}^p, \partial\mathcal{B}^t, \mathbf{u}^p, \partial\mathcal{B}^u$	prescribed tractions and displacements with corresponding boundary
$\mathbf{r}^u, r^\Phi, \dot{\mathbf{r}}^\kappa, \dot{\mathbf{r}}^d$	strong residual form of equilibrium and constitutive subproblem
$G^u, G^\Phi, \dot{G}^\kappa, \dot{G}^d$	weak residual form of equilibrium and constitutive subproblem
$\mathbf{R}_K^u, R_K^\Phi, \Delta R_K^\kappa, \Delta R^d$	discrete algorithmic residua of equilibrium and constitutive subproblem
$\alpha$	slip system angle
$\mathbf{h}, \mathbf{h}^e, \mathbf{h}^p$	total, elastic and plastic distortion
$\tau$	Schmid stress
$H$	height of strip layer
$x_1, x_2$	in-plane coordinate axis
$d, \mathbf{d}$	internal damage variable and its gradient
$Y, \bar{Y}$	local and quasi-nonlocal energy release rate
$\mathcal{B}^d, \partial\mathcal{B}_{int}^d, \partial\mathcal{B}_{ext}^d$	damaged part of the body and corresponding boundary (internal, external)
$H$	damage growth
$p$	volumetric part of Cauchy stress
$s$	deviatoric part of Cauchy stress



# Introduction

The goal of this thesis is a physically motivated and thermodynamically consistent formulation of higher gradient inelastic material behavior. Thereby, the influence of the material *microstructure* is incorporated. Next to theoretical aspects, the thesis is complemented with the algorithmic treatment and numerical implementation of the derived model. Hereby, two major inelastic effects will be addressed: on the one hand *elasto-plastic* processes and on the other hand *damage* mechanisms, which will both be modeled within a *continuum mechanics* framework.

In particular, concentration will be focused on *ductile crystalline* materials as, for example, metals that are essential in many engineering applications. One may think of steel that plays an important role in engineering ranging from robust constructions such as frames in skyscrapers to tiny thin structures used in nanotechnology - that means one may generally deal with increasingly complex materials that possess desirable characteristics at various length scales. Thereby, many materials exhibit partly *irreversible* or *inelastic* behavior that, in most instances, can be treated within the framework of small deformations. Nevertheless, in case of, e.g., metal forming, material testing or extreme load scenarios, one has to consider large deformations in general. Hence, the focus of this thesis will not only be on a detailed *geometrically linear* continuum modeling of inelastic material behavior but the *geometrically non-linear* case will also be addressed in a compact fashion.

In principle, inelastic ductile material behavior may be characterized on a micro-mechanical basis with the help of single crystals. Furthermore, one may even think of polycrystals as being an inordinate assemblage of single crystals. Typically, polycrystals may introduce various complex phenomena, e.g., texture formation, grain boundaries or orientation preferences, which are not subject of this study. Thus, the interest is focused on the thorough investigation of single crystals and corresponding phenomena.

In case of elasto-plasticity, one can identify *dislocations* and dislocation flow as the driving process that reveals itself experimentally as micro-sized slip steps on the crystal faces. Thereby dislocations can encounter obstacles and get pinned resulting in material *hardening*. Adopting the simplest classical view of homogeneous plastic deformations, it suffices to use an isotropic scalar internal hardening variable that accounts for *statistically stored dislocations*.

In addition, the material may possess internal *micro-defects* that may initiate micro-pores or even micro-cracks. Further evolution then triggers the formation of macro-pores and macro-cracks or simply material *deterioration*. In the simplest case such damage process may also be modeled as isotropic with the help of a scalar internal damage variable accounting for micro-defects.

In general, it would be cumbersome to account explicitly for each and every atom within the crystal lattice. Consequently, the ideal forum to derive a theoretically as well as computationally manageable formulation is based on *phenomenological* modeling of fields and fluxes related to the microstructure, in particular, dislocations and micro-defects, within the framework of continuum mechanics. This leads to complex coupled non-linear boundary value problems that can mainly be solved in an approximated manner with the help of numerical methods. Moreover, there are two competing mechanisms: material

*softening* due to damage and dislocation movements and material hardening due to dislocation pile-ups at obstacles. Finally, the softening effect prevails and leads to material instabilities, e.g., *localization*. One of the most effective tools for the numerical computation of such phenomena is offered by the *Finite Element Method*. But the deficiencies of classical local continuum models become particularly obvious in the post-critical regime in terms of a pathological dependency from the chosen discretization. This can be mathematically translated into a loss of ellipticity of the governing equations. It renders physically meaningless results, e.g., shear bands of zero width are computed for ductile materials that are discretized in the limit with an infinite fine mesh.

Over the past decade, much research has therefore been dedicated to modifications of standard local continuum descriptions. These so-called regularizations try to resolve microstructural interactions by introducing an internal length scale. One of the most promising approaches is based on the incorporation of higher gradients. Dislocation densities and incompatibilities are identified in order to influence the hardening behavior, especially in crystal plasticity. It will be shown that, in particular, *geometrically necessary dislocations*, which can be related to the gradient of the classical hardening variable have to be taken into account. It thus seems suitable to generally incorporate the gradient of an internal variable into the free Helmholtz energy in order to set up a phenomenological continuum theory of inelastic material behavior. Remarkably, the microstructural influence is thereby incorporated based on physical arguments.

Due to the inclusion of the microstructural interactions, a special nonlocal enhancement of the local dissipation inequality is applied here. This finally renders the algorithmic solution of a coupled problem culminating in a two-field finite element formulation. Moreover, an active working set search strategy for the determination of the inelastic loading part of the body needs to be provided.

In general, the corresponding theory and numerics will be outlined in every particular chapter according to the inelastic material behavior in question. For demonstrative purposes, most numerical computations are kept one-dimensional, whereas further examples are given under plane strain conditions. Thereby, the implementation of specific material models is realized within the finite element program PHOENIX of the Chair of Applied Mechanics, see the corresponding documentation.

As an introduction, the different concepts of the formulation of inelastic materials with microstructure are outlined in CHAPTER 1. On the one hand, the kinematic description may be enriched with extra *internal degrees of freedom* whereas on the other hand, additional *internal variable* fields and their gradients are incorporated. In the first case *micro-forces* contribute to the total energy flux and render additional micro-force balance equations. The latter approach implies an internal power term in the entropy equation and necessitates the definition of *evolution equations*. The focus of interest is dedicated to the internal variable concept in this thesis.

In CHAPTER 2 the key aspects of a geometrically non-linear *continuum dislocation theory* are introduced within the framework of multiplicative elasto-plasticity. The exploitation of the positive dissipation principle renders a thermodynamically consistent gradient plasticity formulation incorporating geometrically necessary dislocations.

Firstly, with this general formulation at hand, the case of *phenomenological gradient plasticity* is developed in CHAPTER 3. Thereby, not only the theoretical aspects corresponding to the gradient enhancement complemented with a loss of ellipticity analysis are envisioned but the numerical solution of the coupled problem is also investigated. For verification purposes different element formulations are compared. Chapter 3 is completed by a compact introduction of the geometrically non-linear case, which will be illustrated in a numerical example.

Following the preliminary excursion in phenomenological gradient plasticity, the general concept is ap-

plied to the case of single crystals exhibiting *single and double slip* in CHAPTER 4. After a short theoretical set up, the main issue is the performance of the derived small strain algorithm with respect to a model problem taken from the literature.

Secondly, the focus is shifted to *isotropic damage* material behavior in CHAPTER 5 which can be recast into the general framework derived in chapter 2. Next, the underlying thermodynamical aspects including a loss of ellipticity analysis are pointed out for the geometrically linear case. The appropriate algorithmic aspects are then emphasized and the numerical implementation is tested in 1D and 2D examples. Finally, chapter 5 is concluded with a compact introduction of the geometrically non-linear case which will be illustrated with the aid of a numerical example.

Then in CHAPTER 6 the underlying numerical scheme as used throughout the thesis with particular reference to the two-field formulation of isotropic damage will be coupled to the *Material Force Method*. Thereby, the gradient of the damage variable enters the definition of the discrete material node point forces. Moreover, the identification of spurious material forces acts as a sensitive indicator of insufficient mesh discretization. Several examples emphasize the influence of the damage zone in front of a crack tip.

Lastly, an overall SUMMARY concludes the thesis together with a brief outline of open questions due to the simplifications and assumptions applied in this thesis, which is complemented by suggestions of possible future work.





# Einleitung

Es ist das Ziel dieser Dissertation, eine physikalisch motivierte, thermodynamisch konsistente Formulierung von inelastischem Materialverhalten unter Berücksichtigung der dem Material eingepprägten *Mikrostruktur* herzuleiten. Dabei soll neben der Erarbeitung der theoretischen Grundlagen, die algorithmische Aufarbeitung und numerische Implementation des abgeleiteten Materialmodelles im Mittelpunkt stehen. Hierbei sollen im Wesentlichen zwei inelastische Materialverhalten innerhalb der *Kontinuumsmechanik* detailliert behandelt werden: einerseits sind das Prozesse, die im Rahmen der *Elastoplastizität* beschrieben werden können und andererseits Phänomene aus dem Bereich der *Schädigungsmechanik*.

Insbesondere richtet sich das Interesse im Folgenden auf *duktile kristalline Materialien*, wie z.B. Metalle, die in den meisten Ingenieurwendungen unverzichtbar sind. Ein charakteristisches Beispiel hierfür ist Stahl, der eine bedeutende Rolle im Ingenieurwesen einnimmt. Die Einsatzspannbreite könnte nicht vielfältiger sein, wobei Stahl für robuste Strukturen, wie z.B. tragende Rahmenkonstruktionen in Hochhäusern aber auch für winzige, dünne Bauteile in der Nanotechnologie eingesetzt wird. Kurzum im Allgemeinen werden zunehmend komplexere Materialien verwendet, deren erforderliche Eigenschaften auf verschiedenen Längenskalen zu finden sind. Darüber hinaus besitzen viele Materialien häufig *irreversibles* oder *inelastisches* Verhalten, das sich in den meisten Fällen im Rahmen kleiner Verzerrungen beschreiben lässt. Allerdings lassen sich auch viele Anwendungen finden, in denen große Verzerrungen eine Rolle spielen, wie z.B. bei Umformprozessen, Materialtests oder Extremlastfällen. Deshalb wird in dieser Dissertation, neben einer detaillierten *geometrisch linearen* Kontinuumsmodellierung des inelastischen Materialverhaltens, auch der *geometrisch nichtlineare* Fall behandelt.

Prinzipiell lässt sich inelastisches duktilen Materialverhalten anhand mikromechanischer Eigenschaften auf der Basis von Einkristallen beschreiben. Darüber hinaus lassen sich Mehrkristalle aus einer ungeordneten Zusammensetzung von Einkristallen bilden. Typischerweise führt die Betrachtung von Mehrkristallen auf komplexe Phänomene, wie z.B. Texturbildung, Ausbildung von Korngrenzen und damit verbundene Fragestellungen von Anisotropie u.v.m., die jedoch nicht Gegenstand dieser Dissertation sind. Stattdessen werde ich mich hier auf eine Untersuchung von Einkristallen beschränken.

Als treibender Prozess für elastoplastische Deformationen lassen sich *Versetzungen* bzw. der Versetzungsfluss physikalisch motivieren. So findet man an Kristallwänden mikroskopische Gleitstufen, die von Versetzungen herrühren. Darüber hinaus können die Versetzungen bei der 'Durchwanderung' des Kristalles auf Hindernisse treffen, sich festsetzen und somit zur Materialverfestigung beitragen. Im einfachsten Falle einer homogenen plastischen Deformation genügt es sogenannte *statistisch verteilte Versetzungen* anzusetzen. Im Rahmen einer kontinuumsmechanischen Beschreibung ist es dabei ausreichend, eine isotrope skalare interne Verfestigungsvariable als charakteristische Verfestigungsgröße zu definieren.

Weiterhin weisen Materialien in der Regel interne *Mikrodefekte* auf, die wiederum Mikroporen oder sogar Mikrorisse initiieren können. Dies kann sich bei entsprechender Belastung zur Formation von Makroporen und Makrorissen steigern oder ganz allgemein zu einer Materialschädigung führen. Im einfachsten

Fälle lassen sich solche Schädigungsprozesse mit Hilfe einer isotropen, skalaren internen Schädigungsvariablen abbilden.

Trotz steigender Rechnerleistungen ist es für viele Anwendungen zu aufwendig und nicht erforderlich, Atom für Atom im Kristallgitter abzubilden und zu verfolgen. Naheliegender ist somit eine theoretisch wie auch rechenstechnisch handhabbare Formulierung, die sich auf die phänomenologische Modellierung der Feld- und Flussterme bezüglich der Mikrostruktur, respektive Versetzungen und Mikrodefekte, im Rahmen einer kontinuumsmechanischen Herangehensweise konzentriert. Dies führt in der Regel auf komplexe gekoppelte nichtlineare Randwertprobleme, die sich häufig nur approximativ mit Hilfe numerischer Methoden berechnen lassen. Darüber hinaus gibt es zwei konkurrierende Prozesse: *Materialentfestigung* im Zuge von Schädigung und Versetzungsbewegungen auf der einen Seite und *Materialverfestigung* durch Versetzungsakkumulation an Hindernissen andererseits. Letztendlich führen Entfestigungseffekte zu Materialinstabilitäten, wie z.B. *Lokalisierung*. Für die approximative Lösung solcher Problemstellungen bietet sich in effektiver Weise die *Finite Element Methode* an. Hierbei kommt es jedoch gerade im postkritischen Bereich zu Defiziten bei Einsatz klassischerweise lokaler Kontinuumsmodelle. Dies äußert sich in pathologischer Netzabhängigkeit der numerischen Lösung. Mathematisch lässt sich dies auf den Verlust der Elliptizität der zugrunde liegenden Gleichungen zurückführen. Dadurch ergeben sich physikalisch unbrauchbare Ergebnisse, wie z.B. die Prognose von Scherbändern mit verschwindender Breite im Falle einer immer stärker verdichteten Diskretisierung.

Gerade in den letzten zwei Jahrzehnten wurde ein enormer Forschungsaufwand hinsichtlich der Modifizierung der Standardbeschreibung lokaler Kontinuumsmodelle betrieben. Dabei wird durch sogenannte Regularisierungen versucht, die mikromechanischen Interaktionen über die Einführung eines internen Längenmaßstabes zu erfassen. Einer der vielversprechenderen Ansätze basiert dabei auf der Einbeziehung von höheren Gradienten der kontinuumsmechanisch relevanten Variablen. Dies lässt sich insbesondere im Rahmen der Kristallplastizität über eine Beziehung zwischen den Versetzungsdichten bzw. Inkompatibilitäten und dem Verfestigungsverhalten physikalisch motivieren. Dabei wird im Folgenden gezeigt werden, dass sich *geometrisch notwendige Versetzungen* als Gradient der klassischen Verfestigungsvariable ausdrücken lassen und zusätzlich in der freien Helmholtz Energie mit zu berücksichtigen sind.

Die Einbeziehung der Mikrostruktur-Interaktion erfordert eine nichtlokale Erweiterung der lokalen Dissipationsungleichung. Dies führt schließlich auf die algorithmische Lösung eines gekoppelten Problems, das in Form einer Zweifeld-Formulierung im Rahmen der Finiten Element Methode berechnet wird. Dabei müssen aktive Knotensätze, wo sich inelastisches Materialverhalten entwickelt, auf globaler Knotenpunktebene ausgewählt werden, die mit einer entsprechenden Suchstrategie zu ermitteln sind.

Generell werden die zugrunde liegende Theorie und Numerik des behandelten inelastischen Materialverhaltens in dem jeweiligen Kapitel erörtert. Zu Demonstrationszwecken sind die meisten numerischen Berechnungsbeispiele eindimensional gehalten, weiterführende Beispiele basieren auf der Annahme eines ebenen Verzerrungszustandes. Die dazu erforderliche numerische Umsetzung der spezifischen Materialmodelle erfolgte im Rahmen des Finite Element Programms PHOENIX des Lehrstuhls für Technische Mechanik, siehe die dazugehörige Dokumentation.

Zur Einführung in die Thematik werden in KAPITEL 1 die verschiedenen Konzepte zur Formulierung inelastischen Materialverhaltens unter Berücksichtigung der Mikrostruktur beleuchtet. Einerseits ist es möglich, die kinematische Beschreibung mit *internen Freiheitsgraden* zu erweitern. Andererseits können stattdessen *interne Variablen* und deren Gradienten eingeführt werden. Im ersten Fall lassen sich sogenannte *Mikrospannungen* definieren, die in die Gesamtenergiebilanz eingehen und zusätzlich Gleichgewichtsaussagen über die Mikrospannungen erfordern. Der andere Ansatz geht von einem zusätzlichen

internen Beitrag in der Entropiegleichung aus und bedingt die Definition von Evolutionsgleichungen für die internen Variablen. Innerhalb dieser Dissertation wird ausschließlich das interne Variablenkonzept weitergehend verfolgt.

In KAPITEL 2 werden die wesentlichen Aspekte der geometrisch nichtlinearen *kontinuumsmechanischen Versetzungstheorie* im Rahmen der multiplikativen Elastoplastizität erläutert. Dabei liefert die konsequente Anwendung des Prinzips der positiven Dissipation eine thermodynamisch konsistente Formulierung der Gradientenplastizität unter Berücksichtigung geometrisch notwendiger Versetzungen.

Mit Hilfe dieser allgemeinen gradientenerweiterten Formulierung wird zunächst in KAPITEL 3 der *phänomenologische Fall der Gradientenplastizität* abgeleitet. Neben der theoretischen Abhandlung der thermodynamischen Grundlagen verbunden mit einer Elliptizitätsanalyse werden die numerischen Aspekte zur Lösung des gekoppelten Problems dargestellt und Simulationen eines Prototypmodells durchgeführt. Hierbei werden verschiedene Elementformulierungen untersucht und miteinander verglichen. Das Kapitel schließt mit einer kompakten Ausführung des geometrisch nichtlinearen Falles ab, der anhand eines numerischen Beispiels illustriert wird.

Entsprechend der in Kapitel 3 aufgestellten phänomenologischen Formulierung wird das allgemeine Konzept in KAPITEL 4 auf den Fall der Einkristallplastizität für Ein- und Doppelgleitkinematiken angewendet. Nach einer kurzen theoretischen Einführung in die Kristallkinematik, wird der hergeleitete Algorithmus anhand eines Modellproblems aus der Literatur getestet.

Schließlich wird in KAPITEL 5 der Schwerpunkt auf *isotrope Schädigung* verlagert. Das Schädigungsmodell lässt sich wiederum mit Hilfe der allgemeinen Formulierung in Kapitel 2 herleiten. Dabei werden zunächst die thermodynamischen Grundlagen für den geometrisch linearen Fall, verbunden mit einer Elliptizitätsanalyse, erarbeitet. Anschließend wird die algorithmische Umsetzung beschrieben und die numerische Umsetzung in ein- und zweidimensionalen Beispielen getestet. Das Kapitel 5 schließt mit einer kompakten Ausführung des geometrisch nichtlinearen Falles ab, der anhand eines numerischen Beispiels illustriert wird.

Darüber hinaus wird in KAPITEL 6 das numerische Schema, welches dieser Dissertation zugrunde liegt, im Hinblick auf die Zweifeldformulierung bei isotroper Schädigung mit der *Methode der materiellen Kräfte* gekoppelt. Dabei wird der Gradient der Schädigungsvariablen für die Definition diskreter materieller Knotenpunktkräfte verwendet. Ein Vorzug dieser Methode ist die Identifikation von materiellen Fehlkräften, die zur Kennzeichnung unzureichender Netzdiskretisierungen herangezogen werden kann. Des Weiteren werden zahlreiche numerische Beispiele vorgestellt, die den Einfluss der Schädigungszone auf die Rissspitze untersuchen.

Zu guter Letzt werden in einer Zusammenfassung die Ergebnisse der Dissertation festgestellt und in einem kurzem Ausblick auf weiterführende Fragestellungen und auf Punkte, die aufgrund der getroffenen Annahmen offen geblieben sind, hingewiesen.



# Chapter 1

## Concepts of the formulation of inelastic materials with microstructure

In standard local continuum formulations microstructural interactions are neglected. That means no reference to any characteristic length accounting for the structural size of the material is incorporated. There are nevertheless several experimental evidences for microstructural interactions within e.g. plastic deformation phenomena dating back to e.g. the Hall-Petch effect (Hall 1951, Petch 1953), dislocation related hardening effects, see Kocks (1960), or grain size effects in the works by Ashby (1970) which exist. Furthermore, recent micro-scale experiments support the size effect especially in metals such as Stolken and Evans' micro-bend experiments (1998), micro-twist tests on thin copper wires by Fleck et al. (1994), as well as a variety of indentation tests in the sub-micrometer depth regime investigated by e.g. Stelmashenko et al. (1993), Ma and Clarke (1995), Nix and Gao (1998), Tymiak et al. (2001). The underlying physical interpretation is related to the development of geometrically necessary dislocations that cause enhanced hardening. Thereby, the continuum dislocation theory provides a strong tool relating the geometrically necessary dislocations to the curvature of the crystal lattice or to higher gradients of the state variables. In this thesis, the interest is focused on inelastic material behavior, even though, the necessity for enhanced continuum models also arises in elastic bodies if one would like to, e.g., capture dispersion of elastic waves for wave lengths approaching the scale of the atomic lattice, see Eringen (1972). One may also be interested in how to set the length scale of surface instabilities that develop in elastic bodies, see Vardoulakis et al. (1995) or how to describe elastic properties of dislocations and disclinations within a gradient theory, see e.g. Gutkin (2000).

Apart from the physical consideration<sup>1</sup> that microstructural interactions have to be taken into account to fully describe inelastic material behavior, there are shortcomings with respect to the computational treatment of classical local materials that are simple in the sense of Noll (1972) and exhibit softening. They fail to provide mesh objective results after the onset of localization, that translates mathematically into a loss of ellipticity of the governing equations as outlined in Benallal et al. (1993). This renders physically meaningless results which are displayed in a vanishing localized zone and zero amount of dissipated energy driving the failure process.

As a simple remedy one may think of the adjustment of the stress-strain diagram depending on the element size which corresponds to a mesh dependent softening modulus. The crack band model by Bažant and Oh (1983), cohesive zone models as advocated by Needleman (1987) and Tvergaard and Hutchinson (1992) or the fictitious crack models in the spirit of Hillerborg et al. (1976) lie within the

---

<sup>1</sup>Further elaboration of a continuum theory of dislocations will be postponed to chapter 2.

range of such an approach.

Among the most effective remedies against the non-physical behavior displayed by a softening standard continuum and its numerical computation, nonstandard continuum theories have been proposed. On the one hand one may thereby distinguish theories, which introduce extra internal degrees of freedom that result in couple stresses. An additional balance equations thus becomes necessary, for an early example see the micro-polar theory of the Cosserat brothers (1909). On the other hand, the introduction of internal variables and their nonlocal counterparts, e.g. gradients, reflects the microstructural response, see e.g. Maugin and Muschik (1994) for a detailed overview. These two approaches are briefly sketched in the following. Alternatively, variational multi-scale methods to embed micro-mechanical models in the macro-mechanical continuum formulation were proposed by Garikipati (2000; 2002). Furthermore, Miehe et al. (2002) suggested an incremental variational formulation of the global homogenization problem of inelastic solid materials at finite strains whereby a global minimization problem determines the state of the so-called macro-deformation-driven microstructure for finite increments of time.

## 1.1 Internal degrees of freedom

The underlying idea is to formulate continuum models that contain additional fields representing the microstructure, which evolves or changes relative to the (global) bulk material, in response to corresponding forces. In analogy to standard continuum degrees of freedom attached to each material point additional (internal) degrees of freedom, also denoted as *order parameters*<sup>2</sup>, are taken into account by energetical means. The corresponding so-called 'microforces' contribute to the total energy flux and supply rate and applying, e.g., the principle of virtual power renders additional microforce balance equations analogous with the classical momentum balance.

As mentioned above an early attempt in continuum mechanics in this regard of a 'multifield theory' is that of the Cosserat brothers (1909), which was utilized in the mechanics of rods and shells by Ericksen and Truesdell (1958), see also Truesdell and Toupin (1960). Generalizations of this theory, where the additional degrees of freedom are represented by additional director-like vector-valued fields are due to Toupin (1962), Mindlin (1965b) or recently under geometrical considerations due to Epstein and Leon (1998).

The application of micropolar continua to localization problems was proposed by Mühlhaus and Vardoulakis (1987), de Borst and Mühlhaus (1991), Dietsche et al. (1993), Ehlers and Volk (1997). Furthermore a Cosserat based approach to single-elastoviscoplasticity at finite deformation was given by Forest (1997).

Alternative approaches, for an overview see Svendsen (1999) and Mariano (2002), are, e.g., micro-morphic continua, see Mindlin (1965a) or Eringen and Kafadar (1976) extended by Goodman and Cowin (1972) and specialized by Capriz (1989) to 'affine degrees of freedom'. Furthermore, liquid crystal models were analyzed by Ericksen (1961). These theories can be unified by a representation in terms of a fiber bundle, as was shown by Svendsen (1996).

Motivated by the phase transition theory of Landau-Ginzburg, see Kittel (1971) as well as the theory of material inhomogeneities of Eshelby (1951; 1970), the balance of microforces was introduced by Fried and Gurtin (1993; 1994) and Fried (1996) to model the evolution of configurational order during phase transitions. Based on configurational forces, Gurtin (2000) developed a plasticity theory of single crystals accounting for additional degrees of freedom. A so-called deformation theory of plasticity with strain

---

<sup>2</sup>The term 'order parameter' is borrowed of the Landau-Ginzburg theory of phase transition assigning a variable of state which is essentially zero above the temperature of the phase transition and nonzero below.

gradient extensions of the free energy in terms of a power function was motivated by Fleck et al. (1994). Based on dislocation processes, a gradient plasticity theory was worked out by Shizawa and Zbib (1999) and alternatively by Cermelli and Gurtin (2001).

In addition to that, the concept of latent microstructure was introduced by Capriz (1995) indicating that the theory of internal variables can be considered as a multifield theory with appropriate internal constraints. Another approach is based on a gradient generalization of the classical internal variable approach combined with the principle of virtual power, see Maugin (1980) and more recently discussed by Maugin and Muschik (1994). The differences between internal variable formulation and additional degrees of freedom are thereby contrasted. Neglecting micro-inertia associated with additional degrees of freedom, an internal variable formulation can be obtained as a 'special case', but the physical meaning of the internal variables surfaces in additional contributions to the entropy, whereas additional degrees of freedom contribute to the total energy which was also emphasized in Svendsen (2002).

## 1.2 Internal variables

The underlying idea is the introduction of internal variables of state in addition to the usual 'observable' variables of state according to Bridgman, see Maugin (1999). The dependent variables, e.g., stress derived by a constitutive equation are then in general a function of both independent observable and internal variables. The latter necessitates the definition of an evolution equation characterizing its temporal course. Thereby, internal variables are not coupled to any external (micro)force and hence are 'not observable' in the sense that there is no mean of direct outside control, e.g., via prescription of traction-like forces. First initiators of thermodynamic formulations with internal variables date back to Meixner (1961), Coleman and Gurtin (1967) as well as Lubliner (1969; 1972; 1973). They related this approach to the generalized theory of Rational Thermodynamics in the spirit of Coleman, Noll and Truesdell developed in the 1960s.

In contrast to internal degrees of freedom, which contribute to the total energy, internal variables do not appear beforehand in the mechanical work statement of the first law of thermodynamics. Instead of which they are introduced in terms of an additional internal power term in the entropy equation, which is entirely dissipated inside the system. The necessary evolution equation will follow from an appropriately generalized dissipation potential as will be shown in the subsequent chapters.

The general set up for inelastic material based on the outlined framework can be related to the works of Mandel (1972) and Lubliner (1984; 1986). Recent approaches can be found in profound textbooks, e.g. in Maugin (1999), Nguyen (2000) and Jirasek and Bažant (2001). In the special case of multiplicative hyperelasto-plasticity, several fundamental contributions are due to Weber and Anand (1990), Cuitino and Ortiz (1992), Simo and Miehe (1992), Miehe and Stein (1992) as well as Steinmann (1996).

On the one hand, the incorporation of microstructure in terms of internal variables and their spatial gradients, in particular, higher order displacement gradients, dates back to Dillon and Kratochvil (1970), Maugin (1980), Aifantis (1984; 1987; 1992). Further developments were analyzed by, e.g., Fleck and Hutchinson (1993) and Chambon et al. (1998). Beforehand, Lasry and Belytschko (1988) coined the notion of localization limiters. A variational framework to gradient plasticity was proposed by Mühlhaus and Aifantis (1991), a corresponding gradient theory of phenomenological plasticity was developed by de Borst and Mühlhaus (1992). The gradient effect is frequently incorporated by a Laplacian of the internal variable into the yield condition, see, e.g., Zbib and Aifantis (1992), Comi and Perego (1996) or de Borst et al. (1996).

On the other hand, microstructural interactions are introduced in terms of internal variables and

their nonlocal (integral) counterparts by among others Eringen (1983), Bažant (1984), Pijaudier and Bažant(1987). The nonlocality is obtained by weighted averaging over a spatial neighborhood of a local quantity. Application of the nonlocal models to softening plasticity were proposed by Bažant and Lin (1988), Nilsson (1998), Polizzotto and Borino (1998), Ganghoffer & de Borst (2000) and recently by Polizzotto (2002).

Furthermore, thermodynamic considerations of nonlocal and gradient theories of internal variables were addressed by Edelen and Laws (1971), Maugin (1993), Polizzotto et al. (1998), Svedberg (1999), Liebe and Steinmann (2001; 2001b) and Svendsen (2002).

The universality of thermodynamics with internal variables seems intriguing because of its conceptual beauty since it does not require additional balance laws. The fundamentals of Rational Thermodynamics, in particular the consistency with the second law of thermodynamics, are invoked. Especially in the context of single crystals, the phenomenological formulation of elasto-plasticity based on physical observations motivates such an approach as will be outlined in the next chapters.



## Chapter 2

# Continuum dislocation theory

The theory of dislocations has been an active research area for several decades. As outlined in chapter 1, several experimental evidence proves the relevance of microstructural interactions that have been motivated by dislocations in crystal plasticity, see, e.g., the fundamental review article by Asaro 1983. The relation to gradient plasticity was firstly established in the work by Aifantis (1984; 1987; 1992), which gave rise to a stormy development of that topic, see, e.g., an alternative framework set up by Steinmann (1996; 1997). In particular, higher gradients can be physically justified for single and polycrystalline material like metals if one considers the dislocation density and incompatibility, respectively, see, e.g., Menzel and Steinmann (2000) and Svendsen (2002). The framework presented in this chapter dates back to an idea set forth by Nye (1953) that geometrically necessary dislocations can be related to a stress free curvature of the crystal lattice. With this at hand, Seeger (1955) and Kröner (1958) developed a geometrically linear continuum theory of dislocations yielding the computation of residual stresses for prescribed distributions of dislocations.

Alternatively, a relation between the kinematics of dislocations and the torsion within a non-Riemann geometry was established by Kondo (1952), Bilby et al. (1955). These findings paved the way for a geometrically non-linear continuum theory of dislocations provided by Kröner and Seeger (1959), Kröner (1960) and Anthony (1970). For a profound overview on continuum dislocations, the interested reader is referred, e.g., to Kosevich (1979), Truesdell and Noll (1992, Sect. 34), Shizawa and Zbib (1999) and Acharya and Bassani (2000) and the literature cited therein.

In this thesis the concept of dislocations and their flow along slip systems according to the lattice structure of the crystal serves as a basis of phenomenological continuum modeling of inelasticity, in particular single crystal plasticity. In this context, the dislocation flow determines the plastic deformation process. In addition to the initial activation barrier, the accumulating arrest of single dislocations acts as an obstacle for further dislocation flow. Thereby, the dislocation density may be split into *statistically stored dislocations* related to homogeneous plastic deformations and *geometrically necessary dislocations*, which is needed to support an inhomogeneous plastic deformation after removal of the external load. Both contributions are responsible for hardening of a crystalline material. The goal of this chapter is to set up a general thermodynamically consistent, geometrically non-linear, isothermal framework incorporating hardening contributions due to both types of dislocation density, which will be precluded by a section introducing the kinematics of the dislocation tensor.

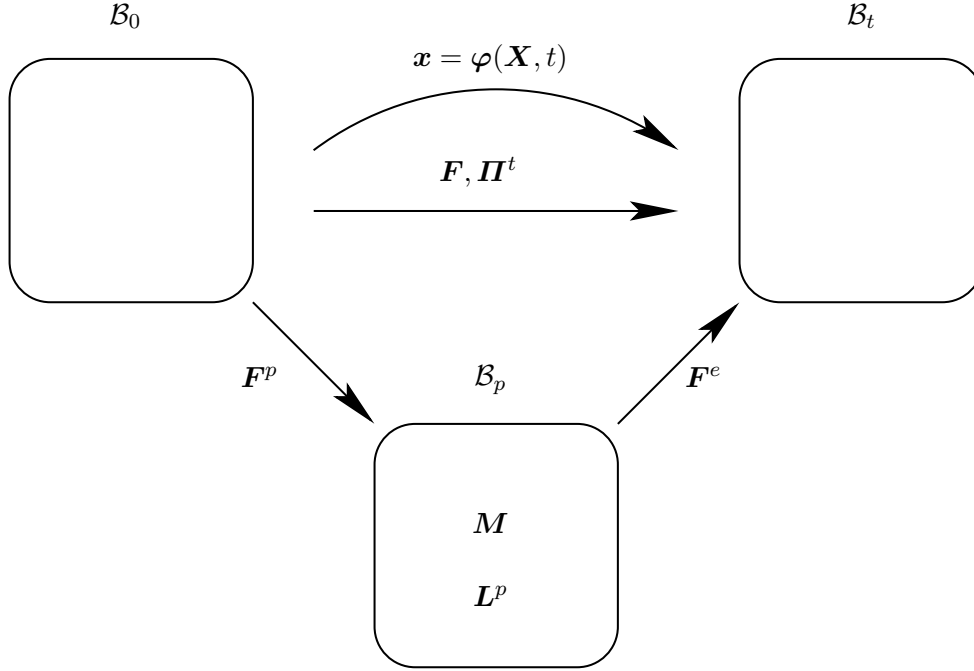


Figure 2.1: Geometrically non-linear kinematics of multiplicative elasto-plasticity

## 2.1 Kinematics of the dislocation tensor

Let  $\mathcal{B}_0$  and  $\mathcal{B}_t$  denote the material and the spatial configuration occupied by the body of interest at time  $t_0$  and  $t$  respectively, see Fig. 2.1 for a graphical representation. Then  $\varphi(\mathbf{X}, t)$  denotes the non-linear deformation map assigning the material placements  $\mathbf{X} \in \mathcal{B}_0$  to the spatial placements  $\mathbf{x} \in \mathcal{B}_t$ . Next, the corresponding tangent map is given by the deformation gradient  $\mathbf{F} = \text{Grad } \varphi$  together with the Jacobian  $J = \det \mathbf{F} > 0$ . Motivated by single crystal plasticity, the multiplicative decomposition of the deformation gradient

$$\mathbf{F} = \text{Grad } \varphi(\mathbf{X}, t) = \mathbf{F}^e \cdot \mathbf{F}^p \quad (2.1)$$

constitutes the basic kinematic assumption and introduces the so-called intermediate (isoclinic) configuration  $\mathcal{B}_p$ . For notational simplicity, the inverses  $\mathbf{F}^{-1}$ ,  $\mathbf{F}^{e-1}$ ,  $\mathbf{F}^{p-1}$  will be denoted by  $\mathbf{f}$ ,  $\mathbf{f}^e$ ,  $\mathbf{f}^p$  in the sequel. Finally, the following characteristic quantities are defined in  $\mathcal{B}_p$

$$\mathbf{M}^t = \mathbf{F}^{et} \cdot \mathbf{\Pi}^t \cdot \mathbf{F}^{pt} \quad \mathbf{L}^p = \dot{\mathbf{F}}^p \cdot \mathbf{f}^p, \quad (2.2)$$

representing the Mandel-type stress tensor  $\mathbf{M}^t$ , with  $\mathbf{\Pi}^t$  the first Piola-Kirchhoff stress tensor that enters the balance of linear momentum, and the plastic 'velocity gradient'  $\mathbf{L}^p$ , respectively, whereby the notation  $[\dot{\bullet}]$  characterizes the material time derivative.

### 2.1.1 Incompatibility measures

The viewpoint of continuum mechanics is adopted here and the dislocation density tensor is introduced based on the notion of the incompatibility or rather the Burgers vector  $\boldsymbol{\beta}$  of the intermediate configuration  $\mathcal{B}_p$ , see, e.g., the exposition in Steinmann (1996). Alternatively, the torsion tensor might be considered within the theory of a Cartan (differential) geometry.

The Burgers vector  $\boldsymbol{\beta}$  in  $\mathcal{B}_p$  may, on the one hand, be established by 'looking forward' from  $\mathcal{B}_0$  to  $\mathcal{B}_p$  to

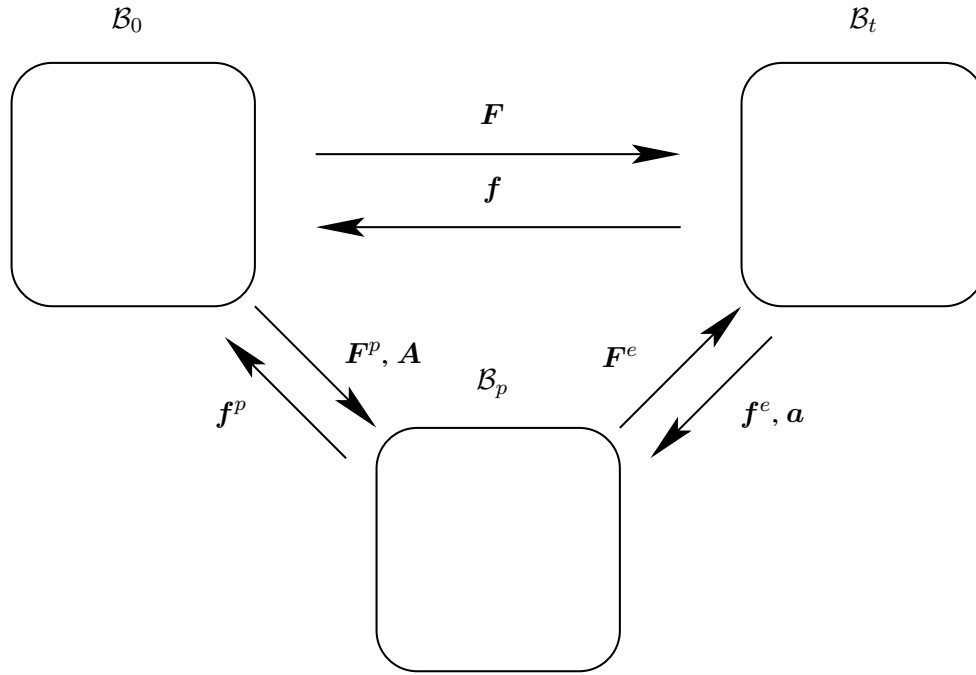


Figure 2.2: Dislocation density tensors

render the closure failure in  $\mathcal{B}_p$  of a contour integral  $\mathcal{C}_0$

$$\beta = \oint_{\mathcal{C}_0} \mathbf{F}^p \cdot d\mathbf{X} = \int_{\mathcal{A}_0} \text{Curl}^t \mathbf{F}^p \cdot \mathbf{N} \, dA = \int_{\mathcal{A}_0} \mathbf{A}^t \cdot \mathbf{N} \, dA. \quad (2.3)$$

Here, the Stokes theorem has been applied, the material  $\text{Curl}^t\{\bullet\} = -\text{Grad}\{\bullet\} : \mathbf{E}$  is defined in terms of the third order material permutation tensor  $\mathbf{E}$  in  $\mathcal{B}_0$  and  $\mathbf{N}$  is the surface normal to  $\mathcal{A}_0$ . The two-point tensor

---


$$\mathbf{A}^t = \text{Curl}^t \mathbf{F}^p \quad (2.4)$$


---

is thus introduced as dislocation density tensor  $\mathbf{A}^t : T\mathcal{B}_0 \rightarrow T\mathcal{B}_p$ .

On the other hand, the Burgers vector  $\beta$  in  $\mathcal{B}_p$  may be established by ‘looking back’ from  $\mathcal{B}_t$  to  $\mathcal{B}_p$  to render the closure failure in  $\mathcal{B}_p$  of a contour integral  $\mathcal{C}_t$

$$\beta = \oint_{\mathcal{C}_t} \mathbf{f}^e \cdot d\mathbf{x} = \int_{\mathcal{A}_t} \text{curl}^t \mathbf{f}^e \cdot \mathbf{n} \, da = \int_{\mathcal{A}_t} \mathbf{a}^t \cdot \mathbf{n} \, da. \quad (2.5)$$

Once again, the Stokes theorem has been applied, the spatial  $\text{curl}^t\{\bullet\} = -\text{grad}\{\bullet\} : \mathbf{e}$  is defined in terms of the third order spatial permutation tensor  $\mathbf{e}$  in  $\mathcal{B}_t$  and  $\mathbf{n}$  is the surface normal to  $\mathcal{A}_t$ . The two-point tensor

---


$$\mathbf{a}^t = \text{curl}^t \mathbf{f}^e \quad (2.6)$$


---

is thus introduced as dislocation density tensor  $\mathbf{a}^t : T\mathcal{B}_t \rightarrow T\mathcal{B}_p$ .

The two dislocation density tensors  $\mathbf{A}$  and  $\mathbf{a}$ , see Fig. 2.2 obviously contain the equivalent information about the compatibility of  $\mathcal{B}_p$ . Comparing Eqs. 2.3 and 2.5, the tensors  $\mathbf{A}$  and  $\mathbf{a}$  are simply related by

the Nanson formula<sup>1</sup>

$$J\mathbf{a}^t \cdot \mathbf{f}^t = \mathbf{A}^t. \quad (2.7)$$

This relation follows as well by a direct computation: To this end, the material gradient of  $\mathbf{F}$  is at first determined based on the multiplicative decomposition

$$\text{Grad } \mathbf{F} = \text{Grad } \mathbf{F}^e : [\mathbf{F}^p \bar{\otimes} \mathbf{1}] + \mathbf{F}^e \cdot \text{Grad } \mathbf{F}^p. \quad (2.8)$$

Here the non-standard dyadic product  $[\{\bullet\} \bar{\otimes} \{\star\}]_{ijkl} = \{\bullet\}_{ik} \{\star\}_{jl}$  of two second order tensors  $\{\bullet\}$  as well as  $\{\star\}$  has been used and  $\mathbf{1}$  denotes the second order identity map.

Next, the relation  $\text{Grad } \mathbf{F}^e = -\mathbf{F}^e \cdot \text{grad } \mathbf{f}^e : [\mathbf{F}^e \bar{\otimes} \mathbf{F}]$  is taken into account, i.e.

$$\text{Grad } \mathbf{F} = -\mathbf{F}^e \cdot \text{grad } \mathbf{f}^e : [\mathbf{F} \bar{\otimes} \mathbf{F}] + \mathbf{F}^e \cdot \text{Grad } \mathbf{F}^p. \quad (2.9)$$

Finally, the compatibility of  $\mathcal{B}_0$  is exploited together with the relation  $\mathbf{e} = J^{-1}[[\mathbf{F} \bar{\otimes} \mathbf{F}] : \mathbf{E} \cdot \mathbf{F}^t]$  between the spatial and the material permutation tensors to render the same result for the dislocation density tensors as given above based on the Nanson formula, i.e.

$$\text{Curl}^t \mathbf{F} = \mathbf{F}^e \cdot [-J \text{curl}^t \mathbf{f}^e \cdot \mathbf{f}^t + \text{Curl}^t \mathbf{F}^p] = \mathbf{0}. \quad (2.10)$$

In this thesis, the restriction to a setting referring to the reference or intermediate configuration is applied since a non-spatial framework turns out to be especially suitable in view of numerical applications, compare with Steinmann (1999).

## 2.2 Exploitation of the Positive Dissipation Principle

With the above-mentioned kinematic arguments at hand, in particular, a relation between the plastic deformation gradient  $\mathbf{F}^p$  and the fundamental dislocation density  $\mathbf{A}$  has been obtained, which characterizes inhomogeneous plastic deformations. Therefore, besides the statistically stored dislocation density represented by a scalar internal variable  $\kappa$ , the geometrically necessary dislocation density, represented by  $\mathbf{A}$ , is also incorporated in the free Helmholtz energy  $\Psi_0$  per unit volume. Thereby, the following additively decomposed format is assumed

$$\Psi_0 = \Psi_0^{mac}(\mathbf{F}^e) + \Psi_0^{dis}(\mathbf{A}) + \Psi_0^{har}(\kappa). \quad (2.11)$$

Here,  $\Psi_0$  is decomposed into a macro, a dislocation and a (isotropic) hardening part for convenience of exposition. Then, exploiting the local format of the Clausius-Duhem inequality incorporating the nonlocality residual  $\mathcal{P}_0$  according to the arguments by Polizzotto and Borino (1998)

$$\mathcal{D}_0 = \mathbf{\Pi}^t : \dot{\mathbf{F}} - \dot{\Psi}_0 + \mathcal{P}_0 \geq 0 \quad (2.12)$$

renders the familiar constitutive relations for the first Piola-Kirchhoff stress tensor  $\mathbf{\Pi}^t$  and the drag stress  $H$  as well as the hyperstress  $\mathbf{Y}^t$  as thermodynamically conjugated to  $\mathbf{A}$

$$\mathbf{\Pi}^t = \frac{\partial \Psi_0^{mac}}{\partial \mathbf{F}^e} \cdot \mathbf{f}^p \quad H = \frac{\partial \Psi_0^{har}}{\partial \kappa} \quad \mathbf{Y}^t = \frac{\partial \Psi_0^{dis}}{\partial \mathbf{A}}. \quad (2.13)$$

<sup>1</sup>Classically relating surface elements in  $\mathcal{B}_0$  to corresponding elements in  $\mathcal{B}_t$  via  $\mathbf{n} da = J \mathbf{f}^t \cdot \mathbf{N} dA$

Please note that the appropriate nonlocality residual  $\mathcal{P}_0$  accounts for the energy exchanges between the particles in the active plastic loading part  $\mathcal{B}_0^p \subseteq \mathcal{B}_0$  due to the mentioned microstructural interactions, compare with Edelen and Laws (1971). These energy exchanges do not affect the system's global energy but must be taken into account when a portion of the body is considered. Therefore, the nonlocality residual must satisfy the so-called insulation condition

$$\int_{\mathcal{B}_0^p} \mathcal{P}_0 \, dV = 0, \quad (2.14)$$

see again Polizzotto and Borino (1998). This means that no energy exchanges occur between the particles in  $\mathcal{B}_0^p$  and those outside  $\mathcal{B}_0^p$ , thus the local dissipation inequality  $\mathcal{D}_0 = \mathbf{\Pi}^t : \dot{\mathbf{F}} - \dot{\Psi}_0 + \mathcal{P}_0 \geq 0$  is true for the whole body  $\mathcal{B}_0$ , but with  $\mathcal{P}_0 = 0$  at points not belonging to  $\mathcal{B}_0^p$ . The proposal advocated here is comparable to the approach by Maugin (1990), who introduced an additional internal power term containing the internal variable and its gradient in the entropy statement, which is entirely dissipated inside the system instead of being developed against the exterior and is thus not influencing the global energy statement.

Based on Eq. (2.13), the reduced format of the local dissipation inequality reads

---


$$\mathcal{D}_0 = \mathbf{M}^t : \mathbf{L}^p - \mathbf{Y}^t : \dot{\mathbf{A}} - H\dot{\kappa} + \mathcal{P}_0 \geq 0. \quad (2.15)$$


---

Note that the gradient of  $\mathbf{F}^p$  enters the local dissipation inequality via  $\mathbf{A}$ , whereby an evolution equation for  $\mathbf{F}^p$  has to be extracted. To overcome this non-trivial task, the proposal of Polizzotto and Borino (1998) is followed by introducing a suitable choice for the bilinear form of the dissipation power as follows

$$\mathcal{D}_0 = \bar{\mathbf{M}}^t : \mathbf{L}^p - H\dot{\kappa} \geq 0. \quad (2.16)$$

Thus, the quasi-nonlocal<sup>2</sup> quantity  $\bar{\mathbf{M}}$  is advocated, which is identified as thermodynamically conjugated to the evolution of the plastic 'velocity gradient'  $\mathbf{L}^p$ . Comparison of the remaining dissipation inequality (2.15) and the bilinear form (2.16) renders an expression for the nonlocality residual

$$\mathcal{P}_0 = \mathbf{Y}^t : \dot{\mathbf{A}} - \mathbf{M}^t : \mathbf{L}^p + \bar{\mathbf{M}}^t : \mathbf{L}^p. \quad (2.17)$$

Then, based on the relation

$$\mathbf{Y} : \text{Curl}^t \dot{\mathbf{F}}^p = [\text{Curl}^t \mathbf{Y} \cdot \mathbf{F}^{pt}] : \mathbf{L}^p + \text{Curl}^t(\mathbf{Y}^t \cdot \dot{\mathbf{F}}^p) : \mathbf{1} \quad (2.18)$$

and applying the insulation condition (2.14) as well as invoking Gauss theorem yields

$$\begin{aligned} \int_{\mathcal{B}_0^p} \mathcal{P}_0 \, dV &= \int_{\mathcal{B}_0^p} \left[ \text{Curl}^t \mathbf{Y} \cdot \mathbf{F}^{pt} - \mathbf{M}^t + \bar{\mathbf{M}}^t \right] : \mathbf{L}^p \, dV \\ &+ \int_{\partial \mathcal{B}_0^p} [\mathbf{Y} \cdot \text{spn}(\mathbf{N})] : \dot{\mathbf{F}}^p \, dA = 0, \end{aligned} \quad (2.19)$$

which must be identically satisfied. From Eq. (2.19), the following sufficient conditions result in

---


$$\bar{\mathbf{M}}^t = \mathbf{M}^t - \text{Curl}^t \mathbf{Y} \cdot \mathbf{F}^{pt} \text{ in } \mathcal{B}_0^p \quad \text{and} \quad [\mathbf{Y} \cdot \text{spn}(\mathbf{N})] : \dot{\mathbf{F}}^p = 0 \text{ on } \partial \mathcal{B}_0^p. \quad (2.20)$$


---

<sup>2</sup>The terminology quasi-nonlocal is chosen subsequently for the proposed model in a gradient format in distinction to nonlocal models in an integral format.

The only driving force conjugated to the evolution of  $L^p$  is therefore identified as the quasi-nonlocal relative stress  $\bar{M}$ . The latter expression renders two conditions according to a decomposition of the plastic subdomain boundary into an external and internal part  $\partial\mathcal{B}_0^p = \partial\mathcal{B}_{0_{int}}^p \cup \partial\mathcal{B}_{0_{ext}}^p$ . Thereby, the so-called constitutive boundary condition of Neumann type is imposed on the external plastic boundary  $\partial\mathcal{B}_{0_{ext}}^p \subseteq \partial\mathcal{B}_0$

$$\mathbf{Y} \cdot \text{spn}(\mathbf{N}) = \mathbf{0} \quad \text{on} \quad \partial\mathcal{B}_{0_{ext}}^p, \quad (2.21)$$

whereby  $\text{spn}\{\bullet\}$  denotes the spin of vector  $\{\bullet\}$ . On the internal plastic boundary  $\partial\mathcal{B}_{0_{int}}^p$ , the so-called continuity boundary condition of Dirichlet type

$$\dot{\mathbf{F}}^p = \mathbf{0} \quad \text{on} \quad \partial\mathcal{B}_{0_{int}}^p \quad (2.22)$$

must be added in order to assure continuity of the stress rate  $\dot{\mathbf{H}}$  across  $\partial\mathcal{B}_{0_{int}}^p$ .

Consequently, for the present case of gradient plasticity, based on Eq. (2.16), a yield condition is readily motivated as

$$\Phi = \varphi(\bar{M}^t) - [Y_0 + H] \leq 0. \quad (2.23)$$

The consideration of the relative stress  $\bar{M}$  as defined in Eq. (2.20) in the yield condition corresponds to classical elasto-plasticity with consideration of kinematic hardening whereby the dislocation stress  $\text{Curl}^t \mathbf{Y}$  resembles a backstress.

Here, the theory is complemented with associated evolution laws for  $L^p$  and  $\dot{\kappa}$

$$L^p = \lambda \frac{\partial \Phi}{\partial \bar{M}^t} \quad \text{and} \quad \dot{\kappa} = -\lambda \frac{\partial \Phi}{\partial H} = \lambda \quad (2.24)$$

whereby  $\lambda \geq 0$  denotes here the plastic multiplier. Remarkably, the evolution equations retain the same structure as for the classical local formulation. In addition, the set of Karush-Kuhn-Tucker equations and the consistency condition read as

$$\Phi(\bar{M}^t, H) \leq 0 \quad \dot{\gamma} \geq 0 \quad \dot{\gamma} \Phi(\bar{M}^t, H) = 0 \quad \dot{\gamma} \dot{\Phi}(\bar{M}^t, H) = 0. \quad (2.25)$$

Finally, for an equivalent stress  $\varphi(\bar{M}^t)$  which is homogeneous of degree one in  $\bar{M}$ , the positive dissipation inequality renders in the case of plastic loading

$$\mathcal{D}_0 = \dot{\gamma} \left[ \bar{M}^t : \frac{\partial \Phi}{\partial \bar{M}^t} - H \right] = \dot{\gamma} \left[ \varphi(\bar{M}^t) - [Y_0 + H] \right] + \dot{\gamma} Y_0 = \dot{\gamma} Y_0 \geq 0. \quad (2.26)$$

### 2.2.1 Simplified gradient model

The above derived general gradient model of dislocation based multiplicative plasticity can be recast into the mathematical framework of multisurface crystal plasticity as outlined, for example, in the works of Koiter (1960) and Mandel (1972). Thereby, the multiple constraints are the yield criterion functions on the given slip planes that can be linearly dependent or redundant. For a discussion of possible non-uniqueness of the set of active systems for a given deformation mode, see, e.g., Taylor (1938), Kocks (1970) or Havner (1982). For a full outline of the underlying theory and numerical treatment in terms of single crystals, the interested reader is referred to Steinmann and Stein (1996), Miehe (1996) and references cited therein. Considering the treatment of ambiguity problems arising in multisurface plasticity, various ways can be applied for a remedy, e.g., by viscoplastic regularization as proposed by Cuitino and Ortiz (1992) or by a so-called ultimate algorithm for a rate-independent theory by Borja

and Wren (1993). Alternatively, Anand and Kothari (1996) used a generalized inverse approach to solve a system of redundant constraints of rate-independent single crystal plasticity. This development motivated Miehe and Schröder (2001) to recently propose a kinematic alternative in terms of a general inverse regularization of the rate-independent case.

First of all, the restriction to a setting of simplified gradient inelasticity is envisioned in the following. Thus, the most simple case of a single crystal with only one active slip system is considered; or rather a one-dimensional setting applicable to phenomenological inelasticity.

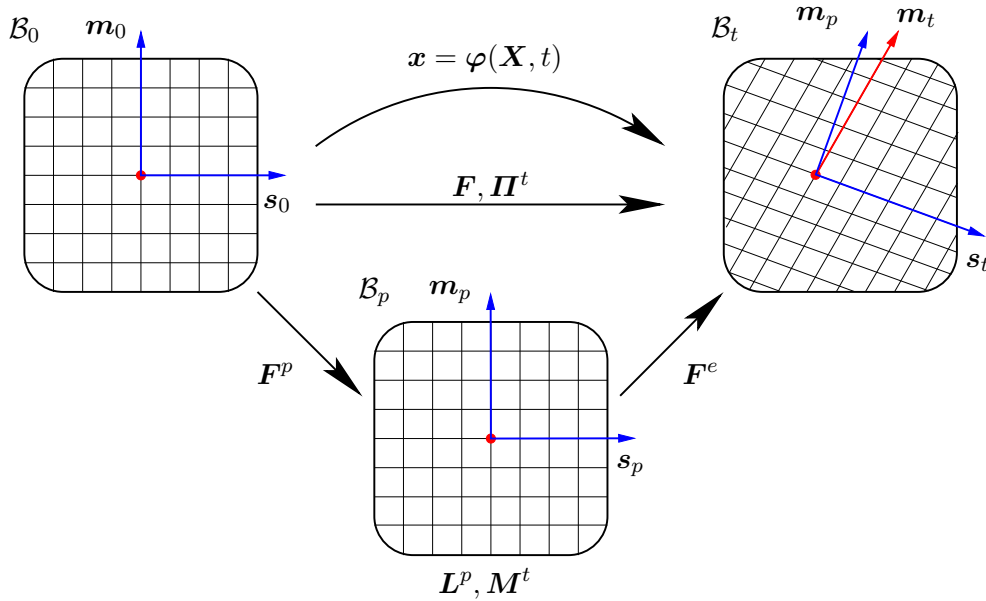


Figure 2.3: Single slip kinematics in a single crystal

In this context, a specific format of the plastic part of the deformation gradient in terms of simple shear is considered

$$\mathbf{F}^p = \mathbf{1} + \gamma \mathbf{s}_p \otimes \mathbf{m}_0 \quad \text{and} \quad \mathbf{f}^p = \mathbf{1} + \gamma \mathbf{s}_0 \otimes \mathbf{m}_p, \quad (2.27)$$

which is obvious if only one single slip system is taken into account, see Fig. 2.3. Here the scalar  $\gamma$  represents the corresponding shear number and the vectors  $s_0$ ,  $m_0$  and  $s_p$ ,  $m_p$  characterize the slip direction and the slip plane normal in  $\mathcal{B}_0$  and  $\mathcal{B}_p$ , respectively, whereby  $s_p \cdot m_0 = 0$  is true. That means, the vectors  $m_p$  and  $s_p$  are assumed to coincide with the corresponding directions in the material configuration  $s_0$  and  $m_0$ , i.e., the lattice vectors of a single-crystalline micro structure are not affected by the action of  $F^p$ , see Le and Stumpf (1998) for an outline. Hence, the intermediate configuration  $\mathcal{B}_p$  is also denoted an isoclinic configuration. Moreover,  $s_p$  and  $m_p$  can be transformed with  $F^e$  via co- and contra-variant push-forward, respectively, into the spatial configuration  $\mathcal{B}_t$  as follows

$$\mathbf{m}_t = \mathbf{f}^{et} \cdot \mathbf{m}_p \quad \text{and} \quad \mathbf{s}_t = \mathbf{F}^e \cdot \mathbf{s}_p. \quad (2.28)$$

Note that  $m_t$  acts as normal vector to the slip plane in  $\mathcal{B}_t$ , whereas the tangent vector along the distorted lattice is denoted by  $\bar{m}_t$ . Obviously, orthogonality is lost  $s_t \cdot \bar{m}_t \neq 0$  due to the elastic deformation process.

Lastly, the material time derivative of  $F^p$  is obtained by

$$\dot{L}^p = \dot{\gamma} \mathbf{s}_p \otimes \mathbf{m}_p \rightarrow \dot{F}^p = \dot{\gamma} \mathbf{s}_p \otimes \mathbf{m}_0 \quad (2.29)$$

Based on the simple shear behavior of a single slip system, the computation of the material time derivative of the dislocation density tensor  $\mathbf{A}$  as introduced in Eq. 2.4 ends up as

$$\dot{\mathbf{A}} = \text{Curl} \dot{\mathbf{F}}^p = \mathbf{E} : [\text{Grad } \dot{\gamma} \otimes \mathbf{m}_0 \otimes \mathbf{s}_p] \quad (2.30)$$

with  $\mathbf{s}_p, \mathbf{m}_0 \doteq \text{const.}$  Thus, for a given slip system, the rate of the dislocation density tensor is completely defined by the material gradient of the rate of the hardening variable. In the sequel the abbreviations  $\mathbf{K} = \text{Grad } \kappa$  and  $\dot{\mathbf{K}} = \text{Grad } \dot{\kappa} = \text{Grad } \dot{\gamma}$  are applied and a free Helmholtz energy function of the reduced format is used for the general geometrically non-linear case in the following format

$$\Psi_0 = \Psi_0^{mac}(\mathbf{F}^e) + \Psi_0^{dis}(\mathbf{K}) + \Psi_0^{har}(\kappa). \quad (2.31)$$

For the geometrically linear case the corresponding free Helmholtz energy function may be identified in terms of the additive decomposition of the total strains  $\boldsymbol{\epsilon} = \boldsymbol{\epsilon}^e + \boldsymbol{\epsilon}^p$  into elastic and plastic parts

$$\Psi_0 = \Psi_0^{mac}(\boldsymbol{\epsilon}^e) + \Psi_0^{dis}(\mathbf{k}) + \Psi_0^{har}(\kappa). \quad (2.32)$$

The dislocation part of the free energy is obviously related to the rate of the gradient of the hardening variable  $\mathbf{k} = \text{grad } \kappa$ . In the next chapter, the focus will be on the small strain case, which will later on be extended to the geometrically non-linear case within a phenomenological gradient plasticity framework.



## Chapter 3

# Higher gradient continuum theory of phenomenological isotropic plasticity

The framework, which was derived earlier is, at first, applied to the geometrically linear case of phenomenological elasto-plasticity in this chapter. The main focus will thereby be on theoretical and algorithmic aspects of a gradient formulation in terms of a case study. In addition to physical considerations, the following proposed gradient plasticity formulation is based on the observation that numerical computations of localized plastic deformations in softening materials, e.g., within a finite element setting, lead to results, which depend in a pathological way on the chosen discretization. For example, shear bands in ductile materials are thereby resolved with a zero lateral width for the limiting case of infinitely refined discretizations. Clearly, in contrast to experimental observations, this unphysical behavior motivates so-called regularization methods to overcome these numerical difficulties. For the present case of phenomenological gradient plasticity, the regularizing behavior is emphasized with a loss of ellipticity analysis since loss of ellipticity corresponds to the onset of localization.

In particular, computational gradient models at the macro-level were proposed by the 'Dutch school', e.g., de Borst et al. (1991), Sluys (1992), Pamin (1994), Geers (1997). One can thereby differentiate explicit gradient models on the one hand and implicit models on the other hand, see, e.g., Peerlings (1999), Peerlings et al. (2002) in case of fracture mechanics or Pamin (1994), Jirasek and Rolshoven (2002) in case of softening plasticity for a discussion of these models.

Thermodynamically motivated formulations of gradient plasticity were derived by Svedberg (1999) and Polizzotto and Borino (1998) in the spirit of the theory, which is being focused on in this thesis.

The goal of this chapter is therefore to set up the theory and the numerics of a thermodynamically consistent formulation of gradient plasticity at small strains. Starting from the classical local continuum formulation, which fails to produce physically meaningful and numerically converging results within localization computations, a thermodynamically motivated gradient plasticity formulation is envisioned. The model is based on an assumption for the Helmholtz free energy incorporating the gradient of the internal history variable. For compatibility requirements between the internal variable and its gradient, (i) a nonlocality residual in the local dissipation inequality is incorporated, (ii) a bilinear form for the dissipation density is introduced and (iii) the insulation condition is applied to render the quasi-nonlocal drag stress, which is conjugated to the independent history variable  $\kappa$ . Then, based on a phenomenological yield condition and the postulate of maximum dissipation, an associated structure is achieved. As the distinctive feature, the Karush-Kuhn-Tucker conditions depend on the quasi-nonlocal drag stress. Furthermore, constitutive and continuity boundary conditions are derived. On the numerical side, due to this special structure, an active set search becomes necessary for the monolithic iterative solution of the

coupled problem within a typical Newton-Raphson strategy. In particular it is notable that the additional discrete algorithmic loading and unloading conditions complemented by an active set search are implemented on a nodal basis. The simultaneous solution of the discrete algorithmic Karush-Kuhn-Tucker conditions in addition to the discretized algorithmic balance of linear momentum offers an elegant solution strategy in the numerical treatment of gradient plasticity. The extension to the geometrically non-linear case follows in the example section, whereby the corresponding modeling aspects are collected in appendix B.

### 3.1 Thermodynamics of phenomenological local plasticity

To set the stage, a brief reiteration of a thermodynamically sound formulation of local plasticity is shown. In classical local plasticity the free Helmholtz energy  $\Psi$  is a function of the elastic macroscopic strain  $\epsilon^e = \epsilon - \epsilon^p$ , derived from the additive decomposition of the macroscopic strain  $\epsilon = \text{grad}^{sym} \mathbf{u}$  into an elastic and a plastic part and a microscopic internal history variable  $\kappa$ , which characterizes isotropic hardening effects

$$\Psi = \Psi(\epsilon, \epsilon^p, \kappa) = \Psi^{mac}(\epsilon - \epsilon^p) + \Psi^{har}(\kappa). \quad (3.1)$$

Here  $\Psi$  is decomposed into a macro and a hardening part for convenience of exposition. Then, exploiting the Clausius-Duhem inequality for the local dissipation  $\mathcal{D} = \boldsymbol{\sigma} : \dot{\epsilon} - \dot{\Psi} \geq 0$  renders the constitutive relations for the macroscopic stress  $\boldsymbol{\sigma}$ , the dissipative stress  $\boldsymbol{\sigma}^p$  and  $H = H(\kappa)$ , the so-called drag stress, as thermodynamically conjugated to  $\epsilon^p$  and  $\kappa$

$$\boldsymbol{\sigma} = \frac{\partial \Psi^{mac}}{\partial \epsilon} \quad \text{and} \quad \boldsymbol{\sigma}^p = \frac{\partial \Psi^{mac}}{\partial \epsilon^p} = -\boldsymbol{\sigma} \quad \text{and} \quad H = \frac{\partial \Psi^{har}}{\partial \kappa}. \quad (3.2)$$

With this at hand, the remaining dissipation inequality reads

$$\mathcal{D} = -\boldsymbol{\sigma}^p : \dot{\epsilon}^p - H\dot{\kappa} = \boldsymbol{\sigma} : \dot{\epsilon}^p - H\dot{\kappa} \geq 0. \quad (3.3)$$

Thus, a yield condition incorporating isotropic hardening is readily motivated as

$$\Phi(\boldsymbol{\sigma}, H) = \varphi(\boldsymbol{\sigma}) - Y = \varphi(\boldsymbol{\sigma}) - [Y_0 + H] \leq 0 \quad \text{with} \quad H = H(\kappa), \quad (3.4)$$

whereby the equivalent stress  $\varphi(\boldsymbol{\sigma})$  is introduced, preferably homogeneous of degree one in  $\boldsymbol{\sigma}$ , together with the initial yield stress  $Y_0$  and the current yield stress  $Y = Y_0 + H$ . Then, based on the postulate of maximum dissipation, the constrained optimization problem

$$\mathcal{L}(\boldsymbol{\sigma}, H; \dot{\epsilon}^p, \dot{\kappa}, \lambda) = -\mathcal{D} + \lambda\Phi = -\boldsymbol{\sigma} : \dot{\epsilon}^p + H\dot{\kappa} + \lambda\Phi(\boldsymbol{\sigma}, H) \rightarrow \text{stat}^1 \quad (3.5)$$

involves the Lagrange multiplier  $\lambda \geq 0$  to enforce  $\Phi \leq 0$  and renders the associated evolution laws for  $\dot{\epsilon}^p$  and  $\dot{\kappa}$

$$\dot{\epsilon}^p = \lambda \frac{\partial \Phi}{\partial \boldsymbol{\sigma}} = \lambda \frac{\partial \varphi}{\partial \boldsymbol{\sigma}} \quad \text{and} \quad \dot{\kappa} = -\lambda \frac{\partial \Phi}{\partial H} = \lambda \quad (3.6)$$

complemented by the set of Karush-Kuhn-Tucker equations and the consistency condition

$$\Phi(\boldsymbol{\sigma}, H) \leq 0 \quad \lambda \geq 0 \quad \lambda\Phi(\boldsymbol{\sigma}, H) = 0 \quad \text{and} \quad \lambda\dot{\Phi}(\boldsymbol{\sigma}, H) = 0. \quad (3.7)$$

### 3.2 Thermodynamics of phenomenological gradient plasticity

Based on the derivation for the simplified gradient model in section 2.2.1, a particular version of the free Helmholtz energy  $\Psi$  for the geometrically linear case will be considered in the sequel. It corresponds to

the general case as derived in Eq. 2.32 and can be stated as follows

---


$$\Psi = \Psi(\boldsymbol{\epsilon}, \boldsymbol{\epsilon}^p, \kappa, \boldsymbol{\kappa}) = \Psi^{mac}(\boldsymbol{\epsilon} - \boldsymbol{\epsilon}^p) + \Psi^{har}(\kappa) + \Psi^{dis}(\boldsymbol{\kappa}). \quad (3.8)$$


---

Thereby the free energy is a function of the macroscopic strain  $\boldsymbol{\epsilon}^e$  and a scalar-valued internal history variable  $\kappa$  representing isotropic hardening mechanisms together with its first gradient  $\text{grad } \kappa = \boldsymbol{\kappa}$  characterizing microstructural interactions related to geometrically necessary dislocations.

Here,  $\Psi$  is decomposed into a macro, hardening and a dislocation related part for convenience of exposition. Following the framework set up in section 2.2, the exploitation of the local format of the Clausius-Duhem inequality incorporating the nonlocality residual  $\mathcal{P}$  renders the common constitutive relations for the macroscopic stress  $\boldsymbol{\sigma}$ , the dissipative stress  $\boldsymbol{\sigma}^p$  and  $H = H(\kappa)$ , as already derived in Eq. 3.2, as well as the vectorial hardening flux  $\mathbf{H}$ , which is thermodynamically conjugated to  $\boldsymbol{\kappa}$

$$\mathbf{H} = \frac{\partial \Psi^{grad}}{\partial \boldsymbol{\kappa}}. \quad (3.9)$$

Consequently, the remaining dissipation inequality now reads

---


$$\mathcal{D} = -\boldsymbol{\sigma}^p : \dot{\boldsymbol{\epsilon}}^p - H\dot{\kappa} - \mathbf{H} \cdot \dot{\boldsymbol{\kappa}} + \mathcal{P} = \boldsymbol{\sigma} : \dot{\boldsymbol{\epsilon}}^p - H\dot{\kappa} - \mathbf{H} \cdot \dot{\boldsymbol{\kappa}} + \mathcal{P} \geq 0. \quad (3.10)$$


---

Note that the present format of the dissipation inequality suggests independent evolution equations for  $\kappa$  and  $\boldsymbol{\kappa}$ . Thus, due to the compatibility between  $\dot{\kappa}$  and  $\dot{\boldsymbol{\kappa}} = \text{grad } \dot{\kappa}$ , these evolution equations would have to be designed such that compatibility is satisfied. Therefore, the bilinear form of the dissipation power is chosen here in the following format

$$\mathcal{D} = \boldsymbol{\sigma} : \boldsymbol{\epsilon}^p - \bar{H}\dot{\kappa}. \quad (3.11)$$

For this specific model, it is thus advocated that the quasi-nonlocal quantity  $\bar{H}$  is identified as thermodynamically conjugated to the (local) evolution of the internal history variable  $\kappa$ , whereas in the general model, see Eq. 2.16, the relative stress  $\bar{\mathbf{M}}$  conjugated to  $\mathbf{L}_p$  bears the nonlocal character. This means a transition of the gradient influence from  $\bar{\mathbf{M}}$  towards  $\bar{H}$  because the rate of the plastic deformation gradient for the simplified model is completely defined by one shear number related to the single slip plane, which corresponds to the hardening variable in the phenomenological case addressed here.

Note that the same expression is elaborated if the derivations are alternatively started from a completely nonlocal setup of the 1<sup>st</sup> and 2<sup>nd</sup> law of thermodynamics, see Svedberg (1998; 1999).

Comparison of the remaining dissipation inequality (3.10) and the bilinear form (3.11) renders an expression for the nonlocality residual

$$\mathcal{P} = H\dot{\kappa} + \mathbf{H} \cdot \dot{\boldsymbol{\kappa}} - \bar{H}\dot{\kappa}. \quad (3.12)$$

Again applying the insulation condition (2.14), integration by parts and invoking Gauss theorem renders

$$\int_{\mathcal{B}^p} \mathcal{P} \, dV = \int_{\mathcal{B}^p} [H - \text{div } \mathbf{H} - \bar{H}] \dot{\kappa} \, dV + \int_{\partial \mathcal{B}^p} [\mathbf{n} \cdot \mathbf{H}] \dot{\kappa} \, dA = 0, \quad (3.13)$$

which must be identically satisfied. Thus, only one evolution equation for  $\kappa$  has to be determined. From Eq. 3.13 the following sufficient conditions result in

---


$$\bar{H} = H - \text{div } \mathbf{H} \quad \text{in } \mathcal{B}^p \quad \text{and} \quad [\mathbf{n} \cdot \mathbf{H}] \dot{\kappa} = 0 \quad \text{on } \partial \mathcal{B}^p. \quad (3.14)$$


---

Therefore the only driving force conjugated to the evolution of the independent arbitrary internal history variable field  $\kappa$  is identified as the quasi-nonlocal drag stress  $\bar{H}$ . The constitutive boundary condition of Neumann type is imposed on the external plastic boundary. Besides the constitutive boundary condition, the continuity boundary condition of Dirichlet type is applied to the internal plastic boundary. They are both derived from the latter expression of Eq. 3.14 and can be stated as follows

$$\mathbf{n} \cdot \mathbf{H} = 0 \quad \text{on} \quad \partial \mathcal{B}_{ext}^p \quad \text{and} \quad \dot{\kappa} = 0 \quad \text{on} \quad \partial \mathcal{B}_{int}^p. \quad (3.15)$$

As a consequence, the quasi-nonlocal drag stress  $\bar{H}$  equals the local drag stress  $H$  for a homogeneous solution.

As a result from the above elaborations, it can be found that compatibility between  $\dot{\kappa}$  and  $\bar{\kappa}$  is automatically satisfied. Consequently, for the present case of gradient plasticity, based on the local dissipation inequality  $\mathcal{D} \geq 0$  in bilinear form, see Eq. 3.11, a yield condition is readily motivated as

$$\Phi(\boldsymbol{\sigma}, \bar{H}) = \varphi(\boldsymbol{\sigma}) - [Y_0 + \bar{H}] \leq 0. \quad (3.16)$$

Note that the quasi-nonlocal current yield stress  $\bar{Y} = Y_0 + \bar{H}$  with  $\bar{H} = \bar{H}(\kappa, \boldsymbol{\kappa})$  is a functional rather than a function of  $\kappa$ .

Then, based on the postulate of maximum dissipation, the constrained optimization problem

$$\mathcal{L}(\boldsymbol{\sigma}, \bar{H}; \dot{\boldsymbol{\epsilon}}^p, \dot{\kappa}, \lambda) = -\mathcal{D} + \lambda \Phi = -\boldsymbol{\sigma} : \dot{\boldsymbol{\epsilon}}^p + \bar{H} \dot{\kappa} + \lambda \Phi(\boldsymbol{\sigma}, \bar{H}) \rightarrow \text{stat} \quad (3.17)$$

involves the Lagrange multiplier  $\lambda \geq 0$  to enforce  $\Phi \leq 0$  and renders the associated evolution laws for  $\dot{\boldsymbol{\epsilon}}^p$  and  $\dot{\kappa}$ . Remarkably, the evolution equations retain the same format as for the local case given in Eq. 3.6. In addition, the set of Karush-Kuhn-Tucker equations and the consistency condition read as

$$\Phi(\boldsymbol{\sigma}, \bar{H}) \leq 0 \quad \lambda \geq 0 \quad \lambda \Phi(\boldsymbol{\sigma}, \bar{H}) = 0 \quad \text{and} \quad \lambda \dot{\Phi}(\boldsymbol{\sigma}, \bar{H}) = 0. \quad (3.18)$$

Finally, for a homogeneous equivalent stress of degree one in  $\boldsymbol{\sigma}$  the positive dissipation inequation renders

$$\mathcal{D} = \lambda[\boldsymbol{\sigma} : \boldsymbol{\nu} - \bar{H}] = \lambda[\varphi(\boldsymbol{\sigma}) - [Y_0 + \bar{H}]] + \lambda Y_0 = \lambda Y_0 \geq 0. \quad (3.19)$$

Here  $\boldsymbol{\nu}$  and the initial yield stress  $Y_0$  will be defined in the following prototype model.

### 3.3 Isotropic local and gradient prototypes

For further elaborations a specific prototype model is chosen for the gradient plasticity case. For the sake of comparison an isotropic local prototype model is supplemented in Table 3.1 where the key ingredients are summarized.

Here in the macro part, the local stored energy  $W_\epsilon$  is assumed to be derived from the additive split of the total strain  $\boldsymbol{\epsilon} = \boldsymbol{\epsilon}^e + \boldsymbol{\epsilon}^p$ , while the gradient part  $W_\kappa$  is expanded into an isotropic quadratic function in  $\boldsymbol{\kappa}$ .  $K$  and  $G$  denote the bulk and shear modulus, respectively, and  $\mathcal{I}^{dev}$  is the fourth order deviatoric unit tensor<sup>2</sup>. The gradient parameter  $c \geq 0$  controls the quasi-nonlocal character of the formulation. Moreover, a linear law is adopted for the drag stress  $H(\kappa)$ , whereby the initial yield stress  $Y_0$  is introduced as well as a linear hardening modulus  $H_0$ .

<sup>2</sup>Here, the unique additive decomposition of  $\mathcal{I} = \mathcal{I}^{vol} + \mathcal{I}^{dev}$  into a volumetric and deviatoric part with  $\mathcal{I}^{vol} := \frac{1}{3}\mathbf{1} \otimes \mathbf{1}$  has been invoked.

---

<b>Free Helmholtz energy <math>\Psi</math></b>	
local	$\Psi(\boldsymbol{\epsilon}^e, \kappa) = W_\epsilon(\boldsymbol{\epsilon}^e) + \int_0^\kappa H(\hat{\kappa}) d\hat{\kappa}$
gradient	$\Psi(\boldsymbol{\epsilon}^e, \boldsymbol{\kappa}, \kappa) = W_\epsilon(\boldsymbol{\epsilon}^e) + \int_0^\kappa H(\hat{\kappa}) d\hat{\kappa} + W_\kappa(\boldsymbol{\kappa})$
Elastically stored energy	$W_\epsilon(\boldsymbol{\epsilon}^e) = \frac{1}{2} \boldsymbol{\epsilon}^e : \boldsymbol{\mathcal{E}}_\epsilon : \boldsymbol{\epsilon}^e$ with $\boldsymbol{\mathcal{E}}_\epsilon = K\mathbf{1} \otimes \mathbf{1} + 2G\boldsymbol{\mathcal{I}}^{dev}$
Gradient part of the free energy	$W_\kappa(\boldsymbol{\kappa}) = \frac{1}{2} \boldsymbol{\kappa} \cdot \boldsymbol{\mathcal{E}}_\kappa \cdot \boldsymbol{\kappa}$ with $\boldsymbol{\mathcal{E}}_\kappa = c\mathbf{1}$
<b>Yield condition of VON MISES-type</b>	
local	$\Phi(\boldsymbol{\sigma}, H) =  \text{dev } \boldsymbol{\sigma}  - [Y_0 + H] \leq 0$
gradient	$\Phi(\boldsymbol{\sigma}, \bar{H}) =  \text{dev } \boldsymbol{\sigma}  - [Y_0 + \bar{H}] \leq 0$
<b>Macroscopic stress</b>	
Cauchy stress	$\boldsymbol{\sigma}(\boldsymbol{\epsilon}^e) = \boldsymbol{\mathcal{E}}_\epsilon : \boldsymbol{\epsilon}^e$
<b>Drag stress</b>	
local	$H(\kappa) = H_0 \kappa$
quasi-nonlocal	$\bar{H}(\boldsymbol{\kappa}) = H - \text{div } \mathbf{H} = H - c \text{ div } \boldsymbol{\kappa}$
Hardening flux	$\mathbf{H}(\boldsymbol{\kappa}) = \boldsymbol{\mathcal{E}}_\kappa \cdot \boldsymbol{\kappa} = c\boldsymbol{\kappa}$
<b>Associated flow rule</b>	
	$\dot{\boldsymbol{\epsilon}}^p = \lambda \boldsymbol{\nu}$ with $\boldsymbol{\nu} = \frac{\text{dev } \boldsymbol{\sigma}}{ \text{dev } \boldsymbol{\sigma} }$
	$\dot{\kappa} = \lambda$

---

Table 3.1: Isotropic local and gradient prototype

Note that it is illustrative to consider the term  $\text{div grad } \kappa$  in the quasi-nonlocal drag stress as related to the curvature of the internal history variable profile. Thus, the plastic flow resistance is clearly increased/decreased compared to the case of local plasticity in regions with negative/positive curvature of the current internal history variable profile, thereby showing a tendency to broaden the  $\kappa$ -profile, see Fig. 3.1.

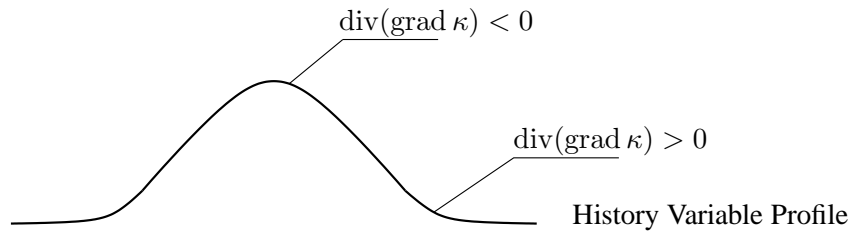


Figure 3.1: History variable profile

### 3.4 Well-posedness of the coupled problem

As mentioned in chapter 1, one of the motivations for incorporating higher gradients of the internal history variable field is to overcome the pathologies encountered in computations, which are related to the ill-posed character of the boundary value problem. As it is well known, this ill-posedness is due to the loss of the ellipticity condition, see Benallal, Billardon and Geymonat (1993).

The loss of ellipticity is commonly investigated by a wave propagation analysis. Thereby, an underlying homogeneous state is assumed before the onset of localization. The following harmonic expansion for

the rates of the displacements  $\dot{\mathbf{u}}$  and the internal history variable  $\dot{\kappa}$  is then chosen as

$$\begin{aligned}\dot{\mathbf{u}} &= \exp(ik[\hat{\mathbf{n}} \cdot \mathbf{x}])\hat{\mathbf{m}} \\ \dot{\kappa} &= \exp(ik[\hat{\mathbf{n}} \cdot \mathbf{x}])\hat{m},\end{aligned}\quad (3.20)$$

which corresponds to the assumption of stationary planar waves. Here,  $\hat{\mathbf{n}}$  and  $\hat{\mathbf{m}}$  ( $\hat{m}$ ) denote the wave propagation direction and the polarization, respectively and the scalar  $i$  and  $k$  are the imaginary number and the wave number. Based on this approach and the incremental equations for the quasi-static balance of linear momentum  $\text{div } \dot{\boldsymbol{\sigma}} = \mathbf{0}$  together with the consistency condition for plastic loading  $\lambda \dot{\Phi} = 0$  with  $\lambda > 0$ , it is then investigated if the homogeneous state admits a bifurcation into a solution of planar wave type. It is thereby assumed that the material remains in a state of loading, i.e., no discontinuous bifurcation is considered. The resulting homogeneous equation system then renders

$$\begin{bmatrix} -k^2 \mathbf{Q}_\epsilon & -ik \mathbf{Q}_\nu \\ ik \mathbf{Q}_\nu & -h - k^2 \mathbf{Q}_\kappa \end{bmatrix} \begin{bmatrix} \hat{\mathbf{m}} \\ \hat{m} \end{bmatrix} = \begin{bmatrix} \mathbf{0} \\ 0 \end{bmatrix}\quad (3.21)$$

and thus allows a closed form expression for the bifurcation condition in terms of the localization tensor

$$\det \left[ \mathbf{Q}_\epsilon - \frac{\mathbf{Q}_\nu \otimes \mathbf{Q}_\nu}{h + k^2 \mathbf{Q}_\kappa} \right] = 0 \quad \longrightarrow \quad 1 - \frac{\mathbf{Q}_\nu \cdot \mathbf{Q}_\epsilon^{-1} \cdot \mathbf{Q}_\nu}{h + k^2 \mathbf{Q}_\kappa} = 0. \quad (3.22)$$

Here, the following abbreviations for the partition of the localization tensor are introduced

$$\begin{aligned}\mathbf{Q}_\epsilon \cdot \hat{\mathbf{m}} &= [\boldsymbol{\mathcal{E}}_\epsilon : [\hat{\mathbf{m}} \otimes \hat{\mathbf{n}}]] \cdot \hat{\mathbf{n}} \\ \mathbf{Q}_\nu &= [\boldsymbol{\mathcal{E}}_\epsilon : \boldsymbol{\nu}] \cdot \hat{\mathbf{n}} \\ \mathbf{Q}_\kappa &= [\boldsymbol{\mathcal{E}}_\kappa \cdot \hat{\mathbf{n}}] \cdot \hat{\mathbf{n}} \stackrel{iso}{=} c \geq 0 \\ h &= \boldsymbol{\nu} : \boldsymbol{\mathcal{E}}_\epsilon : \boldsymbol{\nu} + E_\kappa \quad \text{with} \quad E_\kappa = \frac{\partial H}{\partial \kappa}.\end{aligned}\quad (3.23)$$

As a consequence, the critical hardening modulus follows as

$$E_\kappa^{crit} = \max_{\hat{\mathbf{n}}} (\mathbf{Q}_\nu \cdot \mathbf{Q}_\epsilon^{-1} \cdot \mathbf{Q}_\nu) - \boldsymbol{\nu} : \boldsymbol{\mathcal{E}}_\epsilon : \boldsymbol{\nu} - k^2 \mathbf{Q}_\kappa, \quad (3.24)$$

i.e., the largest hardening modulus that allows for a bifurcation into a planar wave type solution.

Thus, as a first observation for  $\mathbf{Q}_\kappa \stackrel{iso}{=} c > 0$ , the critical hardening modulus in case of gradient plasticity is less than the critical hardening modulus for local plasticity

$$E_\kappa^{local,crit} = \max_{\hat{\mathbf{n}}} (\mathbf{Q}_\nu \cdot \mathbf{Q}_\epsilon^{-1} \cdot \mathbf{Q}_\nu) - \boldsymbol{\nu} : \boldsymbol{\mathcal{E}}_\epsilon : \boldsymbol{\nu} \geq E_\kappa^{crit}, \quad (3.25)$$

i.e., the gradient plasticity case allows for stronger softening until the bifurcation condition is met.

Next, the influence of the wave length on the critical hardening modulus is investigated. To this end, the long and short wave length limits are considered corresponding to  $k \rightarrow 0$ , i.e., the incrementally homogeneous solution, and  $k \rightarrow \infty$ , i.e., the infinitely localized solution, respectively.

On the one hand, the long wave length limit results in a critical hardening modulus, which equals the local critical hardening modulus in the limit  $E_\kappa^{crit} \rightarrow E_\kappa^{local,crit}$ . Thus, the gradient formulation obviously does not effect homogeneous solutions. On the other hand, the short wave length limit renders a critical hardening parameter  $E_\kappa^{crit} \rightarrow -\infty$ , i.e., bifurcations into an incrementally localized solution are effectively excluded.

Finally, for the gradient case the critical wave number  $k$  may be bounded from below with  $E_\kappa \geq E_\kappa^{crit}$

$$0 \leq k^2 \geq \frac{1}{Q_\kappa} \left[ \max_{\hat{\mathbf{n}}} (Q_\nu \cdot Q_\epsilon^{-1} \cdot Q_\nu) - \boldsymbol{\nu} : \boldsymbol{\epsilon} : \boldsymbol{\nu} - E_\kappa \right]. \quad (3.26)$$

Thus, in case of gradient plasticity with the gradient parameter  $c$  in the range  $0 < Q_\kappa \stackrel{iso}{=} c \leq \infty$ , the corresponding wave number is in the range  $\infty > k \geq 0$ , i.e., planar wave type solutions with finite wave length exist. For the limiting case of local plasticity with zero gradient parameter  $Q_\kappa \stackrel{iso}{=} c = 0$ , the corresponding wave number is  $k \rightarrow \infty$ , thus localized solutions exist.

In summary, based on the above analysis, a regularizing influence of the gradient term is expected for softening computations. This will later on be demonstrated in the numerical example section.

### 3.5 Numerical treatment of phenomenological gradient plasticity

For gradient continua, a variety of numerical strategies, different from the ones proposed in this thesis, were investigated, e.g., by Sluys, de Borst and Mühlhaus (1993), Pamin (1994), de Borst and Pamin (1996), Peerlings et al. (1996b; 1996a), Steinmann (1999), Comi (1999) and Chambon, Cailierie and El Hassan (1998). Furthermore, Huerta and Pijaudier-Cabot (1994) studied the influence of the discretization on the regularization performance of different localization limiters. Further contributions to the numerics of phenomenological gradient plasticity at small and large strains were treated by Svedberg and Runesson (1998), Svedberg (1999) and Mikkelsen (1997). Alternatively, Benallal et al. (2002) recently proposed an implicit BEM-formulation for gradient continua and localization phenomena.

For the local continuum description an early attempt to set up a mixed finite element formulation was provided by Pinsky (1986), whereby a plastic strain-like variable is discretized in addition to the displacement field. An alternative proposal based on a complementary mixed finite element formulation is due to Simo, Kennedy and Taylor (1989), wherein the flow rule is enforced in a weak sense at the element level. Likewise, a two-field finite element formulation for elasticity coupled to damage was proposed by Florez-Lopez et al. (1994).

The numerical concept outlined here follows the proposal documented in Liebe and Steinmann (2001).

#### 3.5.1 Strong form of the coupled problem

To set the stage, the pertinent set of equations is first summarized for the solution of the coupled problem in strong form for the following developments.

Let  $\mathcal{B}$  denote the configuration occupied by an elasto-plastic solid. Then, the displacement field  $\mathbf{u} = \mathbf{u}(\mathbf{x})$  and the history variable field  $\kappa = \kappa(\mathbf{x})$  are parameterized in terms of the placements  $\mathbf{x} \in \mathcal{B}$ . These two primary fields are determined by the simultaneous solution of a partial differential equation and a set of Karush-Kuhn-Tucker complementary conditions. The boundary  $\partial\mathcal{B}$  to  $\mathcal{B}$  with outward normal  $\mathbf{n}$  is subdivided into disjoint parts whereby either Neumann or Dirichlet boundary conditions for the two solution fields  $\mathbf{u}(\mathbf{x})$  and  $\kappa(\mathbf{x})$  are prescribed.

Firstly, neglecting inertia, the equilibrium subproblem  $\mathbf{r}^u(\mathbf{u}, \kappa)$  is given by the quasi-static balance of linear momentum in  $\mathcal{B}$  as depicted in Table 3.2, whereby distributed body forces per unit volume in  $\mathcal{B}$  are denoted by  $\mathbf{b}$ .

Thereby, for the displacement field the decomposition of the total boundary reads

$$\partial\mathcal{B} = \partial\mathcal{B}^u \cup \partial\mathcal{B}^t \quad \text{with} \quad \partial\mathcal{B}^u \cap \partial\mathcal{B}^t = \emptyset. \quad (3.27)$$

---

Equilibrium subproblem			
$r^u(\mathbf{u}, \kappa)$	$= \operatorname{div} \boldsymbol{\sigma}(\mathbf{u}, \kappa) + \mathbf{b}$	$= \mathbf{0}$	in $\mathcal{B}$
	$\mathbf{u} - \mathbf{u}^p$	$= 0$	on $\partial\mathcal{B}^u$
	$\mathbf{n} \cdot \boldsymbol{\sigma}(\mathbf{u}, \kappa) - \mathbf{t}^p$	$= 0$	on $\partial\mathcal{B}^t$
Constitutive subproblem			
$r^\Phi(\mathbf{u}, \kappa)$	$= \varphi(\mathbf{u}, \kappa) - \bar{Y}(\kappa)$	$\leq 0$	in $\mathcal{B}$
	$\dot{\kappa}$	$= 0$	on $\partial\mathcal{B}_{int}^p$
	$\mathbf{n} \cdot \mathbf{H}(\kappa)$	$= 0$	on $\partial\mathcal{B}_{ext}^p$

---

Table 3.2: Strong form of the coupled problem

The balance of linear momentum is thus supplemented by Dirichlet and Neumann boundary conditions in terms of the displacement  $\mathbf{u}$  on  $\partial\mathcal{B}^u$  and the traction vector  $\mathbf{t}$  on  $\partial\mathcal{B}^t$ , respectively, see also Fig. 3.2a.

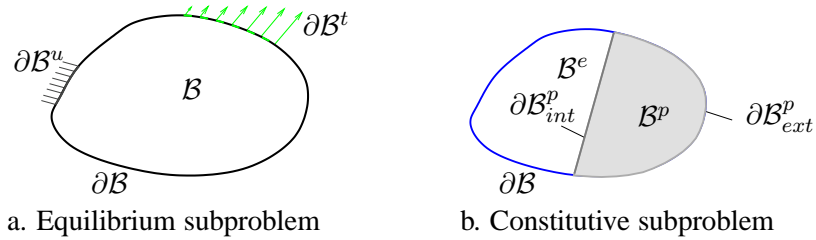


Figure 3.2: Solution domain with corresponding boundaries

Secondly, the constitutive subproblem is given in Table 3.2 by the yield condition  $r^\Phi(\mathbf{u}, \kappa)$ , which incorporates the quasi-nonlocal yield stress  $\bar{Y} = Y_0 + \bar{H}$  in terms of the quasi-nonlocal drag stress  $\bar{H} = H - \operatorname{div} \mathbf{H}$  together with the corresponding Karush-Kuhn-Tucker complementary conditions

$$r^\Phi(\mathbf{u}, \kappa) \leq 0 \quad \text{and} \quad \dot{r}^\kappa(\dot{\kappa}) = \dot{\kappa} \geq 0 \quad \text{and} \quad \dot{r}^\kappa(\dot{\kappa}) r^\Phi(\mathbf{u}, \kappa) = 0 \quad \text{in } \mathcal{B}. \quad (3.28)$$

Thereby, for the plastic solution domain the decomposition of the plastic boundary reads

$$\partial\mathcal{B}^p = \partial\mathcal{B}_{int}^p \cup \partial\mathcal{B}_{ext}^p \quad \text{with} \quad \partial\mathcal{B}_{int}^p \cap \partial\mathcal{B}_{ext}^p = \emptyset. \quad (3.29)$$

Thus, the constitutive subproblem is supplemented by Dirichlet and Neumann boundary conditions in terms of the internal history variable evolution  $\dot{\kappa}$  on  $\partial\mathcal{B}_{int}^p$  and the hardening flux  $\mathbf{n} \cdot \mathbf{H}$  on  $\partial\mathcal{B}_{ext}^p$ , respectively, see also Fig. 3.2b.

The complementary condition  $\dot{\kappa}\Phi = 0$  may be stated alternatively by decomposition of the total solution domain  $\mathcal{B}$  into an inactive elastic and an active plastic domain

$$\mathcal{B}^e = \{\mathbf{x} \in \mathcal{B} | \Phi \leq 0, \dot{\kappa} = 0\} \quad \text{and} \quad \mathcal{B}^p = \{\mathbf{x} \in \mathcal{B} | \Phi = 0, \dot{\kappa} > 0\} \quad (3.30)$$

with the additional completeness and non-overlapping requirements for the solution subdomains

$$\mathcal{B} = \mathcal{B}^e \cup \mathcal{B}^p \quad \text{and} \quad \emptyset = \mathcal{B}^e \cap \mathcal{B}^p. \quad (3.31)$$

### 3.5.2 Weak form of the coupled problem

As a prerequisite for a finite element discretization, the coupled non-linear boundary value problem has to be reformulated in weak form, see Table 3.3.



---

Equilibrium subproblem

$$\begin{aligned} G^u(\mathbf{u}, \kappa; \delta \mathbf{u}) &= \int_{\partial \mathcal{B}^t} \delta \mathbf{u} \cdot \mathbf{t}^p \, dA + \int_{\mathcal{B}} [\delta \mathbf{u} \cdot \mathbf{b} - \text{grad } \delta \mathbf{u} : \boldsymbol{\sigma}(\mathbf{u}, \kappa)] \, dV \\ &= 0 \quad \forall \delta \mathbf{u} \quad \text{in } H_1^0(\mathcal{B}) \end{aligned}$$

Constitutive subproblem

$$\begin{aligned} G^\Phi(\mathbf{u}, \kappa; \delta \kappa) &= \int_{\mathcal{B}} [\delta \kappa [\varphi(\mathbf{u}, \kappa) - Y(\kappa)] - \text{grad } \delta \kappa \cdot \mathbf{H}(\kappa)] \, dV \\ &\leq 0 \quad \forall \delta \kappa > 0 \quad \text{in } H_1^0(\mathcal{B}) \\ \dot{G}^\kappa(\dot{\kappa}; \delta \Phi) &= \int_{\mathcal{B}} \delta \Phi \dot{\kappa} \, dV \\ &\geq 0 \quad \forall \delta \Phi > 0 \quad \text{in } L_2(\mathcal{B}) \end{aligned}$$


---

Table 3.3: Weak form of the coupled problem

Firstly, the quasi-static balance of linear momentum  $\mathbf{b} = -\text{div } \boldsymbol{\sigma}$  and the corresponding Neumann boundary conditions  $\boldsymbol{\sigma} \cdot \mathbf{n} = \mathbf{t}^p$  are tested by a virtual displacement  $\delta \mathbf{u}$  to render the virtual work expression  $G^u$ .

Secondly, on the one hand, the Karush-Kuhn-Tucker condition  $\Phi \leq 0$  and the homogeneous Neumann boundary conditions  $\mathbf{n} \cdot \mathbf{H} = 0$  are tested by  $\delta \kappa$  with  $\delta \kappa > 0$  and on the other hand, the Karush-Kuhn-Tucker condition  $\dot{\kappa} \geq 0$  is tested by  $\delta \Phi$  with  $\delta \Phi > 0$  to render the global statements  $G^\Phi$  and  $\dot{G}^\kappa$ .

Based on these statements the decomposition of the solution domain  $\mathcal{B}$  into an active plastic and an inactive elastic domain  $\mathcal{B} = \mathcal{B}^p \cup \mathcal{B}^e$  and  $\emptyset = \mathcal{B}^e \cap \mathcal{B}^p$  follows implicitly as the support of those admissible test functions  $\delta \kappa, \delta \Phi$  that satisfy

$$\begin{aligned} \mathcal{B}^e &= \{\mathbf{x} \in \mathcal{B} | G^\Phi \leq 0, \dot{G}^\kappa = 0 \quad \forall \delta \kappa, \delta \Phi > 0 \quad \text{in } \mathcal{B}^e\} \\ \mathcal{B}^p &= \{\mathbf{x} \in \mathcal{B} | G^\Phi = 0, \dot{G}^\kappa > 0 \quad \forall \delta \kappa, \delta \Phi > 0 \quad \text{in } \mathcal{B}^p\}. \end{aligned} \quad (3.32)$$

This is indeed quite an implicit definition at this stage since one has to test for all possible combinations of support with all admissible test functions. Note that finally, the above decomposition corresponds to the complementary pointwise condition  $\dot{\kappa} \Phi = 0$ .

### 3.5.3 Temporal discretization of the coupled problem

The above set of equations has to be discretized in time whereby the implicit Euler backward method is applied without loss of generality. The temporal integration of the primary variables  $\mathbf{u}$  and  $\kappa$  then renders a discretized temporal update for the values  $\mathbf{u}_{n+1}$  and  $\kappa_{n+1}$ , see Table 3.4.

Firstly, the algorithmic quasi-static balance of linear momentum  $G^u = 0$  can be trivially derived.

Secondly, the algorithmic Karush-Kuhn-Tucker conditions are obtained whereby the first one represents the algorithmic yield condition  $G^\Phi \geq 0$  and the second one  $\Delta G^\kappa \geq 0$  assures positive increments of the internal history variable.

Moreover, the algorithmic decomposition of the solution domain with  $\mathcal{B} = \mathcal{B}_{n+1}^p \cup \mathcal{B}_{n+1}^e$  and  $\emptyset = \mathcal{B}_{n+1}^e \cap \mathcal{B}_{n+1}^p$  follows implicitly as the support of those admissible test functions  $\delta \kappa, \delta \Phi$  that satisfy

$$\begin{aligned} \mathcal{B}_{n+1}^e &= \{\mathbf{x} \in \mathcal{B} | G_{n+1}^\Phi \leq 0, \Delta G_{n+1}^\kappa = 0 \quad \forall \delta \kappa, \delta \Phi > 0 \quad \text{in } \mathcal{B}_{n+1}^e\} \\ \mathcal{B}_{n+1}^p &= \{\mathbf{x} \in \mathcal{B} | G_{n+1}^\Phi = 0, \Delta G_{n+1}^\kappa > 0 \quad \forall \delta \kappa, \delta \Phi > 0 \quad \text{in } \mathcal{B}_{n+1}^p\}. \end{aligned} \quad (3.33)$$

Note that the above algorithmic decomposition corresponds to the pointwise algorithmic complementary

Equilibrium subproblem

$$\begin{aligned} G^u(\mathbf{u}_{n+1}, \kappa_{n+1}; \delta \mathbf{u}) &= \int_{\partial \mathcal{B}^t} \delta \mathbf{u} \cdot \mathbf{t}_{n+1}^p \, dA + \int_{\mathcal{B}} [\delta \mathbf{u} \cdot \mathbf{b}_{n+1} - \text{grad } \mathbf{u} : \boldsymbol{\sigma}(\mathbf{u}_{n+1}, \kappa_{n+1})] \, dV \\ &= 0 \quad \forall \delta \mathbf{u} \quad \text{in } H_1^0(\mathcal{B}) \end{aligned}$$

Constitutive subproblem

$$\begin{aligned} G^\Phi(\mathbf{u}_{n+1}, \kappa_{n+1}; \delta \kappa) &= \int_{\mathcal{B}} [\delta \kappa [\varphi(\mathbf{u}_{n+1}, \kappa_{n+1}) - Y(\kappa_{n+1})] - \text{grad } \delta \kappa \cdot \mathbf{H}(\kappa_{n+1})] \, dV \\ &\leq 0 \quad \forall \delta \kappa > 0 \quad \text{in } H_1^0(\mathcal{B}) \\ \dot{G}^\kappa(\kappa_{n+1}; \delta \Phi) &= \int_{\mathcal{B}} \delta \Phi [\kappa_{n+1} - \kappa_n] \, dV \\ &\geq 0 \quad \forall \delta \Phi > 0 \quad \text{in } L_2(\mathcal{B}) \end{aligned}$$

Table 3.4: Temporal discretization of the coupled problem

condition  $[\kappa_{n+1} - \kappa_n] \Phi_{n+1} = 0$ .

### 3.5.4 Spatial discretization of the coupled problem

Finally, the algorithmic set of equations has to be discretized in space. To this end, the standard Bubnov-Galerkin finite element method is employed. The whole solution domain  $\mathcal{B}$  is decomposed into finite elements  $\mathcal{B}_e$ . Each element is characterized by nodal degrees of freedom due to the displacement field ( $\circ$ ) and additionally by nodal degrees of freedom due to the internal history variable field ( $\times$ ), see Fig. 3.3.

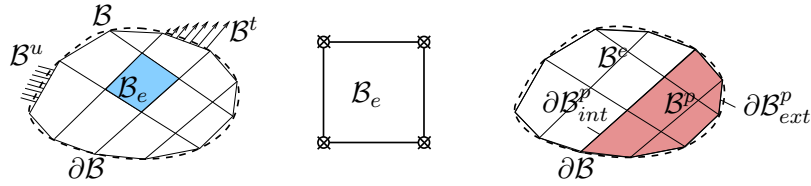


Figure 3.3: Discretized solution domain with corresponding boundaries and exemplary  $Q^0_1 Q^0_1$ -master element

Thereby, first the geometry  $\mathbf{x}$  is elementwise expanded by shape functions  $N_x^k$  in terms of the positions  $\mathbf{x}_k$  of the node points with the elementwise numbering  $k = 1, n_{en}$  corresponding to a global numbering  $K = 1, n_{np}$ , the following elementwise discretization of the solution domain is thus obtained, see Fig. 3.3

$$\mathcal{B} = \bigcup_e \mathcal{B}_e \quad \text{with} \quad \mathbf{x}^h|_{\mathcal{B}_e} = \sum_k N_x^k \mathbf{x}_k. \quad (3.34)$$

Then, in the spirit of the Bubnov-Galerkin finite element method based on the iso-parametric concept, the displacement field  $\mathbf{u}$  together with its variation  $\delta \mathbf{u}$  is elementwise expanded by the same shape functions  $N_u^k = N_x^k$  in terms of the nodal values  $\mathbf{u}_k$  and  $\delta \mathbf{u}_k$

$$\mathbf{u}^h|_{\mathcal{B}_e} = \sum_k N_x^k \mathbf{u}_k \in H_1(\mathcal{B}) \quad \text{and} \quad \delta \mathbf{u}^h|_{\mathcal{B}_e} = \sum_k N_x^k \delta \mathbf{u}_k \in H_1^0(\mathcal{B}). \quad (3.35)$$

Moreover, the history variable field  $\kappa$  together with its variation  $\delta \kappa$  is elementwise expanded by independent shape functions  $N_\kappa^k$  in terms of the nodal values  $\kappa_k$  and  $\delta \kappa_k$

$$\kappa^h|_{\mathcal{B}_e} = \sum_k N_\kappa^k \kappa_k \in H_1(\mathcal{B}) \quad \text{and} \quad \delta \kappa^h|_{\mathcal{B}_e} = \sum_k N_\kappa^k \delta \kappa_k \in H_1(\mathcal{B}). \quad (3.36)$$

Likewise, the test function  $\delta\Phi$  is discretized by the same shape functions  $N_{\Phi}^k = N_{\kappa}^k$  in terms of nodal values  $\delta\Phi_k$

$$\delta\Phi|_{\mathcal{B}_e} = \sum_k N_{\kappa}^k \delta\Phi_k \in L_2(\mathcal{B}). \quad (3.37)$$

Based on the above discretizations, the corresponding gradients  $\epsilon$  and  $\kappa$  take the elementwise format

$$\epsilon^h|_{\mathcal{B}_e} = \left[ \sum_k \mathbf{u}_k \otimes \text{grad } N_x^k \right]^{sym} \quad \text{and} \quad \kappa^h|_{\mathcal{B}_e} = \sum_k \kappa_k \text{grad } N_{\kappa}^k. \quad (3.38)$$

Note that in order to comply with the celebrated LBB-condition for mixed finite elements, the expansions for the internal history variable are typically selected from one polynomial order less than those for the displacements. Finally, the global and elementwise sets of discretization node points may be defined as

$$\mathbb{B} = \bigcup_e \mathbb{B}_e \quad \text{with} \quad \mathbb{B} = \{K | K = 1, n_{np}\} \quad \text{and} \quad \mathbb{B}_e = \{k | k = 1, n_{en}\}. \quad (3.39)$$

Then, based on the spatial discretizations of the primary variables  $\mathbf{u}$  and  $\kappa$ , the residua are collected in Table 3.5.

---

Equilibrium subproblem

$$\begin{aligned} \mathbf{R}_K^u(\mathbf{u}_{n+1}^h, \kappa_{n+1}^h) &= \mathbf{A}_e \int_{\partial\mathcal{B}_e \cap \partial\mathcal{B}^t} N_x^k \mathbf{t}_{n+1}^p \, dA + \int_{\mathcal{B}_e} [N_x^k \mathbf{b}_{n+1} - \text{grad } N_x^k \cdot \boldsymbol{\sigma}(\mathbf{u}_{n+1}^h, \kappa_{n+1}^h)] \, dV \\ &= \mathbf{0} \quad \forall K \quad \text{in } \mathbb{B} \end{aligned}$$

Constitutive subproblem

$$\begin{aligned} R_K^{\Phi}(\mathbf{u}_{n+1}^h, \kappa_{n+1}^h) &= \mathbf{A}_e \int_{\mathcal{B}_e} \left[ N_{\kappa}^k \left[ \varphi(\mathbf{u}_{n+1}^h, \kappa_{n+1}^h) - Y(\kappa_{n+1}) \right] - \text{grad } N_{\kappa}^k \cdot \mathbf{H}(\kappa_{n+1}^h) \right] \, dV \\ &\leq 0 \quad \forall K \quad \text{in } \mathbb{B} \\ \Delta R_K^{\kappa}(\kappa_{n+1}^h) &= \mathbf{A}_e \int_{\mathcal{B}_e} \left[ N_{\kappa}^k \left[ \kappa_{n+1}^h - \kappa_n^h \right] \right] \, dV \\ &\geq 0 \quad \forall K \quad \text{in } \mathbb{B} \end{aligned}$$


---

Table 3.5: Discrete algorithmic form of the coupled problem

Firstly, the discrete algorithmic quasi-static balance of linear momentum  $\mathbf{R}_K^u = \mathbf{0}$  is derived.

Secondly, the discrete algorithmic Karush-Kuhn-Tucker conditions are obtained whereby, in particular, the first one represents the discrete algorithmic yield condition  $R_K^{\Phi} \leq 0$  and the second one assures positive increments of the internal history variable  $\Delta R_K^{\kappa} \geq 0$ .

Moreover, the discrete algorithmic decomposition of the node point set with  $\mathbb{B} = \mathbb{B}_{n+1}^p \cup \mathbb{B}_{n+1}^e$  and  $\emptyset = \mathbb{B}_{n+1}^p \cap \mathbb{B}_{n+1}^e$  takes the following explicit format

$$\begin{aligned} \mathbb{B}_{n+1}^e &= \{K \in \mathbb{B} | R_K^{\Phi} \leq 0, \Delta R_K^{\kappa} = 0\} \\ \mathbb{B}_{n+1}^p &= \{K \in \mathbb{B} | R_K^{\Phi} = 0, \Delta R_K^{\kappa} > 0\}. \end{aligned} \quad (3.40)$$

Now this is indeed a complete explicit definition since one only has to separately check all node points  $K \in \mathbb{B}$ . Finally, note that the above discrete algorithmic decomposition corresponds to the discrete algorithmic complementary condition  $\Delta R_K^{\kappa} R_K^{\Phi} = 0 \quad \forall K \text{ in } \mathbb{B}$ .

Based on the spatial discretization of  $\kappa$ , the residuum  $\Delta R_K^\kappa$  expands into

$$\Delta R_K^\kappa = \sum_L M_{KL}^{\kappa\kappa} \Delta \kappa_L \quad \text{with} \quad M_{KL}^{\kappa\kappa} = \mathbf{A} \int_{\mathcal{B}_e} N_\kappa^k N_\kappa^l dV. \quad (3.41)$$

For the most practical implementation, the positive definite fundamental matrix  $M_{KL}^{\kappa\kappa}$  is simply diagonalized, thus  $\Delta R_K^\kappa \geq 0$  is equivalent to  $\Delta \kappa_L \geq 0$ .

### 3.5.5 Monolithic iterative solution

An efficient algorithm for the solution of the highly non-linear coupled problem stated in the determining residua in Table 3.5 is offered by a monolithic iterative strategy. Here, the discrete algorithmic balance of linear momentum together with the discrete algorithmic Karush-Kuhn-Tucker conditions are solved simultaneously. The crucial point of this coupled formulation lies in the determination of the initially unknown decomposition of the discretization node point set into active and inactive subsets  $\mathbb{B} = \mathbb{B}_{n+1}^p \cup \mathbb{B}_{n+1}^e$  at time step  $t_{n+1}$ , that will be iteratively determined by an active set search as outlined in the subsequent section. Then, for a given active working set  $\mathbb{B}_{act}$ , a typical Newton-Raphson step reads as follows

$$\begin{aligned} \mathbf{R}_K^u + d\mathbf{R}_K^u &= \mathbf{0} \quad \forall K \quad \text{in} \quad \mathbb{B} \\ R_K^\Phi + dR_K^\Phi &= 0 \quad \forall K \quad \text{in} \quad \mathbb{B}_{act}, \end{aligned} \quad (3.42)$$

whereby the linearized residua are expressed by the corresponding iteration matrices, which take the interpretation as global tangent stiffness matrices

$$\begin{aligned} d\mathbf{R}_K^u &= - \sum_{L \in \mathbb{B}} \mathbf{K}_{KL}^{uu} \cdot d\mathbf{u}_L - \sum_{L \in \mathbb{B}_{act}} \mathbf{K}_{KL}^{u\Phi} d\kappa_L \quad \forall K \quad \text{in} \quad \mathbb{B} \\ dR_K^\Phi &= - \sum_{L \in \mathbb{B}} \mathbf{K}_{KL}^{\Phi u} \cdot d\mathbf{u}_L - \sum_{L \in \mathbb{B}_{act}} K_{KL}^{\Phi\Phi} d\kappa_L \quad \forall K \quad \text{in} \quad \mathbb{B}_{act}. \end{aligned} \quad (3.43)$$

Finally, the incremental iterate is updated from the solution of Eq. 3.42 by

$$\begin{aligned} \Delta \mathbf{u}_L &\Leftarrow \Delta \mathbf{u}_L + d\mathbf{u}_L \quad \forall L \quad \text{in} \quad \mathcal{B} \\ \Delta \kappa_L &\Leftarrow \Delta \kappa_L + d\kappa_L \quad \forall L \quad \text{in} \quad \mathcal{B}_{act}. \end{aligned} \quad (3.44)$$

For the problem at hand, the following iteration matrices are introduced

$$\begin{aligned} \mathbf{K}_{KL}^{uu} &= \mathbf{A} \int_{\mathcal{B}_e} \text{grad } N_x^k \cdot \partial_\epsilon \boldsymbol{\sigma} \cdot \text{grad } N_x^l dV \\ \mathbf{K}_{KL}^{u\Phi} &= \mathbf{A} \int_{\mathcal{B}_e} \text{grad } N_x^k \cdot \partial_\kappa \boldsymbol{\sigma} N_\kappa^l dV \\ \mathbf{K}_{KL}^{\Phi u} &= \mathbf{A} \int_{\mathcal{B}_e} N_\kappa^k \partial_\epsilon \varphi \cdot \text{grad } N_x^l dV \\ \mathbf{K}_{KL}^{\Phi\Phi} &= \mathbf{A} \int_{\mathcal{B}_e} \left[ N_\kappa^k [\partial_\kappa \varphi - \partial_\kappa Y] N_\kappa^l - \text{grad } N_\kappa^k \cdot \partial_\kappa \mathbf{H} \cdot \text{grad } N_\kappa^l \right] dV, \end{aligned} \quad (3.45)$$

which includes the corresponding partitions of the tangent operator that have to be provided by the appropriate linearization of the constitutive update, see the following section.

### 3.5.5.1 Constitutive update

A strain-driven constitutive update algorithm typically has to provide the updated stress at time  $t_{n+1}$ . Moreover, its linearization is essential in order to set up the appropriate global iteration matrix for the quadratically converging global Newton-Raphson strategy.

The constitutive update of the geometrically linear elasto-plastic prototype von Mises model, see Table 3.1, for given  $\epsilon_{n+1}, \kappa_{n+1}, \boldsymbol{\kappa}_{n+1}; \boldsymbol{\epsilon}^p, \kappa_n$  is summarized in Table 3.6. Note that despite its implicit character, the constitutive update does not rely on local iterations usually employed in standard return mapping algorithms.

Volumetric stress	$p_{n+1}$	$=$	$K\mathbf{1} : \epsilon_{n+1}$
Deviatoric trial stress	$\mathbf{s}_{trial}$	$=$	$2G\mathcal{I}^{dev} : [\epsilon_{n+1} - \boldsymbol{\epsilon}_n^p]$
Deviatoric stress	$\mathbf{s}_{n+1}$	$=$	$\mathbf{s}_{trial} - 2G\Delta\kappa\boldsymbol{\nu}_{trial}$
von Mises stress	$\varphi_{n+1}$	$=$	$ \mathbf{s}_{trial}  - 2G\Delta\kappa$
Local yield stress	$Y_{n+1}$	$=$	$Y_0 + H(\kappa_{n+1})$
Hardening flux	$\mathbf{H}_{n+1}$	$=$	$c\boldsymbol{\kappa}_{n+1}$
Plastic strain	$\boldsymbol{\epsilon}_{n+1}^p$	$=$	$\boldsymbol{\epsilon}_n^p + \Delta\kappa\boldsymbol{\nu}_{trial}$

Table 3.6: Update of the constitutive variables

Moreover, the linearization of the constitutive update, i.e., the partition of the tangent operator as employed in the global iteration matrix (3.45), is given in Table 3.7. Note that this tangent operator results in a symmetric global iteration matrix.

$\mathbf{u} - \mathbf{u}$ Partition	$\partial_{\boldsymbol{\epsilon}}\boldsymbol{\sigma}$	$=$	$K\mathbf{1} \otimes \mathbf{1} + 2G\delta_1\mathcal{I}^{dev} + \delta_2\boldsymbol{\nu}_{trial} \otimes \boldsymbol{\nu}_{trial}$
			$\delta_1 = 1 - \frac{2G\Delta\kappa}{ \mathbf{s}_{trial} } \quad \delta_2 = \frac{4G^2\Delta\kappa}{ \mathbf{s}_{trial} }$
$\mathbf{u} - \kappa$ Partition	$\partial_{\kappa}\boldsymbol{\sigma}$	$=$	$-2G\boldsymbol{\nu}_{trial}$
$\kappa - \mathbf{u}$ Partition	$\partial_{\boldsymbol{\epsilon}}\varphi$	$=$	$2G\boldsymbol{\nu}_{trial}$
$\kappa - \kappa$ Partition	$\partial_{\kappa}\varphi$	$=$	$-2G$
	$\partial_{\kappa}Y$	$=$	$\partial_{\kappa}H(\kappa_{n+1})$
	$\partial_{\boldsymbol{\kappa}}\mathbf{H}$	$=$	$c\mathbf{1}$

Table 3.7: Partitions of the tangent operator

The above update algorithm is a direct consequence of the implicit Euler backward integration of the flow rule to obtain the updated plastic strain

$$\boldsymbol{\epsilon}_{n+1}^p = \boldsymbol{\epsilon}_n^p + \Delta\kappa\boldsymbol{\nu}_{trial} \quad \text{with} \quad \boldsymbol{\nu}_{trial} = \boldsymbol{\nu}_{n+1} \quad \text{and} \quad \Delta\kappa = \kappa_{n+1} - \kappa_n \quad (3.46)$$

together with the decomposition of the total stress into deviatoric and volumetric parts

$$\boldsymbol{\sigma}_{n+1} = K[\mathbf{1} : \epsilon_{n+1}]\mathbf{1} + 2G\mathcal{I}^{dev} : \boldsymbol{\epsilon}_{n+1}^e = p_{n+1}\mathbf{1} + \mathbf{s}_{n+1}. \quad (3.47)$$

### 3.5.5.2 Active set search

The initially unknown decomposition of the discretization node point set into active and inactive subsets  $\mathbb{B} = \mathbb{B}_{n+1}^p \cup \mathbb{B}_{n+1}^e$  at time step  $t_{n+1}$  is determined iteratively by an active set search. Thereby, the strategy

is borrowed from convex non-linear programming as is frequently used, e.g., in multi-surface and crystal plasticity.

To this end, the active working set is first initialized at the start of the iteration by those nodes, which currently violate the constraint  $R_K^\Phi \leq 0$

$$\mathbb{B}_{act} = \{K \in \mathbb{B} | R_K^\Phi > 0\}. \quad (3.48)$$

Then, the trial iterate is computed from a global Newton-Raphson step, which was described in detail in the preceding section

$$\kappa_K^{trial} = \kappa_K^n + \Delta \kappa_K \quad \forall K \quad \text{in} \quad \mathbb{B}_{act}. \quad (3.49)$$

Next, in order to insure admissible increments of the  $\kappa_K$  in the time step, the new iterate is updated with a Bertsekas projection

$$\kappa_K^{n+1} = \max(\kappa_K^{trial}, \kappa_K^n) \quad \forall K \quad \text{in} \quad \mathbb{B}_{act}. \quad (3.50)$$

Finally, after computing the residua based on  $\kappa_K^{n+1}$ , the active working set is updated by

$$\mathbb{B}_{act} = \mathbb{B}_{act}^\Phi \cup \mathbb{B}_{act}^p \quad (3.51)$$

in accordance with the discrete algorithmic Karush-Kuhn-Tucker conditions

$$\begin{aligned} \mathbb{B}_{act}^\Phi &= \{K \in \mathbb{B} | R_K^\Phi > 0\} \\ \mathbb{B}_{act}^p &= \{K \in \mathbb{B} | \Delta R_K^\kappa > 0\}. \end{aligned} \quad (3.52)$$

The iteration has converged when all discrete algorithmic Karush-Kuhn-Tucker conditions are satisfied, such that the active set coincides with the valid active discretization node point set

$$\emptyset = \mathbb{B}_{act}^\Phi \quad \text{and} \quad \mathbb{B}_{act} = \mathbb{B}_{act}^p \quad \longrightarrow \quad \mathbb{B}_{n+1}^p. \quad (3.53)$$

Otherwise the iteration continues with the computation of an improved trial iterate. This is achieved, e.g., by a monolithic solution together with the discrete algorithmic balance of linear momentum. Thereby, the quadratic convergence of the global Newton-Raphson scheme critically depends on the correct linearization of the constitutive update algorithm.

It is remarkable that the global iteration matrix is symmetric. Moreover, due to the active set strategy, the size of the iteration matrix changes dynamically, which has to be accounted for by the implementation of the equation solver. Nevertheless, the problem size in each iteration is considered to be optimal. Apart from the specific implementation of the equation solver, only standard FE-data structures and corresponding FE-modules are involved.

An alternative possible strategy is based on a staggered global predictor-corrector scheme, which also renders a symmetric iteration matrix of dynamical but optimal size. Nevertheless, it demands somewhat non-standard FE-data structures and corresponding FE-modules and is thus not preferable.

### 3.6 Numerical examples of phenomenological gradient plasticity

With the above algorithm at hand, the performance of the proposed gradient formulation is now investigated. Firstly, a 1D-model problem of a bar loaded in uniaxial tension as frequently treated in the literature is analyzed. Secondly, a 2D-model problem of a square panel under uniaxial tension is considered. In every example, localization is triggered by imperfections and the influence of different discretization

densities is investigated in comparison to the local formulation.

### 3.6.1 1D-model problem: bar under uniaxial tension

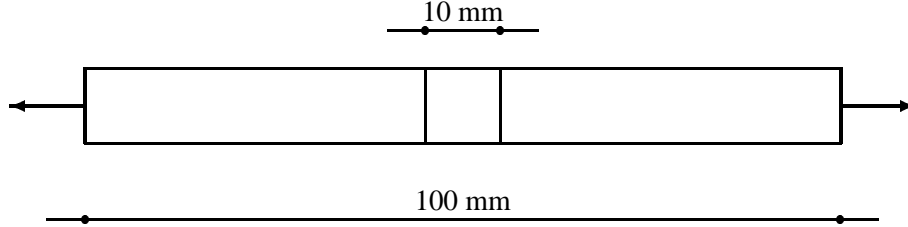


Figure 3.4: 1D-model problem: bar under uniaxial tension

For the sake of demonstration, the bar in Fig. 3.4 loaded in uniaxial tension serves as a 1D-model problem that will be examined in the sequel. The problem statement, which includes a slight graded material imperfection in the middle of the bar, is taken from Peerlings et al. (1996b), whereby the previously derived constitutive and continuity boundary conditions were prescribed at the corresponding boundary. The material is modeled based on a one-dimensional von Mises yield function with isotropic linear hardening or softening, see Table 3.1. The material parameters for the following examples are summed up in Table 3.8.

Elastic Modulus	$E$	=	1.0000	N/mm <sup>2</sup>
Initial yield strength	$Y_0$	=	0.0100	N/mm <sup>2</sup>
Reduced initial yield strength	$Y_{0r}$	=	0.0090	N/mm <sup>2</sup>
Perturbed initial yield strength	$Y_{0p}$	=	0.0089	N/mm <sup>2</sup>
Linear hardening modulus	$H_0$	=	1.5000	N/mm <sup>2</sup>
Linear softening modulus	$H_0$	= -	0.5000	N/mm <sup>2</sup>

Table 3.8: Material parameters: 1D-model problem

The total bar is discretized with 20, 40, 80, 160, 320 and 640 elements. Thereby, due to the symmetry in the problem statement, only one half of the bar is considered. Here, in order to trigger a possible branch switch of the solution path for the softening case, the imperfect domain is additionally perturbed in the first element. The load is applied using arclength control enabling to trace the post-peak branch of the load-displacement curves in softening. The main objective is to show the performance of the gradient model. Therefore, as a comparison, the local model is also addressed. To this end, four different element formulations as described in Table 3.9 are investigated.

Plasticity formulation	Discretization variable	Continuity of approximation	Element type	
local	$\mathbf{u}$	$C^0$	$P^02$	Expansion
local	$\mathbf{u}, \kappa$	$C^0/C^{-1}$	$P^02P^{\bar{1}}1$	Expansion
local	$\mathbf{u}, \kappa$	$C^0/C^0$	$P^02P^01$	Expansion
gradient	$\mathbf{u}, \kappa$	$C^0/C^0$	$P^02P^01$	Expansion

Table 3.9: Classification of element formulations

The first local element type characterizes the classical approach in local plasticity with quadratic element expansions for the displacement. Hereby, the history variable field is not separately discretized. The second choice of a local element formulation describes the same continuous element expansions for the displacement but also discontinuously discretizes the history variable field  $\kappa$ . Therefore, it is capable of representing jumps in the distribution of  $\kappa$ . The underlying implementation of the constitutive update is here based on the gradient model, but with gradient parameter set to  $c = 0$ . The third proposed element type reflects a continuous approach in both the displacement as well as the history variable field. Thereby, jumps in the distribution of  $\kappa$  are difficult to capture as will be shown later on. Here, the corresponding implementation of the constitutive update is also of the gradient type. For the local case  $c = 0$  is used, whereby for the gradient case  $c > 0$  is applied.

### 3.6.1.1 Hardening

Firstly, the behavior of the different element formulations is investigated in hardening. This should emphasize the stability of the algorithm as well as validate the gradient model. Therefore, local hardening elasto-plasticity is applied to the different element formulations, see Table 3.9 for comparison.

Starting point is the response of the classical local  $P^02$  element type displayed in the load-displacement-curve as well as in the history variable distribution, see Fig. 3.5. There is clearly no visible mesh dependence that can be detected here, which is also the case for the discontinuous discretized history variable field of the  $P^02P^1$  formulation, see Fig. 3.6. Here, the same constitutive subroutine as in the gradient model is employed, but with the gradient parameter  $c = 0$ . Thus, an active set search on the element-level has to be performed. Thereby, in order to capture the history variable field, internal, i.e., condensable, degrees of freedom are introduced instead of additional external nodal degrees of freedom, which turn active if the yield condition is violated in a weak sense. The corresponding results of the continuous  $P^02P^0$  formulation for the quasi-local case with  $c = 0$  presents similar results, see Fig. 3.7.

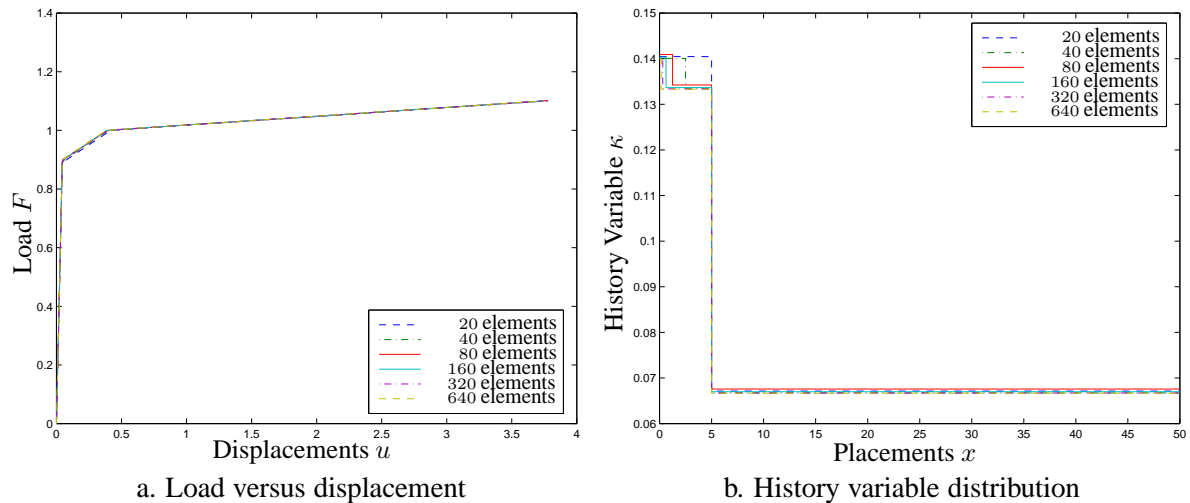


Figure 3.5: Local hardening ( $P^02$  elements)

Note that the capability of resolving the discontinuous distribution of the history variable for the continuous  $P^02P^0$  formulation with  $c = 0$  is reached only in the case of high discretization densities, see Fig. 3.7. Nevertheless, the apparent oscillations are similar to those observed in the Galerkin FE-resolution of convection-diffusion problems in fluid mechanics. Finally in Fig. 3.8, all different element formulations are compared for a constant mesh discretization of 640 elements. Obviously, no apparent differences are exhibited among the different (dis)continuous element expansions. Only in the history



variable distribution are the previously discussed oscillations visible for the  $P^02P^01$  element formulation. Thereby, the introduction of the gradient parameter  $c > 0$  effects the solution such that the distributions are smooth and convergent as will be demonstrated in the following sections.

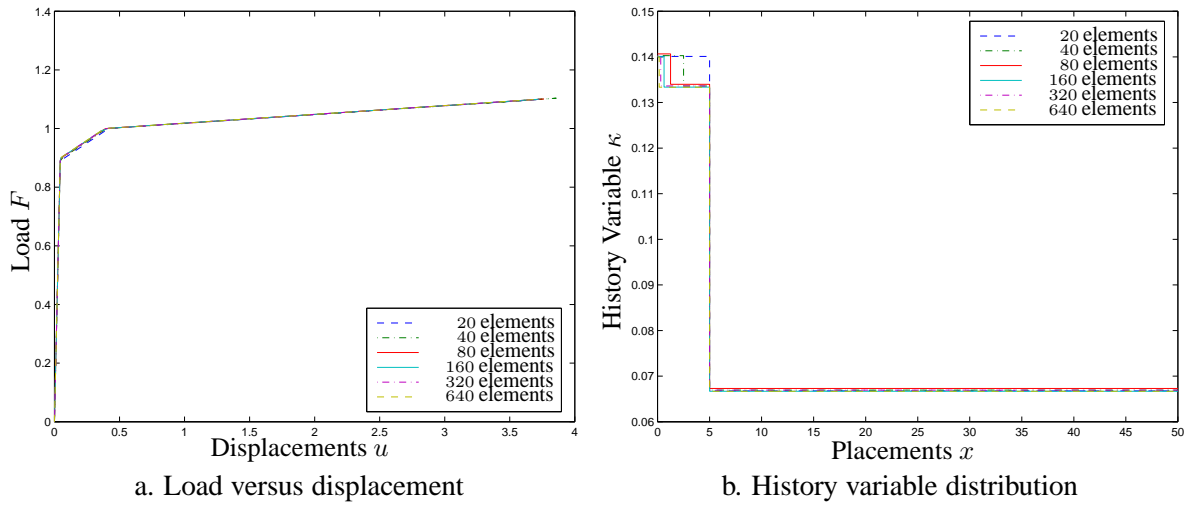


Figure 3.6: Local hardening ( $P^01P^1_2$  elements)

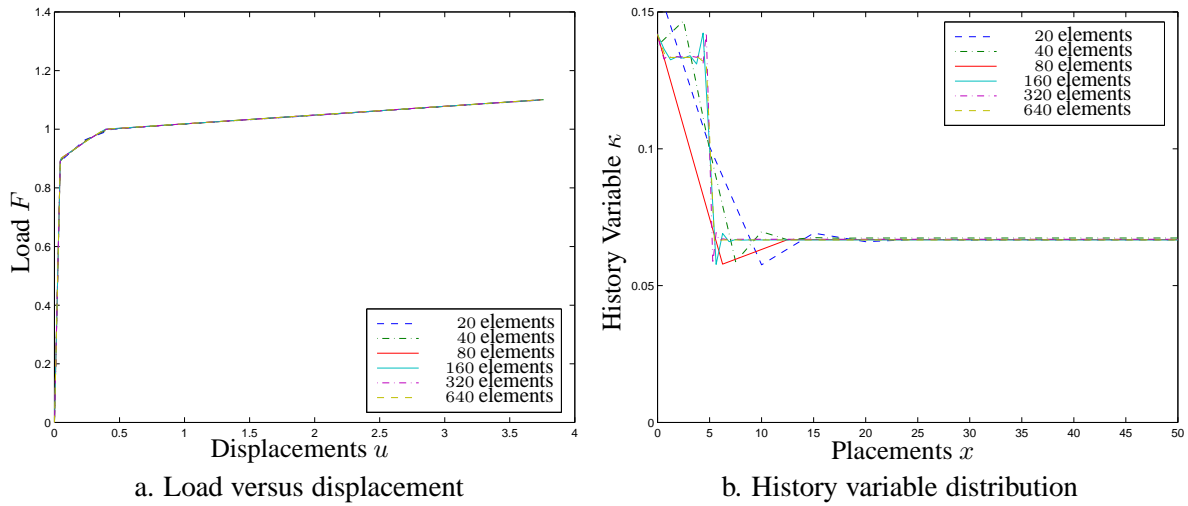


Figure 3.7: Quasi-local hardening ( $P^02P^01$  with  $c = 0$ )

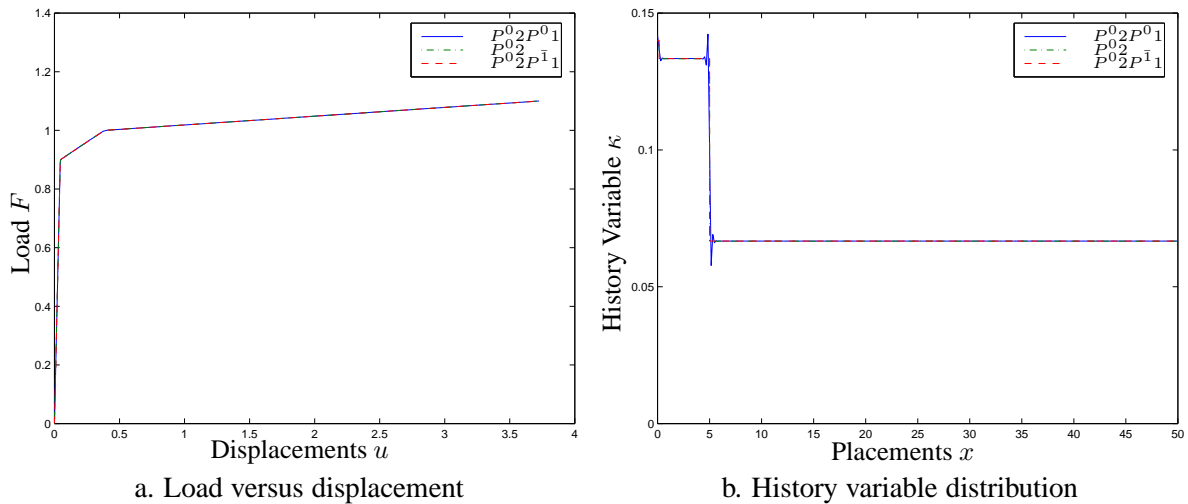


Figure 3.8: Gradient hardening for all different element formulations and constant mesh (640 elements)

Finally, the regularized behavior of the continuous formulation  $P^02P^01$  with  $c > 0$  is considered. Thereby, the effect of modifying the gradient parameter and mesh discretization is investigated. The corresponding results are displayed in Fig. 3.9 to Fig. 3.11 for  $c = 2.5, c = 5.0$  and  $c = 10.0$ , respectively. Obviously, the solutions converge upon mesh refinement. Now, no oscillations occur but are smoothed out over a distributed area along the weakened part of the bar.

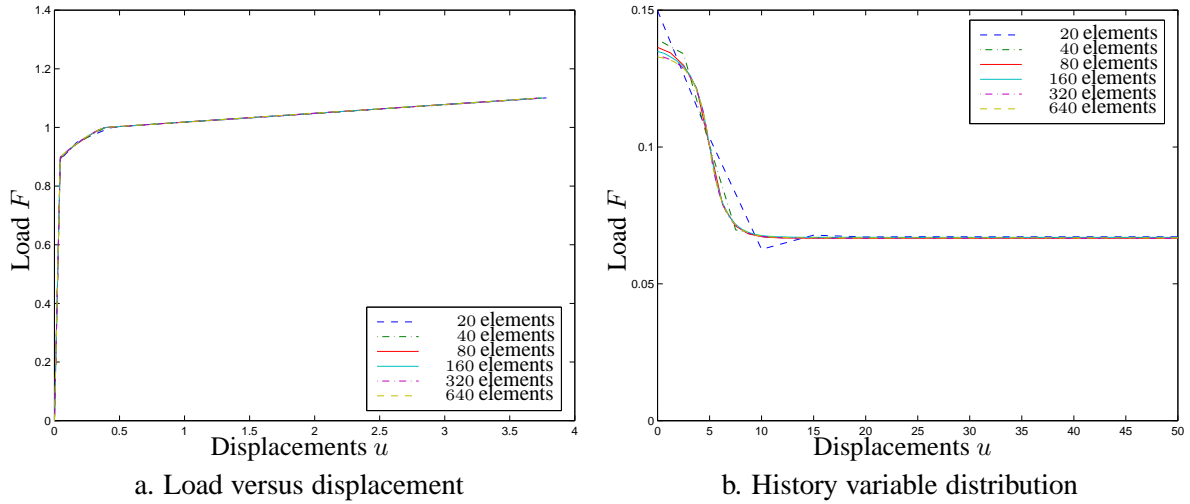


Figure 3.9: Gradient hardening for  $c = 2.5$  ( $P^02P^01$  elements)

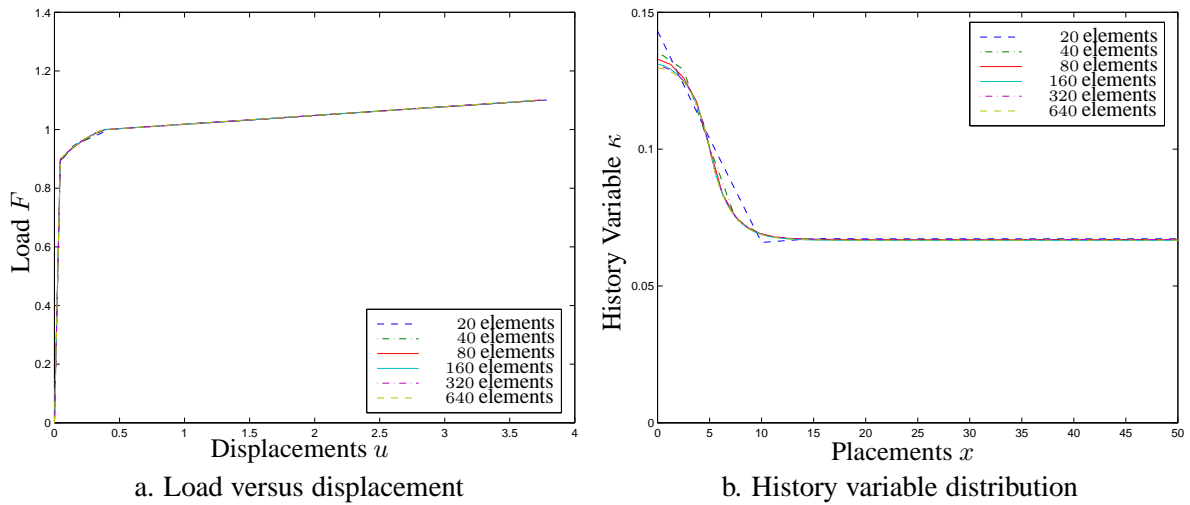


Figure 3.10: Gradient hardening for  $c = 5.0$  ( $P^02P^01$  elements)

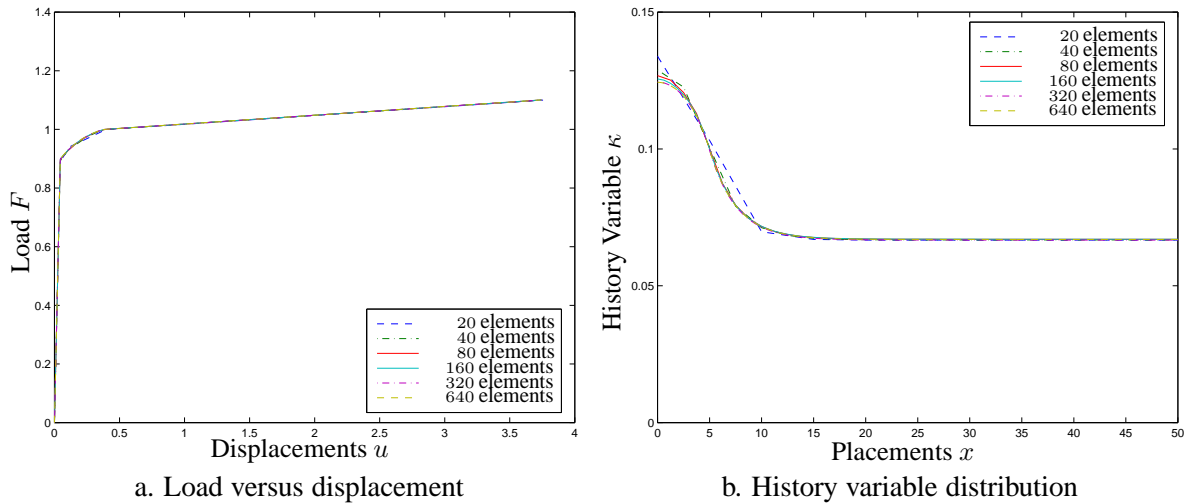


Figure 3.11: Gradient hardening for  $c = 10.0$  ( $P^02P^01$  elements)

Note that the influence of modifying the gradient parameter shows practically no influence in the load-displacement curves, which is emphasized in Fig. 3.12a, but it has moderate influence in the history variable distribution plot, see the close-up in Fig. 3.12b. For comparison the quasi-local case denoted by  $c = 0$  is also depicted. Note, that the history variable distribution shows an increasing ductility for higher values of the gradient parameter  $c$ . Thereby, the localized zone is resolved over more and more elements corresponding to the increase in  $c$ .

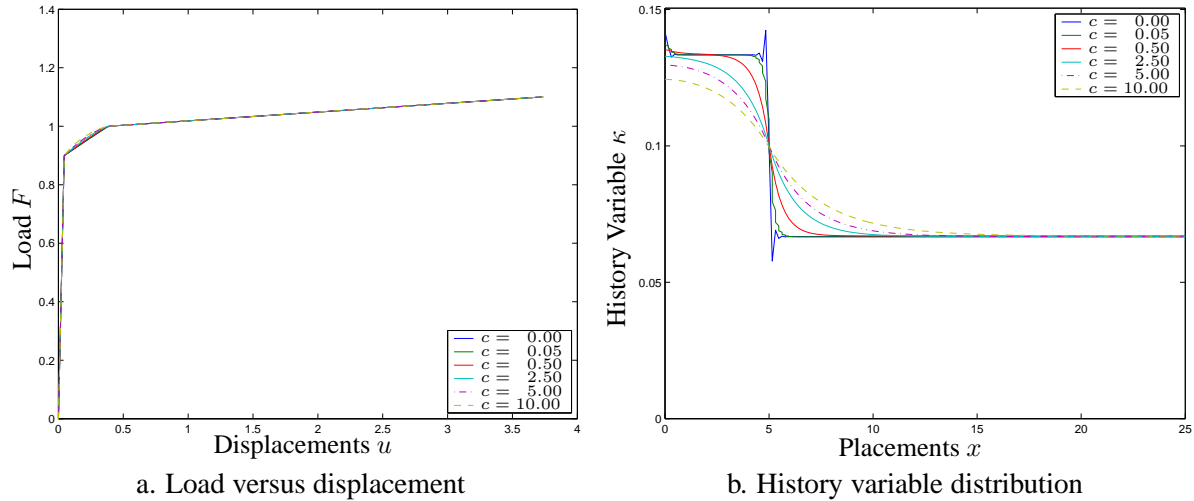


Figure 3.12: Gradient hardening for varied gradient parameter ( $c = 0.0, 0.05, 0.5, 2.5, 5.0, 10.0$  and constant mesh-discretization ( $640 P^0 2P^0 1$  elements))

### 3.6.1.2 Softening

Secondly, a detailed investigation of the behavior of the different element formulations in softening elasto-plasticity is performed. Here, the deficiencies of a local theory are apparent as can be seen in the load versus displacement results based on the  $P^0 2$  formulation displayed in Fig. 3.13a. The typical lack of convergence in the post-peak branch of the curves can be observed upon mesh refinement. This is also emphasized in Fig. 3.13b depicting the corresponding distribution of the history variable, whereby a concentration of plastic evolution is accumulated in only one element.

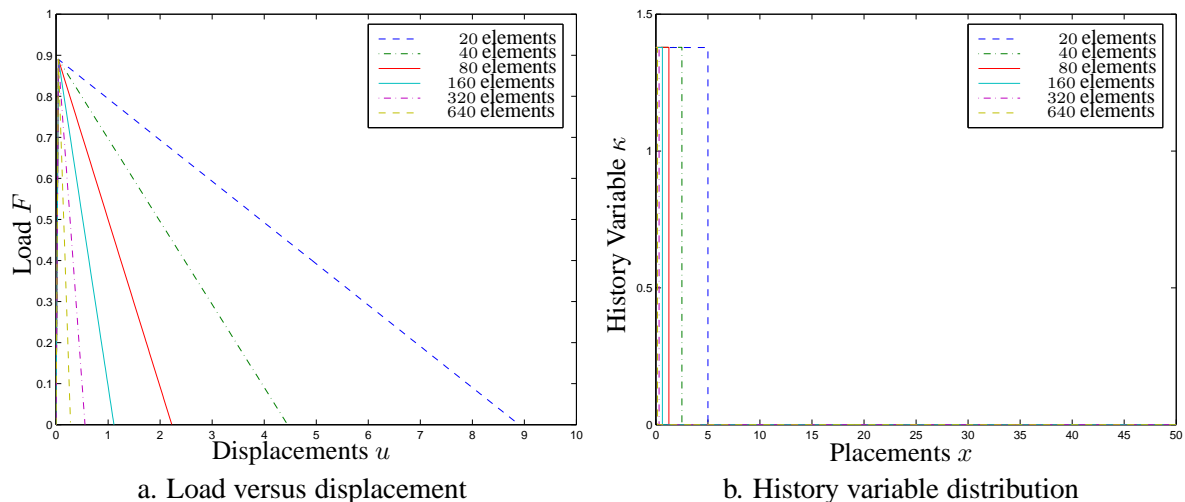


Figure 3.13: Local softening ( $P^0 2$  elements)

Next, the  $P^02P^{\bar{1}}$  element type with discontinuous, i.e., elementwise defined, linear expansions for the history variable field and quadratic expansions for the displacements is tested in the local elasto-plastic response. In comparison, the continuous  $P^02P^01$  formulation is applied with  $c = 0$ , see Fig. 3.14 - Fig. 3.15.

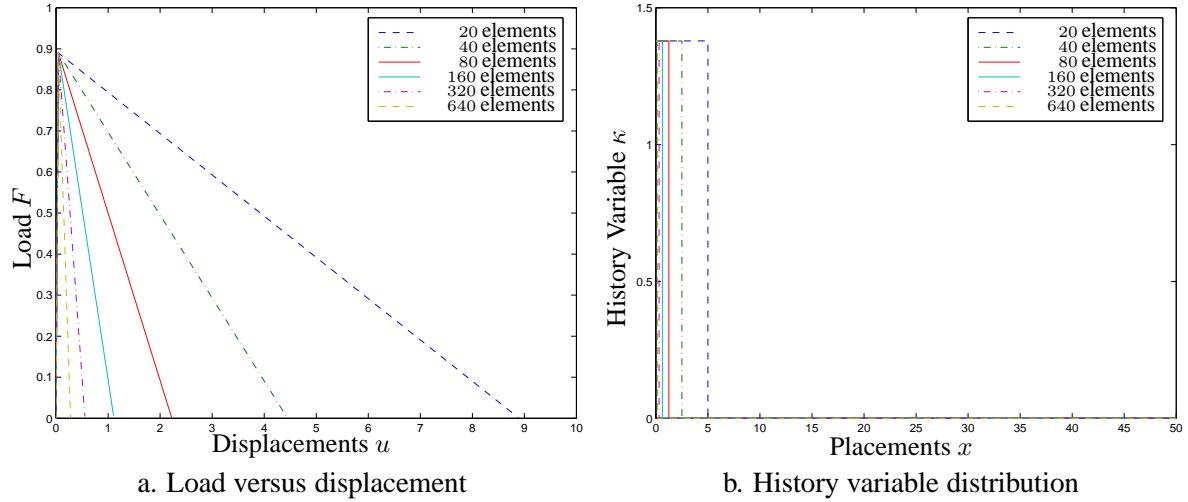


Figure 3.14: Local softening ( $P^02P^{\bar{1}}$  elements)

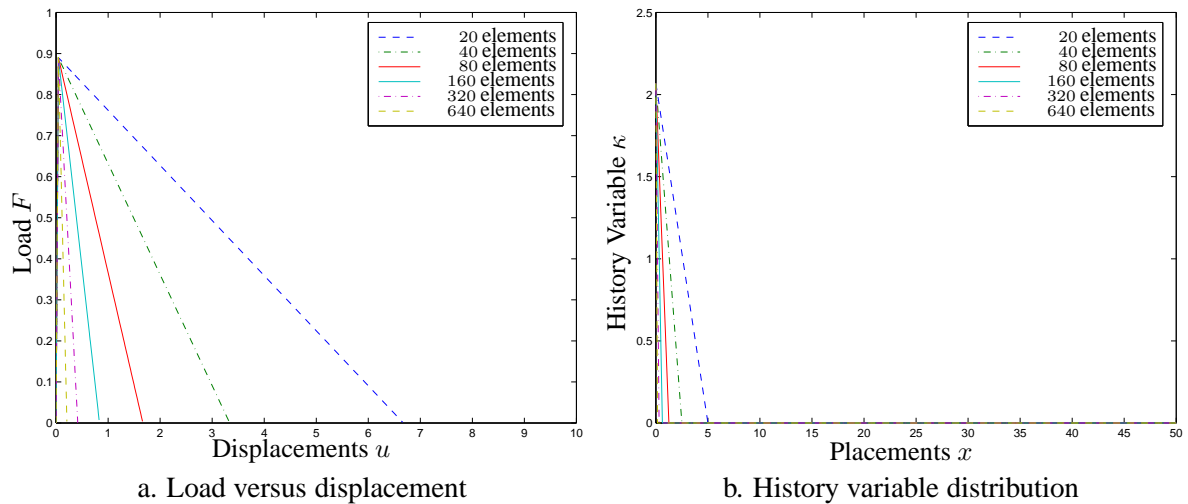


Figure 3.15: Quasi-local softening ( $P^02P^01$  elements)

Here, the spurious mesh dependence of the classical local theory is strongly visible, even though the different (dis)continuous element expansions show no significant difference for the local theory. As one would expect, both  $P^02$  and  $P^02P^{\bar{1}}$  formulations provide almost identical results, whereas the continuous  $P^02P^01$  approach shows deficiencies in capturing the jumps in the distribution of the history variable for quasi-local behavior with  $c = 0$  (Fig. 3.15 in comparison to Fig. 3.13, Fig. 3.14). In contrast, the discontinuous  $P^02P^{\bar{1}}$  element type is perfectly able to display the jump. Note that for the continuous  $P^02P^01$  approach, no oscillations occur in the history variable distribution in softening, see Fig. 3.15b.

Finally, Fig. 3.16 summarizes all different (dis)continuous element formulations for a constant mesh discretization with 640 elements. To emphasize the results, the following figure is a zoom into the localized region. Again, the local classical continuous  $P^02$  and discontinuous  $P^02P^{\bar{1}}$  element formulation coincide, whereas the continuous quasi-local formulation  $P^02P^01$  shows a slightly less ductile behavior in the load-displacement plot as depicted in Fig. 3.16a and does not capture the jump in the history variable distribution, see Fig. 3.16b.

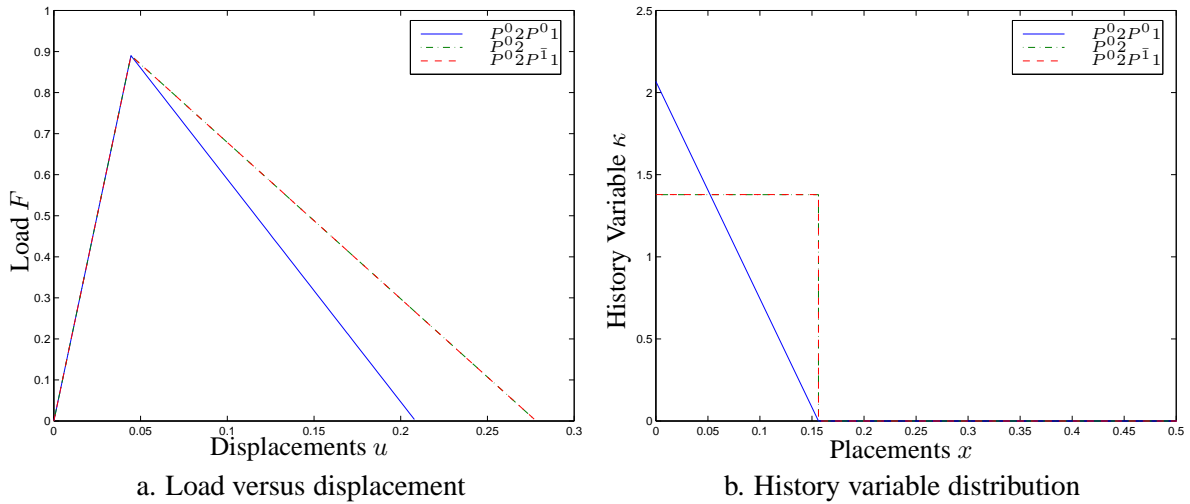


Figure 3.16: Local softening for all different element formulations and constant mesh (640 elements)

To overcome the lack of discretization invariance, the following examples are based on the incorporation of the gradient regularization in the constitutive model as described in the previous sections.

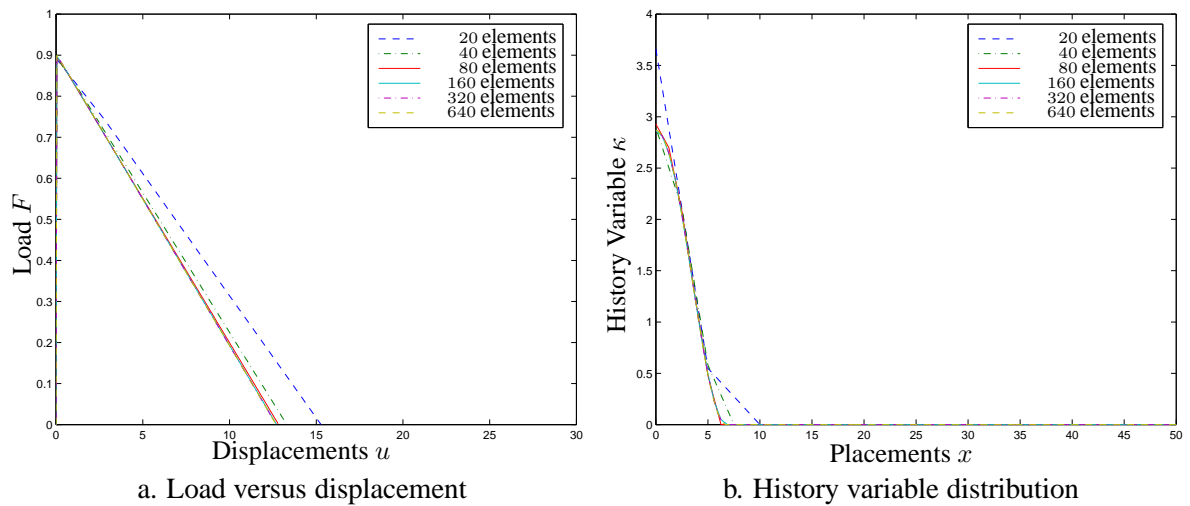


Figure 3.17: Gradient softening for  $c = 2.5$  ( $P^0_2P^0_1$  elements)

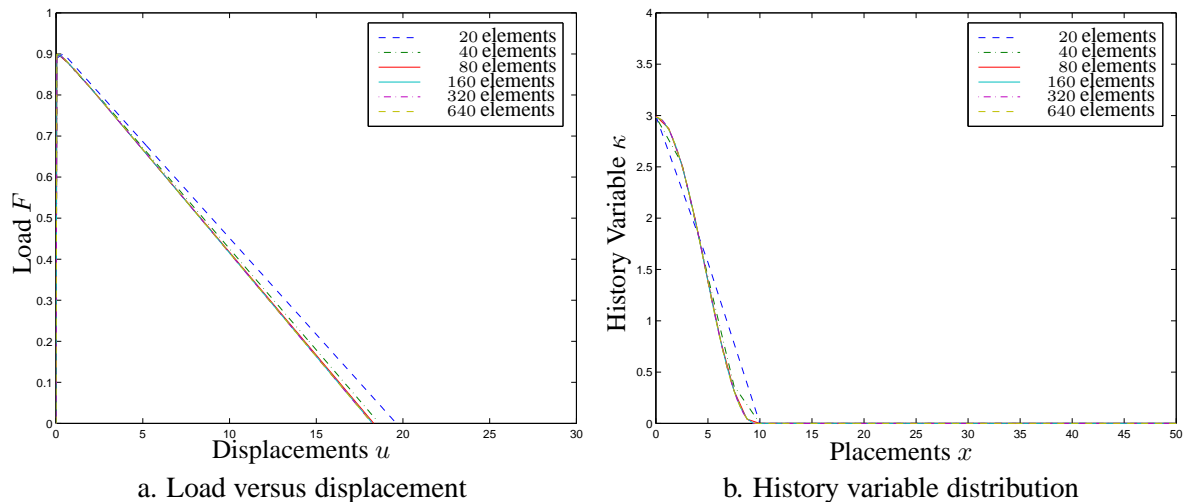


Figure 3.18: Gradient softening for  $c = 5.0$  ( $P^0_2P^0_1$  elements)

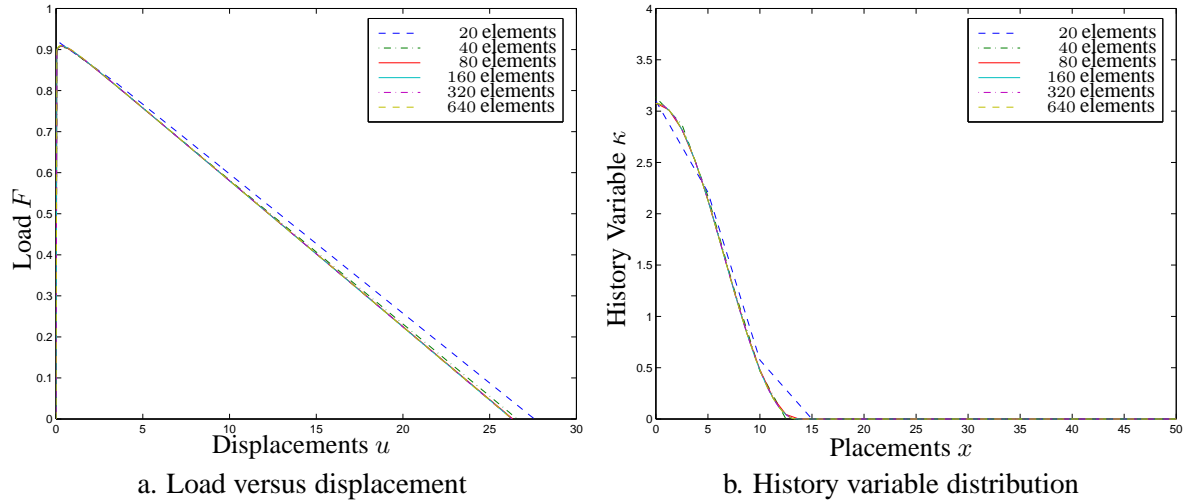


Figure 3.19: Gradient softening for  $c = 10.0$  ( $P^02P^01$  elements)

Firstly, the mesh independence is shown for a constant gradient parameter  $c = 2.5$ , see Fig. 3.17. Even if the gradient parameter is varied, the solution converges upon mesh densification, see Fig. 3.18 and Fig. 3.19. Moreover, higher values of the gradient parameter render a somewhat more ductile post-peak behavior, see Fig. 3.20a. Thereby, the corresponding distribution of the history variable is smooth and convergent, which is emphasized in Fig. 3.20b. Observe, that similar to the investigations in hardening, the localized zone is again resolved over more and more elements corresponding to an increasing gradient parameter  $c$ .

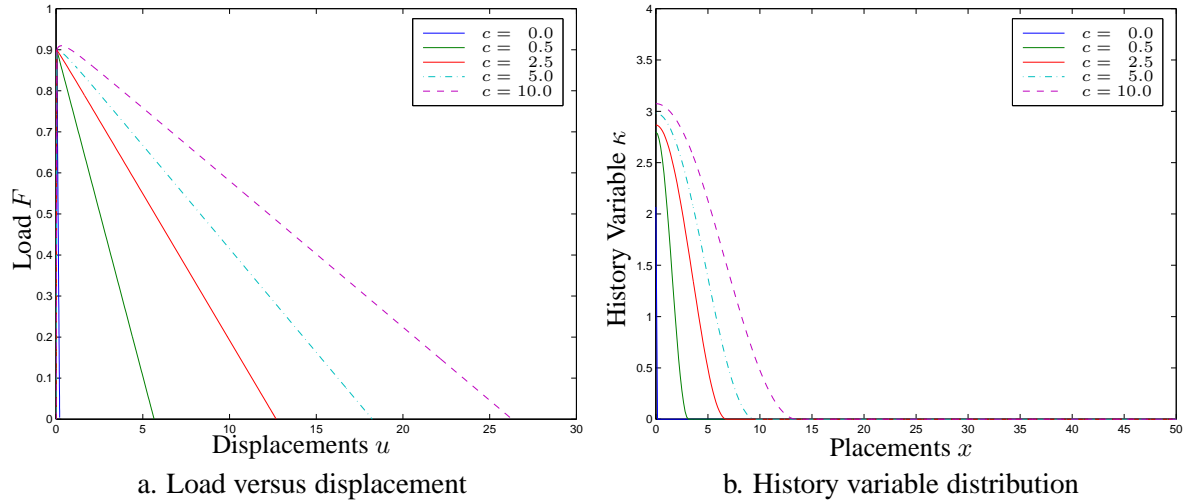


Figure 3.20: Gradient softening for varied gradient parameter ( $c = 0.0, 0.5, 2.5, 5.0, 10.0$  and constant mesh-discretization (640  $P^02P^01$  elements)

### 3.6.2 Geometrically non-linear model problem: panel under tension

Next, for demonstration purposes, the simplified gradient model is applied within an isotropic geometrically non-linear setting to a 2D-model problem, see the appendix B for an outline of the underlying coupled problem. Thereby, the constitutive model is chosen of von Mises type in combination with a specific model for the free energy in terms of logarithmic Hencky strains, see the description in the appendix B.2. Here, a square panel is considered with discretization into  $8 \times 8$ ,  $16 \times 16$ ,  $32 \times 32$   $Q^02Q^01$  elements as exemplarily shown in Fig. 3.21 for  $16 \times 16$  elements.

The left edge of the panel is kept fixed, whereas a uniform displacement is incrementally applied on the nodes of the right edge. The elements can thereby move freely under the linear constraint that neighboring right-edge-nodes retain the same vertical distance to each other under deformation.

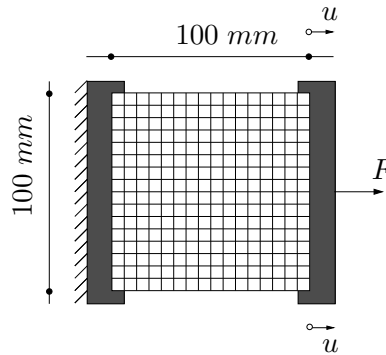


Figure 3.21: 2D-model problem: panel under tension

The material parameters are chosen corresponding to Table 3.10.

Elastic modulus	$E$	=	50000.0	N/mm <sup>2</sup>
Poisson ratio	$\nu$	=	0.3	
Initial yield strength	$Y_0$	=	25.0	N/mm <sup>2</sup>
Reduced initial yield strength	$Y_{0,r}$	=	20.0	N/mm <sup>2</sup>
Linear softening modulus	$H_0$	=	-15.0	N/mm <sup>2</sup>

Table 3.10: Material parameters: 2D-model problem

The localization band is triggered by weakening elements on the diagonal. Firstly, the spurious mesh dependence can be observed in the contour lines of the history variable distribution for the local solution, see Fig. 3.22. This is also emphasized in the load-displacement curves, see Fig. 3.23a, whereby even the finest mesh renders a snap-back post peak response for all mesh discretizations investigated here.

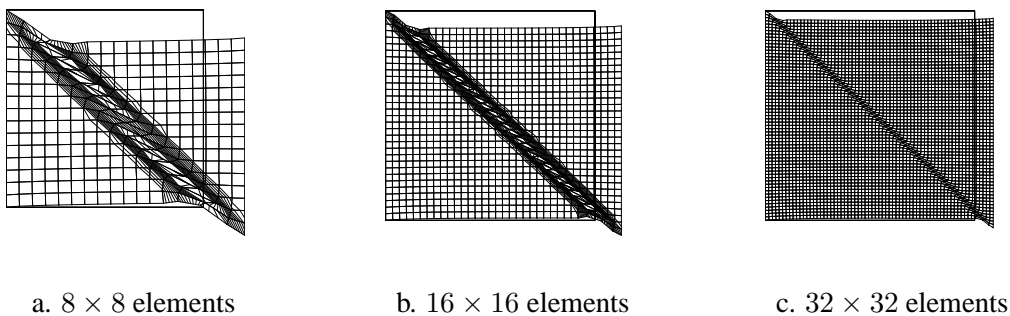


Figure 3.22: History variable distribution in local softening ( $Q^0_2$  elements)

Secondly, Fig. 3.23b depicts the corresponding response for the gradient formulation. Apparently, no visible discretization sensitivity is present in the results.

This is also emphasized by the plot of the history variable distribution across the panel as shown in Fig. 3.24. The first one, see Fig. 3.24a, presents the overlay of the contour lines of the history variable distribution for the two finest mesh discretizations investigated here. This is specified in the following contour plots (Fig. 3.24b-d) confirming the regularizing character of the proposed gradient model also in

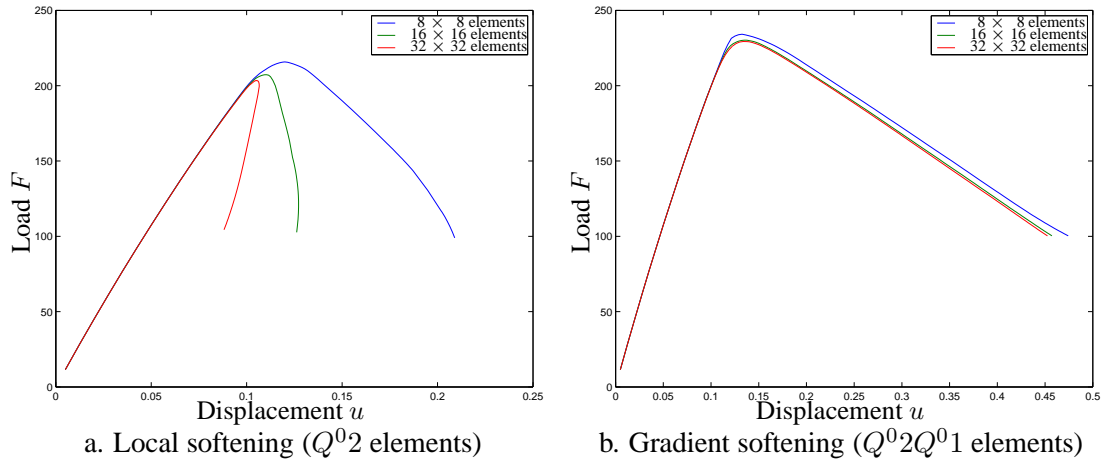


Figure 3.23: Load versus displacement curves

geometrically non-linear elasto-plasticity.

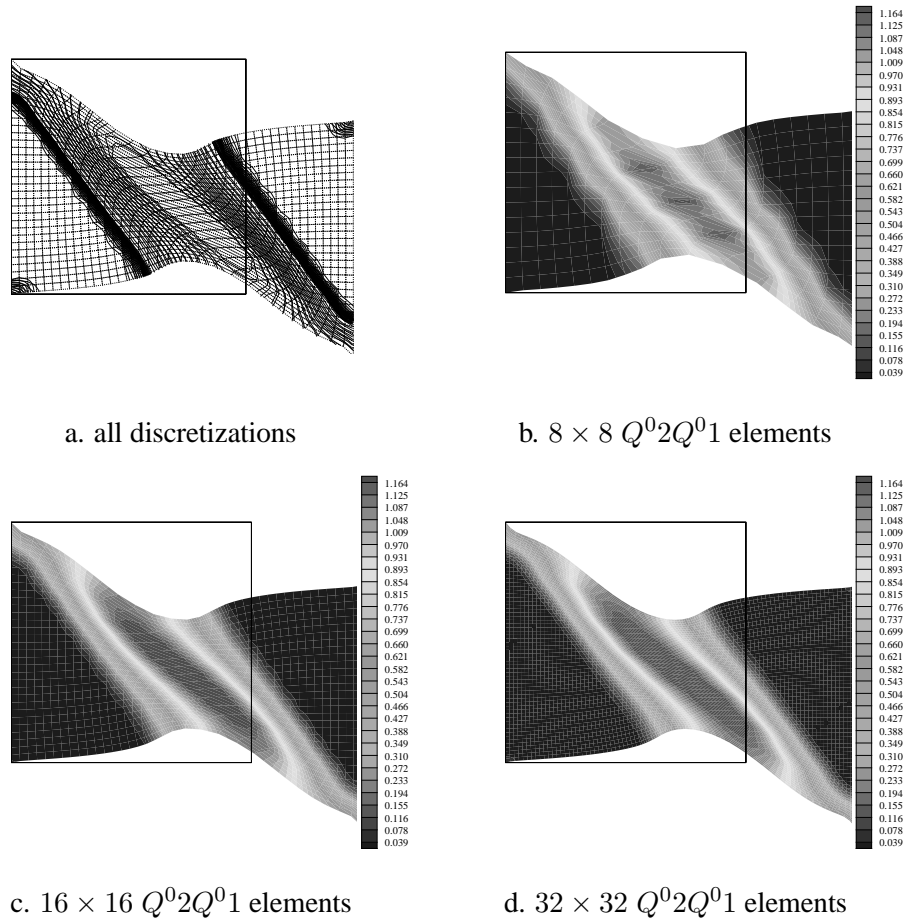


Figure 3.24: History variable contour plot in gradient softening for  $c = 5$



## Chapter 4

# Application of phenomenological gradient plasticity to single crystals

A dislocation based gradient theory has so far been applied to phenomenological plasticity. In the subsequent sections, the main focus will be on crystalline materials like metals, which are particularly suited for a physically motivated gradient formulation based on dislocation densities and incompatibilities, respectively. It was shown in chapter 2 that the density of geometrically necessary dislocations can be related to the (in)compatibility of inelastic deformations, which is basically expressed by the curl of the deformation gradient.

Physically motivated gradient models have especially been developed in recent years. One example is the strain-gradient based crystal plasticity formulation by Shu and Barlow (2000). Their proposal is based on measurements of lattice rotations in a metal-matrix-composite. Alternatively, Sluys and Estrin (2000) analyzed the formation of shear bands based on a single crystal gradient plasticity model. Thereby, diffusion terms of higher order that represent cross slip of dislocations are incorporated in the evolution equations for the dislocation densities. Furthermore, Acharya and Bassani (2000) derived a gradient theory of crystal plasticity based on incompatibilities of the elastic lattice. These incompatibilities are simply incorporated in the hardening behavior. Therefore, the standard structure of the boundary value problem is preserved.

A thermodynamically consistent gradient theory of elasto-plasticity in terms of dislocation densities is proposed by Shizawa and Zbib (1999). They introduced micro-stresses conjugated to the dislocation density that need to be balanced. The macroscopic stresses thereby retained a symmetric structure. Furthermore, they derived evolution equations for the plastic spin and plastic strains. Another dislocation based formulation of inelastic material behavior together with the corresponding thermodynamical aspects is put forth by Svendsen (2002). Thereby, the author set up two models that realize the field relations for the glide-system deformations. On the one hand, Svendsen derived a so-called glide-system-based model in terms of generalized internal variables and on the other hand, a continuum model in terms of internal degrees of freedom, which require additional balance equations. Alternatively, Gurtin (2000) presented a single crystal gradient plasticity by characterizing the geometrically necessary dislocations as gradients with respect to the deformation gradient in terms of additional degrees of freedom. That also results in micro-stress balance equations and has recently been applied to the viscoplastic case by Gurtin (2002).

This chapter concentrates on the internal variable approach motivated in chapter 2, whereby the underlying crystal plasticity fundamentals are motivated by the works of Steinmann (1996; 1997). In particular, the consideration of dislocation densities and incompatibility requirements within a single crystal plasticity framework are based on the ideas by Menzel and Steinmann (2000) and Liebe et al. (2002). Thereby,

the general model of chapter 2 is reduced to the small strain case of single and double slip. The derived theory will be verified on a model problem of simple shear of a crystalline strip as investigated in the literature, e.g., by Shu et al. (2001) and by Svendsen and Reese (2003).

## 4.1 Kinematics of single crystals

A crystal structure typically consists of atoms arranged in a pattern that repeats itself periodically in a three-dimensional geometric lattice. Then, the starting point for modeling single crystal plasticity is the kinematical acknowledgment that the plastic deformation process is characterized by dislocation flow through the crystal lattice, which is denoted as slip. Thereby, certain preferred slip directions  $s_I$  on specific slip planes exist. In general, a slip plane is the plane of greatest atomic density and will be characterized by its normal vector  $m_I$ . In addition to that, the slip direction  $s_I$  is the line of closest-packed atoms within the slip plane. Together, the slip plane normal  $m_I$  and the slip direction  $s_I$  set up the slip system  $I$ . In analogy to the geometrically non-linear case in section 2.2.1, the deformation process that starts in configuration  $\mathcal{B}$  denoted by  $n_{sys}$  slip systems  $\{s_I, m_I\}$ , see Fig. 4.1a is thought to be decomposed into a plastic (flow of dislocations through the lattice along the slip systems  $\{s_{pI}, m_{pI}\}$ ) and a subsequent elastic deformation (distortion of the lattice with corresponding slip systems  $\{s_{tI}, m_{tI}\}$ ), see also Fig. 4.1b,c.

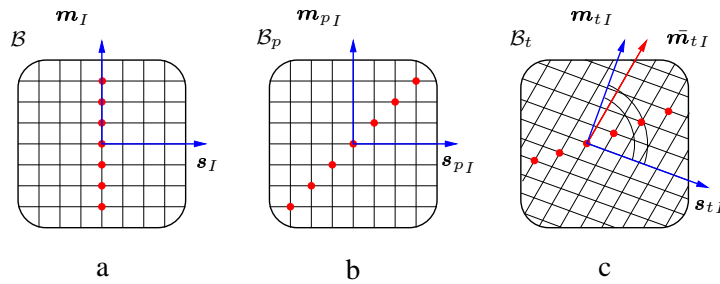


Figure 4.1: Elasto-plastic mechanism in a single crystal lattice

It is again assumed that the orthogonality of the slip normal and slip direction is preserved during plastic deformation  $s_{pI} \cdot m_{pI} = s_I \cdot m_I = 0$ . The composition with the elastic deformation then renders the tangent vector  $\bar{m}_{tI}$  along the distorted lattice, which does no longer coincide with the normal vector  $m_{tI}$  of the slip plane, i.e., loss of orthogonality  $s_{tI} \cdot \bar{m}_{tI} \neq 0$ , see Fig. 4.1c.

Furthermore, the Schmid projection tensor is defined as  $\nu_I = s_I \otimes m_I$ . Then, the driving force behind the plastic deformation process will be denoted by the resolved shear stress acting on a particular slip system  $I$  via the projection of the Cauchy stress

$$\tau_I = \sigma_I^t : [s_I \otimes m_I] = \sigma_I^t : \nu_I, \quad (4.1)$$

which is also denoted as Schmid stress  $\tau_I$ .

Next, different lattice structures will be investigated, which can be illustrated with the help of crystallographic unit cells.

Firstly, the case of a body-centered-cubic (bcc) cell, which is representative for, e.g.,  $\alpha$ -iron (ferrite), chromium or tungsten, is envisioned. Since bcc-crystals possess no closed-packed structure, they do not have a predominant slip plane. Nevertheless, there exists a closed-packed direction  $[111]$ <sup>1</sup> in which slip can only occur. Therefore, slip is found to occur on  $\{110\}$ ,  $\{112\}$  and  $\{123\}$  planes, while the slip

<sup>1</sup>Here use of the so-called Miller indices is made.  $\{hkl\}$  designate a set of face planes that are equivalent by the symmetry of the crystal;  $(hkl)$  designate a set of planes;  $[hkl]$  denote specific directions;  $\langle hkl \rangle$  denote general directions

direction is always  $[111]$ , which renders  $n_{sys} = 48$  possible slip systems. For the sake of illustration of a corresponding yield surface, consider now two representative slip planes  $I = \{1, 2\}$  in a bcc-unit cell, see Fig. 4.2a. For the following example 'plane stress' conditions are applied, whereby  $\sigma^{100}$  and  $\sigma^{010}$  correspond to the axes  $[100]$  and  $[010]$ , respectively.

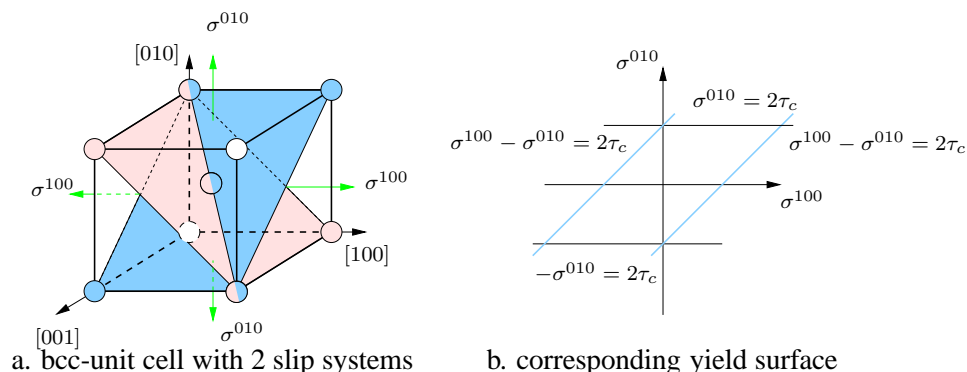


Figure 4.2: Yield surface for two particular slip planes of a bcc-crystal unit-cell under 'plane stress' conditions

Then, the corresponding resolved shear stresses acting on the two slip planes can be determined as

$$\tau_1 = \pm \frac{1}{2}(\sigma^{100} - \sigma^{010}) \quad \text{and} \quad \tau_2 = \pm \frac{1}{2}\sigma^{010}. \quad (4.2)$$

Obviously, the material reaches its yield surface if the resolved shear stress reaches a critical value  $\tau_I = \tau_c$  on slip system  $I$ . Observe, that the resulting yield surface corresponding to each slip system is convex as depicted in Fig 4.2b.

Secondly, the case of a face-centered-cubic (fcc) crystal structure, that can be found in, e.g.,  $\gamma$ -iron (austenite), lead or aluminum, is studied more closely. Here, four non-parallel slip planes  $\{111\}$  of highest atomic density exist, which together render with three possible slip directions  $[110]$  typically  $n_{sys} = 12$  slip systems, see Fig. 4.3. In elasto-plastic single crystalline materials, the total nonsymmetric distortion can additively be decomposed into elastic and plastic parts  $\mathbf{h} = \mathbf{h}^e + \mathbf{h}^p$  within a geometrically linear continuum framework<sup>2</sup>. Based on the constraint  $\nu_1 : \mathbf{1} = 0$ , i.e., the plastic distortion is isochoric  $\mathbf{h}^p : \mathbf{1} = 0$ , only five different slip systems need to be differentiated, see Borja and Wren (1993).

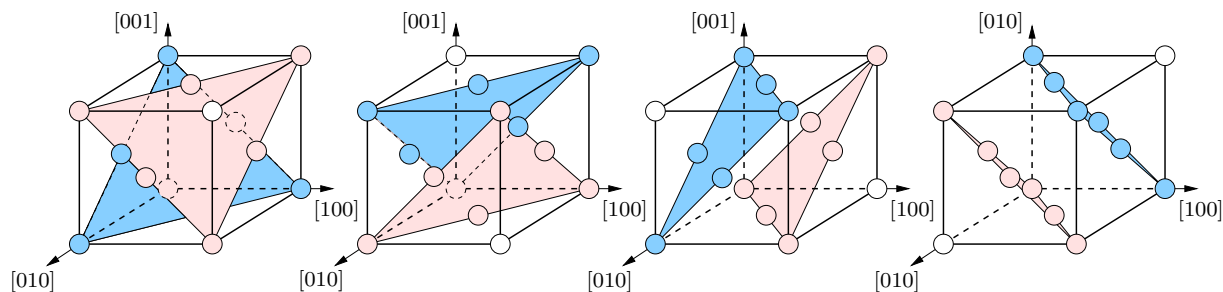


Figure 4.3: Parallel predominant slip system pairs of a fcc-crystal unit-cell

Lastly, for simplification purposes, a planar model as originally proposed by Asaro (1979) is envisioned. It can exemplarily be derived by projecting the fcc-unit cell along direction  $\langle 110 \rangle$ , which renders a

<sup>2</sup>Thereby, the elastic strains are denoted by  $\epsilon^e = [\mathbf{h}^e]^{sym}$ .

rectangle that is depicted as  $(\bar{1}10)$  plane in Fig. 4.4a,b. Thereby, two slip plane pairs from the  $\{111\}$  cluster in Fig. 4.3 degenerate to lines, whereas the other two pairs form an equilateral triangle as exemplarily sketched for the  $(\bar{1}11)$  slip plane. Then, it is sufficient to consider two linear independent slip directions  $s_1$  and  $s_2$  inclined under  $\alpha$  to axis  $[001]$  in addition to the 'slip (in-)plane normal'  $m_1$  and  $m_2$  resulting in symmetric double slip with respect to axis  $[001]$ , see Fig. 4.4c.

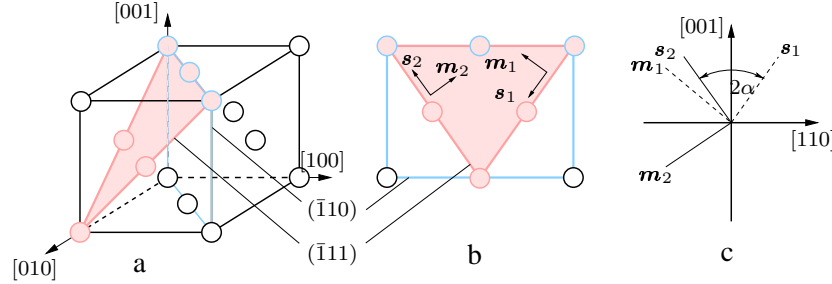


Figure 4.4: Symmetric planar double slip model

In Cartesian coordinates the symmetric double slip system can be represented as follows

$$s_1 = \begin{bmatrix} \sin \alpha \\ -\sin \alpha \end{bmatrix} \quad s_2 = \begin{bmatrix} \cos \alpha \\ \cos \alpha \end{bmatrix} \quad m_1 = \begin{bmatrix} -\cos \alpha \\ -\cos \alpha \end{bmatrix} \quad m_2 = \begin{bmatrix} \sin \alpha \\ -\sin \alpha \end{bmatrix}. \quad (4.3)$$

In particular,  $\alpha = 30^\circ$  models a fcc-crystal that was, among other things, thoroughly investigated in the pioneering work of Asaro (1979) and Peirce et al. (1982).

## 4.2 Thermodynamics of single crystal gradient plasticity

As physically motivated before, the spatial closure failure, now featured within a geometrically linear setting, can be identified as the second order dislocation density tensor corresponding to a given distortion  $\mathbf{h}$

$$\oint_C d\mathbf{u} = \oint_C \mathbf{h} d\mathbf{x} = \int_A \text{curl}^t \mathbf{h} \cdot \mathbf{n} da \rightarrow \mathbf{a} = \text{curl}^t \mathbf{h}. \quad (4.4)$$

Here again, Stokes theorem has been applied and  $\mathbf{n}$  is the surface normal to  $\mathcal{A}$ . Hence, with the above additive decomposition of the total distortion  $\mathbf{h} = \mathbf{h}^e + \mathbf{h}^p$  in mind, the geometrically necessary dislocation density characterizing the incompatibility of the plastic distortion can be derived as

$$\mathbf{a}^p = \text{curl}^t \mathbf{h}^p = \mathbf{e} : \left[ \sum_{I \in \mathcal{J}} \text{grad} \gamma_I \otimes \mathbf{m}_I \otimes \mathbf{s}_I \right]. \quad (4.5)$$

Here, the argument that each slip system acts in terms of simple shear under plastic deformation, as was already proposed in Eq. 2.27, has been invoked. Moreover, the set of active constraints is defined by

$$\mathcal{J} = \{I \in 1, \dots, n_{sys} | \Phi_I = 0 \quad \text{und} \quad \dot{\gamma}_I > 0\}. \quad (4.6)$$

due to the fact that in the general case of  $n_{sys}$  possible slip systems, usually only a limited number of yield conditions are activated. From Eq. 4.5 it is postulated that the evolution of the plastic dislocation density tensor is consequently related to the sum of the gradient of the shear number  $\text{grad} \gamma_I$  for all (active) slip systems  $I \in \mathcal{J}$ . Therefore, the free Helmholtz energy is again enriched with the additional hardening contribution  $\mathbf{k}_I = \text{grad} \kappa_I$  accounting for geometrically necessary dislocations. Then, the

thermodynamic arguments of section 3.2 can be followed in a similar way. This yields the definition of the quasi-nonlocal hardening stress  $\bar{H}_I$  with the corresponding constitutive and continuity boundary conditions on each active slip system in the plastic loading region of the body  $\mathcal{B}^p$ .

Furthermore, associated flow rules for  $\mathbf{h}^p$  and  $\kappa_I$  are derived from the postulate of maximum dissipation. The formulation is complemented by a Schmid law enhanced yield condition and corresponding Karush-Kuhn-Tucker conditions. The key ingredients of rate-independent single crystal gradient plasticity are summarized in the following Table 4.1.

<b>Free Helmholtz energy</b>	$\Psi$	=	$\Psi([\mathbf{h}^e]^{sym}, \kappa_I) = \Psi^{mac}(\boldsymbol{\epsilon}^e) + \Psi^{har}(\kappa_I) + \Psi^{dis}(\mathbf{k}_I)$
<b>Dissipation inequality</b>	$\mathcal{D}$	=	$\boldsymbol{\sigma}^t : \dot{\mathbf{h}}^p - \sum_{I=1}^{n_{sys}} H_I \dot{\kappa}_I + \sum_{I=1}^{n_{sys}} \mathbf{H}_I \cdot \dot{\mathbf{k}} + \mathcal{P} \geq 0$
<b>Macroscopic stress</b>	$\boldsymbol{\sigma}^t$	=	$\boldsymbol{\sigma}^t(\boldsymbol{\epsilon}, \kappa_I) = \frac{\partial \Psi^{mac}}{\partial \boldsymbol{\epsilon}^e}$
<b>Hardening stress</b>	$H_I$	=	$H_I(\kappa_I) = \frac{\partial \Psi^{mac}}{\partial \kappa_I}$
<b>Hardening flux</b>	$\mathbf{H}_I$	=	$\mathbf{H}_I(\mathbf{k}_I) = \frac{\partial \Psi^{dis}}{\partial \mathbf{k}_I}$
<b>Quasi-nonlocal hardening stress</b>	$\bar{H}_I$	=	$\bar{H}_I(\mathbf{k}_I) = H_I - \text{div } \mathbf{H}_I$
<b>Bilinear dissipation potential</b>	$\mathcal{D}$	=	$\boldsymbol{\sigma}^t : \mathbf{h}^p - \sum \bar{H}_I \dot{\kappa}_I$
<b>Nonlocality residual</b>	$\mathcal{P}$	=	$\sum [H_I \dot{\kappa} + \mathbf{H}_I \cdot \dot{\kappa}_I - \bar{H}_I \dot{\kappa}_I]$
<b>Schmid stress</b>	$\tau_I$	=	$\boldsymbol{\sigma}_I^t : \boldsymbol{\nu}_I$
<b>Schmid law enhanced yield condition</b>	$\Phi_I$	=	$\Phi_I(\tau_I, \bar{H}_I) =  \tau_I  - [Y_0 + \bar{H}_I] \leq 0$
<b>Flow rule</b>	$\dot{\mathbf{h}}^p$	=	$\sum_{I \in \mathcal{J}} \dot{\gamma}_I \mathbf{m}_I \otimes \mathbf{s}_I$
<b>History variable evolution</b>	$\dot{\gamma}_I$	=	$\dot{\kappa}_I$
<b>Karush-Kuhn-Tucker complementary conditions</b>	$\Phi_I$	$\leq 0$	and $\dot{\kappa}_I \geq 0$ and $\dot{\kappa}_I \Phi_I = 0$
<b>Boundary conditions</b>	$\dot{\kappa}_I$	=	$0$ on $\partial \mathcal{B}_{int}^p$ and $\mathbf{n} \cdot \mathbf{H}_I = 0$ on $\partial \mathcal{B}_{ext}^p$

Table 4.1: Key ingredients of rate-independent single crystal gradient plasticity

### 4.3 Numerical treatment of single crystal gradient plasticity

The numerical concept is oriented along the lines of section 3.5, which can easily be adopted to single slip. Thereby, the pertinent set of equations for the solution of the coupled non-linear boundary value problem is set up in strong form with the appropriate boundary conditions corresponding to Table 3.2. The variational format is therefrom derived in analogy to Table 3.3. In the spirit of Table 3.4 and section 3.5.4, the temporal and spatial discretization follows, whereby the implicit Euler backward method is applied and the Bubnov-Galerkin finite element method is employed, respectively. In double slip, the formulation becomes more complex as the second slip systems demands an additional constitutive equation. This will exemplarily be illustrated in Table 4.2, where the residua of the equilibrium and

constitutive subproblem are summarized, which will be used within a monolithic iteration strategy. In case of single slip it is obvious that only  $R_K^{\Phi_1}$  is necessary to set up the coupled problem.

Equilibrium subproblem

$$\begin{aligned} \mathbf{R}_K^u &= \mathbf{A}_e \int_{\partial\mathcal{B}_e \cap \partial\mathcal{B}^t} N_x^k \mathbf{t}_{n+1}^p \, dA + \int_{\mathcal{B}_e} [N_x^k \mathbf{b}_{n+1} - \text{grad } N_x^k \cdot \boldsymbol{\sigma}(\mathbf{u}_{n+1}^h, \sum_{I=1,2} \kappa_I^h)] \, dV \\ &= \mathbf{0} \quad \forall K \quad \text{in } \mathbb{B} \end{aligned}$$

Constitutive subproblem

$$\begin{aligned} R_K^{\Phi_1} &= \mathbf{A}_e \int_{\mathcal{B}_e} \left[ N_\kappa^k \left[ \varphi_1(\mathbf{u}_{n+1}^h, \kappa_1^h) - Y_1(\kappa_1) \right] - \text{grad } N_\kappa^k \cdot \mathbf{H}_1(\kappa_1^h) \right] \, dV \\ &\leq 0 \quad \forall K \quad \text{in } \mathbb{B} \end{aligned}$$

$$\begin{aligned} R_K^{\Phi_2} &= \mathbf{A}_e \int_{\mathcal{B}_e} \left[ N_\kappa^k \left[ \varphi_2(\mathbf{u}_{n+1}^h, \kappa_2^h) - Y_2(\kappa_2) \right] - \text{grad } N_\kappa^k \cdot \mathbf{H}_2(\kappa_2^h) \right] \, dV \\ &\leq 0 \quad \forall K \quad \text{in } \mathbb{B} \end{aligned}$$

$$\Delta R_K^{\kappa_1} = \mathbf{A}_e \int_{\mathcal{B}_e} \left[ N_\kappa^k \left[ \kappa_1^h - \kappa_1 \right] \right] \, dV$$

$$\begin{aligned} \Delta R_K^{\kappa_2} &= \mathbf{A}_e \int_{\mathcal{B}_e} \left[ N_\kappa^k \left[ \kappa_2^h - \kappa_2 \right] \right] \, dV \\ &\geq 0 \quad \forall K \quad \text{in } \mathbb{B} \end{aligned}$$

Table 4.2: Discrete algorithmic form of the coupled problem in double slip

Here, two different prototype models are envisioned. On the one hand, a rate-independent single crystal gradient plasticity model is investigated to simulate single slip. Thereby, a Schmid law enhanced yield condition  $\Phi_I = |\tau_I| - [Y_0 + \bar{H}_I] \leq 0$  is applied, i.e.,  $\varphi_I = |\tau_I|$  and  $Y_I = Y_0 - H_I$ . On the other hand, a constitutive viscoplastic assumption for the local part of the Schmid law enhanced 'yield condition'

$$\Phi_I^{loc} = |\tau_I| - Y_I \left( \frac{\Delta\gamma_I}{\gamma_0} \right)^{1/m} \quad (4.7)$$

is used for the simulation of (symmetric) double slip. Here,  $\gamma_0$  denotes the reference slip rate and  $m$  is a rate-dependency parameter.

Note that for the case of double slip or multi slip in general, one has to take care of problems related to redundancy of slip activities. For the treatment of the possible ill-condition of the rate-independent theory due to linear-dependent active slip systems, consult, e.g., the work of Miehe and Schröder (2001) who suggested three possible algorithmic approaches. Moreover, one can resort to a rate-dependent theory in order to remedy the ambiguity problem. On the one hand, one can choose a penalty regularization in terms of Norton type creep functions, see, e.g., Steinmann (1997). Then every slip system is active all the time and questions of active set search and redundancy are effectively excluded. On the other hand, it is possible to formulate a viscoplastic enhanced yield condition as indicated above. Thereby, an active set search for the determination of the initially unknown decomposition of the discretization node point set into active and inactive subsets  $\mathbb{B} = \mathbb{B}_{n+1}^p \cup \mathbb{B}_{n+1}^e$  at time step  $t_{n+1}$  as described in section 3.5.5.2 is

still necessary. But redundancy of slip systems, which can occur, e.g., in case of symmetric double slip if both slip systems are loaded equally, is circumvented.

Finally, for a given active working set  $\mathbb{B}_{act}$ , a typical Newton-Raphson step for double slip reads

$$\begin{aligned} \mathbf{R}_K^u + d\mathbf{R}_K^u &= \mathbf{0} \quad \forall K \quad \text{in } \mathbb{B} \\ R_K^{\Phi_1} + dR_K^{\Phi_1} &= 0 \quad \forall K \quad \text{in } \mathbb{B}_{act} \\ R_K^{\Phi_2} + dR_K^{\Phi_2} &= 0 \quad \forall K \quad \text{in } \mathbb{B}_{act}, \end{aligned} \quad (4.8)$$

whereby the linearized residua are expressed by the corresponding iteration matrices, which take the interpretation as global tangent stiffness matrices

$$\begin{aligned} d\mathbf{R}_K^u &= - \sum_{L \in \mathbb{B}} \mathbf{K}_{KL}^{uu} \cdot d\mathbf{u}_L - \sum_{L \in \mathbb{B}_{act}} \mathbf{K}_{KL}^{u\Phi_1} d\kappa_{1L} - \sum_{L \in \mathbb{B}_{act}} \mathbf{K}_{KL}^{u\Phi_2} d\kappa_{2L} \quad \forall K \quad \text{in } \mathbb{B} \\ dR_K^{\Phi_1} &= - \sum_{L \in \mathbb{B}} \mathbf{K}_{KL}^{\Phi_1 u} \cdot d\mathbf{u}_L - \sum_{L \in \mathbb{B}_{act}} K_{KL}^{\Phi_1 \Phi_1} d\kappa_{1L} - \sum_{L \in \mathbb{B}_{act}} K_{KL}^{\Phi_1 \Phi_2} d\kappa_{2L} \quad \forall K \quad \text{in } \mathbb{B}_{act} \\ dR_K^{\Phi_2} &= - \sum_{L \in \mathbb{B}} \mathbf{K}_{KL}^{\Phi_2 u} \cdot d\mathbf{u}_L - \sum_{L \in \mathbb{B}_{act}} K_{KL}^{\Phi_2 \Phi_1} d\kappa_{1L} - \sum_{L \in \mathbb{B}_{act}} K_{KL}^{\Phi_2 \Phi_2} d\kappa_{2L} \quad \forall K \quad \text{in } \mathbb{B}_{act}. \end{aligned} \quad (4.9)$$

Here, the following iteration matrices have been derived for double slip

$$\begin{aligned} \mathbf{K}_{KL}^{uu} &= \mathbf{A} \int_{\mathcal{B}_e} \text{grad } N_x^k \cdot \partial_{\epsilon} \boldsymbol{\sigma} \cdot \text{grad } N_x^l dV \\ \mathbf{K}_{KL}^{u\Phi_1} &= \mathbf{A} \int_{\mathcal{B}_e} \text{grad } N_x^k \cdot \partial_{\kappa_1} \boldsymbol{\sigma} N_{\kappa}^l dV \\ \mathbf{K}_{KL}^{u\Phi_2} &= \mathbf{A} \int_{\mathcal{B}_e} \text{grad } N_x^k \cdot \partial_{\kappa_2} \boldsymbol{\sigma} N_{\kappa}^l dV \\ \mathbf{K}_{KL}^{\Phi_1 u} &= \mathbf{A} \int_{\mathcal{B}_e} N_{\kappa}^k \partial_{\epsilon} \varphi_1 \cdot \text{grad } N_x^l dV \\ \mathbf{K}_{KL}^{\Phi_2 u} &= \mathbf{A} \int_{\mathcal{B}_e} N_{\kappa}^k \partial_{\epsilon} \varphi_2 \cdot \text{grad } N_x^l dV \\ K_{KL}^{\Phi_1 \Phi_1} &= \mathbf{A} \int_{\mathcal{B}_e} \left[ N_{\kappa}^k [\partial_{\kappa_1} \varphi_1 - \partial_{\kappa_1} Y_1] N_{\kappa}^l - \text{grad } N_{\kappa}^k \cdot \partial_{\boldsymbol{\kappa}_1} \mathbf{H}_1 \cdot \text{grad } N_{\kappa}^l \right] dV \\ K_{KL}^{\Phi_2 \Phi_2} &= \mathbf{A} \int_{\mathcal{B}_e} \left[ N_{\kappa}^k [\partial_{\kappa_2} \varphi_2 - \partial_{\kappa_2} Y_2] N_{\kappa}^l - \text{grad } N_{\kappa}^k \cdot \partial_{\boldsymbol{\kappa}_2} \mathbf{H}_2 \cdot \text{grad } N_{\kappa}^l \right] dV \\ K_{KL}^{\Phi_1 \Phi_2} &= \mathbf{A} \int_{\mathcal{B}_e} \left[ N_{\kappa}^k [\partial_{\kappa_2} \varphi_1 - \partial_{\kappa_2} Y_1] N_{\kappa}^l - \text{grad } N_{\kappa}^k \cdot \partial_{\boldsymbol{\kappa}_2} \mathbf{H}_1 \cdot \text{grad } N_{\kappa}^l \right] dV \\ K_{KL}^{\Phi_2 \Phi_1} &= \mathbf{A} \int_{\mathcal{B}_e} \left[ N_{\kappa}^k [\partial_{\kappa_1} \varphi_2 - \partial_{\kappa_1} Y_2] N_{\kappa}^l - \text{grad } N_{\kappa}^k \cdot \partial_{\boldsymbol{\kappa}_1} \mathbf{H}_2 \cdot \text{grad } N_{\kappa}^l \right] dV. \end{aligned} \quad (4.10)$$

## 4.4 Numerical examples of single crystal gradient plasticity

In the following, single and double slip mechanisms are considered by means of a case study about simple shear of a crystalline strip. The same model problem was treated in an investigation of Shu et al. (2001) and from an alternative perspective from Svendsen and Reese (2003). Corresponding to the literature, a few simplifications are assumed in terms of (i), isothermal and quasi-static conditions, (ii), elastic isotropy and (iii), linear self-hardening alone. The material are chosen in the spirit of the above mentioned literature resembling aluminum ( $E = 60000MPa, \nu = 0.3, Y_0 = 60MPa, H_0 = 100MPa$ ). The model outline is as follows: a strip of height  $H$  in  $x_2$  direction consists of a single crystal

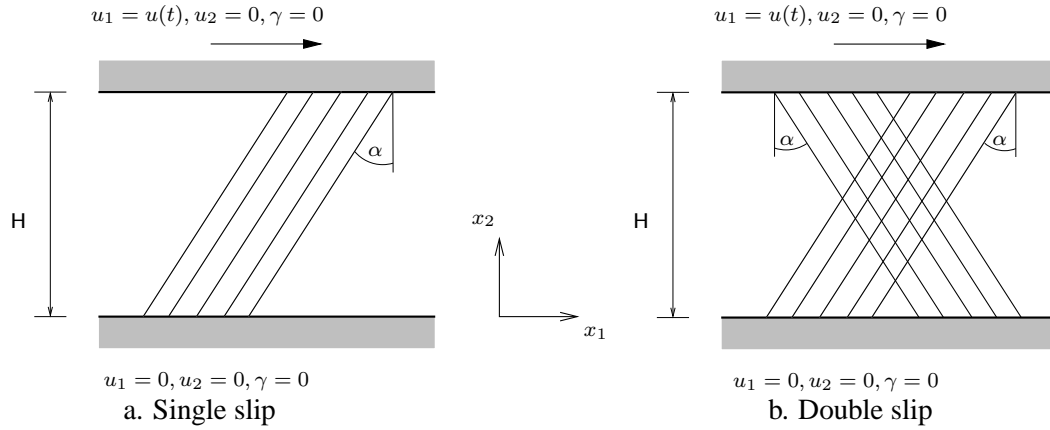


Figure 4.5: Geometry and boundary conditions of the model problem

with one or two slip system(s), respectively and is loaded under simple shear in  $x_1$  direction, see Fig. 4.5. Moreover, the strip is unbounded in the  $x_1$  and  $x_3$  direction. The constraints due to the upper and lower boundary as indicated in Fig. 4.5 have significant influence on the material response. Such specific geometry and boundary conditions resemble the type of plastic constraint found at grain boundaries of a polycrystal, or the surface of a thin film, or at interfaces in a composite. For the problem at hand, a classical local elasto-plastic computation of simple shear would result in homogeneous deformations over the normalized height  $x_2/H$  of the strip, see Fig. 4.6.

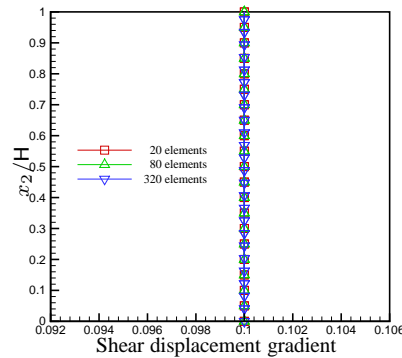


Figure 4.6: Homogeneous deformation of the classical local solution in single slip

The classical local result is in contrast to the discrete dislocation simulations done by Shu et al. (2001), which predict a non-uniform distribution of plastic flow with reduced plastic flow in the boundary layer. This yields the assumption of blocking the dislocation movement at the lower and upper boundary. This condition translates to  $\gamma = 0$  at  $x_2 = 0$  and  $x_2 = H$  in our context, since the development of  $\gamma$  is due to dislocation mobility.

The strip is discretized over the height  $x_2 \in [0, H]$  with a varying number of  $P^0_2P^0_1$  elements. Here, a strip of constant height  $H = 1.0[L]$  is used throughout the simulations but the quantity of the gradient parameter  $c$  is varied, in analogy to the  $H/l$ -investigation in Svendsen and Reese (2003), whereby  $l$  is the characteristic length for energy stored in the material due to local deformation incompatibility. Moreover, here the influence of a variation in the position of the slip systems is also investigated with  $\alpha = [20^\circ, 30^\circ, 40^\circ]$ . The simulation is run under plane strain conditions. In the  $x_1$  direction only one element is considered that is applied with linear constraints to model the prototype of a infinite strip as was investigated by Shu et al. (2001).



4.4.1 Single slip model problem: simple shear of a crystalline strip

Firstly, the results in single slip are discussed. The corresponding shear gradient distribution over the normalized height  $x_2/H$  are shown in Fig. 4.7a-c for a constant number of [20, 80, 320] elements over  $H$  but varying gradient parameter  $c = [0.0, \dots, 1.0, \dots, 100.0]$  and different slip system angle  $\alpha = [20^\circ, 30^\circ, 40^\circ]$ .

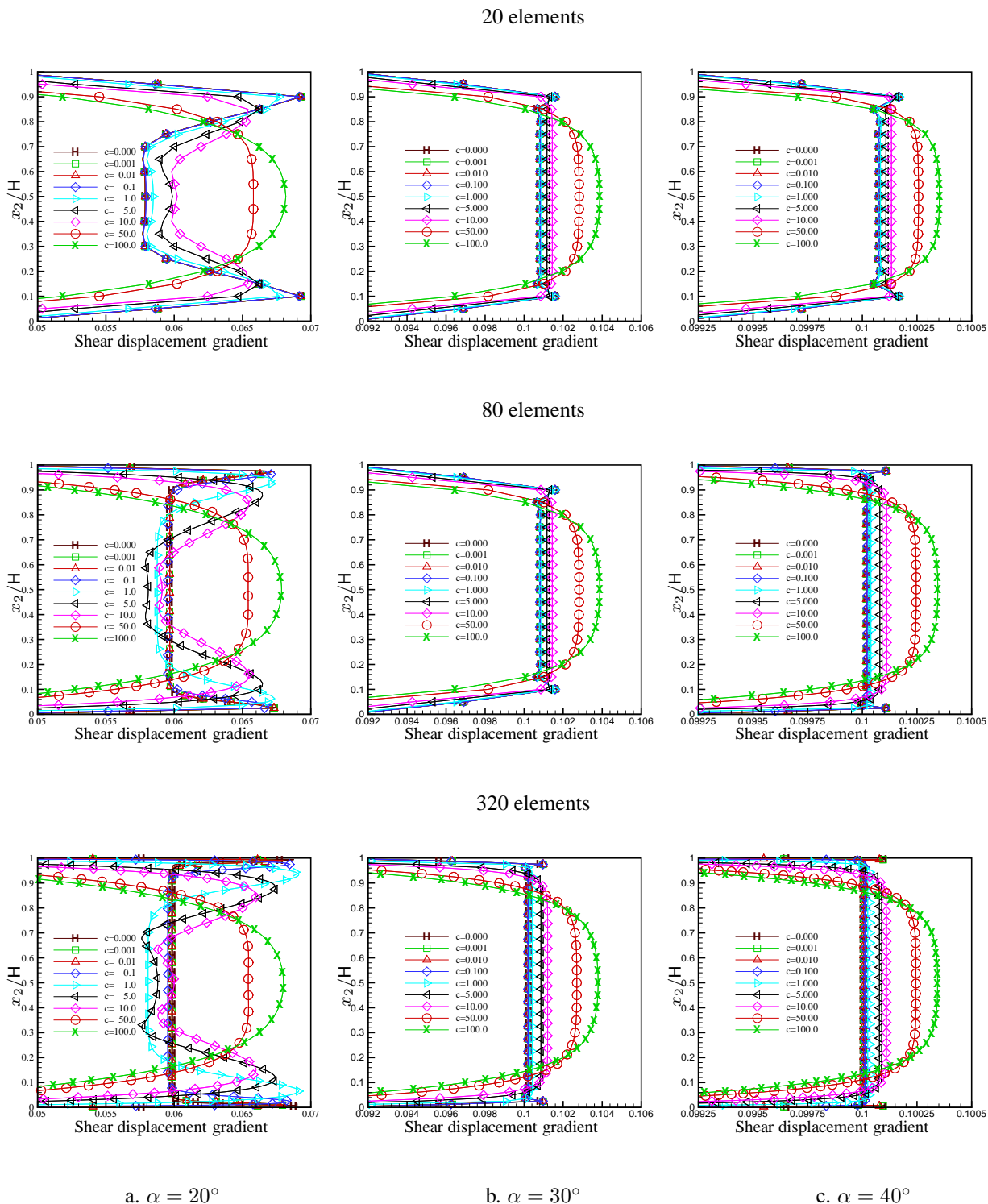


Figure 4.7: Shear displacement gradient vs.  $x_2/H$  - variation of gradient parameter and slip system angle

Obviously, a tendency to a uniform solution is visible for slip systems of  $\alpha \geq 30^\circ$  and small  $c$  ( $c \rightarrow 0$ ). Whereas, if  $c > 1$  an increasingly non-uniform, slightly bulged distribution becomes apparent. This

is accompanied by an increased boundary layer zone corresponding to an increased gradient parameter  $c$ . Furthermore, in the limit of  $c \rightarrow 0$ , oscillations are formed in the transition zone from boundary layer to a rather unimpaired zone in the middle of the strip, see Fig. 4.7a-c. Note that the oscillations are emphasized due to the change of the slip system angle to  $\alpha = 20^\circ$ . Thereby, only a lower strain rate level could be reached with the same load step size in comparison with results of  $\alpha \geq 30^\circ$ , see Fig. 4.7. Eventually, the oscillatory behavior spreads over the whole strip resulting in termination of further meaningful computation for  $\alpha = 20^\circ$ . The investigations in single slip are complemented with the subsequent figures that present the influence of mesh discretization for [20, 80, 320] elements and constant  $c$ . Hereby, different slip system angles are applied.

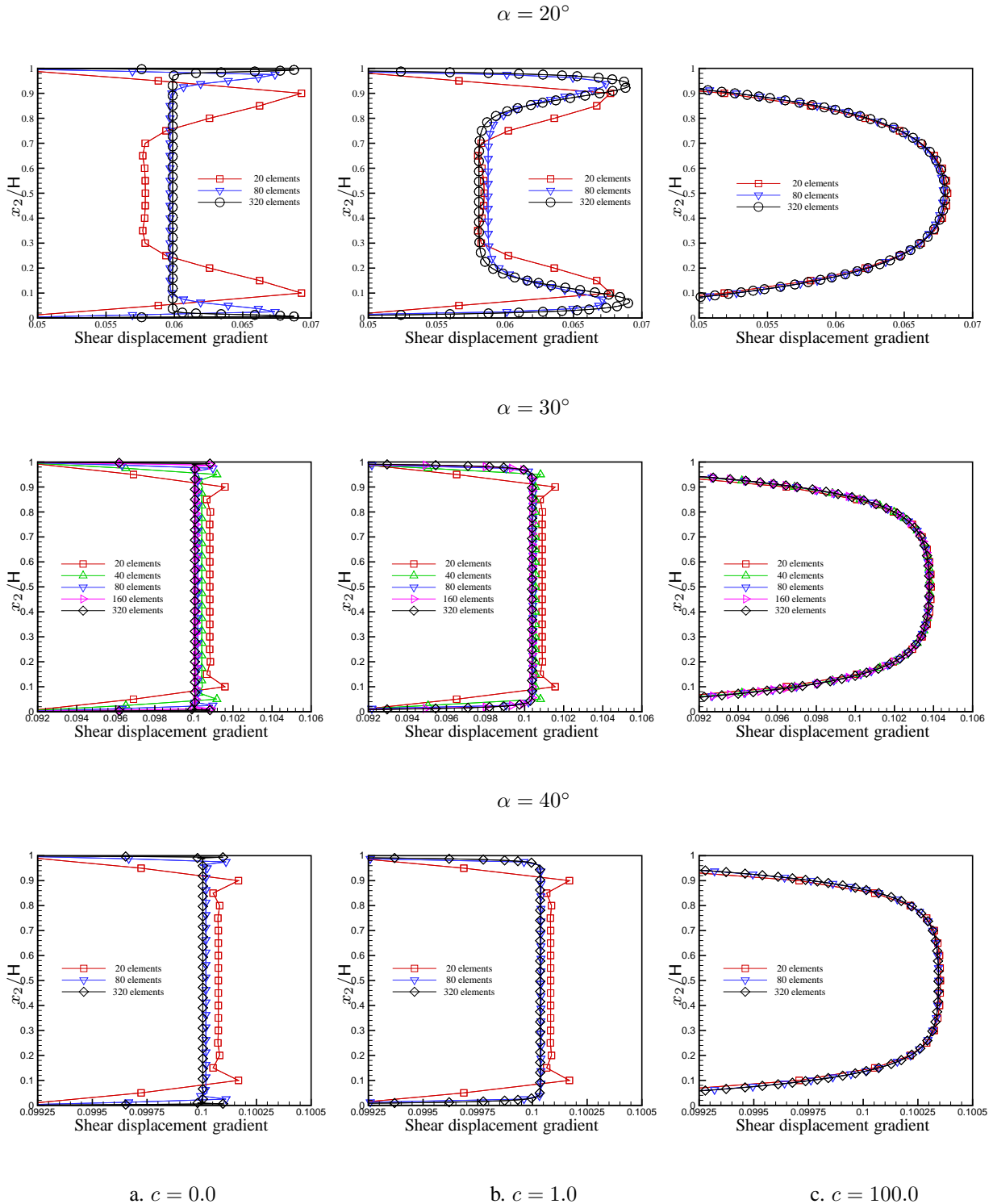


Figure 4.8: Shear displacement gradient vs.  $x_2/H$  - variation of element number and slip system angle

Obviously, in the range of small gradient parameters  $0 \leq c \leq 1$ , the influence of the discretization density becomes significant. A tendency towards a homogeneous deformation can be additionally observed for  $\alpha \geq 30^\circ$ , see Fig. 4.8a,b. Moreover, there are jumps in the shear displacement gradient distribution within one element, see Fig. 4.8a. In particular for  $\alpha = 20^\circ$ , an oscillative behavior is apparent, which is independent of the mesh discretization in the range of dispensable gradient influence  $0 \leq c \leq 1$ .

Consequently, a quasi-local discretization without further regularization is unable to capture the behavior correctly, see also the investigation in section 3.6 for different element types in case of geometrically linear phenomenological gradient plasticity. This unphysical behavior is almost remedied for  $c = 1$  with increasing mesh density, see Fig. 4.8b, i.e., the shear displacement gradient jump is resolved over more than one element. For even higher values of the gradient parameter  $c = 100$ , the discretization has no more influence and oscillations are completely smoothed out. The deformation is apparently inhomogeneous and a boundary layer zone is clearly displayed for all discretization densities and slip system angles, see Fig. 4.8c.

#### 4.4.2 Double slip model problem: simple shear of a crystalline strip

Secondly, the model problem is investigated in case of double slip. Here, the rate-dependent formulation in terms of a constitutive viscoplastic assumption for the local part of the Schmid law enhanced 'yield condition' as introduced in Eq. 4.7 will be focused upon. Therefore, the proposed model problem is additionally regularized by temporal means in order to remedy ambiguity issues. These result from the symmetric orientation of the slip systems with respect to the applied load scenario. Thus, both slip systems get activated simultaneously as the corresponding yield strength and hardening behavior are chosen to be the same. Consequently, a bifurcation problem would be encountered for the rate-independent case without further regularization.

The corresponding shear gradient distribution in double slip is depicted in Fig. 4.9a-c over the normalized height  $x_2/H$ . Thereby, three different discretization densities with [20, 80, 320] elements over  $H$  are investigated. Within each mesh the gradient influence is varied in terms of  $c = [0.0, \dots, 1.0, \dots, 100.0]$ . In addition to that, different slip system angles  $\alpha = [20^\circ, 30^\circ, 40^\circ]$  are considered.

As was already exhibited in single slip, one can again find an almost homogenous behavior for vanishing gradient parameters  $0 \leq c \leq 1$ . This is perfectly remedied for  $c > 1$ , whereby the jumps over one element are smoothed out. Thus due to dislocation pile-up at the lower and upper boundaries, a non-uniform distribution is reached with formation of the typical boundary layer zone as predicted by discrete dislocation simulations that were studied by Shu et al. (2001). The reverse trend towards a progressive disappearance of the boundary layer for an increase of the gradient parameter exceeding a certain limit, which corresponds to a lower bound of the  $H/l$  values that was realized in Svendsen and Reese (2003) is also observed here. This is exemplarily displayed for  $\alpha = 30^\circ$  in Fig. 4.9b setting  $c = 10000$  and  $c \rightarrow \infty$ , respectively, which renders a more and more homogeneous distribution. That means, in the limit of dislocation-size comparable to the specimen height  $H$ , one would expect a very brittle material behavior and consequently no occurrence of a boundary layer. Therefore, a trend to a homogeneous distribution of the shear displacement gradient for very high gradient values corresponding to a lower bound of  $H/l$  seems realistic.

Note that the oscillations are effectively remedied due to the fact that now regularization in time and space affects the underlying system of equations. The distribution of the shear displacement gradient exhibits only jumps in the range of dispensable gradient influence  $0 \leq c \leq 1$ . These jumps vanish for gradient parameter  $c \geq 1$ , which is also emphasized in Fig. 4.10. There, different discretizations are contrasted for constant gradient parameters  $c = (0.0, 1.0, 100.0)$ , respectively, and different slip system

angles  $\alpha = [20^\circ, 30^\circ, 40^\circ]$ , respectively.

Interestingly, the oscillative behavior seems to increase this time with the increasing slip system angle  $\alpha$  in contrast to the single slip case, where pronounced jumps were exhibited for  $\alpha = 20^\circ$ . Again, one can observe the total smoothing of the shear strain gradient profile, whereby mesh discretization becomes indistinguishable.

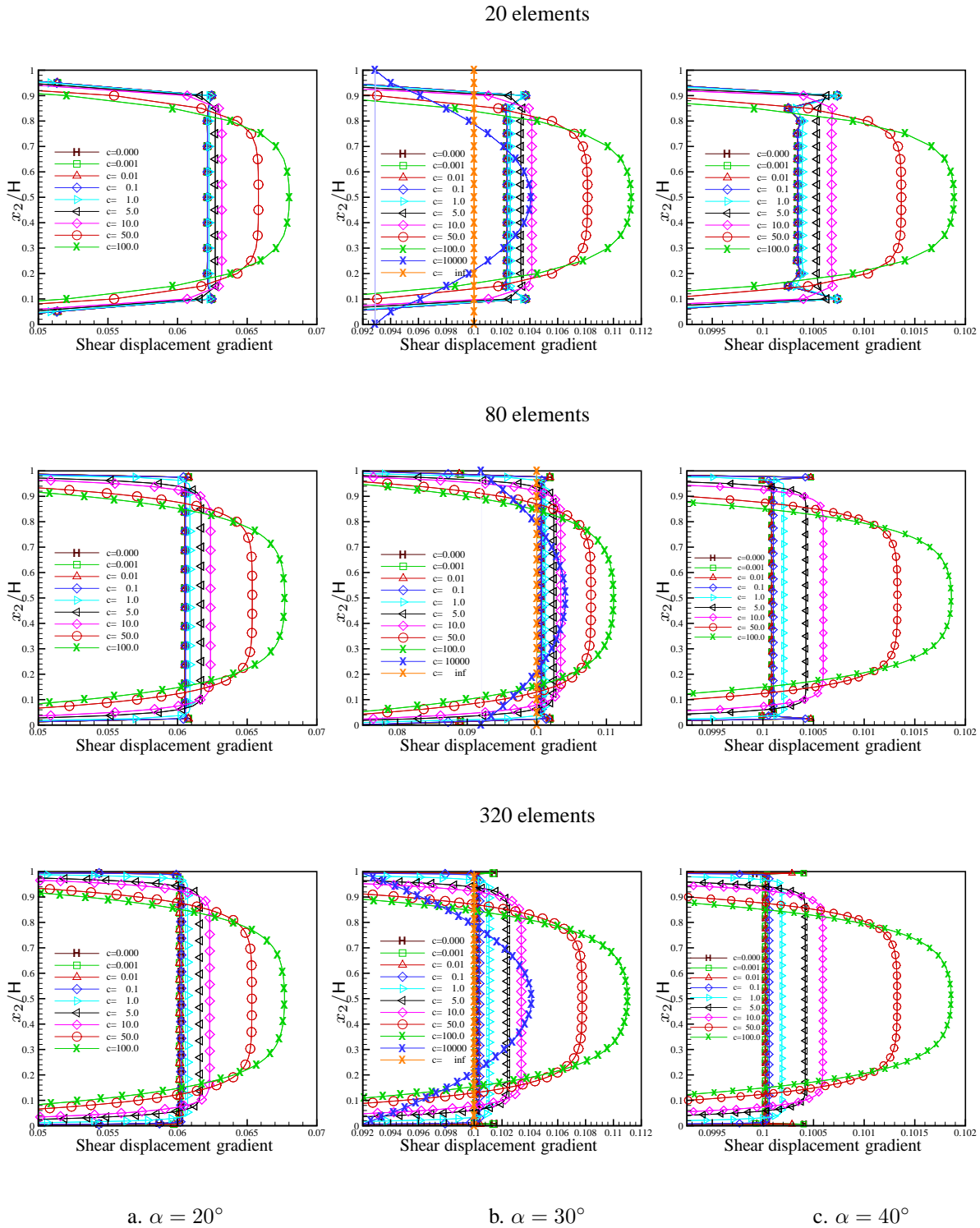


Figure 4.9: Shear displacement gradient vs.  $x_2/H$  - variation of gradient parameter and slip system angle

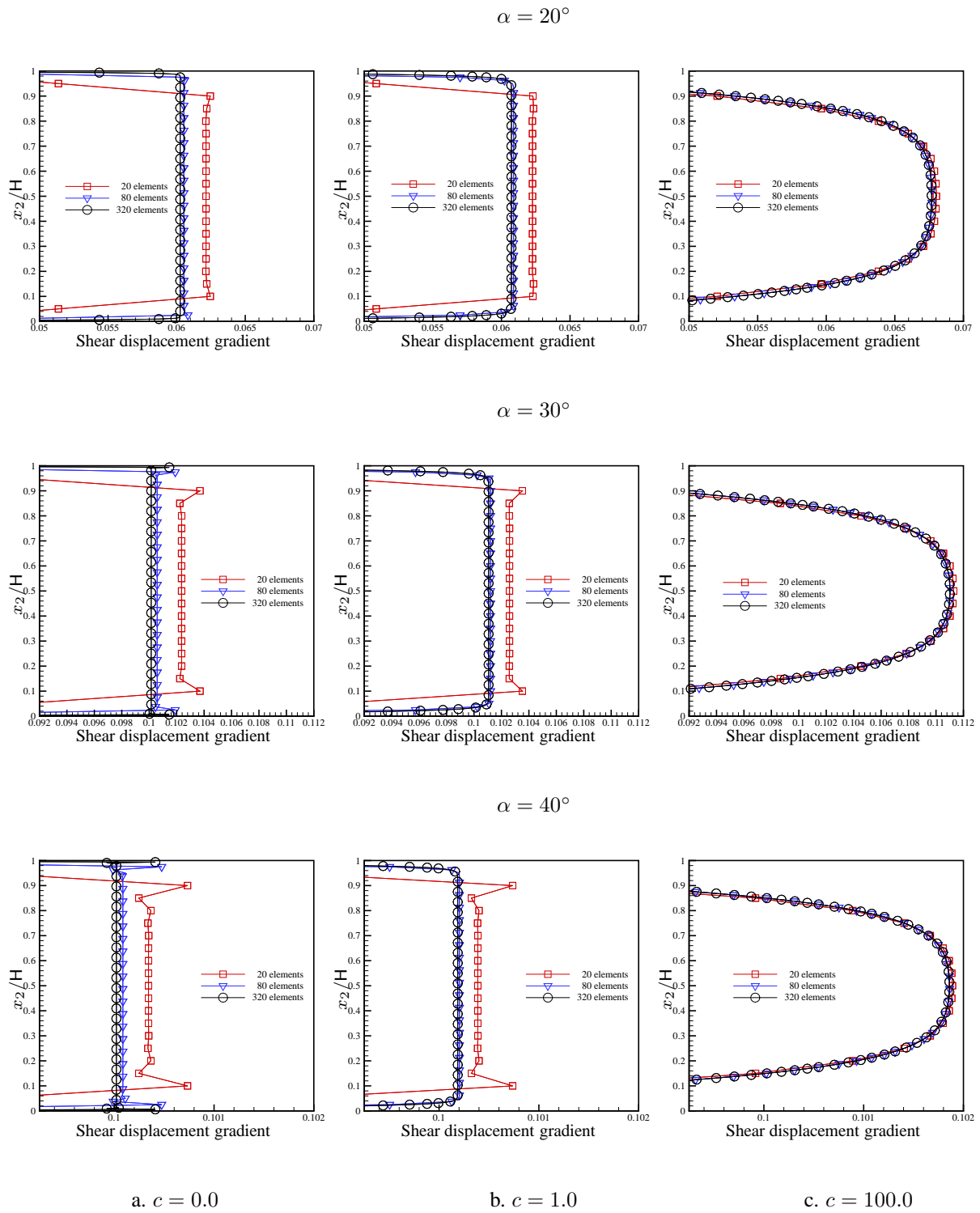


Figure 4.10: Shear displacement gradient vs.  $x_2/H$  - variation of element number and slip system angle

Finally, single slip and double slip phenomena are contrasted for a constant discretization with 320 elements in Fig. 4.11. Obviously, in double slip the shear layer in the middle of the strip becomes more pronounced as is also reported in the corresponding literature. One can thereby detect a progressive development of the boundary layer zone for increasing gradient parameter  $c$ . In case of  $\alpha = 20^\circ$  though, the differences between single and double slip seem to vanish with increasing gradient parameter, see Fig. 4.11a, whereas one can observe the reverse behavior for the other two slip angle cases as depicted in Fig. 4.11b,c.

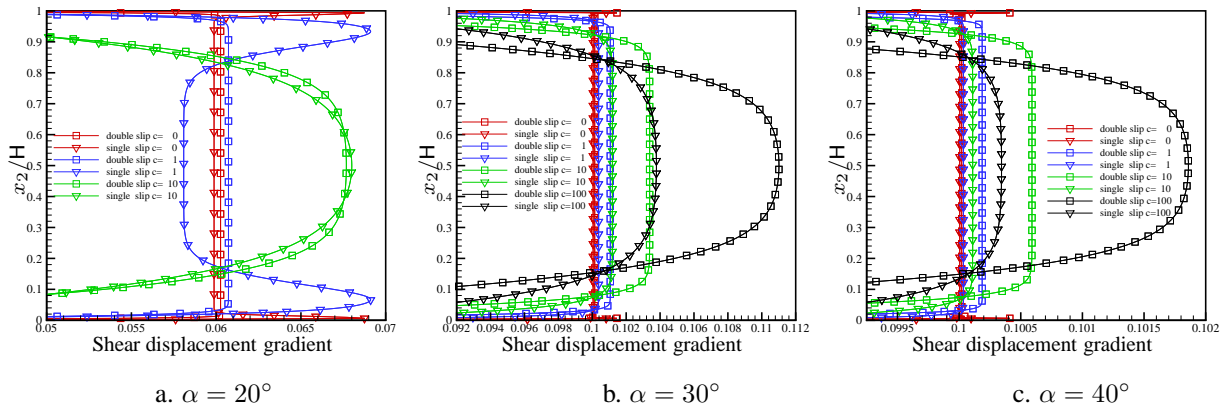


Figure 4.11: Single and double slip mechanism discretized with 320  $P^0_2P^0_1$ -elements

## Chapter 5

# Higher gradient continuum theory of phenomenological isotropic damage

So far, the inelastic material behavior was investigated in terms of plastic deformation. In the following, attention is focused on modeling material deterioration processes that are classically represented within a local framework of standard continuum damage formulations. As a simple measure of elastic degradation, accepting the physical interpretation as stress-bearing area reduction, it is sufficient to consider isotropic damage, see Simo and Ju (1987). It dates back to the early concept of Kachanov (1958) characterized by a scalar damage variable.

A critical issue in the formulation of damage, as already mentioned for the softening plasticity case, is the onset of material instabilities. One can thereby distinguish mainly two failure criteria. On the one hand, the material may exhibit diffuse failure, which is determined by the loss of uniqueness, see, e.g., Hill (1958), Runesson et al. (1991) or Steinmann and Willam (1994). On the other hand, localized failure may occur, which is associated with the formation of spatial discontinuities along singularity surfaces yielding damage accumulation within narrow bands see, e.g., Rice (1976) and Rizzi et al. (1994). In fact, one may distinguish between strong and weak discontinuities due to a transition from homogeneous velocities and/or strain rates to non-homogeneous fields in terms of Hadamards instability classification. Thereby, a weak discontinuity refers to a second order singularity in the strain rate field while the displacement rates are still continuous  $[[\dot{\mathbf{u}}]] = 0$ ,  $[[\dot{\boldsymbol{\epsilon}}]] \neq 0$ , whereby  $[[\bullet]]$  denotes the jump of  $(\bullet)$ . In contrast, a strong discontinuity is characterized by a second order singularity in both rate fields  $[[\dot{\mathbf{u}}]] \neq 0$ ,  $[[\dot{\boldsymbol{\epsilon}}]] \neq 0$ . In many cases, a localization mechanism is favored by strain softening, see Delaplace et al. (1996), which is a result of inhomogeneities on the micro scale. Experimental investigations of a strain softening approach were carried out by Kongshavn and Poursartip (1999). Thereby localized zones, which often form a precursor to the final rupture of the material, display a finite width. But standard continuum descriptions and, in particular, the corresponding numerical solution schemes, fail to obtain such a finite width whereas it is observed in experiments.

An early remedy to this unphysical behavior was developed by Bažant and Pijaudier-Cabot (1988) in terms of a nonlocal integral model. Further investigations with respect to regularization of the localization problem were carried out by Sluys (1992) or de Borst et al. (1993). The first elaborated gradient damage model was proposed by Peerlings et al. (1995; 1996b; 1996a). Furthermore, motivated by observations in plasticity, see the literature review in the preceding chapters, several gradient dependent damage models were proposed, whereby the gradient dependence is essentially incorporated in the loading surface by the Laplacian of an internal variable, see, e.g., Comi (1996; 1999), de Borst et al. (1996) and Benallal and Tvergaard (1995). Especially for the case of nonlocal damage theories, a comparison of

different approaches has been investigated by Jirasek (1998) and more recently by Peerlings et al. (2002) with focus on the differences of explicit and implicit models. Moreover, a coupled elasto-plastic-damage model including the gradient of damage is proposed by Nedjar (2001). The main aspects of the gradient theory presented here have been summarized in Liebe, Steinmann and Benallal (2001a). Recently, a thermodynamically consistent nonlocal formulation for damaging materials was proposed by Benvenuti et al. (2002).

The extension to anisotropic gradient damage is proposed in Kuhl et al. (2000) and Comi (2001), the identification of the additional gradient parameter is considered by Mahnken and Kuhl (1999).

The goal of this chapter is to first derive a theory and the corresponding numerics of a thermodynamically consistent formulation of isotropic gradient damage in small strains. The driving force in local theory, namely the local stored energy, is thereby modified to a quasi-nonlocal quantity in order to take micro defect interactions into account. This quasi-nonlocal quantity enters the damage condition as well as the update of the history variable. A subsequent analysis of the well-posedness of the problem underlines the benefits due to the proposed gradient formulation. Secondly, the chapter is concluded by a numerical analysis of the theoretical set up. Thereby, the corresponding strong and weak forms of the coupled problem will be derived. Then, the finite element discretization will be envisioned, which is used for the monolithic iterative solution of the coupled problem. The algorithm will be applied to a standard model problem of a bar in uniaxial tension for the sake of demonstration. Finally, the gradient framework is extended to the geometrically non-linear case and will be illustrated with a simulation of a 2-dimensional model problem.

## 5.1 Thermodynamics of phenomenological local damage

In order to alleviate the shift of focus towards inelastic material behavior exhibiting material deterioration, a brief reiteration of a thermodynamical sound formulation of local isotropic damage is presented.

---

### Free Helmholtz energy

$$\Psi = \Psi^{mac}(d, \epsilon)$$

### Dissipation inequality

$$\mathcal{D} = Y\dot{d} \geq 0$$

### Macroscopic stress

$$\sigma = \sigma(d, \epsilon) = \frac{\partial \Psi^{mac}}{\partial \epsilon}$$

### Energy release rate

$$Y = Y(d, \epsilon) = -\frac{\partial \Psi^{mac}}{\partial d}$$

### Damage condition

$$\Phi = \Phi(Y; d) = \phi(Y) - d \leq 0$$

### Damage variable evolution and update

$$\dot{d} = \dot{\kappa} \frac{\partial \Phi}{\partial Y} = \dot{\kappa} \frac{\partial \phi}{\partial Y} \quad \text{and} \quad \dot{Y} = \dot{\kappa} > 0 \quad \implies \quad d = \phi(\kappa)$$

### History variable update

$$\kappa = \max_{-\infty < s < t} (Y(s), \kappa_0)$$

### Alternative format of the Karush-Kuhn-Tucker complementary conditions

$$\varphi = Y - \kappa \leq 0 \quad \text{and} \quad \dot{d} \geq 0 \quad \text{and} \quad \dot{\varphi}(Y; \kappa) = 0$$


---

Table 5.3: Key ingredients of local isotropic damage



For an overview, Table 5.3 summarizes the main equations representing the classical local approach in phenomenological continuum damage mechanics for the geometrically linear case. Here, a particular free energy density  $\Psi$  modeling a hyperelastic constitutive response coupled to isotropic damage is envisioned. Thereby, isotropic damage is characterized by a degradation measure in terms of a scalar damage variable  $0 \leq d \leq 1$  that acts as a reduction factor of the local stored energy density of the virgin material. Therefore, the free energy  $\Psi$  is expressed as a function of the macroscopic strain  $\epsilon = \text{grad}^{sym} \mathbf{u}$  and the damage variable  $d$ . The model is based on a dissipation potential, the postulate of maximum dissipation rendering the macroscopic stresses  $\boldsymbol{\sigma}$  and the energy release rate  $Y$ . Next, the evolution of the damage variable  $d$  is defined by adopting the concept proposed by Simo and Ju (1987). Thus, the damage consistency condition in the case of loading is characterized by  $\dot{\Phi} = 0$  and  $\dot{\kappa} > 0$  and allows the closed form update for the damage parameter, see Table 5.3, whereby the history variable  $\kappa$  is computed from  $\kappa = \max_{-\infty < s < t} (Y(s), \kappa_0)$  with  $\kappa_0$  the initial threshold. The formulation is complemented by the corresponding Karush-Kuhn-Tucker conditions, which are stated in alternative format based on the inversion of  $\phi(\bullet)$ .

## 5.2 Thermodynamics of phenomenological gradient damage

Now the simplified gradient model derived in section 2.2.1 will be taken as a framework for a gradient enhanced damage model. Thereby, as a simple phenomenological measure of micro defect interactions, the gradient of the damage field is considered. Then, a particular version of a gradient damage formulation is obtained by choosing the free energy  $\Psi$  as a function of the macroscopic strain  $\epsilon$  and a scalar damage variable  $d$  together with its first gradient  $\mathbf{d} = \text{grad} d$ . For an overview, the determining quantities are summarized in Table 5.4.

Here,  $\Psi$  is decomposed into a macro and a gradient part for convenience of exposition. Then, in analogy to section 3.2 the Clausius-Duhem inequality  $\mathcal{D} = \boldsymbol{\sigma} : \dot{\epsilon} - \dot{\Psi} + \mathcal{P} \geq 0$  is exploited, which incorporates the nonlocality residual  $\mathcal{P}$  according to the arguments by Polizzotto and Borino (1998). This renders the familiar constitutive relations for the macroscopic stress  $\boldsymbol{\sigma} = \boldsymbol{\sigma}(d, \epsilon)$  and the local energy release rate  $Y = Y(d, \epsilon)$  as well as the vectorial damage flux  $\mathbf{Y} = \mathbf{Y}(d)$  as thermodynamically conjugated to  $\mathbf{d}$ . As long as  $d$  remains smooth, i.e.,  $[[d]] = 0$  throughout the body,  $\mathbf{d}$  and consequently  $\mathbf{Y}$  are bounded. Following Edelen and Laws (1971), the appropriate nonlocality residual  $\mathcal{P}$  accounts for the energy exchanges between the particles in the active damaged part  $\mathcal{B}^d \subseteq \mathcal{B}$  due to the envisioned microstructural interactions. Thereby, the so-called insulation condition  $\int_{\mathcal{B}^d} \mathcal{P} dV = 0$  assures that no energy exchanges occur between the particles in  $\mathcal{B}^d$  and those outside  $\mathcal{B}^d$ , e.g., the local dissipation inequality  $\mathcal{D} = \boldsymbol{\sigma} : \dot{\epsilon} - \dot{\Psi} + \mathcal{P} \geq 0$  holds throughout the whole body  $\mathcal{B}$ , but with  $\mathcal{P} = 0$  at points not belonging to  $\mathcal{B}^d$ .

Note that one must again consider the compatibility requirements resulting from the present format of the dissipation inequality that suggests independent evolution equations for  $d$  and  $\mathbf{d}$ . Thus, these evolution equations would have to be designed such that compatibility is satisfied. Again, a possible solution can be achieved by introducing a bilinear form of the dissipation power, see Table 5.4. Consequently, the quasi-nonlocal quantity  $\bar{Y}$  is advocated to be identified as thermodynamically conjugated to the damage variable  $d$ . Comparison of the remaining dissipation inequality and the bilinear form renders an expression for the nonlocality residual. Then, applying the insulation condition, integration by parts and invoking Gauss theorem yields

$$\int_{\mathcal{B}^d} \mathcal{P} dV = \int_{\mathcal{B}^d} [\bar{Y} + \text{div} \mathbf{Y} - Y] \dot{d} dV - \int_{\partial \mathcal{B}^d} [\mathbf{n} \cdot \mathbf{Y}] \dot{d} dA = 0, \quad (5.1)$$

which must be identically satisfied.

**Free Helmholtz energy**

$$\Psi = \Psi(d, \epsilon, \mathbf{d}) = \Psi^{mac}(d, \epsilon) + \Psi^{dis}(\mathbf{d})$$

**Dissipation inequality**

$$\mathcal{D} = Y\dot{d} + \mathbf{Y} \cdot \dot{\mathbf{d}} + \mathcal{P} \geq 0$$

**Macroscopic stress**

$$\boldsymbol{\sigma} = \boldsymbol{\sigma}(d, \epsilon) = \frac{\partial \Psi^{mac}}{\partial \epsilon}$$

**Energy release rate**

$$Y = Y(d, \epsilon) = -\frac{\partial \Psi^{mac}}{\partial d}$$

**Damage flux**

$$\mathbf{Y} = \mathbf{Y}(d) = -\frac{\partial \Psi^{dis}}{\partial \mathbf{d}}$$

**Bilinear dissipation potential**

$$\mathcal{D} = \bar{Y}\dot{d}$$

**Nonlocality residual**

$$\mathcal{P} = \bar{Y}\dot{d} - Y\dot{d} - \mathbf{Y} \cdot \dot{\mathbf{d}}$$

**Damage condition**

$$\Phi = \Phi(\bar{Y}; d) = \phi(\bar{Y}) - d \leq 0$$

**Damage variable evolution and update**

$$\dot{d} = \dot{\kappa} \frac{\partial \Phi}{\partial \bar{Y}} = \dot{\kappa} \frac{\partial \phi}{\partial \bar{Y}} \quad \text{and} \quad \dot{\bar{Y}} = \dot{\kappa} > 0 \quad \implies \quad d = \phi(\kappa)$$

**History variable update**

$$\kappa = \max_{-\infty < s < t} (\bar{Y}(s), \kappa_0)$$

**Karush-Kuhn-Tucker complementary conditions**

$$\varphi = \bar{Y} - \kappa \leq 0 \quad \text{and} \quad \dot{d} \geq 0 \quad \text{and} \quad \dot{d}\varphi(\bar{Y}; \kappa) = 0$$

**Boundary conditions**

$$\dot{d} = 0 \quad \text{on} \quad \partial \mathcal{B}_{int}^d \quad \text{and} \quad \mathbf{n} \cdot \mathbf{Y} = 0 \quad \text{on} \quad \partial \mathcal{B}_{ext}^d$$

Table 5.4: Key ingredients of gradient isotropic damage

Thus, only one evolution equation for  $d$  has to be determined. From Eq. 5.1, the following (necessary and sufficient) conditions result in

$$\bar{Y} = Y - \operatorname{div} \mathbf{Y} \quad \text{in} \quad \mathcal{B}^d \quad \text{and} \quad [\mathbf{n} \cdot \mathbf{Y}]\dot{d} = 0 \quad \text{on} \quad \partial \mathcal{B}^d. \quad (5.2)$$

Therefore, the only driving force conjugated to evolution of the independent arbitrary internal damage field  $d$  is identified as the quasi-nonlocal energy release rate  $\bar{Y}$ . The latter expression renders two conditions according to a split of the damaged subdomain boundary into an external and internal part  $\partial \mathcal{B}^d = \partial \mathcal{B}_{int}^d \cup \partial \mathcal{B}_{ext}^d$ . On the one hand, the so-called constitutive boundary condition of Neumann type is imposed on the external damaged subdomain boundary  $\partial \mathcal{B}_{ext}^d \subseteq \partial \mathcal{B}$ . As a consequence, the quasi-nonlocal energy release rate  $\bar{Y}$  equals the local energy release rate  $Y$  for a homogeneous solution. On the other hand, the so-called continuity boundary condition of Dirichlet type must be added on the internal damaged subdomain boundary  $\partial \mathcal{B}_{int}^d$  in order to assure continuity of the stress rate  $\dot{\boldsymbol{\sigma}}$  across  $\partial \mathcal{B}_{int}^d$ .

As a result from the above elaborations, it can be found that compatibility between  $\dot{d}$  and  $\dot{\mathbf{d}}$  is automatically satisfied. Consequently, for the present case of gradient damage, based on the dissipation inequality  $\mathcal{D} \geq 0$  in bilinear form, see Table 5.4, a damage condition is readily motivated, whereby the function  $\phi = \phi(\bar{Y})$  is introduced as a monotonic function of its argument, for the purely local case see, e.g., Simo

and Ju (1987). Note that the quasi-nonlocal energy release rate  $\bar{Y}$  is a functional<sup>1</sup> rather than a function of  $d$ , likewise it is the functional derivative rather than the derivative of  $\Psi$  with respect to  $d$ .

Then, based on the postulate of maximum dissipation, the constrained optimization problem

$$\mathcal{L}(\bar{Y}; \dot{d}, \dot{\kappa}) = -\mathcal{D} + \dot{\kappa}\Phi = -\bar{Y}\dot{d} + \dot{\kappa}\Phi(\bar{Y}; d) \rightarrow \text{stat} \quad (5.3)$$

involves the Lagrange multiplier  $\dot{\kappa} \geq 0$  to enforce  $\Phi \leq 0$  and renders the associated evolution law for  $d$ . Remarkably, the evolution equation retains the same format as for the local case given in Table 5.3. Moreover, the closed form update for the damage parameter is equivalent to the ones in local damage by replacing the local energy release rate  $Y$  by its quasi-nonlocal counterpart  $\bar{Y}$ . Based on the inversion of  $\phi(\bullet)$ , the damage condition and the Karush-Kuhn-Tucker complementary conditions, may again be expressed in an alternative format.

### 5.3 Isotropic local and gradient prototypes

The key ingredients for a prototype model of isotropic local damage and isotropic gradient damage are summarized and compared respectively in Table 5.5.

Here, the gradient part  $W_d$  is expanded into an isotropic quadratic function in  $d$ .  $K$  and  $G$  again denote the bulk and shear modulus, respectively. The gradient parameter  $c \geq 0$  controls the quasi-nonlocal character of the formulation. Moreover, for the damage evolution  $\phi(\kappa)$ , a simple exponential-type law is adopted, whereby the initial damage threshold  $\kappa_0$  is introduced as well as an exponential parameter  $\beta$ . The corresponding damage evolution with an increasing internal variable  $\kappa > \kappa_0$  is depicted in Fig. 5.1.

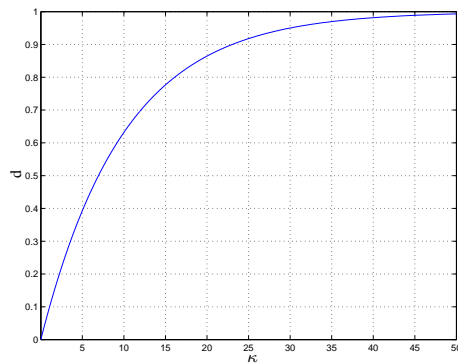


Figure 5.1: Damage evolution versus internal variable

<sup>1</sup>**Remark:** Define the functional  $\Psi : \mathbb{R} \times \mathbb{R}^{n \times n} \times \mathbb{R}^n \rightarrow \mathbb{R}$  as

$$\Psi(d, \boldsymbol{\epsilon}, \mathbf{d}) = \int_{\mathcal{B}} \psi(d, \boldsymbol{\epsilon}, \mathbf{d}) dV \quad \text{with} \quad \psi = \psi^{mac}(d, \boldsymbol{\epsilon}) + \psi^{grad}(\mathbf{d}).$$

The functional derivative of  $\psi$  at  $d, \boldsymbol{\epsilon}, \mathbf{d}$  with respect to  $d$ , denoted by  $\delta\psi/\delta d$ , is implicitly defined by

$$\frac{d}{d\varepsilon} \Psi(d + \varepsilon \delta d; \boldsymbol{\epsilon})|_{\varepsilon=0} = \int_{\mathcal{B}} \frac{\delta\psi}{\delta d} \delta d dV$$

and takes the format

$$\frac{\delta\psi}{\delta d} = \frac{\partial\psi^{mac}}{\partial d} - \text{div} \frac{\partial\psi^{grad}}{\partial \mathbf{d}} = -Y + \text{div} \mathbf{Y} = -\bar{Y}.$$

Thus, the inequality for the dissipation in bilinear format can be alternatively written in terms of the functional derivative  $\mathcal{D} = -\frac{\delta\psi}{\delta d} \dot{d} = \bar{Y} \dot{d} \geq 0$ . For an account on higher gradient continua based on the notion of functional derivatives, refer, e.g., to Maugin (1993).

**Free Helmholtz energy  $\Psi$** 

$$\text{local} \quad \Psi(\boldsymbol{\epsilon}, d) = [1 - d]W_\epsilon(\boldsymbol{\epsilon})$$

$$\text{gradient} \quad \Psi(\boldsymbol{\epsilon}, \mathbf{d}, d) = [1 - d]W_\epsilon(\boldsymbol{\epsilon}) + W_d(\mathbf{d})$$

Elastic part of the free energy

$$W_\epsilon(\boldsymbol{\epsilon}) = \frac{1}{2} \boldsymbol{\epsilon} : \boldsymbol{\mathcal{E}}_\epsilon : \boldsymbol{\epsilon} \quad \text{with } \boldsymbol{\mathcal{E}}_\epsilon = K\mathbf{1} \otimes \mathbf{1} + 2G\boldsymbol{\mathcal{I}}^{dev}$$

Gradient part of the free energy

$$W_d(\mathbf{d}) = \frac{1}{2} \mathbf{d} \cdot \boldsymbol{\mathcal{E}}_d \cdot \mathbf{d} \quad \text{with } \boldsymbol{\mathcal{E}}_d = c\mathbf{1}$$

**Macroscopic stress**

$$\text{nominal} \quad \boldsymbol{\sigma}(\boldsymbol{\epsilon}) = [1 - d]\boldsymbol{\mathcal{E}}_\epsilon : \boldsymbol{\epsilon}$$

$$\text{effective} \quad \tilde{\boldsymbol{\sigma}}(\boldsymbol{\epsilon}) = \boldsymbol{\mathcal{E}}_\epsilon : \boldsymbol{\epsilon}$$

**Energy release rate**

$$\text{local} \quad Y(\boldsymbol{\epsilon}, d) = W_\epsilon(\boldsymbol{\epsilon})$$

$$\text{quasi-nonlocal} \quad \bar{Y}(\boldsymbol{\epsilon}, \mathbf{d}, d) = Y - \text{div } \mathbf{Y} = Y + c \text{ div } \mathbf{d}$$

$$\text{Damage flux} \quad \mathbf{Y}(\mathbf{d}) = -\boldsymbol{\mathcal{E}}_d \cdot \mathbf{d} = -c \mathbf{d}$$

**Damage evolution**

$$d = \phi(\kappa) = 1 - \exp(\beta[\kappa_0 - \kappa])$$

Table 5.5: Isotropic local and gradient prototype

In analogy to phenomenological gradient plasticity, it is illustrative to consider the term  $\text{div grad } d$  in the quasi-nonlocal energy release rate as related to the curvature of the damage profile. Damage evolution is clearly increased/decreased compared to the case of local damage in regions with positive/negative curvature of the current damage profile, thus showing a tendency to broaden the  $d$ -profile, see Fig. 5.2.

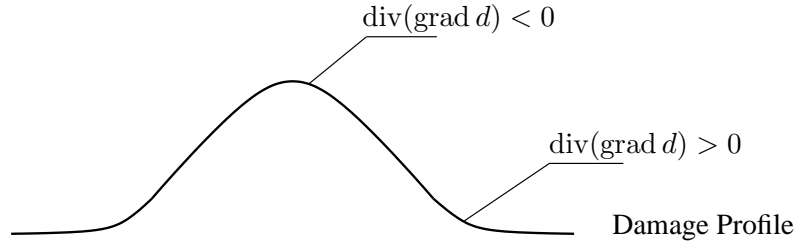


Figure 5.2: Damage variable profile

## 5.4 Well-posedness of the coupled problem

The formalism of a wave propagation analysis is applied to the gradient damage case in analogy to the investigation of the ill-posed character of the boundary value problem in gradient plasticity, see section 3.4. As it is well known, this ill-posedness is due to the loss of the ellipticity condition and also due to the failure of the complementing conditions in the elliptic regime, see Benallal, Billardon and Geymonat (1993). A similar analysis, which is not carried out here may be performed for the complementing conditions.

Again, an underlying homogeneous state is assumed before the onset of localization. Then, the following harmonic approach is chosen for the rates of the displacements  $\dot{\mathbf{u}}$  and the internal variable  $\dot{d}$ , which

corresponds to the assumption of stationary planar waves in analogy to Eq. 3.20

$$\begin{aligned}\dot{\mathbf{u}} &= \exp(ik[\hat{\mathbf{n}} \cdot \mathbf{x}])\hat{\mathbf{m}} \\ \dot{d} &= \exp(ik[\hat{\mathbf{n}} \cdot \mathbf{x}])m.\end{aligned}\quad (5.4)$$

Based on this approach and the incremental equations for the quasi-static balance of linear momentum  $\text{div } \dot{\boldsymbol{\sigma}} = \mathbf{0}$  together with the consistency condition for loading  $\dot{\Phi} = 0$ , it is then investigated if the homogeneous state admits a bifurcation into a solution of planar wave type. The resulting homogeneous equation system renders for the above prototype model

$$\begin{bmatrix} -k^2[1-d]\mathbf{Q}_\epsilon & -ik\tilde{\mathbf{t}} \\ ik\tilde{\mathbf{t}} & -h - k^2Q_d \end{bmatrix} \begin{bmatrix} \hat{\mathbf{m}} \\ \hat{m} \end{bmatrix} = \begin{bmatrix} \mathbf{0} \\ 0 \end{bmatrix}\quad (5.5)$$

and thus allows a closed form expression for the bifurcation condition in terms of the localization tensor

$$\det \left[ [1-d]\mathbf{Q}_\epsilon - \frac{\tilde{\mathbf{t}} \otimes \tilde{\mathbf{t}}}{h + k^2Q_d} \right] = 0 \quad \longrightarrow \quad 1 - \frac{\tilde{\mathbf{t}} \cdot \mathbf{Q}_\epsilon^{-1} \cdot \tilde{\mathbf{t}}}{[1-d]} \frac{1}{[h + k^2Q_d]} = 0. \quad (5.6)$$

Here, the following abbreviations are introduced for the partition of the localization tensor

$$\begin{aligned}\mathbf{Q}_\epsilon \cdot \hat{\mathbf{m}} &= [\boldsymbol{\mathcal{E}}_\epsilon : [\hat{\mathbf{m}} \otimes \hat{\mathbf{n}}]] \cdot \hat{\mathbf{n}} \\ \tilde{\mathbf{t}} &= \tilde{\boldsymbol{\sigma}} \cdot \hat{\mathbf{n}} \\ Q_d &= [\boldsymbol{\mathcal{E}}_d \cdot \hat{\mathbf{n}}] \cdot \hat{\mathbf{n}} \stackrel{iso}{=} c \geq 0 \\ h &= 1/H \quad \text{with} \quad H = \frac{\partial \phi}{\partial \kappa}.\end{aligned}\quad (5.7)$$

Note that the elastic acoustic tensor  $\mathbf{Q}_\epsilon$  is positive definite, i.e.,  $\det \mathbf{Q}_\epsilon > 0$ , which yields the term  $\tilde{\mathbf{t}} \cdot \mathbf{Q}_\epsilon^{-1} \cdot \tilde{\mathbf{t}} > 0 \forall \tilde{\mathbf{t}} \neq 0$ . Moreover, due to the inverse definition of the critical deterioration modulus  $h$  with regard to the monotonic function  $\phi$ ,  $h$  ranges between 0 and  $\infty$  corresponding to a strong growth of the damage variable  $d$  with respect to  $\kappa$  and no growth, respectively.

As a consequence, the critical deterioration modulus  $h^{crit} \in [0, \infty]$ , i.e., the largest deterioration modulus corresponding to the fastest damage growth  $H^{crit} \in [\infty, 0]$ , which allows for a bifurcation into a planar wave type solution, follows as

$$h^{crit} = \frac{1}{H^{crit}} = \frac{1}{[1-d]} \max_{\hat{\mathbf{n}}} (\tilde{\mathbf{t}} \cdot \mathbf{Q}_\epsilon^{-1} \cdot \tilde{\mathbf{t}}) - k^2Q_d \geq 0. \quad (5.8)$$

Thus, bifurcation for the gradient model for an infinite homogeneous solid is first possible when it occurs for the local model. It appears that for  $Q_d \stackrel{iso}{=} c > 0$ , the critical deterioration modulus  $h^{crit}$  in the case of gradient damage is less than the critical deterioration modulus  $h_{local}^{crit}$  for local damage

$$h_{local}^{crit} = \frac{1}{[1-d]} \max_{\hat{\mathbf{n}}} (\tilde{\mathbf{t}} \cdot \mathbf{Q}_\epsilon^{-1} \cdot \tilde{\mathbf{t}}) \geq h^{crit}, \quad (5.9)$$

which is similar to the findings in gradient plasticity. Hence, the gradient case allows for faster damage growth  $H^{crit} \geq H_{local}^{crit}$ . Next, the influence of the wavelength on the critical deterioration modulus is investigated. In order to do this, the long and short wave length limits are considered corresponding to  $k \rightarrow 0$ , i.e., the incrementally homogeneous solution, and  $k \rightarrow \infty$ , i.e., the infinitely localized solution, respectively.

On the one hand, the long wavelength limit results in a critical deterioration modulus, which equals

the local critical deterioration modulus in the limit  $h^{crit} \rightarrow h^{local,crit}$ . Thus, the gradient formulation obviously does not effect homogeneous solutions. On the other hand, the short wavelength limit renders a critical deterioration parameter  $h^{crit} \rightarrow -\infty$ , i.e., bifurcation into incrementally localized solutions is effectively excluded, since  $h \geq 0$  holds as long as  $d < 1$ , see Fig. 5.3.

Finally, for the gradient case the critical wavenumber  $k_c$  (cutting wavelength) may be bounded from below with  $h \geq h^{crit} \geq 0$  as follows

$$0 \leq k_c^2 \geq \frac{1}{Q_d} \left[ \frac{1}{[1-d]} \max_{\tilde{\mathbf{n}}} (\tilde{\mathbf{t}} \cdot \mathbf{Q}_\epsilon^{-1} \cdot \tilde{\mathbf{t}}) - h \right]. \quad (5.10)$$

Thus, in case of gradient damage with the gradient parameter  $c$  in the range  $0 < Q_d \stackrel{iso}{=} c \leq \infty$ , the corresponding wavenumber is in the range  $\infty > k \geq 0$ , i.e., planar wave type solutions with finite wave length exist. For the limiting case of local damage with zero gradient parameter  $Q_d \stackrel{iso}{=} c = 0$ , the corresponding wave number is  $k \rightarrow \infty$ , thus localized solutions exist. If  $d$  reaches the limit  $d = 1$  then the corresponding wavenumber becomes infinite  $k \rightarrow \infty$ , which materializes as a line crack, see Fig. 5.3.

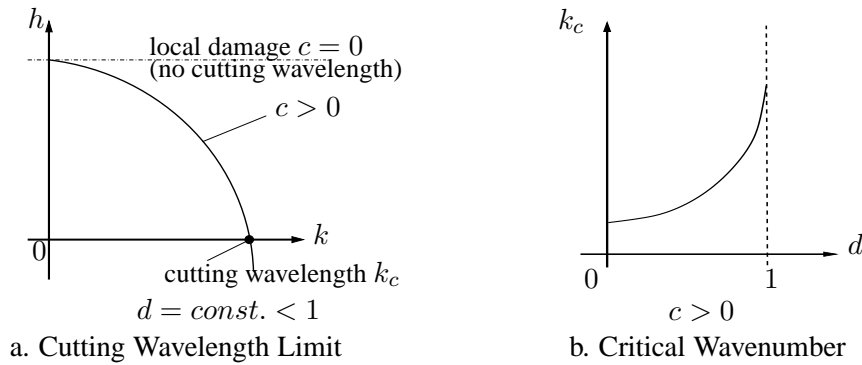


Figure 5.3: Limiting Values

Therefore, there exist two competing processes: stabilization of localization phenomena due to the regularization driven by the gradient incorporation and evolution of full damage and thus total degradation of the material strength and loss of stability. There is, however, still a large difference with the local case.

Thus, in summary, based on the above analysis, a regularizing influence of the gradient term is expected for damage computations, especially in the initial state of damage  $d < 1$ . This will be numerically demonstrated later in the numerical example section.

## 5.5 Numerical treatment of phenomenological gradient damage

The numerical treatment of the proposed gradient damage formulation is closely related to the one described in gradient plasticity, compare to section 3.5. Thereby starting from a coupled problem constituted by an equilibrium subproblem and a constitutive subproblem, a two-field formulation is provided, whereby the damage variable is discretized in addition to the displacement field.

### 5.5.1 Strong form of the coupled problem

To set the stage for the following developments, the pertinent set of equations is at first summarized for the solution of the coupled boundary value problem in strong form.

Let  $\mathcal{B}$  denote the configuration occupied by a solid body. The displacement field  $\mathbf{u} = \mathbf{u}(\mathbf{x})$  and the damage field  $d = d(\mathbf{x})$  are then parameterized in terms of the placements  $\mathbf{x} \in \mathcal{B}$ . These two primary fields are determined by the simultaneous solution of a partial differential equation and a set of Karush-Kuhn-Tucker complementary conditions. The boundary  $\partial\mathcal{B}$  to  $\mathcal{B}$  with outward normal  $\mathbf{n}$  is subdivided into disjoint parts, whereby either Neumann or Dirichlet boundary conditions for the two solution fields  $\mathbf{u}(\mathbf{x})$  and  $d(\mathbf{x})$  are prescribed, see Fig. 5.4.

Firstly, neglecting inertia, the equilibrium subproblem  $r^u(\mathbf{u}, d)$  is given by the quasi-static balance of linear momentum in  $\mathcal{B}$  as depicted in Table 5.6, whereby distributed body forces per unit volume in  $\mathcal{B}$  are denoted by  $\mathbf{b}$ .

---

Equilibrium subproblem			
$r^u(\mathbf{u}, d)$	$=$	$\text{div } \boldsymbol{\sigma}(\mathbf{u}, d) + \mathbf{b}$	$= \mathbf{0}$ in $\mathcal{B}$
		$\mathbf{u} - \mathbf{u}^p$	$= 0$ on $\partial\mathcal{B}^u$
		$\mathbf{n} \cdot \boldsymbol{\sigma}(\mathbf{u}, d) - \mathbf{t}^p$	$= 0$ on $\partial\mathcal{B}^t$
Constitutive subproblem			
$r^\varphi(\mathbf{u}, d)$	$=$	$\varphi(\mathbf{u}, d) - \bar{Y}(d)$	$\leq 0$ in $\mathcal{B}$
		$\dot{d}$	$= 0$ on $\partial\mathcal{B}_{int}^d$
		$\mathbf{n} \cdot \mathbf{Y}(d)$	$= 0$ on $\partial\mathcal{B}_{ext}^d$

---

Table 5.6: Strong form of the coupled problem

Then, for the displacement field, the decomposition of the total boundary reads

$$\partial\mathcal{B} = \partial\mathcal{B}^u \cup \partial\mathcal{B}^t \quad \text{with} \quad \partial\mathcal{B}^u \cap \partial\mathcal{B}^t = \emptyset. \quad (5.11)$$

Thus, the balance of linear momentum is supplemented by Dirichlet and Neumann boundary conditions in terms of the displacement  $\mathbf{u}$  on  $\partial\mathcal{B}^u$  and the traction vector  $\mathbf{t}$  on  $\partial\mathcal{B}^t$ , respectively, see also Fig. 5.4a.

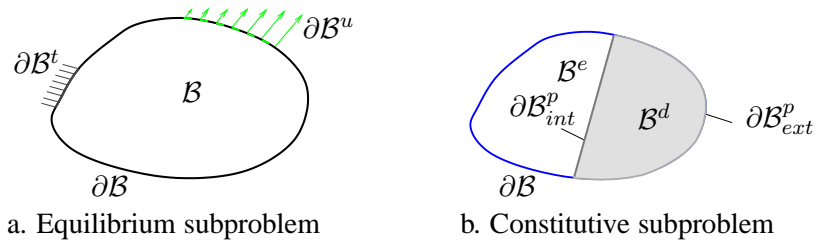


Figure 5.4: Solution domain with corresponding boundaries

Secondly, the constitutive subproblem is given by the damage condition  $r^\varphi(\mathbf{u}, d)$  incorporating the quasi-nonlocal energy release rate  $\bar{Y} = Y - \text{div } \mathbf{Y}$  as given in Table 5.6 together with the corresponding Karush-Kuhn-Tucker complementary conditions

$$r^\varphi(\mathbf{u}, d) \leq 0 \quad \dot{r}^d(\dot{d}) = \dot{d} \geq 0 \quad \dot{r}^d(\dot{d}) r^\varphi(\mathbf{u}, d) = 0 \quad \text{in } \mathcal{B}. \quad (5.12)$$

Then, for the damaged solution subdomain, the decomposition of the damaged subdomain boundary reads

$$\partial\mathcal{B}^d = \partial\mathcal{B}_{int}^d \cup \partial\mathcal{B}_{ext}^d \quad \text{with} \quad \partial\mathcal{B}_{int}^d \cap \partial\mathcal{B}_{ext}^d = \emptyset. \quad (5.13)$$

Thus, the constitutive subproblem is supplemented by Dirichlet and Neumann boundary conditions in

terms of the damage variable evolution  $\dot{d}$  on  $\partial\mathcal{B}_{int}^d$  and the damage flux  $\mathbf{n} \cdot \mathbf{Y}$  on  $\partial\mathcal{B}_{ext}^d$ , respectively, see also Fig. 5.4b.

The complementary condition  $\dot{d}\varphi = 0$  may be alternatively stated by decomposition of the total solution domain  $\mathcal{B}$  into an inactive elastic and an active damaged domain

$$\mathcal{B}^e = \{\mathbf{x} \in \mathcal{B} | \varphi \leq 0, \dot{d} = 0\} \quad \text{and} \quad \mathcal{B}^d = \{\mathbf{x} \in \mathcal{B} | \varphi = 0, \dot{d} > 0\} \quad (5.14)$$

with the additional completeness and non-overlapping requirements for the solution sub-domains

$$\mathcal{B} = \mathcal{B}^e \cup \mathcal{B}^d \quad \text{and} \quad \emptyset = \mathcal{B}^e \cap \mathcal{B}^d. \quad (5.15)$$

### 5.5.2 Weak form of the coupled problem

In analogy to section 3.5.2, the coupled non-linear boundary value problem has to be reformulated in weak form by weighting with the corresponding virtual quantities. This renders the global virtual statements for the equilibrium and constitutive subproblem, respectively, see Table 5.7.

---

Equilibrium subproblem	$\begin{aligned} G^u(\mathbf{u}, d; \delta\mathbf{u}) &= \int_{\partial\mathcal{B}^t} \delta\mathbf{u} \cdot \mathbf{t}^p \, dA + \int_{\mathcal{B}} [\delta\mathbf{u} \cdot \mathbf{b} - \text{grad } \delta\mathbf{u} : \boldsymbol{\sigma}(\mathbf{u}, d)] \, dV \\ &= 0 \quad \forall \delta\mathbf{u} \quad \text{in} \quad H_1^0(\mathcal{B}) \end{aligned}$
Constitutive subproblem	$\begin{aligned} G^\varphi(\mathbf{u}, d; \delta d) &= \int_{\mathcal{B}} [\delta d [Y(\mathbf{u}, d) - \kappa(d)] + \text{grad } \delta d \cdot \mathbf{Y}(d)] \, dV \\ &\leq 0 \quad \forall \delta d > 0 \quad \text{in} \quad H_1^0(\mathcal{B}) \\ \dot{G}^d(\dot{d}; \delta\varphi) &= \int_{\mathcal{B}} \delta\varphi \dot{d} \, dV \\ &\geq 0 \quad \forall \delta\varphi > 0 \quad \text{in} \quad L_2(\mathcal{B}) \end{aligned}$

---

Table 5.7: Weak form of the coupled problem

Based on these statements, the decomposition of the solution domain  $\mathcal{B}$  into an active damaged and inactive elastic domain  $\mathcal{B} = \mathcal{B}^d \cup \mathcal{B}^e$  and  $\emptyset = \mathcal{B}^e \cap \mathcal{B}^d$  follows implicitly as the support of those admissible test functions  $\delta d$  and  $\delta\varphi$ , which satisfy

$$\begin{aligned} \mathcal{B}^e &= \{\mathbf{x} \in \mathcal{B} | G^\varphi \leq 0, \dot{G}^d = 0 \quad \forall \delta d, \delta\varphi > 0 \quad \text{in} \quad \mathcal{B}^e\} \\ \mathcal{B}^d &= \{\mathbf{x} \in \mathcal{B} | G^\varphi = 0, \dot{G}^d > 0 \quad \forall \delta d, \delta\varphi > 0 \quad \text{in} \quad \mathcal{B}^d\}. \end{aligned} \quad (5.16)$$

This is indeed quite an implicit definition at this stage since one has to test for all possible combinations of support with all admissible test functions. Note that the above decomposition corresponds to the pointwise complementary condition  $\dot{d}\varphi = 0$ .

### 5.5.3 Temporal discretization of the coupled problem

The above set of equations has to be discretized in time, whereby the implicit Euler backward method is implied without loss of generality. Then, the temporal integration of the primary variables  $\mathbf{u}$  and  $d$  renders a discretized temporal update for the values  $\mathbf{u}_{n+1}$  and  $d_{n+1}$ , see Table 5.8.

Moreover, the algorithmic decomposition of the solution domain with  $\mathcal{B} = \mathcal{B}_{n+1}^d \cup \mathcal{B}_{n+1}^e$  and  $\emptyset =$



Equilibrium subproblem

$$\begin{aligned} G^u(\mathbf{u}_{n+1}, d_{n+1}; \delta \mathbf{u}) &= \int_{\partial \mathcal{B}^t} \delta \mathbf{u} \cdot \mathbf{t}_{n+1}^p \, dA + \int_{\mathcal{B}} [\delta \mathbf{u} \cdot \mathbf{b}_{n+1} - \text{grad } \mathbf{u} : \boldsymbol{\sigma}(\mathbf{u}_{n+1}, d_{n+1})] \, dV \\ &= 0 \quad \forall \delta \mathbf{u} \quad \text{in } H_1^0(\mathcal{B}) \end{aligned}$$

Constitutive subproblem

$$\begin{aligned} G^\varphi(\mathbf{u}_{n+1}, d_{n+1}; \delta d) &= \int_{\mathcal{B}} [\delta d [Y(\mathbf{u}_{n+1}, d_{n+1}) - \kappa(d_{n+1})] + \text{grad } \delta d \cdot \mathbf{Y}(d_{n+1})] \, d \\ &\leq 0 \quad \forall \delta d > 0 \quad \text{in } H_1^0(\mathcal{B}) \\ \dot{G}^d(d_{n+1}; \delta \varphi) &= \int_{\mathcal{B}} \delta \varphi [d_{n+1} - d_n] \, dV \\ &\geq 0 \quad \forall \delta \varphi > 0 \quad \text{in } L_2(\mathcal{B}) \end{aligned}$$

Table 5.8: Temporal discretization of the coupled problem

$\mathcal{B}_{n+1}^e \cap \mathcal{B}_{n+1}^d$  follows implicitly as the support of those admissible test functions  $\delta d$  and  $\delta \varphi$  which satisfy

$$\begin{aligned} \mathcal{B}_{n+1}^e &= \{\mathbf{x} \in \mathcal{B} \mid G_{n+1}^\varphi \leq 0, \Delta G_{n+1}^d = 0 \quad \forall \delta d, \delta \varphi > 0 \quad \text{in } \mathcal{B}_{n+1}^e\} \\ \mathcal{B}_{n+1}^d &= \{\mathbf{x} \in \mathcal{B} \mid G_{n+1}^\varphi = 0, \Delta G_{n+1}^d > 0 \quad \forall \delta d, \delta \varphi > 0 \quad \text{in } \mathcal{B}_{n+1}^d\}. \end{aligned} \quad (5.17)$$

Note that the above algorithmic decomposition corresponds to the pointwise algorithmic complementary condition  $[d_{n+1} - d_n]\varphi_{n+1} = 0$ .

#### 5.5.4 Spatial discretization of the coupled problem

Finally, the algorithmic set of equations has to be discretized in space. In order to achieve this, the standard Bubnov-Galerkin finite element method is employed. The whole solution domain  $\mathcal{B}$  is decomposed into finite elements  $\mathcal{B}_e$ . Each element is characterized by nodal degrees of freedom due to the displacement field ( $\circ$ ) and additionally by nodal degrees of freedom due to the damage field ( $\times$ ), see Fig. 5.5.

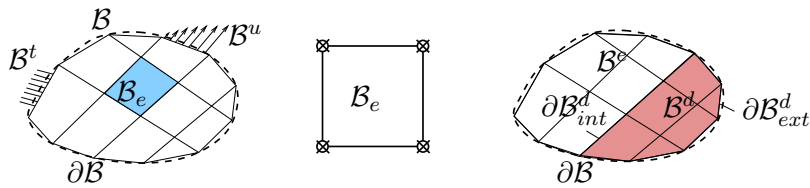


Figure 5.5: Discretized solution domain with corresponding boundaries and exemplary  $Q^0_1 Q^0_1$ -master element

The geometry  $\mathbf{x}$  and the displacement field  $\mathbf{u}$  together with its variation  $\delta \mathbf{u}$  is elementwise expanded by the same shape functions  $N_x^k$  in analogy to section 3.5.4.

The damage field  $d$ , together with its variation  $\delta d$ , is discretized in the same manner as the internal variable field, see Eq. 3.36. A  $C^0$  discretization of the damage field clearly leads to a smearing in the purely local case. Nevertheless, the gradient case is of main concern. Then, the global and elementwise sets of discretization node points may be defined as

$$\mathbb{B} = \bigcup_e \mathbb{B}_e \quad \text{with} \quad \mathbb{B} = \{K \mid K = 1, n_{np}\} \quad \text{and} \quad \mathbb{B}_e = \{k \mid k = 1, n_{en}\}. \quad (5.18)$$

Based on the spatial discretizations of the primary variables  $\mathbf{u}$  and  $d$ , the discrete algorithmic residua are

collected in Table 5.9.

Equilibrium subproblem

$$\begin{aligned} \mathbf{R}_K^u(\mathbf{u}_{n+1}^h, d_{n+1}^h) &= \mathbf{A}_e \int_{\partial \mathcal{B}_e \cap \partial \mathcal{B}^t} N_x^k \mathbf{t}_{n+1}^p \, dA + \int_{\mathcal{B}_e} [N_x^k \mathbf{b}_{n+1} - \text{grad } N_x^k \cdot \boldsymbol{\sigma}(\mathbf{u}_{n+1}^h, d_{n+1}^h)] \, dV \\ &= \mathbf{0} \quad \forall K \quad \text{in } \mathbb{B} \end{aligned}$$

Constitutive subproblem

$$\begin{aligned} R_K^\varphi(\mathbf{u}_{n+1}^h, d_{n+1}^h) &= \mathbf{A}_e \int_{\mathcal{B}_e} [N_d^k [Y(\mathbf{u}_{n+1}^h, d_{n+1}^h) - \kappa(d_{n+1}^h)] + \text{grad } N_d^k \cdot \mathbf{Y}(d_{n+1}^h)] \, dV \\ &\leq 0 \quad \forall K \quad \text{in } \mathbb{B} \\ \Delta R_K^d(d_{n+1}^h) &= \mathbf{A}_e \int_{\mathcal{B}_e} [N_d^k [d_{n+1}^h - d_n^h]] \, dV \\ &\geq 0 \quad \forall K \quad \text{in } \mathbb{B} \end{aligned}$$

Table 5.9: Discrete algorithmic form of the coupled problem

Moreover, the discrete algorithmic decomposition of the node point set with  $\mathbb{B} = \mathbb{B}_{n+1}^d \cup \mathbb{B}_{n+1}^e$  and  $\emptyset = \mathbb{B}_{n+1}^d \cap \mathbb{B}_{n+1}^e$  takes the following explicit format

$$\begin{aligned} \mathbb{B}_{n+1}^e &= \{K \in \mathbb{B} | R_K^\varphi \leq 0, \Delta R_K^d = 0\} \\ \mathbb{B}_{n+1}^d &= \{K \in \mathbb{B} | R_K^\varphi = 0, \Delta R_K^d > 0\}. \end{aligned} \quad (5.19)$$

Now, this is indeed a complete explicit definition since one only has to separately check all node points  $K \in \mathbb{B}$ . Note that the above discrete algorithmic decomposition corresponds to the discrete algorithmic complementary condition  $\Delta R_K^d R_K^\varphi = 0 \quad \forall K \text{ in } \mathbb{B}$ .

Based on the spatial discretization of  $d$ , the residuum  $\Delta R_K^d$  expands into

$$\Delta R_K^d = \sum_L M_{KL}^{dd} \Delta d_L \quad \text{with} \quad M_{KL}^{dd} = \mathbf{A}_e \int_{\mathcal{B}_e} N_d^k N_d^l \, dV. \quad (5.20)$$

For the most practical implementation, the positive definite fundamental matrix  $M_{KL}^{dd}$  is simply diagonalized, thus  $\Delta R_K^d \geq 0$  is equivalent to  $\Delta d_L \geq 0$ .

### 5.5.5 Monolithic iterative solution

In the preceding chapters, the monolithic iterative solution strategy has proven to be an efficient algorithm for the solution of the coupled problem stated in the above sections. Therefore, the simultaneous solution of the discrete algorithmic quasi-static balance of linear momentum together with the discrete algorithmic Karush-Kuhn-Tucker complementary conditions is computed again.

The initially unknown decomposition of the discretization node point set into active and inactive subsets  $\mathbb{B} = \mathbb{B}_{n+1}^d \cup \mathbb{B}_{n+1}^e$  at time step  $t_{n+1}$  is determined iteratively by an active set search as was shown in section 3.5.5.2. Then, for a given active working set  $\mathbb{B}_{act}$ , a typical Newton-Raphson step reads as follows

$$\begin{aligned} \mathbf{R}_K^u + d\mathbf{R}_K^u &= \mathbf{0} \quad \forall K \quad \text{in } \mathbb{B} \\ R_K^\varphi + dR_K^\varphi &= 0 \quad \forall K \quad \text{in } \mathbb{B}_{act}, \end{aligned} \quad (5.21)$$

whereby the linearized residua are expressed by the corresponding iteration matrices, which take the interpretation as global tangent stiffness matrices

$$\begin{aligned} d\mathbf{R}_K^u &= - \sum_{L \in \mathbb{B}} \mathbf{K}_{KL}^{uu} \cdot d\mathbf{u}_L - \sum_{L \in \mathbb{B}_{act}} \mathbf{K}_{KL}^{u\varphi} dd_L \quad \forall K \text{ in } \mathbb{B} \\ d\mathbf{R}_K^\varphi &= - \sum_{L \in \mathbb{B}} \mathbf{K}_{KL}^{\varphi u} \cdot d\mathbf{u}_L - \sum_{L \in \mathbb{B}_{act}} \mathbf{K}_{KL}^{\varphi\varphi} dd_L \quad \forall K \text{ in } \mathbb{B}_{act}. \end{aligned} \quad (5.22)$$

The determination of the correct active working set based on the strategy, which was earlier discussed is clearly of crucial importance.

Finally, the incremental iterate is updated from the solution of Eq. 5.21 by

$$\begin{aligned} \Delta \mathbf{u}_L &\leftarrow \Delta \mathbf{u}_L + d\mathbf{u}_L \quad \forall L \text{ in } \mathbb{B} \\ \Delta d_L &\leftarrow \Delta d_L + dd_L \quad \forall L \text{ in } \mathbb{B}_{act}. \end{aligned} \quad (5.23)$$

For the problem at hand, the following iteration matrices are introduced as

$$\begin{aligned} \mathbf{K}_{KL}^{uu} &= \mathbf{A}_e \int_{\mathcal{B}_e} \text{grad } N_x^k \cdot \partial_{\epsilon} \boldsymbol{\sigma} \cdot \text{grad } N_x^l dV \\ \mathbf{K}_{KL}^{u\varphi} &= \mathbf{A}_e \int_{\mathcal{B}_e} \text{grad } N_x^k \cdot \partial_d \boldsymbol{\sigma} N_d^l dV \\ \mathbf{K}_{KL}^{\varphi u} &= \mathbf{A}_e \int_{\mathcal{B}_e} N_d^k \partial_{\epsilon} Y \cdot \text{grad } N_x^l dV \\ \mathbf{K}_{KL}^{\varphi\varphi} &= \mathbf{A}_e \int_{\mathcal{B}_e} \left[ N_d^k [\partial_d Y - \partial_d \kappa] N_d^l + \text{grad } N_d^k \cdot \partial_d \mathbf{Y} \cdot \text{grad } N_d^l \right] dV, \end{aligned} \quad (5.24)$$

which incorporate the appropriate partitions of the tangent operator, see Table 5.12.

Note that the global iteration matrix is symmetric and changes its size dynamically, which has to be accounted for by the implementation of the equation solver. Nevertheless, the problem size in each iteration is considered to be optimal. Aside from the specific implementation of the equation solver, only standard FE-data structures and corresponding FE-modules are involved.

### 5.5.5.1 Constitutive update

A strain-driven constitutive update algorithm typically has to provide the updated dependent variables such as stress, damage flux, etc. at time  $t_{n+1}$ . Its consistent linearization is essential in order to set up the appropriate global iteration matrix for the quadratically converging global Newton-Raphson strategy. The constitutive update of the geometrically linear damage prototype for given  $\boldsymbol{\epsilon}_{n+1}$ ,  $d_{n+1}$  is summarized in Table 5.10.

---

<b>Input:</b> $\boldsymbol{\epsilon}_{n+1}, d_{n+1}, \mathbf{d}_{n+1}$	
Nominal stress	$\boldsymbol{\sigma}_{n+1} = [1 - d_{n+1}] \boldsymbol{\mathcal{E}}_{\epsilon} : \boldsymbol{\epsilon}_{n+1}$
Effective stress	$\tilde{\boldsymbol{\sigma}}_{n+1} = \boldsymbol{\mathcal{E}}_{\epsilon} : \boldsymbol{\epsilon}_{n+1}$
Damage flux	$\mathbf{Y}_{n+1} = -c \mathbf{d}_{n+1}$
Local energy release rate	$Y_{n+1} = \frac{1}{2} \boldsymbol{\epsilon}_{n+1} : \boldsymbol{\mathcal{E}}_{\epsilon} : \boldsymbol{\epsilon}_{n+1}$
Internal variable update	$\kappa_{n+1} = \phi^{-1}(d_{n+1}) = \kappa_0 - \frac{1}{\beta} \ln(1 - d_{n+1})$

---

Table 5.10: Update of the constitutive variables for gradient damage

Note that despite its implicit character, the constitutive update does not rely on local iterations usually employed in standard update algorithms.

Clearly, here the damage variable  $d$  is a given input for the update of the internal variable  $\kappa$ . Thereby, the choice of a simple exponential-type evolution law, see Table 5.5 for the damage evolution, comes in handy because it allows a closed form update for the internal variable  $\kappa$ . Otherwise, an additional local iteration for  $\kappa = \phi^{-1}(d)$  would become necessary but does not limit the generality of the formulation proposed here. Note that the update algorithm in the local case varies significantly, as is summarized in Table 5.11 for comparison.

---

<b>Input:</b> $\epsilon_{n+1}, \kappa_n$		
Local energy release rate	$Y_{n+1} =$	$Y(\epsilon_{n+1})$
Internal variable update	$\kappa_{n+1} =$	$\max(Y_{n+1}, \kappa_n, \kappa_0)$
Damage variable update	$d_{n+1} =$	$\phi(\kappa_{n+1})$

---

Table 5.11: Update algorithm for local damage

Here, only the strains  $\epsilon_{n+1}$  are given and in a first step the local energy release rate  $Y_{n+1}$  is computed. Based on this, the history variable  $\kappa_{n+1}$  is determined either from the maximum of the new local energy release rate  $Y_{n+1}$ , the old value  $\kappa_n$  or the initial damage threshold  $\kappa_0$ . Finally, the updated damage variable  $d_{n+1}$  is computed from the new history variable  $\kappa_{n+1}$ . Thus, in contrast to the gradient update algorithm, the damage variable  $d$  is a dependent variable in the local case.

Finally, the linearization of the constitutive update, i.e., the partition of the tangent operator as employed in the global iteration matrix, is given in Table 5.12. It is remarkable that this tangent operator results in a symmetric global iteration matrix.

---

$\mathbf{u} - \mathbf{u}$ Partition	$\partial_{\epsilon}$	$\boldsymbol{\sigma} =$	$[1 - d]\boldsymbol{\mathcal{E}}_{\epsilon}$	
$\mathbf{u} - d$ Partition	$\partial_d$	$\boldsymbol{\sigma} =$	$-\tilde{\boldsymbol{\sigma}}$	
$d - \mathbf{u}$ Partition	$\partial_{\epsilon}$	$Y =$	$\tilde{\boldsymbol{\sigma}}$	
$\kappa - \kappa$ Partition	$\partial_d$	$Y =$	$-c\mathbf{1}$	
	$\partial_d$	$Y =$	$0$	$\partial_d \kappa = \frac{1}{[1 - d]\beta}$

---

Table 5.12: Partitions of the tangent operator

## 5.6 Numerical examples of phenomenological gradient damage

The derived gradient damage formulation is now applied to computational examples showing the performance of the elaborated model by modifying the gradient parameter as well as discretization density in deterioration processes.

### 5.6.1 1D-model problem: bar under uniaxial tension

As a model problem, the bar in Fig. 5.6, which is loaded in uniaxial tension will be examined in the sequel for the sake of demonstration.

The problem statement, which includes a slight material imperfection in the middle of the bar, is taken from Peerlings, de Borst, Brekelmans and de Vree (1996b), whereby homogeneous Neumann boundary

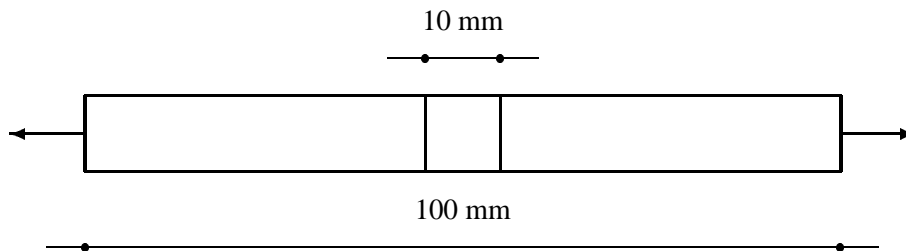


Figure 5.6: 1D-model problem: bar under uniaxial tension

conditions for the damage flux were prescribed at the external boundary. The material is modeled based on a linear elastic gradient damage formulation with a simple exponential-type evolution law for the damage evolution as was introduced in Table 5.5. The material parameters for the following examples are summed up in Table 5.13.

Elastic modulus	$E$	=	10000.00	N/mm <sup>2</sup>
Reduced elastic modulus	$E_r$	=	9000.00	N/mm <sup>2</sup>
Initial damage threshold	$\kappa_0$	=	0.01	N/mm <sup>2</sup>
Exponential hardening modulus	$\beta$	=	0.01	

Table 5.13: Material parameters

The total bar is discretized with 80, 160, 320, 640, 1280 and 2560 elements. Thereby, due to the symmetry in the problem statement, only one half of the bar is considered. The load is applied using arclength control enabling to trace the post-peak branch of the load-displacement curves in damage. The main objective is to show the performance of the gradient model. Therefore, as a comparison, the local model is also addressed. For different possibilities of discretization techniques for the local and quasi-local case, consult the investigation in section 3.6.1 for gradient plasticity. On the one hand, the classical approach in local isotropic damage with linear element expansions for the displacement is focused upon. Clearly, the local damage variable field is not separately discretized. On the other hand, the element type for gradient damage reflects a continuous approach in both the displacement as well as the damage variable field. Hereby, it appeared that the choice of linear expansions in both discretized fields renders the most effective and efficient results. This can be explained by means of the discretized Karush-Kuhn-Tucker complementary conditions, which seem to be affected mainly by the choice of discretization order. Using quadratic expansions for the displacements yield piecewise linear strains and would result in a quadratic expansion of the elastically stored energy  $Y$ . This quantity would then be coupled with a highly non-linear history variable expression  $\kappa$  and a piecewise constant damage gradient, which causes oscillations in both the damage variable distribution as well as in the load-displacement curves. Therefore, linear-linear approximations ( $P^01P^01$ ) are used for the following examples in gradient isotropic damage, which give stable results in our experience. The different element formulations are described in Table 5.14.

Damage formulation	Discretization variable	Continuity of approximation	Element type	
local	$\mathbf{u}$	$C^0$	$P^01$	expansion
gradient	$\mathbf{u}, d$	$C^0/C^0$	$P^01P^01$	expansion

Table 5.14: Classification of element formulations

Firstly, for validation of the gradient model, the local isotropic damage case is investigated. Here, in order to trigger localization, a graded imperfection in the middle of the bar is additionally introduced. That means that the first element has the lowest elastic modulus and the neighboring elements have a slightly increased elastic modulus  $E_g = 9500.0N/mm^2$  compared to the rest of the bar elements with the highest elastic modulus, see Table 5.13 for reference. The resulting load-displacement curves for the classical local  $P^0$ 1 element type are displayed in Fig. 5.7a. The typical deficiency in terms of a quasi-lack of convergence in the post-peak branch of the curves can be observed upon mesh refinement. This is particularly emphasized in Fig. 5.7b depicting the corresponding distribution of the damage variable, whereby a concentration of damage evolution is accumulated in only one element.

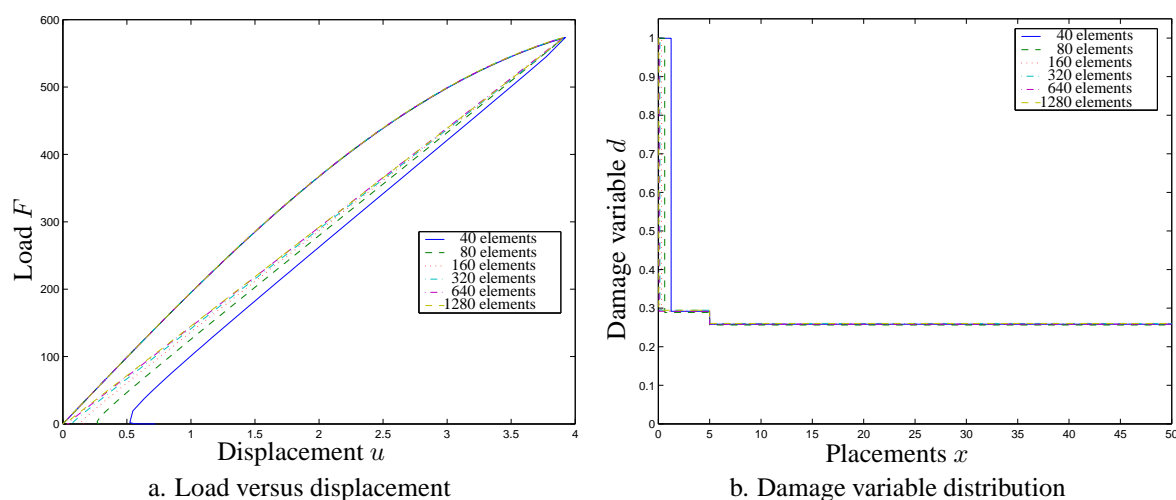


Figure 5.7: Local damage ( $P^0$ 1 elements)

Secondly, to overcome the lack of discretization invariance, the following examples are based on the incorporation of the gradient regularization in the constitutive model as described in the previous sections. Thereby, the quasi-mesh independence is shown for a constant gradient parameter  $c = 100.0$  upon mesh densification, see Fig. 5.8.

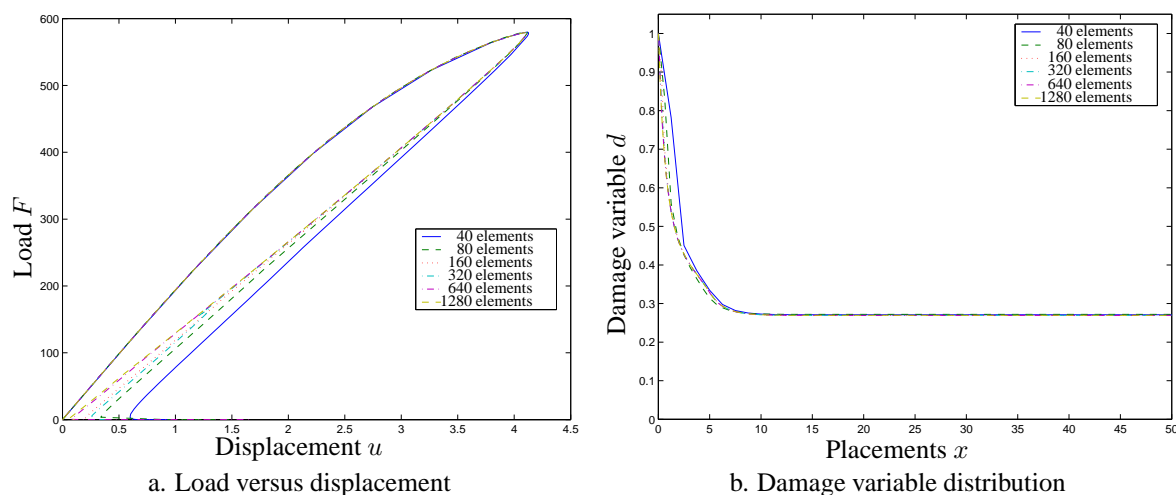


Figure 5.8: Gradient damage  $c = 100.0$  ( $P^0$ 1 $P^0$ 1 elements)

Furthermore, it can clearly be seen that the solution converges upon mesh densification for a different choice of the gradient parameters, see Fig. 5.9.

Note that modifying the gradient parameter results in the variation of the ductility in the load-displacement curves, see Fig. 5.9a, as well as in the damage variable distribution, see Fig. 5.9b. It appears that, higher values of the gradient parameter render a somewhat more ductile behavior. In any case, the corresponding distribution of the localized zone is smooth and convergent.

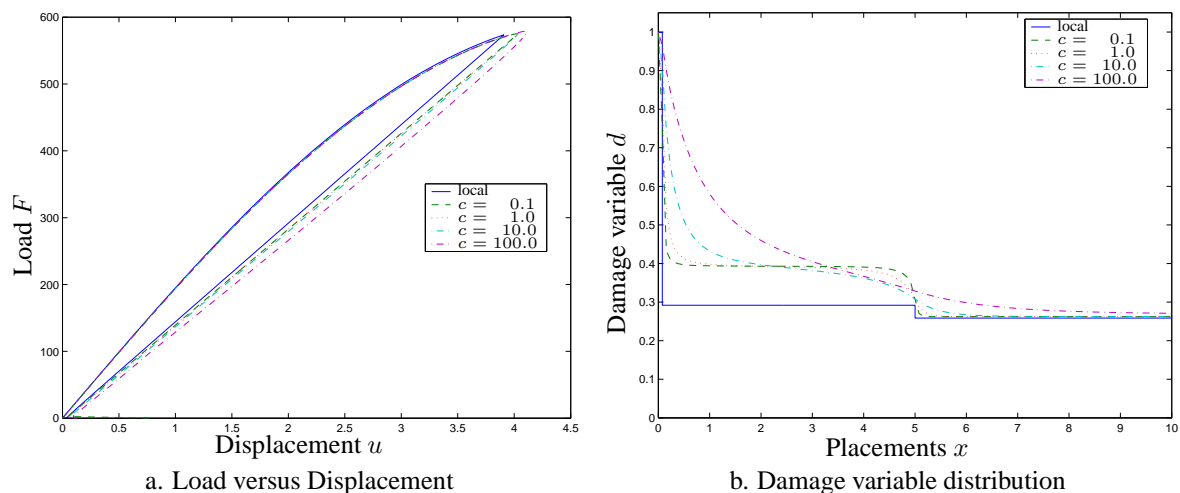


Figure 5.9: Gradient damage for constant mesh discretization (640 elements) and varied  $c = 0.0, 0.1, 1.0, 10.0, 100.0$

Hereby, the regularizing effect of the incorporation of gradients into the damage model is obvious as the jumps in the damage variable distribution in the local model are smoothed out in the gradient one. Moreover, the overall solution shows a shrinkage of the localized band width upon further loading into a crack line mode, i.e., a gradual transition from a damaged zone into a line crack. This phenomena is emphasized in Fig. 5.10, where the evolution of the active constraints is displayed over the total arclength for a discretization with 320 elements.

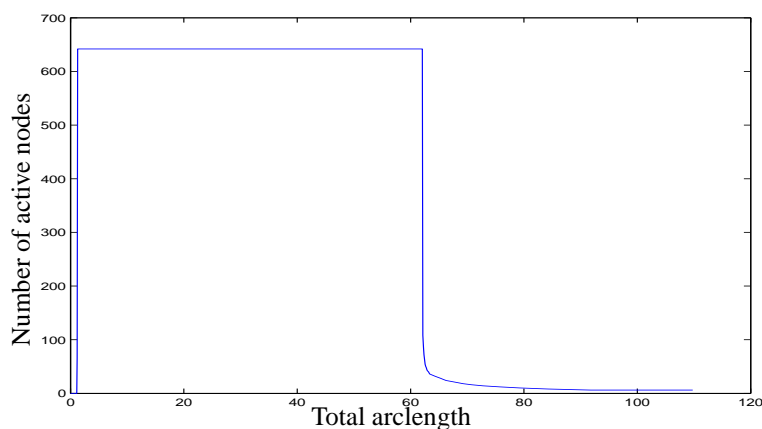


Figure 5.10: Active constraints versus total arclength with a constant mesh-discretization (320  $P^01P^01$  elements) and  $c = 100.0$

Within a relatively small arclength increment, all nodes become active in the beginning. Then, all nodes

remain active until the snap back point is reached in the load-displacement curve. Finally, a gradual transition, i.e., the shrinkage of the localized band, into a line crack is displayed by a gradual reduction of the number of active nodes, which is also emphasized by Table 5.15. In addition to that, it demonstrates the convergence of the iterative determination of the active constraints.

increment no.	arclength	damage value	residuuum-norm	active nodes
1	0.020	0.0000000	1.43741E-13	0
12	1.170		1.32282E-06	64
			1.81125E-05	66
			1.11209E-11	66
13	1.270		1.93543E-05	all
			2.11507E-08	
191	62.070		1.60279E-02	all
			6.25944E-04	
		4.18238E-01	5.75176E-08	
192	62.170		1.47320E-01	120
			3.44733E-02	102
			8.38091E-03	104
			4.46743E-03	106
			9.13569E-04	108
		4.28916E-01	1.65705E-09	108
...				...
205	64.270		4.57892E-01	34
			1.07979E-01	32
			1.76714E-05	32
		5.82703E-01	3.67567E-10	32
245	84.270		1.17320E-01	8
			2.36715E-05	8
		8.80275E-01	2.70375E-10	8
260	91.770		9.23177E-02	8
			1.40062E-03	6
		9.28905E-01	3.19045E-09	6
303	108.270		3.02718E-03	6
		9.99882E-01	4.04977E-09	6

Table 5.15: Convergence Study for 320  $P^01P^01$  elements and  $c = 100.0$

Fig. 5.11 shows the evolution of damage for a constant gradient parameter  $c = 100$  and constant discretization density with  $320P^1P^1$  elements. From Table 5.15, it can be seen that damage has evolved in all elements up to a value of  $d \approx 0.4$ . The snap back point is then reached and the number of active nodes decreases gradually with evolving damage until only a fixed number of 3 nodes in this example remains active. Within the post-peak branch of the load-displacement curve, full damage finally occurs within the element of highest imperfection. The snap back mechanism is accompanied by a shrinkage of the localized zone. It remains finite in width though, in contrast to the local case. There, localiza-



tion is resolved over a single element, which turns infinitely small in the limit of an infinite fine mesh discretization.

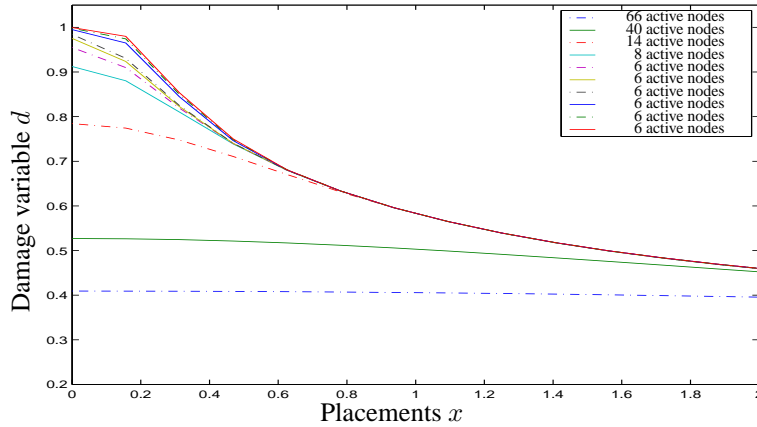


Figure 5.11: Damage evolution at constant mesh discretization ( $320 P^0_1P^0_1$  elements) and constant gradient parameter  $c = 100.0$

### 5.6.2 2D-model problem: panel in tension

Finally, in order to show the performance of the damage gradient formulation in plane strain, the panel in Fig. 5.12 is investigated under tension. Again, a slight material imperfection has been included in the center elements. The material is modeled in analogy to the 1D-example, see Table 5.13. The panel is discretized with  $20 \times 10$  and  $40 \times 20 Q_1Q_1$ -elements (continuous approximation of both displacement field and damage field). Here also, the damage variable distribution is of main concern which emphasizes the convergent performance of the gradient damage formulation as displayed in Fig. 5.13 and Fig. 5.14.

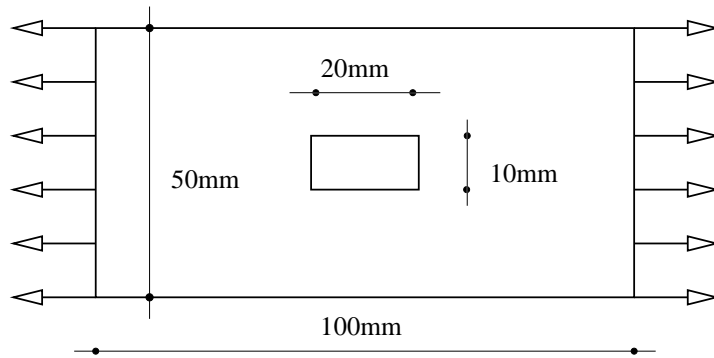


Figure 5.12: 2D-model problem: panel with center-imperfection

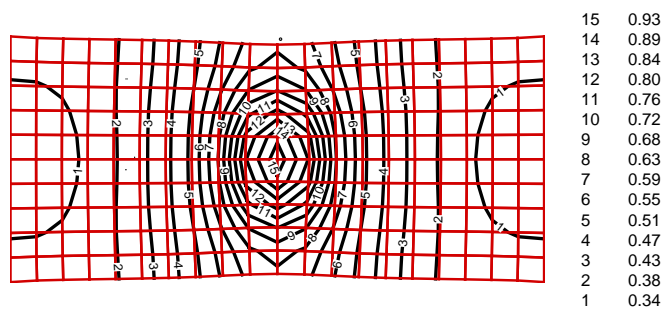


Figure 5.13: Damage distribution shortly before reaching  $d=1$ ,  $c=100$ , coarse mesh

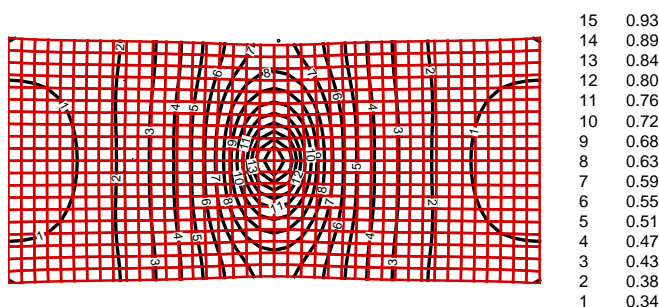


Figure 5.14: Damage distribution shortly before reaching  $d=1$ ,  $c=100$ , fine mesh

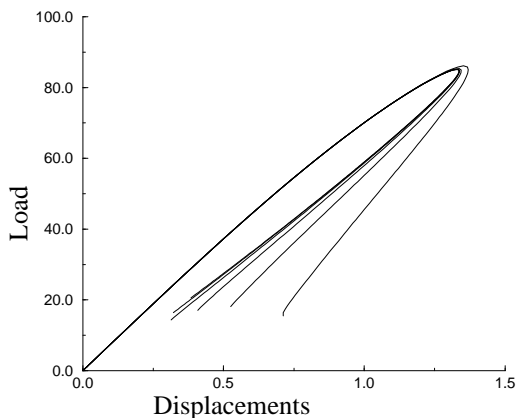
The presented figures show a contour line plot of the damage distribution before the specimen reaches complete damage in the element with imperfection. Thereby, the damage zone gradually spreads around the imperfection zone towards the less damaged boundary region.

### 5.6.3 Geometrically non-linear model problem: bar under uniaxial tension

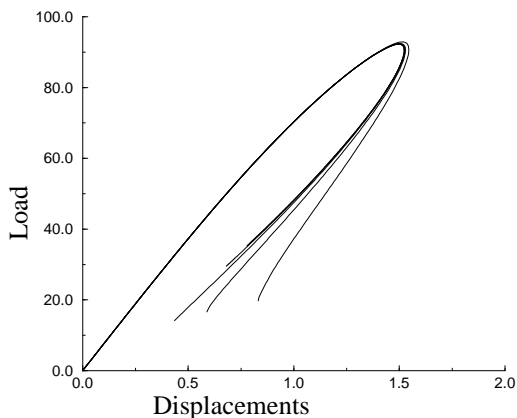
Next, for demonstration purposes, the above gradient damage model is applied within an isotropic geometrically non-linear setting, see appendix A for kinematical aspects and appendix C for constitutive modeling aspects of the underlying coupled problem, respectively. The virgin material is modeled based on a compressible Neo-Hookean formulation in terms of the stretch  $\lambda$ , which coincides with  $\mathbf{F}$  in 1D, see the description in the appendix C.2.

The model geometry is taken as in the geometrically linear case compare with Fig. 5.6 with discretization of the total bar into 10, 20, 40, 80, 160 and 320 elements, whereby the load is applied with arclength control. The element type is chosen to be continuous in the displacement field as well as in the damage variable field ( $C^0/C^0$ ). For the same reasons as discussed in the geometrically linear case, it appeared that the choice of linear expansions in both discretized fields provides the most effective and efficient results. The material parameters are set to  $\mu = 2100N/mm^2$ ,  $\mu_r = 1000N/mm^2$ ,  $\kappa_0 = 1.0N/mm^2$  and  $h = 0.1mm^2/N$  in accordance with the constitutive model in appendix C.

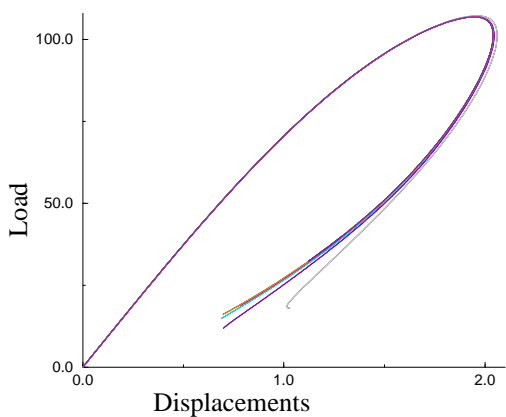
The load versus displacement curves in Fig. 5.15 show mesh-convergence for higher discretization densities. Thereby, discretization with only 20 or 40 elements exhibit the poorest performance at least for small gradient parameters, here  $c = 10$ , which is remedied for higher values of  $c$ . Clearly, for different gradient parameters, the solution converges upon mesh densification. Note that modifying the gradient parameter again results in the variation of the ductility in the post-peak behavior after the onset of damage, see the load-displacement curves in Fig. 5.15a-c. Thereby, the distribution of the damage variable is smooth and convergent as exemplarily emphasized for a gradient parameter  $c = 1000$  in Fig. 5.15d. Remarkably, the overall solution here shows a snap back behavior with corresponding shrinkage of the localized band width upon further loading into a line crack mode, i.e., a gradual transition from a damaged zone into a line crack, which corresponds to the results and active nodes investigation performed in section 5.6.1.



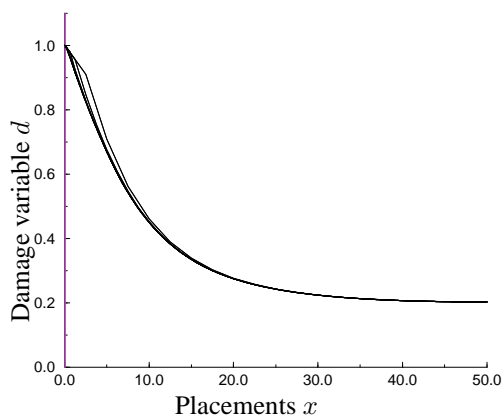
a. Load-displacement curve for  $c = 10$



b. Load-displacement curve for  $c = 100$



c. Load-displacement curve for  $c = 1000$



d. Damage distribution for  $c = 1000$

Figure 5.15: Gradient damage formulation applied to 320,160,80,40,20,10  $P^1P^1$ -elements for different gradient parameter  $c$



## Chapter 6

# Material Force Method coupled to damage

The objective of this chapter is the exploitation of the notion of material forces in computational continuum damage mechanics. Thereby, the benefits of the two-field finite element formulation as proposed in the previous chapter are employed with respect to the computation of the so-called material node point (surface) forces. Clearly, the internal variable approach of the last chapter is combined with the material force concept. Thereby, distributed material volume forces that are conjugated to the damage field arise. Thus, the Galerkin discretization of the damage variable as an independent field becomes necessary in addition to the deformation field. The corresponding numerical scheme was already provided by the proposed gradient damage formulation in the previous chapter. In the following, the restriction to a quasi-local geometrically non-linear isotropic continuum damage formulation is applied, i.e., the gradient aspect is left aside by choosing  $c = 0$ . Here, mere interest is dedicated to the investigation of the evolving damage zone with respect to a crack tip. Thereby, material forces are considered as the optimal tool to reveal the response to variations of material placements of 'physical particles' with respect to the ambient material, which may also indicate insufficient discretizations.

Consequently, the main concern of this chapter is to establish a theoretical and computational link between defect mechanics and continuum damage mechanics with the use of the *Material Force Method*. The developments derived here are essentially based on the exposition of the continuum mechanics of inhomogeneities as comprehensively outlined by Maugin (1993; 1995), Gurtin (1999) and recent contributions by Steinmann et al. (2001), Steinmann (2002) and Denzer et al. (2002). Material (configurational) forces are in contrast to the common spatial (mechanical) forces in the sense of Newton, which are considered as the response to variations of spatial placements of 'physical particles' with respect to the ambient space. Material forces as advocated by Maugin (1996; 1997; 2000b) are especially suited for the assessment of general defects as inhomogeneities, interfaces, dislocations and cracks, where the material forces are directly related to the classical  $J$ -Integral in fracture mechanics. First numerical concepts of material forces within the FE-method date back to Braun (1997), who derived for the hyperelastic case node point forces from the discretized potential energy with respect to the material node point positions, that contain the material stress in the spirit of Eshelby (1951; 1975).

Note that the method advocated here is not restricted to hyperelastic materials only, see also Steinmann (2003) or Kuhl and Steinmann (2003) for thermo-hyperelastic applications. The derivations presented in the subsequent sections are along the lines of a proposal by Liebe, Denzer and Steinmann (2003).

In the following, on the one hand, the classical balance of momentum and, on the other hand, a constitutive subproblem corresponding to the Karush-Kuhn-Tucker conditions are set up in a coupled fashion, which are enforced in a weak sense. The underlying kinematics, strain and stress measures together with

the derivation of the quasi-static balance of momentum in material and spatial setting, respectively, are collected in appendix A. Special interest is thus focused in this chapter on a hyperelastic formulation coupled to damage. Beforehand, the continuum format of the classical  $J$ -integral is described. Then, the variational format of the coupled problem will be derived. It will be solved using a monolithic solution strategy. The resulting material node point quantities, which shall be denoted discrete material node point forces, are demonstrated to be closely related to the classical  $J$ -integral in fracture mechanical problems. In particular, the additional information perceived with the help of the Material Force Method will be investigated for different specimen with an elliptic hole (varying the ratio of the semi-axes) and a center cracked tension (CCT) specimen, respectively, while the damage zone evolves. For validation purposes, a classical fracture mechanical problem formulated in a modified boundary layer style with a prescribed material load at the boundary is finally studied. Thereby, a shielding effect of the distributed damage field with respect to the macroscopic crack will be clearly demonstrated.

## 6.1 Continuum format of $J$ -integral

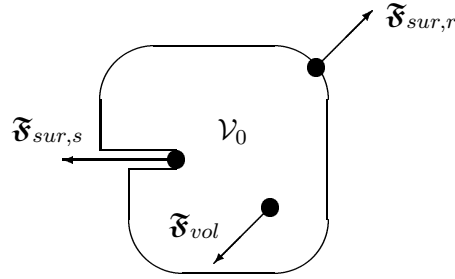


Figure 6.1: Arbitrary subdomain with regular and singular part of its boundary: a single material force acts on the singular part of the boundary

Consider the arbitrary subdomain  $\mathcal{V}_0$  of the reference configuration  $\mathcal{B}_0$  in Fig. 6.1 depicting a continuum with a crack. The boundary  $\partial\mathcal{V}_0$  is thereby assumed to be decomposed into a regular and a singular part  $\partial\mathcal{V}_0 = \partial\mathcal{V}_0^r \cup \partial\mathcal{V}_0^s$  with  $\emptyset = \partial\mathcal{V}_0^r \cap \partial\mathcal{V}_0^s$ . Here, the singular part of  $\partial\mathcal{V}_0$  denotes a crack tip.

The subdomain is loaded along  $\partial\mathcal{V}_0^r$  by material description surface tractions in terms of the material description Cauchy stress  $\Sigma$ , projected by the reference surface normal  $N$ , and within  $\partial\mathcal{V}_0$  by material description volume forces  $B_0$ , stemming, e.g., from material inhomogeneities (see section 6.2). Taking into account the decomposition of the boundary  $\partial\mathcal{V}_0$  into a regular and a singular boundary, the statement of quasi-static equilibrium of material forces for the subdomain with reference configuration  $\mathcal{V}_0$  is then defined as

$$\mathfrak{F}_{sur,s} = -\mathfrak{F}_{sur,r} - \mathfrak{F}_{vol}. \quad (6.1)$$

Thereby, the resulting material description regular surface and volume forces are given by

$$\mathfrak{F}_{sur,r} = \int_{\partial\mathcal{V}_0^r} \Sigma^t \cdot N \, dA \quad \text{and} \quad \mathfrak{F}_{vol} = \int_{\mathcal{V}_0} B_0 \, dV. \quad (6.2)$$

Note that the resulting material force acting on the singular boundary  $\mathfrak{F}_{sur,s} = \int_{\partial\mathcal{V}_0^s} \Sigma^t \cdot N \, dA$  coincides with the (vectorial)  $J$ -integral as originally proposed by Rice (1968b) modulo a change of sign, which

stems from the integration along the regular part instead along the singular part of  $\partial\mathcal{V}_0$

$$-\mathfrak{F}_{sur,s} = \mathfrak{J} = \lim_{\partial\mathcal{V}_0^r \rightarrow 0} \int_{\partial\mathcal{V}_0^r} \boldsymbol{\Sigma}^t \cdot \mathbf{N} \, dA. \quad (6.3)$$

## 6.2 Spatial versus material motion problem

Starting from the spatial balance of momentum  $\mathbf{0} = \text{Div } \boldsymbol{\Pi}^t + \mathbf{b}_0$ , a covariant pullback to the material manifold is performed. To this end, the following identity is considered

$$\mathbf{F}^t \cdot \text{Div } \boldsymbol{\Pi}^t = \text{Div}(\mathbf{F}^t \cdot \boldsymbol{\Pi}^t) - \text{Grad } \mathbf{F}^t : \boldsymbol{\Pi}^t. \quad (6.4)$$

Sufficient smoothness is then assumed and the integrability condition for  $\mathbf{F}$  is recalled, i.e.,  $\text{Grad } \mathbf{F}^t : \boldsymbol{\Pi}^t = \boldsymbol{\Pi}^t : \text{Grad } \mathbf{F}$ . Next, a general internal variable based constitutive assumption is chosen for the free energy density per unit volume in  $\mathcal{B}_0$ , which is denoted by

$$\Psi_0 = \Psi_0(\mathbf{F}, \mathbf{a}; \mathbf{X}). \quad (6.5)$$

Here,  $\mathbf{a}$  denotes an internal variable to be specified together with its conjugated counterpart  $A = -\partial_{\mathbf{a}}\Psi_0$ . Then, the total material gradient can be written in terms of the free energy as follows

$$\text{Grad } \Psi_0 = \text{Div}(\Psi_0 \mathbf{1}) = \boldsymbol{\Pi}^t : \text{Grad } \mathbf{F} - A \text{Grad } \mathbf{a} + \partial_{\mathbf{X}} \Psi_0, \quad (6.6)$$

whereby  $\partial_{\mathbf{X}} \Psi_0$  denotes the explicit material gradient due to material inhomogeneities. Hence, assembling terms, the following energy-momentum format of the material motion Cauchy-stress (in the sense of Eshelby (1975) holds

$$\boldsymbol{\Sigma}^t = \Psi_0 \mathbf{1} - \mathbf{F}^t \cdot \boldsymbol{\Pi}^t = \Psi_0 \mathbf{1} - \mathbf{M}^t. \quad (6.7)$$

Moreover, distributed volume forces  $\mathbf{B}_0$  per unit volume  $\mathcal{B}_0$  can be retrieved from relation (6.6) in the following manner

$$\mathbf{B}_0 = A \text{Grad } \mathbf{a} - \partial_{\mathbf{X}} \Psi_0 - \mathbf{F}^t \cdot \mathbf{b}_0. \quad (6.8)$$

As a first observation, the necessity for a separate discretization of the internal variable arises in order to determine the gradient term  $A \text{Grad } \mathbf{a}$ .

Summarizing, the material motion balance of momentum is obtained as

$$\mathbf{0} = \mathbf{F}^t \cdot [\text{Div } \boldsymbol{\Pi}^t + \mathbf{b}_0] \quad \longrightarrow \quad \mathbf{0} = \text{Div } \boldsymbol{\Sigma}^t + \mathbf{B}_0. \quad (6.9)$$

## 6.3 Hyperelasticity coupled to isotropic damage

In this section, a particular free energy density modeling a hyperelastic constitutive response coupled to isotropic damage is presented. Thereby, isotropic damage is characterized by a degradation measure in terms of a scalar damage variable  $0 \leq d \leq 1$  that acts as a reduction factor of the local stored energy density of the virgin material  $W_0 = JW_t$  per unit volume in  $\mathcal{B}_0$  (or  $W_t = jW_0$  per unit volume in  $\mathcal{B}_t$ , respectively), which is supposed to be an objective and isotropic function in  $\mathbf{F}$  (or  $\mathbf{f}$ , respectively). Observe that the familiar constitutive relations of the spatial motion problem are formally dual to the presentation of the appropriate constitutive relations of the material motion problem, see Shield (1967), Chadwick (1975) and Ericksen (1998) for the case of hyperelasticity.

### 6.3.1 Spatial motion problem

In the case of the spatial motion problem with hyperelasticity coupled to isotropic damage, the free energy density  $\Psi_0$  is a function of the deformation gradient  $\mathbf{F}$  and the internal variable representing damage  $a = d(\mathbf{X})$  with possible explicit dependence on the material placement  $\mathbf{X}$

$$\Psi_0 = \Psi_0(d, \mathbf{F}; \mathbf{X}) = [1 - d]W_0(\mathbf{F}; \mathbf{X}). \quad (6.10)$$

Then, exploiting the Clausius-Duhem inequality  $\mathbf{II}^t : \mathbf{D}_t \mathbf{F} - \mathbf{D}_t \Psi_0 \geq 0$ <sup>1</sup> and assuming that appropriate invariance requirements under superposed spatial rigid body motion are fulfilled, the familiar constitutive equations for the material motion stresses in  $\mathcal{B}_0$  are given as

$$\mathbf{II}^t = [1 - d] \frac{\partial W_0}{\partial \mathbf{F}} \quad \implies \quad \boldsymbol{\sigma}^t = j \mathbf{II}^t \cdot \mathbf{F}^t = [1 - d] \left[ W_t \mathbf{1} - \mathbf{f}^t \cdot \frac{\partial W_t}{\partial \mathbf{f}} \right]. \quad (6.11)$$

Note that the presented format of the spatial motion Cauchy stress  $\boldsymbol{\sigma}^t$  is formally comparable to the energy-momentum tensor of Eshelby (1975). Recall that  $W_t = jW_0$  denotes the energy density per unit volume in  $\mathcal{B}_t$ . In the case of spatial objectivity, i.e.,  $W_0$  is invariant under superposition of spatial rigid body motions, the spatial motion Cauchy stress turns out to be symmetric  $\boldsymbol{\sigma}^t = \boldsymbol{\sigma}$ .

Furthermore, the local damage energy release rate  $Y_0$  per unit volume is introduced in  $\mathcal{B}_0$  as thermodynamically conjugated to  $d$

$$Y_0 = - \frac{\partial \Psi_0}{\partial d} = W_0. \quad (6.12)$$

It thus turns out that  $W_0$  is conjugated to the evolution of the independent damage field  $d$ . The reduced dissipation inequality consequently reads  $\mathcal{D}_0 = Y_0 \mathbf{D}_t d \geq 0$ . A damage condition is readily motivated as

$$\Phi(Y_0; d) = \phi(Y_0) - d \leq 0 \quad (6.13)$$

with  $\phi(\bullet)$  a monotonic function of its argument, see, e.g., Simo and Ju (1987) for the small strain case. Then, based on the postulate of maximum dissipation, an associated damage evolution law is given in terms of a Lagrange multiplier  $\kappa$

$$\mathbf{D}_t d = \mathbf{D}_t \kappa \partial_{Y_0} \Phi. \quad (6.14)$$

This is complemented by the set of Karush-Kuhn-Tucker loading/unloading conditions

$$\Phi(Y_0; d) \leq 0 \quad \text{and} \quad \mathbf{D}_t \kappa \geq 0 \quad \text{and} \quad \mathbf{D}_t \kappa \Phi(Y_0; d) = 0. \quad (6.15)$$

Moreover, the consistency condition in the case of loading characterized by  $\Phi = 0$  and  $\mathbf{D}_t \kappa > 0$  allows for the closed form update for the damage parameter

$$\mathbf{D}_t \Phi(Y_0; d) = 0 \quad \longrightarrow \quad \mathbf{D}_t Y_0 = \mathbf{D}_t \kappa \geq 0 \quad \longrightarrow \quad d = \phi(\kappa), \quad (6.16)$$

whereby  $\kappa$  is computed as

$$\kappa = \max_{-\infty < s < t} (Y_0(s), \kappa_0) \quad (6.17)$$

with  $\kappa_0$  being the initial damage threshold. Finally, based on the inversion of  $\phi(\bullet)$ , the damage condition

---

<sup>1</sup>For the derivation of the Material Force Method it now becomes meaningful to distinguish time derivatives at fixed material placements in contrast to time derivatives at fixed spatial placements, see appendix A.



and the Karush-Kuhn-Tucker complementary conditions may be expressed in an alternative format as

$$\varphi(Y_0; \kappa) = Y_0 - \kappa \leq 0 \quad \text{and} \quad D_t d \geq 0 \quad \text{and} \quad D_t d \varphi(Y_0; \kappa) = 0. \quad (6.18)$$

The complementary condition  $D_t d \varphi = 0$  may alternatively be stated by decomposition of the total solution domain  $\mathcal{B}_0$  into an inactive elastic and an active damaged domain

$$\mathcal{B}_0^e = \{\mathbf{X} \in \mathcal{B}_0 | \varphi \leq 0, D_t d = 0\} \quad \text{and} \quad \mathcal{B}_0^d = \{\mathbf{X} \in \mathcal{B}_0 | \varphi = 0, D_t d > 0\} \quad (6.19)$$

with the additional completeness and non-overlapping requirements for the solution sub-domains

$$\mathcal{B}_0 = \mathcal{B}_0^e \cup \mathcal{B}_0^d \quad \text{and} \quad \emptyset = \mathcal{B}_0^e \cap \mathcal{B}_0^d. \quad (6.20)$$

### 6.3.2 Material motion problem

In the case of the material motion problem with hyperelasticity coupled to isotropic gradient damage the free energy  $\Psi_t$  is considered as a function of the deformation gradient  $\mathbf{f}$  and the damage variable  $a = d(\mathbf{x}) = d(\mathbf{X}) \circ \Phi(\mathbf{x})$ , whereby the explicit dependence on the material placement is captured by the field  $\mathbf{X} = \Phi(\mathbf{x})$

$$\Psi_t = \Psi_t(d, \mathbf{f}, \Phi(\mathbf{x})) = [1 - d] W_t(\mathbf{f}, \Phi(\mathbf{x})). \quad (6.21)$$

Then, again assuming that appropriate invariance requirements under superposed spatial rigid body motion are fulfilled, the familiar constitutive equations for the macroscopic material stresses in  $\mathcal{B}_t$  are given as

$$\Sigma^t = j \pi^t \cdot \mathbf{f}^t = [1 - d] \left[ W_0 \mathbf{1} - \mathbf{F}^t \cdot \frac{\partial W_0}{\partial \mathbf{F}} \right] \iff \pi^t = [1 - d] \frac{\partial W_t}{\partial \mathbf{f}}. \quad (6.22)$$

Clearly,  $\Sigma^t$  is the so-called Eshelby stress involved in many problems of defect mechanics. Carefully observe that the material motion Cauchy stress turns out to be symmetric  $\Sigma^t = \Sigma$  only in the case of material objectivity or rather isotropy, i.e.,  $W_t$  is invariant under superposition of material rigid body motions.

Here,  $W_0 = J W_t$  denotes the energy density per unit volume in  $\mathcal{B}_0$ . The thermodynamic stress of the material motion problem conjugated to the damage variable corresponds trivially via the Jacobian  $J$  to the one of the spatial motion problem, i.e.,  $Y_t = W_t$  with  $Y_0 = J Y_t$ .

Note that the distributed volume forces as derived in Eq. 6.8 now take the following particular format with respect to the incorporation of damage

$$\mathbf{B}_0 = Y_0 \text{ Grad } d - \partial_{\mathbf{x}} \Psi_0 - \mathbf{F}^t \cdot \mathbf{b}_0. \quad (6.23)$$

Now, the relation to the last chapter can be clearly established because the gradient of the damage variable enters the stage. It therefore seems most natural to make use of the numerical scheme of a two-field finite element formulation applied throughout this thesis.

## 6.4 Numerical treatment of continuum damage coupled to the Material Force Method

In particular, within the framework of approximative numerical solution methods, one can consider the above derived material balance of momentum as an additional constraint that has to be fulfilled by the

numerical solution, see also the reasoning by Maugin (2000a). Thereby, the algorithmic representation of the material balance of momentum resulting in the notion of discrete material forces is proposed as the so-called Material Force Method, see Steinmann (2000; 2001). The Material Force Method is especially appealing in the numerical treatment of problems in fracture mechanics, see also the applications in Müller et al. (2002) and Müller and Maugin (2002).

The notion of distributed material volume forces which are conjugated to the damage field necessitates the set up a two field formulation, i.e., the additional discretization of the damage variable as an independent field next to the deformation field. Moreover, the identification of spurious material forces acts as a sensitive indicator of insufficient mesh discretization.

### 6.4.1 Weak form of the coupled problem

As a prerequisite for a finite element discretization, the non-linear boundary value problem has to be reformulated in weak or rather variational form. Again, the duality of the spatial and material point of view is elaborated.

#### 6.4.1.1 Spatial motion problem

Firstly, the pointwise statement of the spatial balance of momentum  $-\operatorname{div} \boldsymbol{\sigma}^t = \mathbf{b}_t$  is tested by spatial virtual displacements  $\delta\varphi = \mathbf{w}$  under the necessary smoothness and boundary assumptions to render the virtual work expression

$$\underbrace{\int_{\partial B_t} \mathbf{w} \cdot \boldsymbol{\sigma}^t \cdot \mathbf{n} \, da}_{\mathfrak{w}^{sur}} = \underbrace{\int_{B_t} \operatorname{grad} \mathbf{w} : \boldsymbol{\sigma}^t \, dv}_{\mathfrak{w}^{int}} - \underbrace{\int_{B_t} \mathbf{w} \cdot \mathbf{b}_t \, dv}_{\mathfrak{w}^{vol}} \quad \forall \mathbf{w}. \quad (6.24)$$

For a conservative system, the different energetic terms  $\mathfrak{w}^{sur}$ ,  $\mathfrak{w}^{int}$  and  $\mathfrak{w}^{vol}$  may be interpreted by considering the spatial variation at fixed  $\mathbf{X}$  of the free energy density  $\Psi_0$ . As a result, the contribution  $\mathfrak{w}^{sur}$  denotes the spatial variation of  $\Psi_0$  due to its complete dependence on the spatial position, whereas the contributions  $\mathfrak{w}^{int}$  and  $\mathfrak{w}^{vol}$  denote the spatial variations of  $\Psi_0$  due to its implicit and explicit dependence on the spatial position, respectively.

Secondly, the weak form of the constitutive subproblem is proposed in order to cope with the damage field. As shown in chapter 6.3.2, the distributed volume forces require the gradient w.r.t. to the damage variable. It thus becomes necessary to separately discretize  $d$  as an additional field. A constitutive subproblem is therefore advocated, which is represented by the variational format of the Karush-Kuhn-Tucker complementary conditions  $\varphi \leq 0$  and  $\mathbf{D}_t d \geq 0$ . These are tested by  $\delta d$  with  $\delta d > 0$  and by  $\delta\varphi$  with  $\delta\varphi > 0$ , respectively, to render the global statements

$$\mathfrak{w}^\varphi = \int_{B_0} \delta d [Y_0 - \kappa] \, dV \leq 0 \quad \text{and} \quad \mathfrak{w}^d = \int_{B_0} \delta\varphi \mathbf{D}_t d \, dV \geq 0. \quad (6.25)$$

Based on these statements, the decomposition of the solution domain  $B_0$  into an active damaged and inactive elastic domain  $B_0 = B_0^d \cup B_0^e$  and  $\emptyset = B_0^e \cap B_0^d$  follows implicitly as the support of those admissible test functions  $\delta d$  and  $\delta\varphi$ , which satisfy

$$\begin{aligned} B_0^e &= \{ \mathbf{X} \in B_0 \mid \mathfrak{w}^\varphi \leq 0, \mathfrak{w}^d = 0 \, \forall \delta d, \delta\varphi > 0 \text{ in } B_0^e \} \\ B_0^d &= \{ \mathbf{X} \in B_0 \mid \mathfrak{w}^\varphi = 0, \mathfrak{w}^d > 0 \, \forall \delta d, \delta\varphi > 0 \text{ in } B_0^d \}. \end{aligned} \quad (6.26)$$

### 6.4.1.2 Material motion problem

Here, the pointwise statement of the material balance of momentum  $-\text{Div } \Sigma^t = \mathbf{B}_0$  is tested by material virtual displacements  $\delta\Phi = \mathbf{W}$  under the necessary smoothness and boundary assumptions to render the virtual work expression

$$\underbrace{\int_{\partial\mathcal{B}_0} \mathbf{W} \cdot \Sigma^t \cdot \mathbf{N} \, dA}_{\mathfrak{B}^{sur}} = \underbrace{\int_{\mathcal{B}_0} \text{Grad } \mathbf{W} : \Sigma^t \, dV}_{\mathfrak{B}^{int}} - \underbrace{\int_{\mathcal{B}_0} \mathbf{W} \cdot \mathbf{B}_0 \, dV}_{\mathfrak{B}^{vol}} \quad \forall \mathbf{W}. \quad (6.27)$$

Again for a conservative system, the different energetic terms  $\mathfrak{B}^{sur}$ ,  $\mathfrak{B}^{int}$  and  $\mathfrak{B}^{vol}$  may be interpreted by considering the material variation at fixed  $\mathbf{x}$  of the free energy density  $\Psi_t$ . As a result, the contribution  $\mathfrak{B}^{sur}$  denotes the material variation of  $\Psi_t$  due to its complete dependence on the material position, whereas the contributions  $\mathfrak{B}^{int}$  and  $\mathfrak{B}^{vol}$  denote the material variations of  $\Psi_t$  due to its implicit and explicit dependence on the material position, respectively.

Note that the two variational formulations in Eqs. 6.24 and 6.27 are connected by  $\mathbf{w} = -\mathbf{W} \cdot \mathbf{F}^t$  and  $\mathbf{W} = -\mathbf{w} \cdot \mathbf{f}^t$  for the relation between the spatial and material virtual displacements, see also Maugin & Trimarco (1992). Taking the relations derived in chapter 6.2 into account, applying integration by parts and invoking the Gauss theorem, one may expand, e.g.,  $\int_{\mathcal{B}_0} \mathbf{w} \cdot \text{Div } \mathbf{\Pi}^t \, dV$  into  $\int_{\mathcal{B}_0} \mathbf{W} \cdot [\text{Div } \Sigma^t + \mathbf{B}_0 + \mathbf{F}^t \cdot \mathbf{b}_0] \, dV$ .<sup>2</sup>

## 6.4.2 Discretization of the coupled problem

The above variational set of quasi-static balances of momentum will be discretized by the standard Bubnov-Galerkin finite element method rendering discrete spatial and material node point (surface) forces.

### 6.4.2.1 Spatial motion problem

Firstly, the geometry  $\mathbf{X}$  is elementwise expanded by shape functions  $N_X^k$  in terms of the positions  $\mathbf{X}_k$  of the node points with the elementwise numbering  $k = 1, n_{en}$  corresponding to a global numbering  $K = 1, n_{np}$  and the following elementwise discretization of the material solution domain is obtained

$$\mathcal{B}_0 = \bigcup_e \mathcal{B}_0^e \quad \text{with} \quad \mathbf{X}^h|_{\mathcal{B}_0^e} = \sum_k N_X^k \mathbf{X}_k. \quad (6.28)$$

Then, in the spirit of the Bubnov-Galerkin finite element method based on the iso-parametric concept, the deformation map  $\varphi$  together with its variation  $\delta\varphi = \mathbf{w}$  is elementwise expanded by the same shape functions  $N_\varphi^k = N_X^k$  in terms of the nodal values  $\varphi_k$  and  $\delta\varphi_k = \mathbf{w}_k$

$$\varphi^h|_{\mathcal{B}_0^e} = \sum_k N_\varphi^k \varphi_k \quad \text{and} \quad \mathbf{w}^h|_{\mathcal{B}_0^e} = \sum_k N_\varphi^k \mathbf{w}_k. \quad (6.29)$$

<sup>2</sup>Convince yourself by considering the following derivation:

$$\begin{aligned} -\mathbf{W} \cdot \mathbf{F}^t \cdot \text{Div } \mathbf{\Pi}^t &= -\mathbf{W} \cdot \text{Div}(\mathbf{F}^t \cdot \mathbf{\Pi}^t) + \mathbf{W} \cdot \mathbf{\Pi}^t : \text{Grad } \mathbf{F} \\ &= -\mathbf{W} \cdot \text{Div}(\mathbf{F}^t \cdot \mathbf{\Pi}^t) + \mathbf{W} \cdot [\text{Div}(\Psi_0 \mathbf{1}) + A \text{Grad } \mathbf{a} - \partial_X \Psi_0] \\ &= \mathbf{W} \cdot [\text{Div } \Sigma^t + \mathbf{B}_0 + \mathbf{F}^t \cdot \mathbf{b}_0] \end{aligned}$$

The damage variable field  $d$ , together with its variation  $\delta d$  is expanded elementwise by independent shape functions  $N_d^k$  in terms of the nodal values  $d_k$  and  $\delta d_k$

$$d^h|_{\mathcal{B}_0^e} = \sum_k N_d^k d_k \quad \text{and} \quad \delta d^h|_{\mathcal{B}_0^e} = \sum_k N_d^k \delta d_k. \quad (6.30)$$

Likewise, the test function  $\delta\varphi$  is discretized by the same shape functions  $N_\varphi^k = N_d^k$  in terms of nodal values  $\delta\varphi_k$

$$\delta\varphi|_{\mathcal{B}_0^e} = \sum_k N_d^k \delta\varphi_k. \quad (6.31)$$

Thereby, the shape functions render a globally  $C^0$ -continuous interpolation by assembling all elementwise expansions. Furthermore, the elementwise Jacobi matrix

$$\mathbf{J}_0 = \text{Grad}_\xi \mathbf{X}^h|_{\mathcal{B}_0^e} = \sum_{n=1} \mathbf{X}_k \otimes \text{Grad}_\xi N_X^k \quad (6.32)$$

is needed to compute the material gradients  $\text{Grad}\{\bullet\} = \text{Grad}_\xi\{\bullet\} \cdot \mathbf{J}_0^{-1}$  by the chain rule.

Lastly, based on the above discretizations, the corresponding gradients  $\mathbf{F}$ ,  $\text{Grad} \mathbf{w}$  and  $\text{Grad} d$  take the elementwise format

$$\begin{aligned} \mathbf{F}^h|_{\mathcal{B}_0^e} &= \sum_k \boldsymbol{\varphi}_k \otimes \text{Grad} N_\varphi^k \\ \text{Grad} \mathbf{w}^h|_{\mathcal{B}_0^e} &= \sum_k \mathbf{w}_k \otimes \text{Grad} N_\varphi^k \\ \text{Grad} d^h|_{\mathcal{B}_0^e} &= \sum_k d_k \quad \text{Grad} N_d^k. \end{aligned}$$

Then, based on the spatial discretizations of the primary variables  $\varphi$  and  $d$  the discretized internal and volume contributions to the spatial virtual work follow as

$$\mathfrak{w}_h^{int} = \mathbf{A}_e \sum_k \mathbf{w}_k \cdot \int_{\mathcal{B}_t^e} \boldsymbol{\sigma}^t \cdot \text{Grad} N_\varphi^k \, dv \quad (6.33)$$

$$\mathfrak{w}_h^{vol} = \mathbf{A}_e \sum_k \mathbf{w}_k \cdot \int_{\mathcal{B}_0^e} N_\varphi^k \mathbf{b}_t \, dv. \quad (6.34)$$

Thus implying the arbitrariness of the spatial virtual node point displacements  $\mathbf{w}_k$  the discrete algorithmic spatial node point (surface) forces are obtained at global node  $K$  as follows

$$\mathfrak{f}_{sur,K}^h = \mathbf{A}_e \int_{\mathcal{B}_t^e} \left[ \boldsymbol{\sigma}^t \cdot \text{Grad} N_\varphi^k - N_\varphi^k \mathbf{b}_t \right]_{n+1} \, dv. \quad (6.35)$$

Here, the implicit Euler backward method is assumed for the time discretization without loss of generality. Thereby, the temporal integration of the primary variables  $\varphi$  and  $d$  renders a discretized temporal update for the values  $\varphi_{n+1}$  and  $d_{n+1}$ .

Furthermore, the discrete algorithmic Karush-Kuhn-Tucker complementary conditions are obtained at global node  $K$ , whereby the first one represents the discrete algorithmic damage condition and the second one assures positive increments of the damage variable

$$\mathfrak{r}_K^\varphi = \mathbf{A}_e \int_{\mathcal{B}_0} \left[ N_d^k [Y_0 - \kappa] \right]_{n+1} \, dV \quad \text{and} \quad \mathfrak{r}_K^d = \mathbf{A}_e \int_{\mathcal{B}_0} \left[ N_d^k [d_{n+1}^h - d_n^h] \right] \, dV, \quad (6.36)$$

whereby  $[\bullet]_n$  and  $[\bullet]_{n+1}$  denote successive time steps.

Moreover, the discrete algorithmic decomposition of the node point set with  $\mathbb{B} = \mathbb{B}_{n+1}^d \cup \mathbb{B}_{n+1}^e$  and  $\emptyset = \mathbb{B}_{n+1}^d \cap \mathbb{B}_{n+1}^e$  takes the following explicit format

$$\begin{aligned}\mathbb{B}_{n+1}^e &= \{K \in \mathbb{B} | r_K^\varphi \leq 0, r_K^d = 0\} \\ \mathbb{B}_{n+1}^d &= \{K \in \mathbb{B} | r_K^\varphi = 0, r_K^d > 0\}.\end{aligned}\quad (6.37)$$

The initially unknown decomposition of the discretization node point set into active and inactive subsets  $\mathbb{B} = \mathbb{B}_{n+1}^d \cup \mathbb{B}_{n+1}^e$  at time step  $t_{n+1}$  is determined iteratively by an active set search. Thereby, the strategy is borrowed from convex non-linear programming, see Luenberger (1973), as is frequently used, e.g., in multi-surface and crystal plasticity. A corresponding detailed solution strategy with respect to geometrically (non-)linear gradient damage was already shown in chapter 5.

### 6.4.2.2 Material motion problem

Alternatively, the geometry  $\boldsymbol{x}$  may now be elementwise expanded by shape functions  $N_x^k$  in terms of the positions  $\boldsymbol{x}_k$  of the node points with the elementwise numbering  $k = 1, n_{en}$  corresponding to a global numbering  $K = 1, n_{np}$ , the following elementwise discretization of the spatial solution domain is thus obtained

$$\mathcal{B}_t = \bigcup_e \mathcal{B}_t^e \quad \text{with} \quad \boldsymbol{x}^h|_{\mathcal{B}_t^e} = \sum_k N_x^k \boldsymbol{x}_k. \quad (6.38)$$

Then, in the spirit of the Bubnov-Galerkin finite element method based on the iso-parametric concept, the deformation map  $\boldsymbol{\Phi}$  together with its variation  $\delta\boldsymbol{\Phi} = \boldsymbol{W}$  is elementwise expanded by the same shape functions  $N_\Phi^k = N_x^k$  in terms of the nodal values  $\boldsymbol{\Phi}_k$  and  $\delta\boldsymbol{\Phi}_k = \boldsymbol{W}_k$

$$\boldsymbol{\Phi}^h|_{\mathcal{B}_t^e} = \sum_k N_\Phi^k \boldsymbol{\Phi}_k \quad \text{and} \quad \boldsymbol{W}^h|_{\mathcal{B}_t^e} = \sum_k N_\Phi^k \boldsymbol{W}_k. \quad (6.39)$$

Thereby, the shape functions render a globally  $C^0$ -continuous interpolation by assembling all elementwise expansions. Furthermore, the elementwise Jacobi matrix

$$\boldsymbol{J}_t = \text{Grad}_\xi \boldsymbol{x}^h|_{\mathcal{B}_t^e} = \sum_{n=1} \boldsymbol{x}_k \otimes \text{Grad}_\xi N_x^k \quad (6.40)$$

is needed to compute the gradients  $\text{grad}\{\bullet\} = \text{Grad}_\xi\{\bullet\} \cdot \boldsymbol{J}_t^{-1}$  by the chain rule.

Lastly, based on the above discretizations, the corresponding gradients  $\boldsymbol{f}$  and  $\text{grad} \boldsymbol{W}$  take the elementwise format

$$\begin{aligned}\boldsymbol{f}^h|_{\mathcal{B}_t^e} &= \sum_k \boldsymbol{\Phi}_k \otimes \text{grad} N_\Phi^k \\ \text{grad} \boldsymbol{W}^h|_{\mathcal{B}_t^e} &= \sum_k \boldsymbol{W}_k \otimes \text{grad} N_\Phi^k.\end{aligned}$$

Finally, the discretized internal and volume contributions to the material virtual work for each element follow as

$$\mathfrak{B}_e^{\text{int}} = \mathbf{A}_e \sum_k \boldsymbol{W}_k \cdot \int_{\mathcal{B}_0^e} \boldsymbol{\Sigma}^t \cdot \text{grad} N_\Phi^k dV \quad (6.41)$$

$$\mathfrak{B}_e^{\text{vol}} = \mathbf{A}_e \sum_k \boldsymbol{W}_k \cdot \int_{\mathcal{B}_0^e} N_\Phi^k \boldsymbol{B}_0 dV. \quad (6.42)$$

Thus implying the arbitrariness of the material virtual node point displacements  $\boldsymbol{W}_k$ , the discrete algo-

rithmic material node point (surface) forces at global node point  $K$  are obtained as follows

$$\mathfrak{F}_{sur,K}^h = \mathbf{A} \int_e \int_{\mathcal{B}_0^e} \left[ \boldsymbol{\Sigma}^t \cdot \text{grad } N^k - N_{\Phi}^k \mathbf{B}_0 \right]_{n+1} dV, \quad (6.43)$$

whereby the material surface forces  $\mathfrak{F}_{sur,K}^h$  are denoted by 'SUR' in the diagrams, which are displayed in the following example section. On the one hand, one may furthermore separate

$$\mathfrak{F}_{int,K}^h = \mathbf{A} \int_e \int_{\mathcal{B}_0^e} \left[ \boldsymbol{\Sigma}^t \cdot \text{grad } N_x^k \right]_{n+1} dV \quad (6.44)$$

the internal part of the discrete algorithmic material node point (surface) forces denoted by 'INT' and on the other hand,

$$\mathfrak{F}_{vol,K}^h = \mathbf{A} \int_e \int_{\mathcal{B}_0^e} \left[ N_{\Phi}^k \mathbf{B}_0 \right]_{n+1} dV \quad (6.45)$$

the volume part of the discrete algorithmic material node point (surface) forces denoted by 'VOL', which will be used later in the example section. In summary, the obvious result holds

$$\mathfrak{F}_{sur,K}^h = \mathfrak{F}_{int,K}^h - \mathfrak{F}_{vol,K}^h. \quad (6.46)$$

Based on these results, the Material Force Method is advocated with the notion of global discrete material node point (surface) forces that (in the sense of Eshelby) are generated by variations relative to the ambient material at fixed spatial positions. Such forces corresponding to the material motion problem are trivially computable once the spatial motion problem has been solved. Moreover, due to the interpretation of material forces as being energetically conjugate to configurational changes, discrete material forces at the boundary may be considered as a measure of the geometrical shape sensitivity of a specimen.

### 6.4.2.3 Discretized format of J-integral: Material Force Method

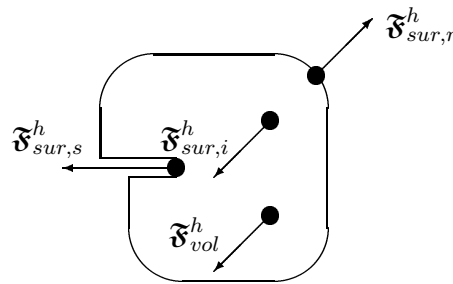


Figure 6.2: Balance of discrete material node point forces

Consider the resulting discrete material node point (surface) force  $\mathfrak{F}_{sur,s}^h$  acting on a crack tip, see Fig. 6.2. In analogy to the continuum format of the quasi-static equilibrium of material forces, the exact value  $\mathfrak{F}_{sur,s}$  in Eq. 6.1 can be approximated by the discrete regular surface part  $\mathfrak{F}_{sur,r}^h$  and the discrete volume part  $\mathfrak{F}_{vol}^h$  of the discrete material node point (surface) forces

$$\mathfrak{F}_{sur,s}^h \approx -\mathfrak{F}_{sur,r}^h - \mathfrak{F}_{vol}^h. \quad (6.47)$$

These in turn are balanced by discrete singular material surface forces  $\mathfrak{F}_{sur,s}^h$  and (spurious) discrete

internal material surface forces  $\mathfrak{F}_{sur,i}^h$ , which stem from an insufficient discretization accuracy as follows

$$-\mathfrak{F}_{sur,r}^h - \mathfrak{F}_{vol}^h = \mathfrak{F}_{sur,s}^h + \mathfrak{F}_{sur,i}^h. \quad (6.48)$$

Note thus, that the sum of all discrete algorithmic material node point surface forces  $\mathfrak{F}_{sur,K}^h$  corresponds according to Eq. 6.43 to the resulting value

$$\mathfrak{F}_{sur,s} \approx \sum_{K \in \mathcal{V}_0^h \setminus \partial \mathcal{V}_0^{r,h}} \mathfrak{F}_{sur,K}^h = \mathfrak{F}_{sur,s}^h + \mathfrak{F}_{sur,i}^h. \quad (6.49)$$

An improved value for  $\mathfrak{F}_{sur,s}$  is thus obtained by summing up all discrete material node point surface forces in the vicinity of the crack tip, see also Denzer et al. (2002). Observe that the presence of spurious discrete internal material surface forces  $\mathfrak{F}_{sur,i}^h$  as implied by Eq. 6.48 indicates that a change of the node point positions of the discretization renders an improved mesh with less potential energy content in the conservative case, see also the reasoning by Braun (1997) and Maugin (2000a).

## 6.5 Numerical examples of the Material Force Method coupled to damage

In this section, the computational performance and versatility of the proposed Material Force Method coupled to isotropic damage is investigated. To this end, the results of a geometrically non-linear computation are first obtained for a specimen with an elliptic hole with varying axis ratios under tension are studied. Next, these results are compared with a center cracked (CCT) fracture mechanics specimen in tension. Finally, for validation purposes, a convergence study of a 'Modified Boundary Layer'-formulation (MBL-formulation) is performed for a straight, traction free crack.

### 6.5.1 Specimen with elliptic hole

Firstly, different specimen with an elliptic hole are considered in tension with plane strain constraint, whereby the axis ratios is varied ranging from a full circle ( $a/b = 1.0$ ) to a slender ellipse ( $a/b = 0.1$ ), see Fig. 6.3. The height to width ratio is  $H/W = 3$ . The specimen is discretized by bilinear  $Q1$ -elements. The mesh is densified towards the hole boundary.

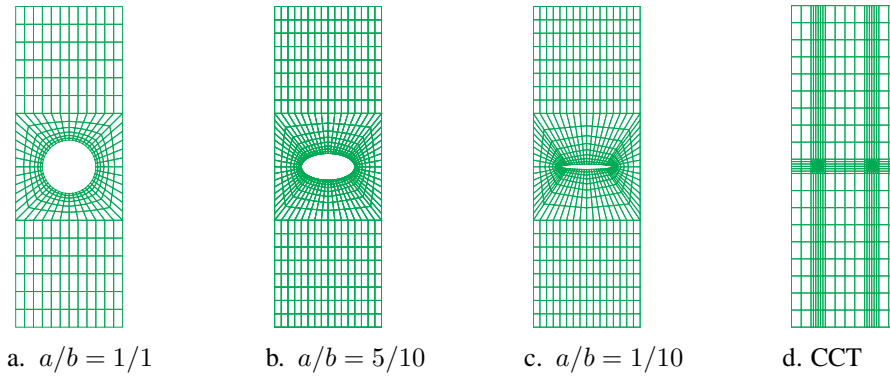


Figure 6.3: Specimen geometries

The virgin material is modeled based on a compressible Neo-Hookean formulation  $W_0 = \mu \left[ \frac{I_1 - \ln J}{2} - 3 \right] + \lambda \ln^2 J / 2$  with the shear modulus  $\mu = 27540$  MPa and the bulk modulus  $K = \lambda + 2/3\mu = 59666$  MPa corresponding roughly to aluminum.

For the damage evolution, the simple exponential-type law used in chapter 5 is also adopted here with an assumed initial damage threshold  $\kappa_0 = 0.01$  MPa and the exponential parameter chosen to  $\beta = 0.1$ . The choice of the supposed damage evolution may naturally influence the overall behavior of the considered specimen.

A constant elongation is incrementally applied by prescribed displacements at the top surface, the lateral movement of the nodes at the top and bottom surface are unconstrained.

Firstly, the damage variable distribution within zooms of the typical scenario around the hole is depicted for varying axis ratios  $a/b$ . Thereby, an evolving damage zone is shown ranging from the purely undamaged elastic state (Fig. 6.4a) to a state with completely damaged nodes (Fig. 6.4d). There are two intermediate states represented exhibiting the first appearance of damaged nodes (Fig. 6.4b) and a further advanced damage state of the first active nodes (Fig. 6.4c).

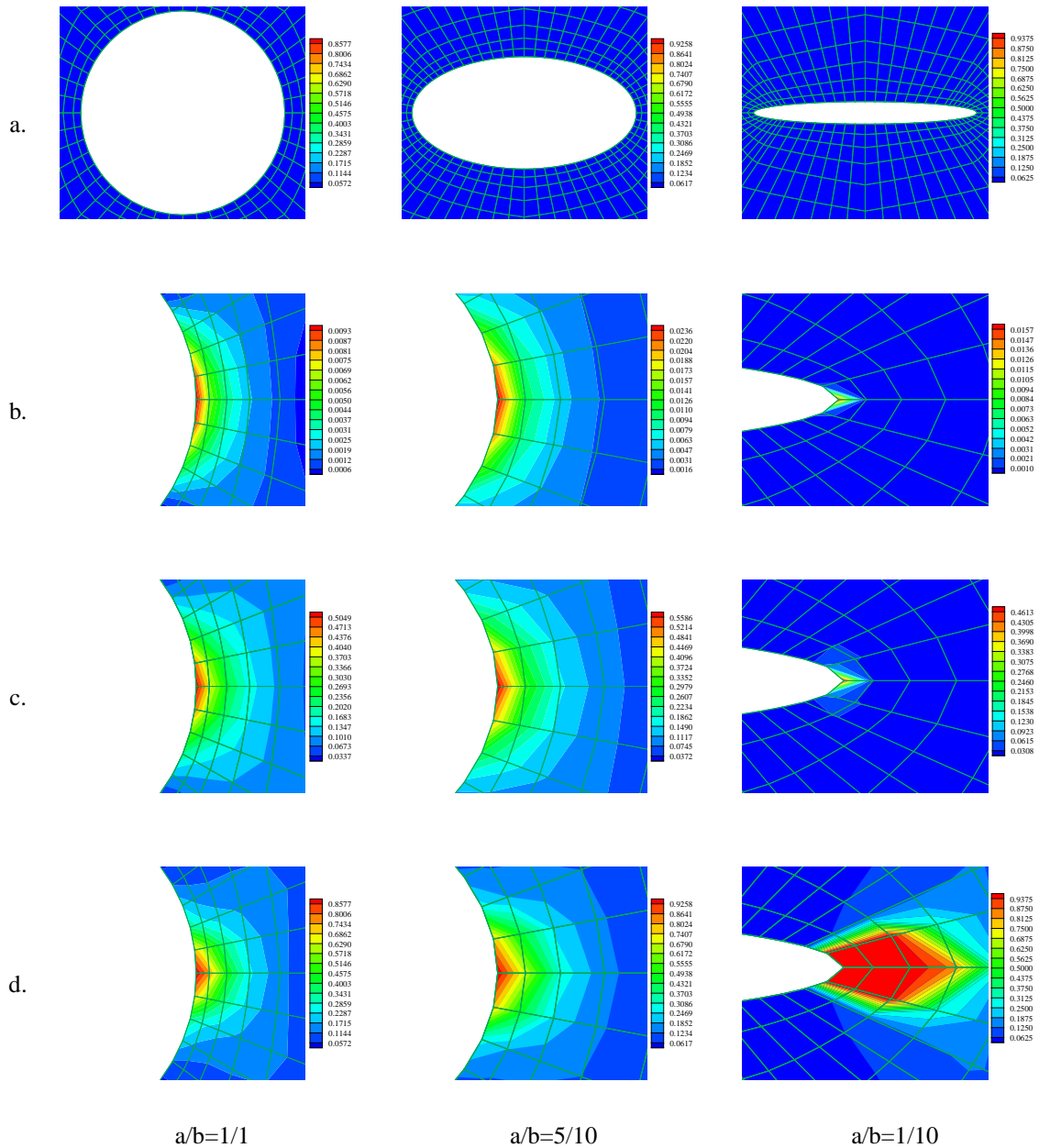


Figure 6.4: Damage variable evolution



Then, the computed discrete material node point surface forces are visualized in Fig. 6.5.

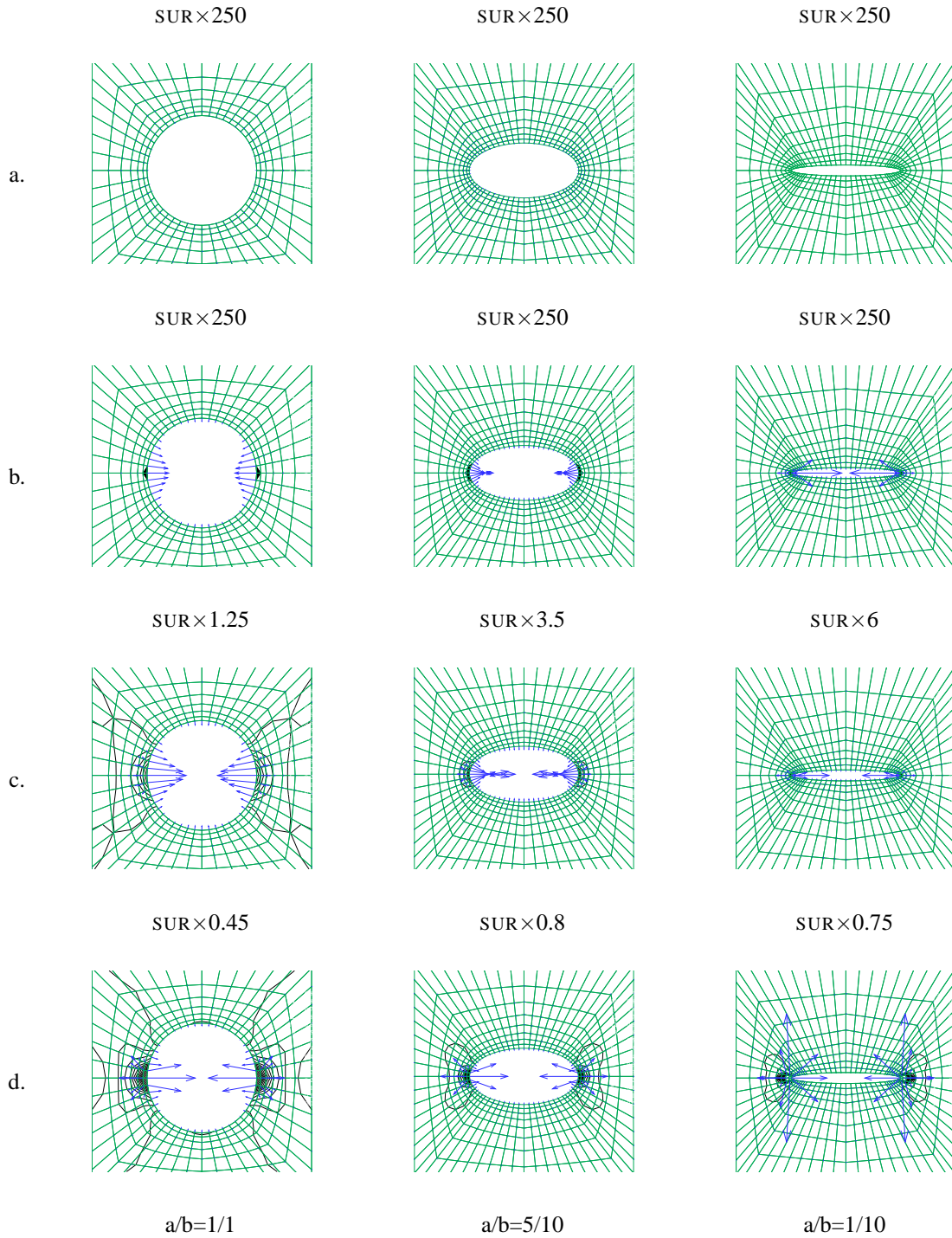


Figure 6.5: Discrete material node point (surface) forces 'SUR'

Due to the fact that  $\mathfrak{F}_{sur,K}^h = \mathfrak{F}_{int,K}^h - \mathfrak{F}_{vol,K}^h$  holds, the (negative) volume part of the discrete material node point forces 'VOL' is plotted separately, see Fig. 6.6 as well as the internal part of the discrete material node point (surface) forces 'INT', see Fig. 6.7.

The contour lines representing the damage state are superposed for convenience in every figure. Thereby, the discrete material node point surface forces 'SUR' point into the directions of an energy increase upon replacement of the material node point position. Thus, the initiation of a crack in the direction opposite to the material (surface) force, in particular the replacement of the material position at the root of the notch

node point, which enlarges the macro crack into the virgin material, corresponds to an energy release. Observe that the (negative) volume part of the discrete material node point forces 'VOL' points along the (negative) gradient  $\text{Grad } d$  of the damage field, which appears to reduce the far-field material loading and hence the resulting material node point surface force at the root of the notch.

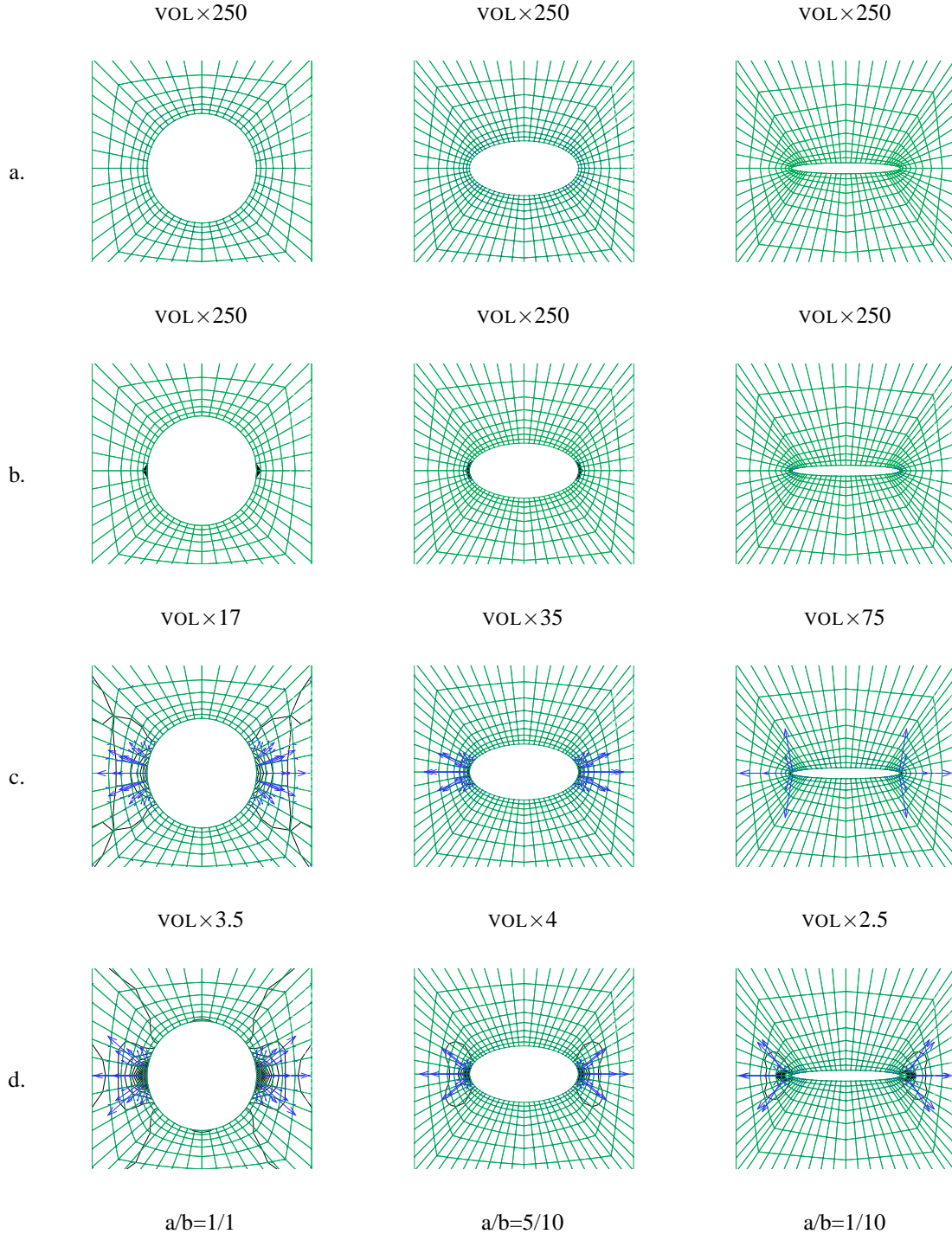


Figure 6.6: Discrete (negative) volume part of material node point forces 'VOL'

Note in addition that the (negative) volume part of the discrete material node point forces 'VOL' are of one order smaller in magnitude compared to the internal part of the discrete material node point (surface) forces 'INT', compare Fig. 6.6 and Fig. 6.7.

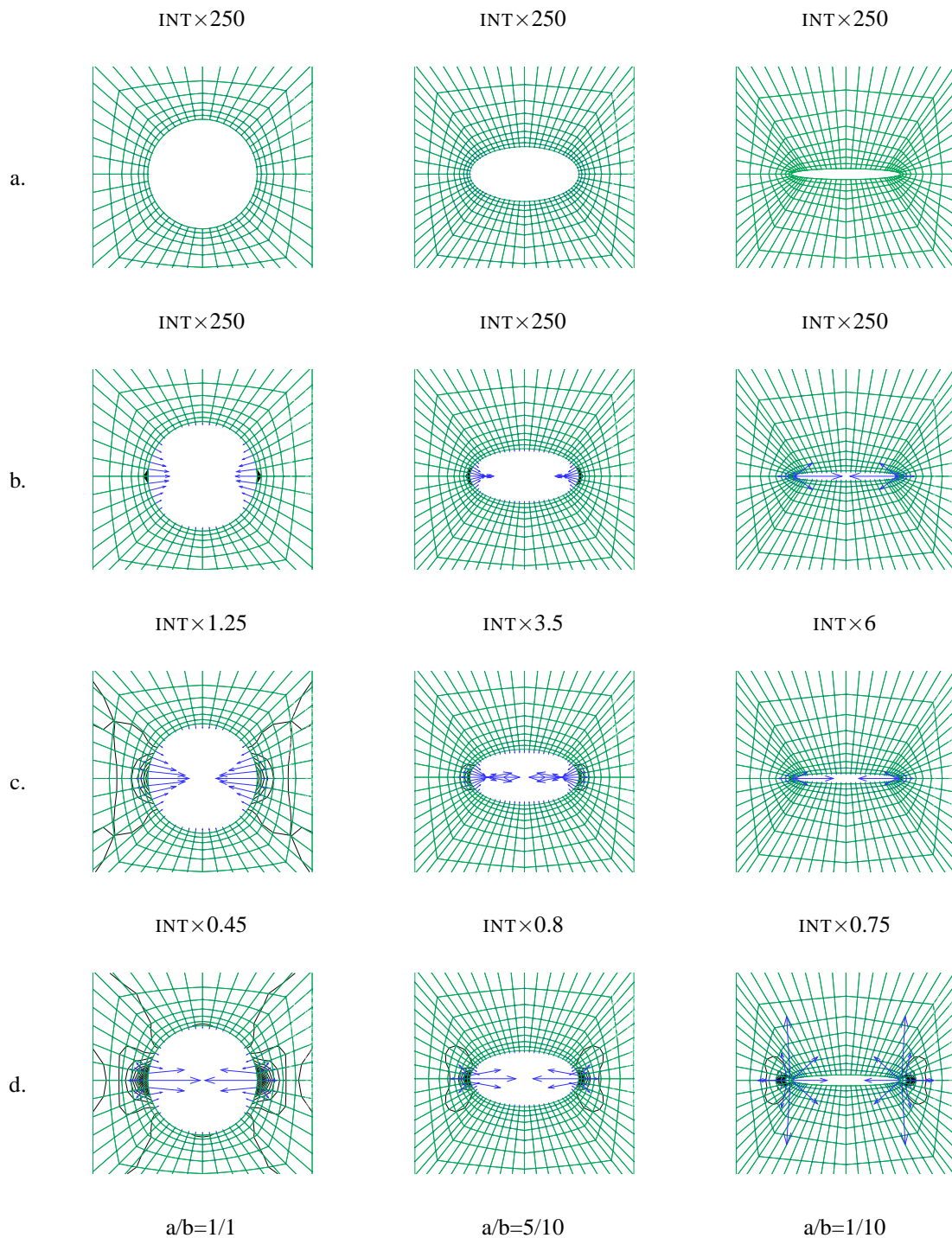


Figure 6.7: Discrete internal part of material node point forces 'INT'

Remarkably, the more slender the elliptic hole gets, the more diverted the material node point (surface) forces 'SUR' become at the root of the notch with an increasing damage zone. This is due to the fact that the finite elements in the vicinity of the notch get highly distorted for  $a/b = 1/10$ , see Fig. 6.5. On the contrary, it is notable that within a circular hole, the material node point (surface) forces get aligned perpendicular to the load direction corresponding to a possible horizontal line crack initiation, see Fig. 6.5. In order to cope with a real crack, a CCT-specimen is investigated next, whereby the specimen is discretized in a suitable way to avoid highly distorted elements.

### 6.5.2 Specimen with center crack

Next, the influence of a center cracked fracture specimen in tension is studied, see Fig. 6.3d, whereby the geometry and material model is chosen as in the previous example. This time, the mesh is discretized with bi-quadratic  $S2$ -serendipity elements and is heavily densified in the vicinity of the crack tip, whereas the elements connected to the crack tip node are standard  $P2$ -triangular elements. A constant elongation is applied incrementally by prescribed displacements at the top surface, the lateral movement of the nodes at the top and bottom surface are unconstrained.

Here, the damage variable distribution is considered for different damage states ranging from the purely undamaged elastic stage to the state where nodes around the crack tip are completely damaged, see zooms of the typical scenario at the crack tip, Fig. 6.8.

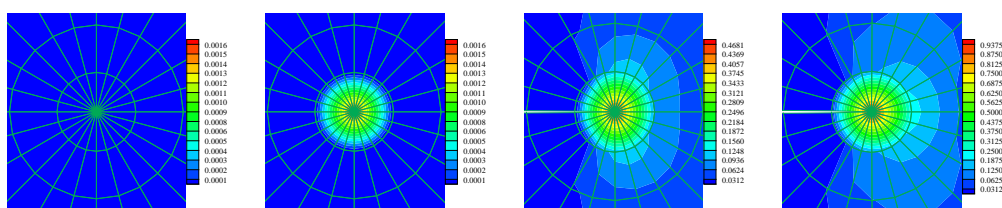


Figure 6.8: Damage distribution at crack tip for different damage states

The computed discrete material node point (surface) forces again point into the direction of an energy increase upon replacement of the material node point position. Thus, the growth of the crack in the direction opposite to the material force, i.e., the replacement of the material position of the crack tip node point attempts to advance the crack tip further into the material, corresponds to an energy release. Observe the similar damage zone as for the case of the slender elliptic hole, compare with Fig. 6.4, i.e., it almost resembles the singular crack tip of the CCT-specimen investigated here. Due to better discretization of the crack vicinity of the CCT-specimen, less diverted spurious material node point forces can be found along the crack tip. A single material node point (surface) force can instead essentially be found perpendicular to the load direction pointing into the crack, see Fig. 6.9. The spurious material forces therefore act as a sensitive indicator for the mesh quality.

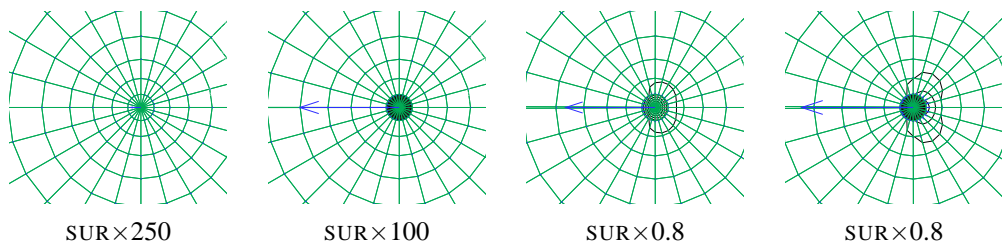


Figure 6.9: Discrete material node point (surface) forces for different damage states

Once again, the discrete (negative) volume part of the material node point forces points along the (negative) gradient of the damage field into the material surrounding the crack tip, see Fig. 6.10. Note that the volume part 'VOL' is of one order smaller in magnitude compared to the internal part 'INT'. Therefore the shielding effect against the external material loading is not very evident and in this example no significant difference between the total discrete material node point (surface) forces and the internal part can be found, see Fig. 6.11.



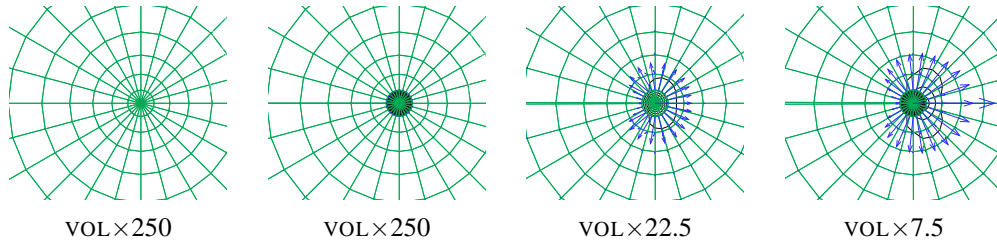


Figure 6.10: Discrete (negative) volume part of material node point forces for different damage states

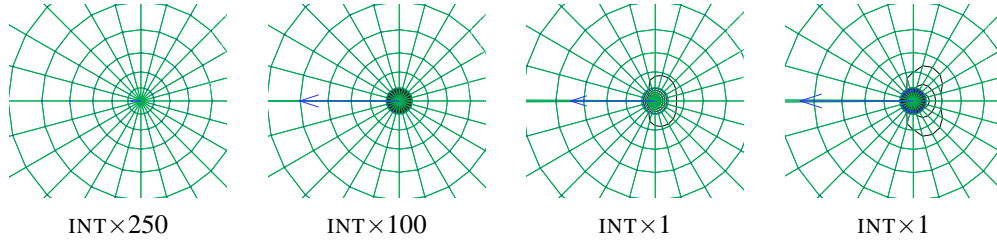


Figure 6.11: Discrete internal part of material node point forces for different damage states

### 6.5.3 MBL-specimen

For validation purposes, a 'Modified Boundary Layer' formulation (MBL-formulation) (Hutchinson (1968); Rice (1968a)) of a straight, traction free crack is investigated. The discretization and the material model are the same as in the previous example. The MBL-formulation is based on an isolated treatment of the crack tip region, which is independent of the surrounding specimen. Under 'Small Scale Damage' (SSD)<sup>3</sup> conditions, this region is chosen in such a way that a small crack tip damage zone, dominated by the non-linear part of the material formulation, is surrounded by a large elastic boundary layer mainly controlled by elastic material behavior. The damaged zone near the crack tip is defined by that region where the damage threshold  $\kappa_0$  is exceeded as is shown in the contour plot of the damage variable in Fig. 6.12a.

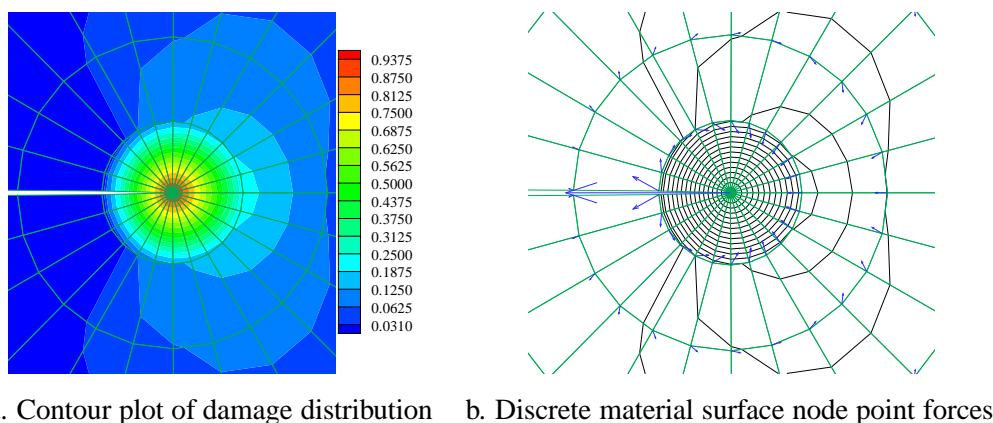


Figure 6.12: MBL-specimen under 'Small Scale Damage' (SSD) conditions

Thereby, the first term of the asymptotic linear elastic stress series near a crack tip is applied, which is given by Williams (1957) as  $\sigma = \frac{K_I}{\sqrt{2\pi r}} \mathbf{f}(\theta)$ . Here  $K_I$  denotes the stress intensity factor and  $\mathbf{f}(\theta)$  are given functions depending only on the angle  $\theta$  measured counterclockwise from the positive x-axis.

<sup>3</sup>according to 'Small Scale Yielding' (SSY) conditions in classical fracture mechanics

Under SSD-conditions, the linear elastic relation for the J-integral  $J_{pre} = K_I^2/E'$  with  $E' = E/[1 - \nu^2]$  for plane strain holds. To ensure SSD-conditions in the MBL-formulation, a circular area around the crack tip is discretized with a radius  $R$  at least 1000 times larger than the maximum size of the damaged zone. In Fig. 6.12b, a close-up of the corresponding discrete material surface node point forces are depicted for the MBL-specimen within the highly damaged crack tip region.

Then, the influence of the damage zone near the crack tip is examined. A purely elastic state is therefore compared with an advanced damaged state, see Fig. 6.13.

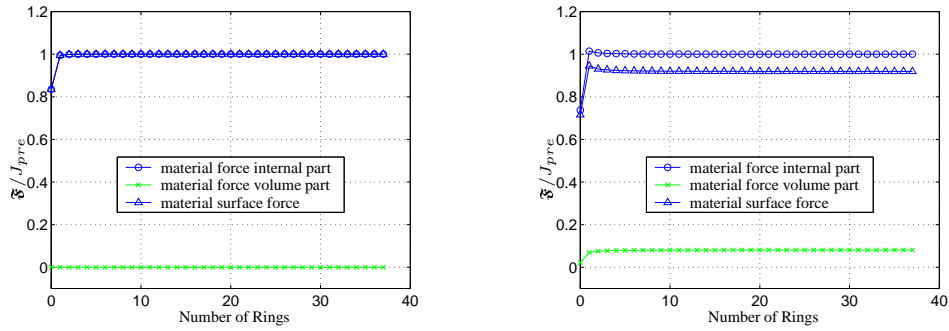


Figure 6.13: Purely elastic state vs. advanced damage state

According to Eqs. 6.48/6.49, the sum of all discrete algorithmic material node point surface forces renders an improved value for the material force at the crack tip. The sum is taken over a varying number of rings of elements around the crack tip. After only a few number of rings, the internal part of the material node point surface force is converged to the prescribed material load and remains constant. Due to the increasing damage zone around the crack tip, the volume part of the discrete material node point forces increases accordingly with the gradient of the damage field. Therefore, the discrete material node point surface force on the crack tip is decreased due to the evolving damage around the crack tip compared to the purely elastic state. Thus, the crack tip might be considered as being shielded by the distributed damage field. This 'shield' is formed closely around the crack tip and converges after a few rings to a constant value.

# Summary and Outlook

The multi-scale nature of almost all engineering materials calls for advanced formulations that incorporate the microstructural response by physical means. Thereby, one has to choose from a variety of different regularizations that can capture the size effect and avoid spurious localization giving rise to pathological mesh sensitivity. It could be shown that physical considerations suggest the use of higher gradients of an internal variable. Therefore, in the thesis presented, the focus was a higher gradient formulation of inelastic materials, which is thermodynamically consistent and physically motivated. Here, two different material behaviors were investigated: on the one hand, elasto-plastic processes and on the other hand, damage processes.

The underlying physical motivation is based on the consideration of plastic flow in single crystals. Thereby, the dislocation density tensor was related to additional hardening contributions corresponding to inhomogeneous plastic deformations. Thus, in addition to classical statistically stored dislocations corresponding to homogeneous plastic deformations, geometrically necessary dislocations were also accounted for.

With the help of a simplified model of single slip, the geometrically necessary dislocation density could be related to the gradient of the shear number, or more general to the gradient of an internal variable. Hence, the free Helmholtz energy was extended with a dislocation related part with respect to the gradient of an internal variable.

Then, the exploitation of thermodynamic principles, e.g., positive dissipation, rendered compatibility requirements between the internal variable and its gradient whereby (i) a nonlocality residual was incorporated in the local dissipation inequality, (ii) a bilinear form for the dissipation density was introduced and (iii) the insulation condition was applied to render the quasi-nonlocal drag stress, which is conjugated to the independent internal variable.

Based on a phenomenological yield/damage condition and the postulate of maximum dissipation, an associated structure of the underlying evolution equations was achieved. As the distinctive feature, the Karush-Kuhn-Tucker conditions depend on the quasi-nonlocal drag stress. Furthermore, constitutive and continuity boundary conditions were derived.

On the numerical side, an active set search became necessary for the monolithic iterative solution of the coupled problem. Thereby, additional discrete algorithmic loading and unloading conditions were evaluated on a nodal basis rendering an updated active set. In particular, a constitutive subproblem in terms of discrete algorithmic Karush-Kuhn-Tucker conditions had to be solved simultaneously in addition to the standard equilibrium subproblem of the discretized algorithmic balance of linear momentum. The solution was computed within a typical Newton-Raphson strategy.

The theoretical and numerical framework was set up for different inelastic material behavior. In a first extensive study, phenomenological elasto-plasticity was investigated for both the geometrically linear

and non-linear case. Thereby, a 1D-model problem was on focus to alleviate further simulations. A regularizing effect of classical local mesh-sensitive simulations could clearly be shown. In addition to that, the benefit of the gradient enhancement was emphasized with a loss of ellipticity analysis. Thereby, the well-posedness of the underlying equations could be preserved for the critical case of softening and material deterioration, respectively. Furthermore, a study of different element types validated the influence of the chosen continuity of approximation of the discretized fields. Next to the local formulation, which discretizes only the displacement field, a quasi-local formulation was applied. Thereby, the internal variable field was independently discretized in various ways.

Next, the gradient formulation was applied to single crystal plasticity. The simulation also showed the positive influence of the gradient enrichment in single and double slip. Here, the results in discrete dislocation simulations as stated in the literature could quantitatively be retrieved. Furthermore, a study of different slip system orientations complemented the investigations.

The second part of this thesis was devoted to the application of the gradient formulation to isotropic damage mechanics. Here, the geometrically linear and non-linear cases were applied. It appeared that the choice of linear expansions in both discretized fields rendered the most effective and efficient results for the gradient formulation. Thereby, the discretized Karush-Kuhn-Tucker conditions mainly seemed to be affected by the choice of discretization order. Again, the 1D-model problem of a bar under uniaxial tension was investigated. The typical deficiency of the classical local formulation was clearly remedied, which was especially valuable in the post-peak behavior. Moreover, the overall solution showed a shrinkage of the localized band width upon further loading into a crack line mode, i.e., a gradual transition from a damaged zone into a line crack.

Lastly, the numerical treatment of isotropic damage in terms of a two field finite element formulation proved especially suitable for the application to the Material Force Method. Thereby, distributed material volume forces arose, which were conjugated to the damage field. Hence, the additional discretization of the damage variable as an independent field next to the deformation field became necessary. In various examples with regard to fracture mechanics, it could be shown that the evolving damage zone shields the crack tip. Hence, the resulting material surface force at the crack tip did not experience the same portion of the applied external material load as compared to the hyperelastic case. Moreover, the Material Force Method could reveal insufficient discretizations as was investigated exemplarily on specimen with different hole geometries together with a CCT-specimen.

This thesis may be understood as an introduction to a physically motivated gradient theory that has been successfully applied within elasto-plasticity and damage mechanics. A number of limitations have been invoked throughout the study to alleviate further developments. Some examples are given below.

- So far, the modeling was restricted to isotropic materials. But one will find mostly anisotropic behavior in reality. Therefore, the proposed gradient formulation has to be extended to be applicable for anisotropic materials. Thereby, it has to be decided, which and how many different length scales with respect to the gradient of diverse scalar-valued internal variables need to be used, see, e.g., Comi (2001). Within the gradient formulation proposed here, it might be sufficient to define the gradient part of the free energy  $W_\kappa$  with an appropriated anisotropic expression for  $\mathbf{E}_\kappa$ .
- The physical motivation for the incorporation of higher gradients in the free Helmholtz energy is based on crystal plasticity phenomena. Here, the gradient formulation was only investigated in quantitatively modeling single and double slip in single crystals. It remains a future task to extend the numerical algorithm to multi-slip kinematics. Thereby, one has to consider the ambiguity



problem for the rate-independent case in more detail. Furthermore, the computational effort will increase significantly due to the active set search on a nodal basis as the number of nodal degrees of freedom increases due to the number of possible slip systems. Here, it could be helpful to resort to parallel programming tools.

- Moreover, the crystal plasticity gradient formulation has to be numerically applied to the geometrically non-linear case. Then, the treatment of the evolution of the geometrically necessary dislocation density, or more specifically of  $\text{Curl}\dot{\mathbf{F}}$ , remains a crucial issue. First proposals, e.g., by Svendsen (2002) define a quasi-linearly dependent evolution equation with respect to  $\dot{\gamma}$  and  $\text{Grad}\gamma$ , which renders a complex algorithmic formulation.
- Another important aspect is the treatment of material behavior that consists of polycrystals. Then, a variety of physical phenomena, e.g., dislocation pile up at grain boundaries, texture development, grain size effects etc., need to be accounted for. Thereby, each grain may be treated as a single crystal but the grain boundaries need special treatment. A recent approach has been investigated by Evers et al. (2002), whereby they resolve the grain boundary with so-called bi-crystal volume elements.
- In Chapter 6 the numerical advantages of a two-field element formulation were used in the context of the Material Force Method coupled to damage. Here, it would be desirable to incorporate the gradient enhancement to rule out, e.g., mesh-sensitivity. Therefore, it would be necessary to discretize not only the internal (damage) variable, but also its gradient, which would give rise to higher continuity requirements of the ansatz-functions.
- Furthermore, it would be desirable to couple elasto-plastic material behavior with damage mechanics. It would then be to question, which internal variable shall be enriched by its gradient. Since both, the damage variable and the history variable in plasticity, are influenced by the microstructure, it needs to be investigated if, on the one hand, it is necessary to incorporate both gradients in the free Helmholtz energy. Otherwise, it might be sufficient to add the gradient influence to the most critical mechanism only.
- Lastly, the highest judging of whether a theory is applicable and workable can only be verified by experiments. Therefore, the parameter set plays a crucial role. Here, rather simple demonstrative prototypes have been extended with the proposed higher gradients. Thereby, the gradient parameter would have to be fitted on experimental results, if it cannot be uniquely defined from the microstructure of the material. Throughout this thesis, the influence of the variation of the gradient parameter was mostly studied, whereby only quantitative verification to experimental observations was made. Realistic parameter identification remains a vital challenge for future developments.



# Appendix A

## A few notes about continuum mechanics

A short summary of the governing kinematics and quasi-static balance of momentum for the general geometrically non-linear case is outlined in the following. It forms a basis for the constitutive routines and finite element implementations as derived throughout this thesis. Starting with kinematic aspects corresponding to the spatial and material motion problem, the strains, velocities and velocity gradients are introduced. Furthermore, the balance equations are specified in terms of the corresponding stress measures of the material and spatial motion problem.

### A.1 Kinematics

To set the stage, the underlying basic geometrically non-linear kinematics of the quasi-static spatial and material motion problem are briefly reviewed.

#### A.1.1 Spatial motion problem

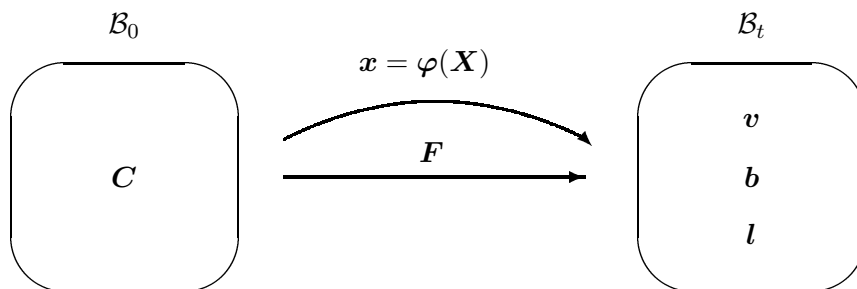


Figure A.1: Kinematics of the Spatial Motion Problem

Let  $\mathcal{B}_0$  denote the material configuration occupied by the body of interest at time  $t_0$ . Then  $\varphi(\mathbf{X})$  denotes the non-linear deformation map assigning the material placements  $\mathbf{X} \in \mathcal{B}_0$  of a 'physical particle' to the spatial placements  $x = \varphi(\mathbf{X}) \in \mathcal{B}_t$  of the same 'physical particle'. Thus, the spatial placements are followed through the ambient space at fixed material position, i.e., the observer takes the Lagrangian viewpoint.

Next, the spatial motion linear tangent map is given by the deformation gradient  $F = \text{Grad } \varphi$  transforming line elements from the tangent space  $T\mathcal{B}_0$  to line elements from the tangent space  $T\mathcal{B}_t$ , see Fig. A.1

$$\mathbf{F} : T\mathcal{B}_0 \longrightarrow T\mathcal{B}_t \quad \text{with} \quad d\mathbf{X} \mapsto d\mathbf{x} = \mathbf{F}(\mathbf{X}) \cdot d\mathbf{X}. \quad (\text{A.1})$$

Then, the spatial motion Jacobian, i.e., the determinant of  $\mathbf{F}$  is denoted by  $J = \det \mathbf{F}$  and relates volume elements  $dV \in \mathcal{B}_0$  to volume elements  $dv \in \mathcal{B}_t$ .

A typical strain measure of the material motion problem can be introduced as the right spatial motion *Cauchy-Green* strain tensor  $\mathbf{C}$ ,

$$\mathbf{C} = \mathbf{F}^t \cdot \mathbf{g} \cdot \mathbf{F}, \quad (\text{A.2})$$

i.e., the spatial motion pull back of the covariant spatial metric  $\mathbf{g}$ . Moreover, the spatial velocity  $\mathbf{v}$  is defined as the material time derivative of the spatial motion map  $\varphi$

$$\mathbf{v} = D_t \varphi(\mathbf{X}, t) \quad (\text{A.3})$$

with  $D_t\{\bullet\} = \partial_t\{\bullet\}|_X$  being the material time derivative  $D_t$  of an arbitrary quantity  $\{\bullet\}$  at fixed material placement  $\mathbf{X}$ . Thereby, the material gradient of  $\mathbf{v}$  is equal to the material time derivative of the spatial deformation gradient  $\mathbf{F}$  while its spatial gradient is denoted as  $\mathbf{l}$  as follows

$$D_t \mathbf{F} = \text{Grad } \mathbf{v} \quad \mathbf{l} = \text{grad } \mathbf{v}. \quad (\text{A.4})$$

The material time derivative of the spatial motion Jacobian  $J$  can thus be expressed through the well-known *Euler* identity  $D_t J = J \text{div } \mathbf{v}$  with  $\text{div } \mathbf{v} = \mathbf{F}^t : D_t \mathbf{F}$  denoting the spatial divergence of the spatial velocity  $\mathbf{v}$ .

### A.1.2 Material motion problem

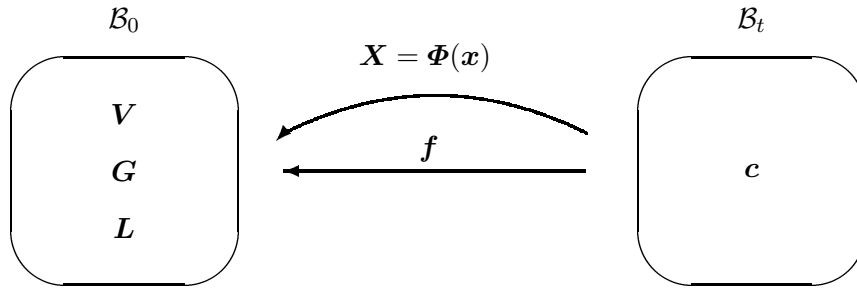


Figure A.2: Kinematics of the Material Motion Problem

Likewise in the material motion problem,  $\mathcal{B}_t$  denotes the spatial configuration occupied by the body of interest at time  $t$ . Then  $\Phi(\mathbf{x})$  denotes the non-linear deformation map assigning the spatial placements  $\mathbf{x} \in \mathcal{B}_t$  of a 'physical particle' to the material placements  $\mathbf{X} = \Phi(\mathbf{x}) \in \mathcal{B}_0$  of the same 'physical particle'. Thus, the material placements are followed through the ambient material at fixed spatial position, i.e., the observer takes essentially the Eulerian viewpoint.

Next, the material motion linear tangent map is given by the deformation gradient  $\mathbf{f} = \text{grad } \Phi$  transforming line elements from the tangent space  $T\mathcal{B}_t$  to line elements from the tangent space  $T\mathcal{B}_0$ , see Fig. A.2

$$\mathbf{f} : T\mathcal{B}_t \longrightarrow T\mathcal{B}_0 \quad \text{with} \quad d\mathbf{x} \mapsto d\mathbf{X} = \mathbf{f}(\mathbf{x}) \cdot d\mathbf{x}. \quad (\text{A.5})$$

Then, the material motion Jacobian, i.e. the determinant of  $\mathbf{f}$  is denoted by  $j = \det \mathbf{f}$  and relates volume elements  $dv \in \mathcal{B}_t$  to volume elements  $dV \in \mathcal{B}_0$ .

The corresponding strain measure is denoted by the material motion pull back of the covariant material metric  $\mathbf{G}$

$$\mathbf{c} = \mathbf{f}^t \cdot \mathbf{G} \cdot \mathbf{f} \quad (\text{A.6})$$

as the right material motion *Cauchy-Green* strain tensor  $\mathbf{c}$ . Moreover, the material velocity  $\mathbf{V}$  is defined as the spatial time derivative of the material motion map  $\Phi$

$$\mathbf{V} = d_t \Phi(\mathbf{x}, t) \quad (\text{A.7})$$

with  $d_t \{\bullet\} = \partial_t \{\bullet\}|_x$  being the spatial time derivative  $d_t$  of an arbitrary quantity  $\{\bullet\}$  at fixed spatial placement  $\mathbf{x}$ . Thereby, the spatial gradient of  $\mathbf{V}$  is equal to the spatial time derivative of the material deformation gradient  $\mathbf{f}$  while its material gradient is denoted as  $\mathbf{L}$  as follows

$$d_t \mathbf{f} = \text{grad } \mathbf{V} \quad \mathbf{L} = \text{Grad } \mathbf{V}. \quad (\text{A.8})$$

Consequently, the spatial time derivative of the material motion Jacobian  $j$  can be expressed through the well-known *Euler* identity  $d_t j = j \text{Div } \mathbf{V}$  with  $\text{Div } \mathbf{V} = \mathbf{f}^t : d_t \mathbf{f}$  denoting the spatial divergence of the spatial velocity  $\mathbf{V}$ .

### A.1.3 Spatial versus material motion problem

No distinction is made between  $\mathbf{F}^{-1}$  and  $\mathbf{f}$  in the spatial motion problem or  $\mathbf{f}^{-1}$  and  $\mathbf{F}$  in the material motion problem, respectively, since they are inverse to each other. This can be easily seen by considering the identity maps  $id_{\mathcal{B}_0} = \Phi \circ \varphi(\mathbf{X}) = \Phi(\varphi(\mathbf{X}))$  and  $id_{\mathcal{B}_t} = \varphi \circ \Phi(\mathbf{x}) = \varphi(\Phi(\mathbf{x}))$ .

On the one hand, the spatial deformation map  $\varphi(\mathbf{X})$  relates compatible configurations  $\mathcal{B}_0$  and  $\mathcal{B}_t = \varphi(\mathcal{B}_0)$ . The integrability condition  $\text{Curl } \mathbf{F} = \mathbf{0}$  for the deformation gradient thus renders the identity  $\text{Grad } \mathbf{F}^t : \{\bullet\} = \{\bullet\} : \text{Grad } \mathbf{F}$  for any second order two-point tensor  $\{\bullet\}$  mapping between the tangent spaces to  $\mathcal{B}_0$  and  $\mathcal{B}_t$ . On the other hand, the material deformation map  $\Phi(\mathbf{x})$  relates compatible configurations  $\mathcal{B}_t$  and  $\mathcal{B}_0 = \Phi(\mathcal{B}_t)$ . The integrability condition  $\text{curl } \mathbf{f} = \mathbf{0}$  for the deformation gradient thus renders the identity  $\text{grad } \mathbf{f}^t : \{\bullet\} = \{\bullet\} : \text{grad } \mathbf{f}$  for any second order two-point tensor  $\{\bullet\}$  mapping between the tangent spaces to  $\mathcal{B}_t$  and  $\mathcal{B}_0$ .

## A.2 Quasi-static balance of momentum

In the following, the appropriate formats of the familiar quasi-static balance of momentum shall be derived. On the one hand, a vectorial statement is obtained in spatial description for the corresponding spatial motion problem. By analogy, the quasi-static balance of momentum for the material motion problem are formally postulated (for the time being) on the other hand. That renders a vectorial statement in material description, see, e.g., Maugin (1993; 1995).

### A.2.1 Spatial motion problem

For the spatial motion problem, the familiar quasi-static balance of momentum reads

$$-\text{Div } \mathbf{II}^t = \mathbf{b}_0 \quad \longrightarrow \quad -\text{div } \boldsymbol{\sigma}^t = \mathbf{b}_t, \quad (\text{A.9})$$

which involves the momentum flux  $\mathbf{\Pi}^t$ , a two–point tensor that shall be called the spatial motion first Piola–Kirchhoff stress, see Fig. A.3, and the momentum source  $\mathbf{b}_0$ , a vector in spatial description with material reference called the spatial motion volume force density.

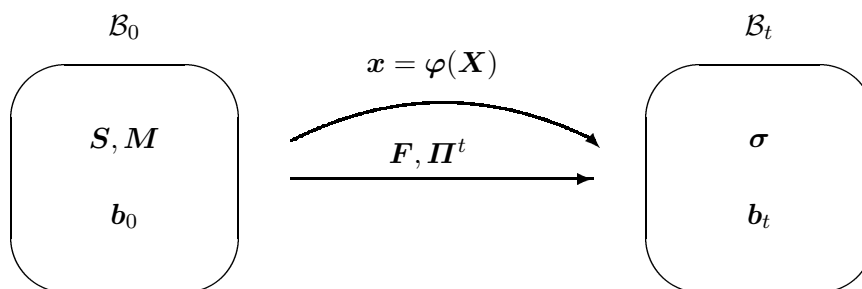


Figure A.3: Kinetics of the Spatial Motion Problem

The Piola transformation of  $\mathbf{\Pi}^t$  is denoted the spatial motion Cauchy stress  $\boldsymbol{\sigma}^t = j\mathbf{\Pi}^t \cdot \mathbf{F}^t$ , the spatial motion volume force density with spatial reference is given by  $\mathbf{b}_t = j\mathbf{b}_0$ . Finally, for completeness, the spatial motion stresses  $\mathbf{S}^t = \mathbf{f} \cdot \mathbf{\Pi}^t$  and  $\mathbf{M}^t = \mathbf{F}^t \cdot \mathbf{\Pi}^t$  may be defined, which denote the spatial motion second Piola–Kirchhoff and the Mandel stress, respectively.

### A.2.2 Material motion problem

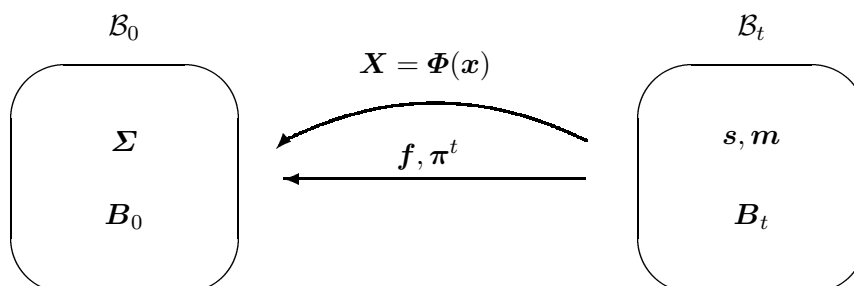


Figure A.4: Kinetics of the Material Motion Problem

For the material motion problem the quasi–static balance of momentum is at first postulated formally and reads in analogy to the spatial motion problem

$$-\operatorname{div} \boldsymbol{\pi}^t = \mathbf{B}_t \quad \longrightarrow \quad -\operatorname{Div} \boldsymbol{\Sigma}^t = \mathbf{B}_0 \quad (\text{A.10})$$

It involves the momentum flux  $\boldsymbol{\pi}^t$ , a two–point tensor that shall be called the material motion first Piola–Kirchhoff stress, see Fig. A.4, and the momentum source  $\mathbf{B}_t$ , a vector in material description with spatial reference called the material motion volume force density.

The Piola transformation of  $\boldsymbol{\pi}^t$  is denoted the material motion Cauchy stress<sup>1</sup>  $\boldsymbol{\Sigma}^t = J\boldsymbol{\pi}^t \cdot \mathbf{f}^t$ , which is often credited to Eshelby, the spatial motion volume force density with material reference is given by  $\mathbf{B}_0 = J\mathbf{B}_t$ . Finally, for completeness and analogy, the material motion stresses  $\mathbf{s}^t = \mathbf{F} \cdot \boldsymbol{\pi}^t$  and  $\mathbf{m}^t = \mathbf{f}^t \cdot \boldsymbol{\pi}^t$  may again be defined, which denote the material motion second Piola–Kirchhoff and the Mandel stress, respectively.

<sup>1</sup>In chapter 6 the terminology energy–momentum tensor or configurational stress tensor will also be used.

## Appendix B

# Geometrically non-linear phenomenological gradient plasticity

Based on multiplicative elasto-plasticity and the simplified model, compare with Eq. 2.31, the free Helmholtz energy function reads

$$\Psi_0 = \Psi_0^{mac}(\mathbf{F}^e) + \Psi_0^{har}(\kappa) + \Psi_0^{dis}(\mathbf{K}). \quad (\text{B.1})$$

incorporating the dislocation density tensor related to  $\mathbf{K} = \text{Grad } \kappa$ . Application of the thermodynamic arguments of section 2.2 renders the pertinent set of equations for the solution of the coupled problem for the primary variables  $\varphi$  and  $\kappa$  in strong and weak form as summarized in Table B.1.

---

### Balance of linear momentum

strong in  $\mathcal{B}_0$

$$\mathbf{r}^\varphi = \text{Div } \mathbf{\Pi}^t(\varphi, \kappa) + \mathbf{b}_0$$

weak in  $\mathcal{B}_0$

$$G^\varphi = \int_{\partial\mathcal{B}_0} \delta\varphi \cdot \mathbf{t}_0^p \, dA + \int_{\mathcal{B}_0} \delta\varphi \cdot \mathbf{b}_0 \, dV - \int_{\mathcal{B}_0} [\text{Grad } \delta\varphi : \mathbf{\Pi}^t(\varphi, \kappa)] \, dV$$

### Karush-Kuhn-Tucker conditions

strong in  $\mathcal{B}_0$

$$r^\Phi = \varphi(\varphi, \kappa) - \bar{Y}_0(\kappa)$$

$$r^\kappa = \dot{\kappa}$$

weak in  $\mathcal{B}_0$

$$G^\Phi = \int_{\mathcal{B}_0} [\delta\kappa [\varphi(\varphi, \kappa) - Y_0(\kappa)] - \text{Grad } \delta\kappa \cdot \mathbf{H}(\kappa)] \, dV$$

$$\dot{G}^\kappa = \int_{\mathcal{B}_0} \delta\Phi \dot{\kappa} \, dV$$

### Decomposition of solution domain

strong in  $\mathcal{B}_0$

$$\mathcal{B}_0^e = \{\mathbf{X} \in \mathcal{B}_0 \mid \Phi \leq 0, \dot{\kappa} = 0\}$$

$$\mathcal{B}_0^p = \{\mathbf{X} \in \mathcal{B}_0 \mid \Phi = 0, \dot{\kappa} > 0\}$$

weak in  $\mathcal{B}_0$

$$\mathcal{B}_0^e = \{\mathbf{X} \in \mathcal{B}_0 \mid G^\Phi \leq 0, \dot{G}^\kappa = 0 \forall \delta\kappa, \delta\Phi > 0 \text{ in } \mathcal{B}_0^e\}$$

$$\mathcal{B}_0^p = \{\mathbf{X} \in \mathcal{B}_0 \mid G^\Phi = 0, \dot{G}^\kappa > 0 \forall \delta\kappa, \delta\Phi > 0 \text{ in } \mathcal{B}_0^p\}$$


---

Table B.1: Strong & weak form of the coupled problem

Firstly, neglecting inertia, the equilibrium subproblem is given by the material balance of linear momentum  $\mathbf{r}^\varphi(\boldsymbol{\varphi}, \kappa) = \mathbf{0}$  and the corresponding Neumann boundary conditions  $\mathbf{\Pi}^t \cdot \mathbf{N} = \mathbf{t}_0^p$ , which are tested by a virtual deformation map  $\delta\boldsymbol{\varphi}$  to render the virtual work expression  $G^\varphi(\boldsymbol{\varphi}, \kappa; \delta\boldsymbol{\varphi}) = 0 \forall \delta\boldsymbol{\varphi}$ .

Secondly, the Karush-Kuhn-Tucker condition  $r^\Phi(\boldsymbol{\varphi}, \kappa) = \Phi \leq 0$  and the homogeneous Neumann boundary conditions  $\mathbf{N} \cdot \mathbf{H} = 0$  are tested by  $\delta\kappa$  with the constraint  $\delta\kappa > 0$  on the one hand and on the other hand, the Karush-Kuhn-Tucker condition  $r^\kappa(\dot{\kappa}) = \dot{\kappa} \geq 0$  is tested by  $\delta\Phi$  with the constraint  $\delta\Phi > 0$  to render the global statements  $G^\Phi(\boldsymbol{\varphi}, \kappa; \delta\kappa) \leq 0 \forall \delta\kappa$  and  $\dot{G}^\kappa(\dot{\kappa}; \delta\Phi) \geq 0 \forall \delta\Phi$ .

Thirdly, based on these statements, the decomposition of the solution domain  $\mathcal{B}_0$  into an active plastic and an inactive elastic domain  $\mathcal{B}_0 = \mathcal{B}_0^p \cup \mathcal{B}_0^e$  with  $\emptyset = \mathcal{B}_0^e \cap \mathcal{B}_0^p$  follows implicitly as the support of the admissible test functions  $\delta\kappa, \delta\Phi$  above. This is indeed a quite implicit definition at this stage since one has to test for all possible combinations of support with all admissible test functions. Finally, note that the above decomposition corresponds to the complementary pointwise condition  $\dot{\kappa}\Phi = 0$ .

## B.1 Discretization in time and space of the coupled problem

The above set of equations has to be discretized in time, whereby we apply the implicit Euler backward method without loss of generality. One should note here that the plastic incompressibility constraint  $\mathbf{F}^p \in SL(3)$ , with  $SL(3)$  the unimodular group, is generally violated, for remedies see, e.g., Miehe (1999). Then, the time integration of the primary variables  $\boldsymbol{\varphi}$  and  $\kappa$  renders a discretized time update for the values  $\boldsymbol{\varphi}_{n+1}$  and  $\kappa_{n+1}$ . Finally, the algorithmic set of equations has to be discretized in space. To this end, we resort to the standard Bubnov-Galerkin finite element method, which is resolved in analogy to section 3.5.4. The resulting scheme is summarized in Table B.2.

Firstly, based on the temporal discretization of the primary variables  $\boldsymbol{\varphi}$  and  $\kappa$ , the algorithmic balance of linear momentum as  $G^\varphi(\boldsymbol{\varphi}_{n+1}, \kappa_{n+1}; \delta\boldsymbol{\varphi}) = 0 \forall \delta\boldsymbol{\varphi}$  in  $\mathcal{B}_0$  is obtained. Then, based on the spatial discretizations of the primary variables  $\boldsymbol{\varphi}$  and  $\kappa$ , the discrete algorithmic balance of linear momentum follows as  $\mathbf{R}_K^\varphi(\boldsymbol{\varphi}_{n+1}^h, \kappa_{n+1}^h) = \mathbf{0} \forall K$  in  $\mathbb{B}$ .

Secondly, the algorithmic Kuhn-Tucker conditions is set up, whereby the first one represents the algorithmic yield condition and the second one assures positive increments of the internal variable  $G^\Phi(\boldsymbol{\varphi}_{n+1}, \kappa_{n+1}; \delta\kappa) \leq 0 \forall \delta\kappa$  in  $\mathcal{B}_0$  and  $\Delta G^\kappa(\kappa_{n+1}; \delta\Phi) \geq 0 \forall \delta\Phi > 0$  in  $\mathcal{B}_0$ . Then, the discrete algorithmic Kuhn-Tucker conditions follow, whereby in particular the first one represents the discrete algorithmic yield condition  $R_K^\Phi(\boldsymbol{\varphi}_{n+1}^h, \kappa_{n+1}^h) \leq 0 \forall K$  in  $\mathbb{B}$  and the second one assures positive increments of the internal variable  $\Delta R_K^\kappa(\kappa_{n+1}^h) \geq 0 \forall K$  in  $\mathbb{B}$ .

Thirdly, the algorithmic decomposition of the solution domain with  $\mathcal{B}_0 = \mathcal{B}_{0_{n+1}}^p \cup \mathcal{B}_{0_{n+1}}^e$  and  $\emptyset = \mathcal{B}_{0_{n+1}}^e \cap \mathcal{B}_{0_{n+1}}^p$  follows implicitly as the support of the admissible test functions  $\delta\kappa, \delta\Phi$ . Note that the above algorithmic decomposition corresponds to the pointwise algorithmic complementary condition  $[\kappa_{n+1} - \kappa_n]\Phi_{n+1} = 0$ .

Finally, the above domain decomposition has to be discretized in space, which indeed renders a complete explicit definition since one only has to separately check all node points  $K \in \mathbb{B}$ . Note that the above discrete algorithmic decomposition corresponds to the discrete algorithmic complementary condition  $\Delta R_K^\kappa R_K^\Phi = 0 \forall K$  in  $\mathbb{B}$ .

Based on the spatial discretization of  $\kappa$ , the residuum  $\Delta R_K^\kappa$  in Table B.2 expands into

$$\Delta R_K^\kappa = \sum_L M_{KL}^{\kappa\kappa} \Delta\kappa_L \quad \text{with} \quad M_{KL}^{\kappa\kappa} = \mathbf{A} \int_{\mathcal{B}_e} N_\kappa^k N_\kappa^l dV. \quad (\text{B.2})$$

For the most convenient implementation, the positive definite fundamental matrix  $M_{KL}^{\kappa\kappa}$  is simply diag-



**Balance of linear momentum**algorithmic in  $\mathcal{B}_0$ 

$$G_{n+1}^\varphi = \int_{\partial\mathcal{B}_0} \delta\varphi \cdot \mathbf{t}_{0n+1}^p \, dA + \int_{\mathcal{B}_0} [\delta\varphi \cdot \mathbf{b}_{0n+1}] \, dV - \int_{\mathcal{B}_0} [\text{Grad } \delta\varphi : \mathbf{II}^t(\varphi_{n+1}, \kappa_{n+1})] \, dV$$

discrete in  $\mathbb{B}$ 

$$R_K^\varphi = \mathbf{A}_e \int_{\partial\mathcal{B}_{e_0} \cap \partial\mathcal{B}_0^t} N_X^k \mathbf{t}_{0n+1}^p \, dA + \int_{\mathcal{B}_{e_0}} [N_X^k \mathbf{b}_{0n+1}] \, dV - \int_{\mathcal{B}_{e_0}} [\text{Grad } N_X^k \cdot \mathbf{II}^t(\varphi_{n+1}^h, \kappa_{n+1}^h)] \, dV$$

**Kuhn-Tucker conditions**algorithmic in  $\mathcal{B}_0$ 

$$G_{n+1}^\Phi = \int_{\mathcal{B}_0} [\delta\kappa [\varphi(\varphi_{n+1}, \kappa_{n+1}) - Y_0(\kappa_{n+1})]] \, dV - \int_{\mathcal{B}_0} [\text{Grad } \delta\kappa \cdot \mathbf{H}(\kappa_{n+1})] \, dV$$

$$\Delta G_{n+1}^\kappa = \int_{\mathcal{B}_0} \delta\Phi [\kappa_{n+1} - \kappa_n] \, dV$$

discrete in  $\mathbb{B}$ 

$$R_K^\Phi = \mathbf{A}_e \int_{\mathcal{B}_{e_0}} [N_\kappa^k [\varphi(\varphi_{n+1}^h, \kappa_{n+1}^h) - Y_0(\kappa_{n+1}^h)]] \, dV - \int_{\mathcal{B}_{e_0}} [\text{Grad } N_\kappa^k \cdot \mathbf{H}(\kappa_{n+1}^h)] \, dV$$

$$\Delta R_K^\kappa = \mathbf{A}_e \int_{\mathcal{B}_{e_0}} [N_\kappa^k [\kappa_{n+1}^h - \kappa_n^h]] \, dV$$

**Decomposition of solution domain**algorithmic in  $\mathcal{B}_0$ 

$$\mathcal{B}_{0n+1}^e = \{\mathbf{X} \in \mathcal{B}_0 | G_{n+1}^\Phi \leq 0, \Delta G_{n+1}^\kappa = 0 \forall \delta\kappa, \delta\Phi > 0 \text{ in } \mathcal{B}_{0n+1}^e\}$$

$$\mathcal{B}_{0n+1}^p = \{\mathbf{X} \in \mathcal{B}_0 | G_{n+1}^\Phi = 0, \Delta G_{n+1}^\kappa > 0 \forall \delta\kappa, \delta\Phi > 0 \text{ in } \mathcal{B}_{0n+1}^p\}$$

discrete in  $\mathbb{B}$ 

$$\mathbb{B}_{n+1}^e = \{K \in \mathbb{B} | R_K^\Phi \leq 0, \Delta R_K^\kappa = 0\}$$

$$\mathbb{B}_{n+1}^p = \{K \in \mathbb{B} | R_K^\Phi = 0, \Delta R_K^\kappa > 0\}$$

Table B.2: Algorithmic and discrete form of the coupled problem

onalized,  $\Delta R_K^\kappa \geq 0$  is thus equivalent to  $\Delta\kappa_L \geq 0$ .

The initially unknown decomposition into discrete active and inactive node point subsets  $\mathbb{B} = \mathbb{B}_{n+1}^p \cup \mathbb{B}_{n+1}^e$  at time step  $t_{n+1}$  is determined iteratively along the lines described in section 3.5.5.2. Then, the discrete algorithmic equilibrium and constitutive subproblem are solved simultaneously within a monolithic iterative solution as was schematically outlined in section 3.5.5.

**B.2 Prototype isotropic gradient plasticity model**

The logarithmic von Mises type model problem investigated in section 3.6.2 is based on the following isotropic gradient prototype summarized in Table B.3. The corresponding local prototype is also depicted for comparison.

The elastic part  $\Psi_0^{mac}$  of the free energy is expressed in terms of the elastic logarithmic Hencky strain  $\epsilon^e = 1/2 \ln \mathbf{b}^e$  with  $\mathbf{b}^e = \mathbf{F}^e \cdot \mathbf{F}^{e^t}$  resulting in a numerical convenient implementation in principal stretches and stresses, respectively. The additional gradient part  $\Psi_0^{dis}$  of the free energy is expanded into an isotropic quadratic function in  $\mathbf{K}$ . Note that the formulation itself is more general and could be adopted to gradient anisotropy. Here, the gradient parameter  $c \geq 0$  controls the quasi-nonlocal character of the formulation,  $\lambda$  and  $\mu$  denote the Lamé parameters. Moreover, a linear law is adopted for the local drag stress  $H(\kappa)$  characterized by the initial yield strength  $Y_0$  together with a linear hardening modulus  $H_0$ .

**Free Helmholtz energy  $\Psi$** 

$$\text{local} \quad \Psi_0(\boldsymbol{\epsilon}^e, \kappa) = \Psi_0^{mac}(\boldsymbol{\epsilon}^e) + \int_0^\kappa H(\hat{\kappa}) \, d\hat{\kappa}$$

$$\text{gradient} \quad \Psi_0(\boldsymbol{\epsilon}^e, \mathbf{K}, \kappa) = \Psi_0^{mac}(\boldsymbol{\epsilon}^e) + \Psi_0^{dis}(\mathbf{K}) + \int_0^\kappa H(\hat{\kappa}) \, d\hat{\kappa}$$

elastic part of the free energy

$$\Psi_0^{mac}(\boldsymbol{\epsilon}^e) = \frac{1}{2} \lambda [\boldsymbol{\epsilon}^e : \mathbf{1}]^2 + \mu \boldsymbol{\epsilon}^e : \boldsymbol{\epsilon}^e$$

gradient part of the free energy

$$\Psi_0^{dis}(\mathbf{K}) = \frac{1}{2} \mathbf{K} \cdot \boldsymbol{\mathcal{E}}_\kappa \cdot \mathbf{K} \quad \text{with} \quad \boldsymbol{\mathcal{E}}_\kappa = c \mathbf{1}$$

**von Mises yield condition**

$$\text{local} \quad \Phi(\boldsymbol{\tau}, H) = \|\text{dev } \boldsymbol{\tau}\| - \sqrt{\frac{2}{3}} [Y_0 + H] \leq 0$$

$$\text{gradient} \quad \Phi(\boldsymbol{\tau}, \bar{H}) = \|\text{dev } \boldsymbol{\tau}\| - \sqrt{\frac{2}{3}} [Y_0 + \bar{H}] \leq 0$$

**Drag stress**

$$\text{local} \quad H(\kappa) = H_0 \kappa$$

$$\text{quasi-nonlocal} \quad \bar{H}(\kappa) = H - \text{Div } \mathbf{H}$$

$$\text{hardening flux} \quad \mathbf{H}(\mathbf{K}) = c \mathbf{K}$$

**Evolution laws**

$$\begin{aligned} \mathcal{L} \mathbf{b}^{e-1} \cdot \mathbf{b}^e &= 2\dot{\gamma} \frac{\text{dev } \boldsymbol{\tau}}{\|\text{dev } \boldsymbol{\tau}\|} \\ \dot{\kappa} &= \dot{\gamma} \sqrt{\frac{2}{3}} \end{aligned}$$

Table B.3: Isotropic local and gradient prototype

Furthermore, the consequences of isotropy have been explicitly incorporated when expressing the yield condition and in particular, the evolution law for the plastic flow. Here  $\mathcal{L} \mathbf{b}^{e-1} = 2 \mathbf{f}^t \cdot [\mathbf{F}^{p^t} \cdot \dot{\mathbf{F}}^p]^{sym} \cdot \mathbf{f}$  is the common abbreviation for the so-called Lie derivative of  $\mathbf{b}^{e-1}$  and  $\boldsymbol{\tau}^t = \mathbf{f}^{e^t} \cdot \mathbf{M}^t \cdot \mathbf{F}^{e^t}$  denotes the Kirchhoff stress in  $\mathcal{B}_t$ , which is obtained from the mixed-variant push-forward operation of the Mandel stress tensor in  $\mathcal{B}_p$ .

Finally, note that some minor adaptations of factors, e.g.,  $1 \mapsto \sqrt{2/3}$ , are necessary for the 1D case.

**B.3 Constitutive update**

The constitutive update of logarithmic von Mises prototype model for given  $\mathbf{F}_{n+1, \kappa_{n+1}}, \mathbf{K}_{n+1}; \mathbf{F}_n^p, \kappa_n$  is sketched in Table B.4. Thereby, the spectral decomposition of the elastic finger tensor  $\mathbf{b}^e = \sum_A \lambda_A^{e^2} \mathbf{n}_A \otimes \mathbf{n}_A$  is used in terms of the principal elastic stretches  $\lambda_A^e$  and the eigenbasis  $\mathbf{n}_A \otimes \mathbf{n}_A$ . Note that despite its implicit character, the constitutive update does not rely on local iterations usually employed in standard return mapping algorithms.

The proposed update algorithm is derived based on the multiplicative decomposition and on the assumption of isothermal, isotropic, rate-independent elasto-plastic material behavior. The algorithmic treatment of the incremental constitutive relations above relies on the execution of an elastic trial step for which the multiplicative decomposition at hand is given by  $\mathbf{F}_{trial}^e = \mathbf{F}_{n+1} \cdot \mathbf{f}_n^p$ . This implies that the plastic flow during the trial elastic deformation is frozen, see Simo (1992). The elastic trial step leads to the spatial eigenvalue problem, see Table B.4, which is solved for  $\lambda_{A_{trial}}^e$  and enables the computation of the trial stress  $\boldsymbol{\tau}_{trial}$ . Finally, the update of the elastic finger tensor in strain space can be expressed in terms of the logarithmic elastic Hencky tensor in the well-known format from small strain plasticity

---

<b>Input:</b> $\mathbf{F}_{n+1}, \mathbf{F}_n^p; \kappa_{n+1}, \kappa_n$			
Plastic multiplier	$\Delta\gamma$	$=$	$\sqrt{\frac{3}{2}}[\kappa_{n+1} - \kappa_n]$
Trial elastic strain tensor	$\mathbf{b}_{trial}^e$	$=$	$\mathbf{F}_{n+1} \cdot \mathbf{C}_n^{p^{-1}} \cdot \mathbf{F}_{n+1}^t$
Solve elastic eigenvalue problem	$\lambda_{Atrial}^e$	$\Leftarrow$	$[\mathbf{b}_{trial}^e - \lambda_{Atrial}^{e2} \mathbf{1}] \cdot \mathbf{n}^A = \mathbf{0}$
Trial stress	$\boldsymbol{\tau}_{trial}$	$=$	$\lambda_{Atrial}^e \frac{\partial \Psi^{mac}}{\partial \lambda_{Atrial}^e} \mathbf{n}_A \otimes \mathbf{n}_A$
Deviatoric trial stress	$\text{dev } \boldsymbol{\tau}_{trial}$	$=$	$\boldsymbol{\tau}_{trial} - \frac{1}{3}[\boldsymbol{\tau}_{trial} : \mathbf{1}]\mathbf{1}$
Stress update	$\text{dev } \boldsymbol{\tau}_{n+1}$	$=$	$\text{dev } \boldsymbol{\tau}_{trial} - 2G \Delta\gamma \boldsymbol{\nu}_{trial} \quad \boldsymbol{\nu}_{trial} = \frac{\text{dev } \boldsymbol{\tau}_{trial}}{\ \text{dev } \boldsymbol{\tau}_{trial}\ }$
von Mises stress update	$\varphi_{n+1}$	$=$	$\ \text{dev } \boldsymbol{\tau}_{trial}\  - 2G\Delta\gamma$
Local yield stress	$Y_{n+1}$	$=$	$Y_0 + H(\kappa_{n+1})$
Hardening flux	$\mathbf{H}_{n+1}$	$=$	$c \mathbf{K}_{n+1}$
Update elastic strain tensor	$\ln \mathbf{b}_{n+1}^e$	$=$	$\ln \mathbf{b}_{trial}^e - 2\Delta\gamma \boldsymbol{\nu}_{trial}$
Update plastic strain tensor	$\mathbf{C}_{n+1}^{p^{-1}}$	$=$	$\mathbf{f}_{n+1} \cdot \mathbf{b}_{n+1}^e \cdot \mathbf{f}_{n+1}^t$

---

Table B.4: Update of the constitutive variables

$\boldsymbol{\epsilon}_{n+1}^e = \boldsymbol{\epsilon}_n^e - \Delta\gamma \boldsymbol{\nu}_{trial}$ . Thus, as a consequence, essentially standard geometrically linear return map algorithms may be employed. Moreover, the linearization of the constitutive update rendering the partitions of the constitutive tangent operator as incorporated in the global iteration matrix follows in analogy to the local case as documented in Simo (1992) and results in a symmetric global iteration matrix.



## Appendix C

# Geometrically non-linear phenomenological gradient damage

In contrast to averaging methods, see, e.g., Steinmann (1999) for an outline, the free Helmholtz energy is based on the derived simplified model 2.31 as follows

$$\Psi = \Psi(d, \mathbf{F}, \mathbf{D}) = \Psi^{mac}(d, \mathbf{F}) + \Psi^{grad}(\mathbf{D}) \quad \text{with} \quad \Psi^{mac} = [1 - d]W(\mathbf{F}) \quad (\text{C.1})$$

incorporating the deformation gradient  $\mathbf{F}$ , the damage variable  $d$  and the material gradient of the damage field  $\mathbf{D} = \text{Grad } d$ . Application of the thermodynamic arguments of section 2.2 renders the pertinent set of equations for the solution of the coupled problem for the primary variables  $\varphi$  and  $d$  in strong and weak form as summarized in Table C.1.

Neglecting inertia, the equilibrium subproblem is given by the material balance of linear momentum  $r^\varphi(\varphi, d) = \mathbf{0}$  and the corresponding Neumann boundary conditions  $\mathbf{II}^t \cdot \mathbf{N} = \mathbf{t}_0^p$ , which are tested by a virtual deformation map  $\delta\varphi$  to render the virtual work expression  $G^\varphi(\varphi, d; \delta\varphi) = 0 \forall \delta\varphi$ .

Secondly, the Karush-Kuhn-Tucker condition  $r^\varphi(\varphi, d) \leq 0$  and the homogeneous Neumann boundary conditions  $\mathbf{N} \cdot \mathbf{Y} = 0$  are tested by  $\delta d$  with the constraint  $\delta d > 0$  on the one hand, and on the other hand, the Karush-Kuhn-Tucker condition  $r^d(\dot{d}) = \dot{d} \geq 0$  is tested by  $\delta\Phi$  with the constraint  $\delta\Phi > 0$  to render the global statements  $G^\Phi(\varphi, d; \delta d) \leq 0 \forall \delta d$  and  $\dot{G}^d(\dot{d}; \delta\Phi) \geq 0 \forall \delta\Phi$ .

Thirdly, based on these statements, the decomposition of the solution domain  $\mathcal{B}_0$  into an active damaged and an inactive elastic domain  $\mathcal{B}_0 = \mathcal{B}_0^d \cup \mathcal{B}_0^e$  with  $\emptyset = \mathcal{B}_0^e \cap \mathcal{B}_0^d$  follows implicitly as the support of the admissible test functions  $\delta d, \delta\Phi$  above. This is indeed quite an implicit definition at this stage since one has to test for all possible combinations of support with all admissible test functions. Finally, note that the above decomposition corresponds to the complementary pointwise condition  $\dot{d}\Phi = 0$ .

### C.1 Discretization in time and space of the coupled problem

The above set of equations has to be discretized in time. Then, the time integration of the primary variables  $\varphi$  and  $d$  renders a discretized time update for the values  $\varphi_{n+1}$  and  $d_{n+1}$ . Finally, the algorithmic set of equations has to be discretized in space. To this end, we resort to the standard Bubnov-Galerkin finite element method, which is resolved in analogy to section 3.5.4. The resulting scheme is summarized in Table C.2.

Firstly, based on the temporal discretization of the primary variables  $\varphi$  and  $d$ , the algorithmic balance of linear momentum as  $G^\varphi(\varphi_{n+1}, d_{n+1}; \delta\varphi) = 0 \forall \delta\varphi$  in  $\mathcal{B}_0$  is obtained. Then, based on the spatial

**Balance of linear momentum**strong in  $\mathcal{B}_0$ 

$$\mathbf{r}^\varphi = \text{Div } \mathbf{II}^t(\varphi, d) + \mathbf{b}_0$$

weak in  $\mathcal{B}_0$ 

$$G^\varphi = \int_{\partial\mathcal{B}_0} \delta\varphi \cdot \mathbf{t}_0^p \, dA + \int_{\mathcal{B}_0} \delta\varphi \cdot \mathbf{b}_0 \, dV - \int_{\mathcal{B}_0} [\text{Grad } \delta\varphi : \mathbf{II}^t(\varphi, d)] \, dV$$

**Karush-Kuhn-Tucker conditions**strong in  $\mathcal{B}_0$ 

$$r^\Phi = \varphi(\varphi, d) - \bar{Y}_0(d)$$

$$r^d = \dot{d}$$

weak in  $\mathcal{B}_0$ 

$$G^\Phi = \int_{\mathcal{B}_0} [\delta d [Y_0(\varphi, d) - \kappa(d)]] \, dV + \int_{\mathcal{B}_0} [\text{Grad } \delta d \cdot \mathbf{Y}(d)] \, dV$$

$$\dot{G}^d = \int_{\mathcal{B}_0} \delta\Phi \dot{d} \, dV$$

**Decomposition of solution domain**strong in  $\mathcal{B}_0$ 

$$\mathcal{B}_0^e = \{\mathbf{X} \in \mathcal{B}_0 \mid \Phi \leq 0, \dot{d} = 0\}$$

$$\mathcal{B}_0^d = \{\mathbf{X} \in \mathcal{B}_0 \mid \Phi = 0, \dot{d} > 0\}$$

weak in  $\mathcal{B}_0$ 

$$\mathcal{B}_0^e = \{\mathbf{X} \in \mathcal{B}_0 \mid G^\Phi \leq 0, \dot{G}^d = 0 \vee \delta d, \delta\Phi > 0 \text{ in } \mathcal{B}_0^e\}$$

$$\mathcal{B}_0^d = \{\mathbf{X} \in \mathcal{B}_0 \mid G^\Phi = 0, \dot{G}^d > 0 \vee \delta d, \delta\Phi > 0 \text{ in } \mathcal{B}_0^d\}$$

Table C.1: Strong &amp; weak form of the coupled problem

discretizations of the primary variables  $\varphi$  and  $d$ , the discrete algorithmic balance of linear momentum follows as  $\mathbf{R}_K^\varphi(\varphi_{n+1}^h, d_{n+1}^h) = \mathbf{0} \forall K \text{ in } \mathbb{B}$ .

Secondly, the algorithmic Kuhn-Tucker conditions are set up, whereby the first one represents the algorithmic yield condition and the second one assures positive increments of the internal variable  $G^\Phi(\varphi_{n+1}, d_{n+1}; \delta d) \leq 0 \forall \delta d \text{ in } \mathcal{B}_0$  and  $\Delta G^d(d_{n+1}; \delta\Phi) \geq 0 \forall \delta\Phi > 0 \text{ in } \mathcal{B}_0$ . Then, the discrete algorithmic Kuhn-Tucker conditions follow, whereby the first one represents the discrete algorithmic yield condition  $R_K^\Phi(\varphi_{n+1}^h, d_{n+1}^h) \leq 0 \forall K \text{ in } \mathbb{B}$  in particular and the second one assures positive increments of the internal variable  $\Delta R_K^d(d_{n+1}^h) \geq 0 \forall K \text{ in } \mathbb{B}$ .

Thirdly, the algorithmic decomposition of the solution domain with  $\mathcal{B}_0 = \mathcal{B}_{0_{n+1}}^d \cup \mathcal{B}_{0_{n+1}}^e$  and  $\emptyset = \mathcal{B}_{0_{n+1}}^e \cap \mathcal{B}_{0_{n+1}}^d$  follows implicitly as the support of the admissible test functions  $\delta d, \delta\Phi$ . Note that the above algorithmic decomposition corresponds to the pointwise algorithmic complementary condition  $[d_{n+1} - d_n] \Phi_{n+1} = 0$ .

For the spatial discretization, we resort to the Bubnov-Galerkin finite element method with typical polynomial expansions  $\delta \mathbf{x}^h, \mathbf{x}^h, \mathbf{X}^h \in P^m$  and  $\delta d^h, d^h, \delta\varphi^h \in P^n$ . In addition to that, the decomposition of the solution domain transforms into a discrete algorithmic decomposition on a nodal basis

$$\mathbb{B} = \mathbb{B}^e \cup \mathbb{B}^d \quad \text{and} \quad \emptyset = \mathbb{B}^e \cap \mathbb{B}^d. \quad (\text{C.2})$$

The initially unknown decomposition of the discretization node point set into active and inactive subsets  $\mathbb{B} = \mathbb{B}_{n+1}^d \cup \mathbb{B}_{n+1}^e$  at time step  $t_{n+1}$  is determined iteratively by an active set search as proposed in section 3.5.5.2.

**Balance of linear momentum**algorithmic in  $\mathcal{B}_0$ 

$$G_{n+1}^\varphi = \int_{\partial\mathcal{B}_0} \delta\varphi \cdot \mathbf{t}_{0_{n+1}}^p \, dA + \int_{\mathcal{B}_0} [\delta\varphi \cdot \mathbf{b}_{0_{n+1}}] \, dV - \int_{\mathcal{B}_0} [\text{Grad } \delta\varphi : \mathbf{II}^t(\varphi_{n+1}, d_{n+1})] \, dV$$

discrete in  $\mathbb{B}$ 

$$R_K^\varphi = \mathbf{A}_e \int_{\partial\mathcal{B}_{e_0} \cap \partial\mathcal{B}_{e_0}^t} N_X^k \mathbf{t}_{0_{n+1}}^p \, dA + \int_{\mathcal{B}_{e_0}} [N_X^k \mathbf{b}_{0_{n+1}}] \, dV - \int_{\mathcal{B}_{e_0}} [\text{Grad } N_X^k \cdot \mathbf{II}(\varphi_{n+1}^h, d_{n+1}^h)] \, dV$$

**Kuhn-Tucker conditions**algorithmic in  $\mathcal{B}_0$ 

$$G_{n+1}^\Phi = \int_{\mathcal{B}_0} [\delta d [Y_0(\varphi_{n+1}, d_{n+1}) - \kappa(d_{n+1})] + \text{Grad } \delta d \cdot \mathbf{Y}(d_{n+1})] \, dV$$

$$\Delta G_{n+1}^d = \int_{\mathcal{B}_0} \delta\Phi [d_{n+1} - d_n] \, dV$$

discrete in  $\mathbb{B}$ 

$$R_K^\Phi = \mathbf{A}_e \int_{\mathcal{B}_{e_0}} [N_d^k [Y_0(\varphi_{n+1}^h, d_{n+1}^h) - \kappa(d_{n+1}^h)] + \text{Grad } N_d^k \cdot \mathbf{Y}(d_{n+1}^h)] \, dV$$

$$\Delta R_K^d = \mathbf{A}_e \int_{\mathcal{B}_{e_0}} [N_d^k [d_{n+1}^h - d_n^h]] \, dV$$

**Decomposition of solution domain**algorithmic in  $\mathcal{B}_0$ 

$$\mathcal{B}_{0_{n+1}}^e = \{\mathbf{X} \in \mathcal{B}_0 | G_{n+1}^\Phi \leq 0, \Delta G_{n+1}^d = 0 \forall \delta d, \delta\Phi > 0 \text{ in } \mathcal{B}_{0_{n+1}}^e\}$$

$$\mathcal{B}_{0_{n+1}}^d = \{\mathbf{X} \in \mathcal{B}_0 | G_{n+1}^\Phi = 0, \Delta G_{n+1}^d > 0 \forall \delta d, \delta\Phi > 0 \text{ in } \mathcal{B}_{0_{n+1}}^d\}$$

discrete in  $\mathbb{B}$ 

$$\mathbb{B}_{n+1}^e = \{K \in \mathbb{B} | R_K^\Phi \leq 0, \Delta R_K^d = 0\}$$

$$\mathbb{B}_{n+1}^d = \{K \in \mathbb{B} | R_K^\Phi = 0, \Delta R_K^d > 0\}$$

Table C.2: Algorithmic and discrete form of the coupled problem

**C.2 Prototype isotropic gradient damage model**

The virgin material is modeled based on a compressible Neo-Hooke formulation in terms of the stretch  $\lambda$ , which coincides with  $\mathbf{F}$  in 1D. The local stored energy function therefore reads as

$$W = \frac{1}{2}\mu[\lambda^2 - 1] - \mu \ln \lambda \quad \text{with} \quad W(1) = 0 \quad (\text{C.3})$$

with  $\mu$  being the elastic modulus, rendering the following Cauchy stress  $\sigma = \partial_\lambda W$

$$\sigma = \mu[\lambda - \frac{1}{\lambda}], \quad (\text{C.4})$$

which fulfills the critical limit conditions of hyperelasticity

$$\sigma(1) = 0 \quad \sigma(\infty) = \infty \quad \sigma(0) = -\infty. \quad (\text{C.5})$$

The gradient part  $\psi^{grad}$  is chosen to an isotropic quadratic damage gradient energy in  $D$

$$\psi^{grad}(D) = \frac{1}{2}D \cdot \mathcal{E}_d \cdot D := \frac{1}{2}c|D|^2 \quad \text{with} \quad \mathcal{E}_d = c. \quad (\text{C.6})$$

Accordingly, the damage flux  $Y$  and the quasi-nonlocal energy release rate are given by

$$Y = -cD = -c \text{Grad } d \quad \text{and} \quad \bar{Y} = Y_0 - \text{Div } Y = Y_0 + \text{Div}(c \text{Grad } d). \quad (\text{C.7})$$

The material parameters are chosen to  $\mu = 2100\text{N/mm}^2$ ,  $\mu_r = 1000\text{N/mm}^2$ ,  $\kappa_0 = 1.0\text{N/mm}^2$  and  $\beta = 0.1\text{mm}^2/\text{N}$ , whereby  $\beta$  and the initial damage threshold  $\kappa_0$  specify a constitutive damage evolution law, which was previously used in the geometrically linear case, see Table 5.5.

### C.3 Constitutive update

The constitutive update of the geometrically non-linear damage prototype for the compressible Neo-Hooke 1D-model problem is summarized in Table C.3 for given  $\lambda_{n+1}, d_{n+1}, D_{n+1}$ .

---

<b>Input:</b> $\lambda_{n+1}, \mathbf{f}_{p_n}; \kappa_{n+1}, \kappa_n$	
Nominal Stress	$\sigma_{n+1} = [1 - d_{n+1}] \mu [\lambda_{n+1} - \frac{1}{\lambda_{n+1}}]$
Effective Stress	$\tilde{\sigma}_{n+1} = \mu [\lambda_{n+1} - \frac{1}{\lambda_{n+1}}]$
Damage Flux	$Y_{n+1} = -c D_{n+1}$
Local Energy Release Rate	$Y_{n+1} = \frac{1}{2} \mu [\lambda_{n+1}^2 - 1] - \mu \ln \lambda_{n+1}$
Internal Variable Update	$\kappa_{n+1} = \phi^{-1}(d_{n+1}) = \kappa_0 - \frac{1}{\beta} \ln(1 - d_{n+1})$

---

Table C.3: Update of the constitutive variables

Again, the implicit constitutive update does not rely on local iterations usually employed in standard return mapping algorithms. Moreover, the consequent linearization of the constitutive update results in a symmetric global iteration matrix.



# Bibliography

- Acharya, A., Bassani, J., 2000. Lattice incompatibility and the gradient theory of crystal plasticity. *J. Mech. Phys. Solids* 48 (8), 1565–1595.
- Aifantis, E., 1984. On the microstructural origin of certain inelastic models. *J. Eng. Mater. Technol.* 106, 326–330.
- Aifantis, E., 1987. The physics of plastic deformations. *Int. J. Plasticity* 3, 211–247.
- Aifantis, E., 1992. On the role of gradients in the localization of deformation and fracture. *Int. J. Engrg. Science* 30, 1279–1299.
- Anand, L., Kothari, M., 1996. A computational procedure for rate-independent crystal plasticity. *J. Mech. Phys. Solids* 44, 525–558.
- Anthony, K., 1970. Die Theorie der Disklinationen. *Arch. Rat. Mech. Anal.* 39, 43–88.
- Archarya, A., Bassani, J., 2000. Lattice incompatibility and a gradient theory of crystal plasticity. *J. Mech. Phys. Solids* 48, 1565–1595.
- Asaro, R., 1979. Geometrical effects in the inhomogeneous deformation of ductile single crystals. *Acta Metall.* 27, 445–453.
- Asaro, R., 1983. Crystal plasticity. *J. Appl. Mech., ASME* 50, 921–934.
- Ashby, M., 1970. The deformation of plastically non-homogeneous materials. *Phil. Magazine* 21, 399–424.
- Bažant, Z., 1984. Size effect in blunt fracture: concrete, rock, metal. *ASCE, J. of Engrg. Mechanics* 110, 518–535.
- Bažant, Z., Lin, F.-B., 1988. Nonlocal yield-limit degradation. *Int. J. Num. Meth. Eng.* 26, 1805–1823.
- Bažant, Z., Oh, B., 1983. Crack band theory for fracture of concrete. *Materials and Structures (RILEM, Paris)* 16, 155–177.
- Bažant, Z., Pijaudier-Cabot, G., 1988. Nonlocal continuum damage, localization instability and convergence. *ASME J. Appl. Mech.* 55, 287–293.
- Benallal, A., Billardon, R., Geymonat, G., 1993. Bifurcation and localization in rate-independent materials: some general considerations. In: *CISM Lecture Notes No. 327*. Springer-Verlag.
- Benallal, A., Fudoli, C., Ventirini, W., 2002. An implicit bem formulation for gradient plasticity and localization phenomena. *Int. J. Num. Meth. Eng.* 53, 1853–1870.

- Benallal, A., Tvergaard, V., 1995. Nonlocal continuum effects on bifurcation in the plane strain tension-compression test. *J. Mech. Phys. Solids* 43, 741–770.
- Benvenuti, E., Borino, G., Tralli, A., 2002. A thermodynamically consistent nonlocal formulation for damaging materials. *European Journal of Mechanics A/Solids* 21, 535–553.
- Bilby, B., Bullough, R., Smith, E., 1955. Continuous Distributions of Dislocations: A New Application of the Methods of Non-Riemannian Geometry. *Proc. Roy. Soc.*, A231, 263-273.
- Borja, R., Wren, J., 1993. Discrete micromechanics of elastoplastic crystals. *Int. J. Num. Meth. Eng.* 36, 3815–3840.
- Borst, R. d., Benallal, A., Heeres, O., 1996. A gradient-enhanced damage approach to fracture. *J. Phys.* IV 6, 491–502.
- Borst, R. d., Mühlhaus, H., 1991. Continuum models for discontinuous media. In: *Fracture Processes in Concrete, Rock and Ceramics*. E&FN Spon/Chapman & Hall, London.
- Borst, R. d., Mühlhaus, H., 1992. Gradient-dependent plasticity: Formulation and algorithmic aspects. *Int. J. Num. Meth. Eng.* 35, 521–539.
- Borst, R. d., Sluys, L., Mühlhaus, H.-B., Pamin, J., 1993. Fundamental issues in finite element analysis of localization of deformation. *Eng. Comp.* 10, 99–121.
- Braun, M., 1997. Configurational forces induced by finite-element discretization. In: *Proc. Estonian Acad. Sci. Phys. Math.* Vol. 46.
- Capriz, G., 1989. *Continua with microstructure*. Springer Verlag, Berlin.
- Capriz, G., 1995. Continua with latent microstructure. *Arch. Rat. Mech. Anal.* 90, 43–56.
- Cermelli, P., Gurtin, M., 2001. On the characterization of geometrically necessary dislocations in finite plasticity. *J. Mech. Phys. Solids* 49 (7), 1539–1568.
- Chadwick, P., 1975. Applications of an energy-momentum tensor in non-linear elastostatics. *J. Elasticity* 5, 249–258.
- Chambon, R., Caillerie, D., El Hassan, N., 1998. One-dimensional localisation studied with a second grade model. *Eur. J. Mech. A/Solids* 17, 637–656.
- Coleman, B., Gurtin, M., 1967. Thermodynamics with internal state variables. *J. Chem. Phys.* 47, 597–613.
- Comi, C., 1996. A gradient damage model for dynamic localization problems. *Rend. Sc. Istituto Lombardo A* 130, 119–141.
- Comi, C., 1999. Computational modelling of gradient-enhanced damage in quasi-brittle materials. *Mech. Cohes.-Frict. Mater.* 4, 17–36.
- Comi, C., 2001. A non-local model with tension and compression damage mechanisms. *Euro. J. Mech. A/Solids* 20, 1–22.
- Comi, C., Perego, U., 1996. A generalized variable formulation for gradient-dependent softening plasticity. *Int. J. Num. Meth. Eng.* 39, 3731–3755.

- Cosserat, E., Cosserat, F., 1909. Sur la theorie des corps deformables. Duod, Paris.
- Cuitino, A., Ortiz, M., 1992. Computational modelling of single crystals. *Modelling Simul. Mater. Sci. Eng.* 1, 225–263.
- de Borst, R., Pamin, J., 1996. Some novel developments in finite element procedures for gradient-dependent plasticity and finite elements. *Int. J. Num. Meth. Eng.* 39, 2477–2505.
- Delaplace, A., Pijaudier-Cabot, G., Roux, S., 1996. Progressive damage in discrete models and consequences on continuum modelling. *Mech. Cohes.-Frict. Mater.* 4, 99–136.
- Denzer, R., Barth, F., Steinmann, P., 2002. Studies in elastic fracture mechanics based on the material force method. *Int. J. Num. Meth. Eng.* Accepted.
- Dietsche, A., Steinmann, P., Willam, K., 1993. Micropolar elasto-plasticity and its role in localization analysis. *Int. J. Plasticity* 9, 813–831.
- Dillon, O., Kratochvil, J., 1970. A strain gradient theory of plasticity. *Int. J. Solids Struct.* 6, 1513–1533.
- Edelen, D., Laws, N., 1971. On the thermodynamics of systems with nonlocality. *Arch. Rat. Mech. Anal.* 43, 24–35.
- Ehlers, W., Volk, W., 1997. On shear band localization phenomena of liquid-saturated granular elasto-plastic porous solid materials accounting for fluid viscosity and micropolar solid rotations. *Mechanics of Cohesive-frictional Materials* 2, 301–320.
- Epstein, M., de Leon, M., 1998. Geometrical theory of uniform cosserat media. *Geom. Phys.* 26, 127–170.
- Ericksen, J., 1961. Conservation laws for liquid crystals. *Trans. Soc. Rheol.* 5, 23–34.
- Ericksen, J., 1998. On nonlinear elasticity theory for crystal defects. *Int. J. Plasticity* 14, 9–24.
- Ericksen, J., Truesdell, C., 1958. Exact theory of stress and strain in rods and shells. *Arch. Rat. Mech. Anal.* 1, 295–323.
- Eringen, A., 1972. Linear theory of nonlocal elasticity and dispersion of plane waves. *Int. J. Engrg. Science* 10, 425–435.
- Eringen, A., 1983. On nonlocal plasticity. *Int. J. Engrg. Science* 21, 741–751.
- Eringen, A., Kafadar, C., 1976. Polar field theories. in *Continuum Physics IV*, Academic Press, New York.
- Eshelby, J., 1951. The force on an elastic singularity. *Philosophical transactions of the Royal Society of London A* 244, 87–112.
- Eshelby, J., 1970. Energy relations and the energy-momentum tensor in continuum mechanics. in *Inelastic Behavior of Solids* M.F. Kanninen, W.F. Alder, A.R. Rosenfeld and R.I. Jaffe, eds., McGraw-Hill.
- Eshelby, J., 1975. The elastic energy-momentum tensor. *J. Elasticity* 5, 321–335.
- Evers, L., Parks, D., Brekelmans, W., Geers, M., 2002. Crystal plasticity model with enhanced hardening by geometrically necessary dislocation accumulation. *J. Mech. Phys. Solids* 50, 2403–2424.

- Fleck, N., Hutchinson, J., 1993. A phenomenological theory for strain gradient effects in plasticity. *J. Mech. Phys. Solids* 41, 1825–1857.
- Fleck, N., Muller, G., Ashby, M., Hutchinson, J., 1994. Strain gradient plasticity: Theory and experiment. *Acta Metall. Mater.* 42, 475–487.
- Florez-Lopez, J., Benallal, A., Geymonat, G., Billardon, R., 1994. A two-field finite element formulation for elasticity coupled to damage. *Comput. Methods Appl. Mech. Engrg.* 114, 193–212.
- Forest, S., Cailletaud, G., Sievert, R., 1997. A cosserat theory for elastoviscoplastic single crystals at finite deformation. *Arch. Mech.* 49, 705–736.
- Fried, E., 1996. Continua described by a microstructural field. *Z. angew.Math. Phys.* 47, 168–175.
- Fried, E., Gurtin, M., 1993. Continuum theory of thermally-induced phase transitions based on an order parameter. *Physica D* 68, 326–343.
- Fried, E., Gurtin, M., 1994. Dynamic solid-solid transitions with phase characterized by an order parameter. *Physica D* 72, 287–308.
- Ganghoffer, J., de Borst, R., 2000. A new framework in nonlocal mechanics. *Int. J. Engrg. Science* 38, 453–486.
- Garikipati, K., 2000. A variational multiscale approach to strain localization — formulation for multidimensional problems. *Comput. Methods Appl. Mech. Engrg.* 188, 39–60.
- Garikipati, K., 2002. A variational multiscale method to embed micromechanical surface laws in the macromechanical continuum formulation. *Computer Modeling in Engineering & Sciences* 3, 175–184.
- Geers, M., 1997. Experimental analysis and computational modelling of damage and fracture. Ph.D. thesis, Eindhoven University of Technology, The Netherlands.
- Goodman, D., Cowin, S., 1972. A theory of granular materials. *Arch. Rat. Mech. Anal.* 44, 249–266.
- Gurtin, M., 1999. *Configurational Forces as Basic Concepts of Continuum Physics*. Springer.
- Gurtin, M., 2000. On the plasticity of single crystals: free energy, microforce, plastic-strain gradients. *J. Mech. Phys. Solids* , 989–1036.
- Gurtin, M., 2002. A gradient theory of single-crystal viscoplasticity that accounts for geometrically necessary dislocations. *J. Mech. Phys. Solids* 50, 5–32.
- Gutkin, M., 2000. Nanoscopics of dislocations and disclinations in gradient elasticity. *Rev. Adv. Mater. Sci.* , 27–60.
- Hall, E., 1951. The deformation and aging of mild steel. *Proc.Phys.Soc.* B64, 747–753.
- Havner, K., 1982. The theory of finite plastic deformation of crystalline solids. In: *Mech. Solids*. Pergamon Press, Oxford, pp. 265–302.
- Hill, R., 1958. A general theorie of uniqueness and stability in elastic-plastic solids. *J. Mech. Phys. Solids* 6, 236–249.

- Hillerborg, A., Modeer, M., Petersson, P., 1976. Analysis of a crack formation and crack growth in concrete by means of fracture mechanics and finite elements. *Cement and Concrete Research* 6, 773–782.
- Huerta, A., Pijaudier-Cabot, G., 1994. Discretization influence on regularization by two localization limiters. *ASCE J. Eng. Mech.* 120, 1198–1218.
- Hutchinson, J., 1968. Plastic stress and strain fields at a crack tip. *J. Mech. Phys. Solids* 16, 109–114.
- Jirasek, M., 1998. Nonlocal models for damage and fracture: comparison of approaches. *Int. J. Solids Struct.* 35, 4133–4145.
- Jirasek, M., Bazant, Z., 2001. *Inelastic analysis of structures*. Wiley.
- Jirasek, M., Rolshoven, S., 2002. Comparison of integral-type nonlocal plasticity models for strain-softening materials. *Int. J. Eng. Sci.* , in press.
- Kachanov, L., 1958. Time to the rupture process under creep conditions. *Izv. Akad. Nauk SSR Otd. Tech. Nauk* 8, 26–31.
- Kittel, C., 1971. *Introduction to Solid State Physics*. J. Wiley, New York.
- Kocks, U., 1960. Polyslip in single crystals. *Acta Metallurgica* 8, 345–352.
- Kocks, U., 1970. The relation between polycrystal deformation and single-crystal deformation. *Metall. Trans.* 1, 1121–1143.
- Koiter, W., 1960. *General Theorems of Elasto-Plastic Solids*. *Progress in Solid Mechanics*. Eds. I.N. Sneddon and R. Hill, North Holland Publishing Company.
- Kondo, K., 1952. On the Geometrical and Physical Foundations of the Theory of Yielding. *Proc. 2. Japan Nat. Congress Appl. Mech.*
- Kongshavn, I., Poursartip, A., 1999. Experimental investigation of a strain-softening approach to predicting failure in notched fibre-reinforced composite laminates. *Comp. Sci. and Tech.* , 29–40.
- Kosevich, A., 1979. Crystal dislocations and the theory of elasticity. In: Nabarro, F. (Ed.), *Dislocations in Solids (The Elastic Theory)*. Vol. 1. North-Holland Publishing Company, pp. 33–141.
- Kröner, E., 1958. Kontinuumstheorie der Versetzungen und Eigenspannungen. *Erg. Angew. Math.* 5, 1–179.
- Kröner, E., 1960. Allgemeine Kontinuumstheorie der Versetzungen und Eigenspannungen. *Arch. Rat. Mech. Anal.* 4, 273–334.
- Kröner, E., Seeger, A., 1959. Nichtlineare Elastizitätstheorie der Versetzungen. *Arch. Rat. Mech. Anal.* 3, 97–111.
- Kuhl, E., Ramm, E., de Borst, R., 2000. An anisotropic gradient damage model for quasi-brittle materials. *Comput. Methods Appl. Mech. Engrg.* 183, 87–103.
- Kuhl, E., Steinmann, P., 2003. On spatial and material settings of thermo-hyperelastodynamics for open systems. *Acta Mechanica* 160, 179–217.

- Lasry, D., Belytschko, T., 1988. Localization limiters in transient problems for strain-softening in statics and dynamics. *Int. J. Solid Structures* 24, 581–597.
- Le, K., Stumpf, H., 1998. Strain measures, integrability condition and frame indifference in the theory of oriented media. *Int. J. Solids Struct.* 35 (9), 783–798.
- Liebe, T., Denzer, R., Steinmann, P., 2003. Application of the material force method to isotropic continuum damage. *Comput. Methods Appl. Mech. Engrg.* 30, 171–184.
- Liebe, T., Menzel, A., Steinmann, P., 2002. Theory and numerics of geometrically non-linear gradient plasticity. *Int. J. Engrg. Science* in print.
- Liebe, T., Steinmann, P., 2001. Theory and numerics of a thermomechanically consistent framework for geometrically linear gradient plasticity. *Int. J. Num. Meth. Eng.* 51, 1437–1467.
- Liebe, T., Steinmann, P., Benallal, A., 2001a. Some aspects of a gradient damage formulation. *Revue européenne des éléments finis* 10, 157–172.
- Liebe, T., Steinmann, P., Benallal, A., 2001b. Theoretical and computational aspects of a thermodynamically consistent framework for geometrically linear gradient damage. *Comput. Methods Appl. Mech. Engrg.* 190, (6555–6576).
- Lubliner, J., 1969. On fading memory in materials of the evolutionary type. *Acta Mech.* 8, 75–81.
- Lubliner, J., 1972. On the thermodynamic foundations of nonlinear solid mechanics. *Int. J. Nonlinear Mech.* , 237–254.
- Lubliner, J., 1973. On the structure of rate equations of material with internal variables. *Acta Mech.* 17, 109–119.
- Lubliner, J., 1984. A maximum-dissipation principle in generalized plasticity. *Acta Mech.* 52, 225–237.
- Lubliner, J., 1986. Normality rules in large-deformation plasticity. *Mech. Mat.* 5, 29–34.
- Luenberger, D., 1973. *Introduction to Linear and Nonlinear Programming*. Addison-Wesley Pub, Reading Massachusetts.
- Ma, Q., Clarke, D., 1995. Size dependent hardness in silver single crystals. *J. Materials Research* 1, 261–278.
- Mahnken, R., Kuhl, E., 1999. Parameter identification of gradient enhanced damage models with the finite element method. *Eur. J. Mech. A/ Solids* 18, 819–835.
- Mandel, J., 1972. *Plasticité Classique et Viscoplasticité*. Cours au CISM No. 97, Udine '71. Springer-Verlag, Berlin etc.
- Mariano, P., 2002. Multifield Theories in Mechanics of Solids. Vol. 38 of *Advances in Applied Mechanics*. Academic Press, pp. 1–93.
- Maugin, G., 1980. The method of virtual power in continuum mechanics; application to coupled fields. *Acta. Mech.* 35, 1–70.
- Maugin, G., 1990. On internal variables and dissipative structures. *Int. J. Non-equil. Thermo.* 15, 173–192.

- Maugin, G., 1993. *Material Inhomogeneities in Elasticity*, 1st Edition. Chapman & Hall, London.
- Maugin, G., 1995. Material forces: Concepts and applications. *Appl. Mech. Rev.* 48, 213–245.
- Maugin, G., 1996. Canonical momentum and energy in elastic systems with additional state variables. *C. R. Acad. Sci. Paris 323Iib*, 407–412.
- Maugin, G., 1997. Thermomechanics of inhomogeneous-heterogeneous systems: Applications to the irreversible progress of two- and three-dimensional defects. *ARI* 50, 41–56.
- Maugin, G., 1999. *The Thermomechanics of Nonlinear Irreversible Behaviors*. World Scientific Publishing Co. Pte. Ltd., Singapore.
- Maugin, G., 2000a. Geometry of material space: Its consequences in modern computational means. *Technische Mechanik* 20, 95–104.
- Maugin, G., 2000b. On the universality of the thermomechanics of forces driving singular sets. *Arch. Appl. Mech.* 70, 31–45.
- Maugin, G., Muschik, W., 1994. Thermodynamics with internal variables, i. general concepts, ii. applications. *J. Non-Equilib. Thermod.* 19, 217–249, 250–289.
- Maugin, G., Trimarco, C., 1992. Pseudomomentum and material forces in nonlinear elasticity: variational formulations and application to brittle fracture. *Acta. Mech.* 94, 1–28.
- Meixner, J., 1961. Zur Thermodynamik der irreversiblen Prozesse. *Zeit. Phys. Chem.* 16, 145–155.
- Menzel, A., Steinmann, P., 2000. On the continuum formulation of higher gradient plasticity for single and polycrystals. *J. Mech. Phys. Solids* 48, 1777–1796, Erratum 49 (2001) 1179–1180.
- Miehe, C., 1996. Exponential map algorithm for stress updates in anisotropic multiplicative elastoplasticity for single crystals. *Int. J. Num. Meth. Eng.* 39, 3367–3390.
- Miehe, C., Schotte, J., Lambrecht, M., 2002. Homogenization of inelastic solid materials at finite strains based on incremental minimization principles. Application to texture analysis of polycrystals. *J. Mech. Phys. Solids* 50, 2123–2167.
- Miehe, C., Schröder, 2001. A comparative study of stress update algorithms for rate-independent and rate dependent crystal plasticity. *Int. J. Num. Meth. Eng.* 50, 273–298.
- Miehe, C., Schröder, J., Schotte, J., 1999. Computational homogenization analysis in finite plasticity simulation of texture development in polycrystalline materials. *Comput. Methods Appl. Mech. Engrg.* 171, 387–418.
- Miehe, C., Stein, E., 1992. A canonical model of multiplicative elasto-plasticity. Formulation and aspects of the numerical implementation. *Eur. J. Mech. A/Solids* 11, 25–43.
- Mikkelsen, L., 1997. Post-necking behaviour modelled by a gradient dependent plasticity theory. *Int. J. Solids Struct.* 34, 4531–4546.
- Mindlin, R., 1965a. On the equations of elastic materials with microstructure. *Int. J. Solids Struct.* 1, 73–78.

- Mindlin, R., 1965b. Stress functions for a cosserat continuum. *Int. J. Solids Struct.* 1, 265–271.
- Mühlhaus, H., Aifantis, E., 1991. A variational principle for gradient plasticity. *Int. J. Solids Struct.* 28, 845–857.
- Mühlhaus, H., Vardoulakis, I., 1987. The thickness of shear bands in granular materials. *Geotechnique* 37, 271–283.
- Müller, R., Kolling, S., Gross, D., 2002. On configurational forces in the context of the Finite Element method. *Int. J. Num. Meth. Eng.* 53, 1557–1574.
- Müller, R., Maugin, G., 2002. On material forces and Finite Element discretization. *Comp. Mech.* 29, 52–60.
- Nedjar, B., 2001. Elastoplastic-damage modelling including the gradient of damage. Formulation and computational aspects. *Int. J. Solids Struct.* 38, 5421–5451.
- Needleman, A., 1987. A continuum model for void nucleation by inclusion debonding. *Journal of Applied Mechanics* 54, 525–531.
- Nguyen, Q., 2000. *Stability and nonlinear solid mechanics*. Wiley, Chichester.
- Nilsson, C., 1998. On nonlocal rate-independent plasticity. *Int. J. Plast.* 14, 551–575.
- Nix, W., Gao, H., 1998. Indentation size effects in crystalline materials: A law for strain gradient plasticity. *Journal of the Mechanics and Physics of Solids* 46, 411–425.
- Noll, W., 1972. A new mathematical theory of simple materials. *Arch. Rat. Mech. Anal.* 48, 1–50.
- Nye, J., 1953. Some geometrical relations in dislocated crystals. *Acta Metallurgica* 1, 153–162.
- Pamin, J., 1994. Gradient-dependent plasticity in numerical simulation of localization phenomena. Ph.d.dissertation, Delft University of Technology, Delft.
- Peerlings, R., 1999. Enhanced damage modelling for fracture and fatigue. Ph.D. thesis, Eindhoven University of Technology, The Netherlands.
- Peerlings, R., de Borst, R., Brekelmans, W., de Vree, J., 1996a. Some observations on localization in non-local and gradient damage models. *Eur. J. Mech. A/Solids* 15, 937–953.
- Peerlings, R., de Borst, R., Brekelmans, W., Geers, M., 2002. Localisation issues in local and nonlocal continuum approaches to fracture. *Eur. J. Mech. A/Solids* 21, 175–189.
- Peerlings, R., de Borst, R. and Brekelmans, W., de Vree, J., 1995. Computational modelling of gradient-enhanced damage for fracture and fatigue problems. In: Owen, D., Onate, E. (Eds.), *Computational Plasticity, Fundamentals and Applications*. Proc. 4th Int. Conf. Pineridge Press, Swansea, U.K.
- Peerlings, R., de Borst, R. and Brekelmans, W., de Vree, J., 1996b. Gradient enhanced damage for quasi-brittle materials. *Int. J. Num. Meth. Eng.* 39, 3391–3403.
- Peirce, D., Asaro, R., Needleman, A., 1982. An analysis of nonuniform and localized deformation in ductile single crystals. *Acta metall.* 30, 1087–1119.
- Petch, N., 1953. The cleavage strength of polycrystals. *J. Iron Steel Inst.* 174, 25–28.



- Pijaudier-Cabot, G., Bazant, Z., 1987. Nonlocal damage theory. *ASCE J. Eng. Mech.* 113, 1512–1533.
- Pinsky, P., 1986. A finite element formulation for elastoplasticity based on a three-field variational equation. *Comput. Methods Appl. Mech. Engrg.* 61, 41–60.
- Polizzotto, C., 2002. Thermodynamics and continuum fracture mechanics for nonlocal-elastic plastic materials. *Eur. J. Mech. A/Solids* 21, 85–103.
- Polizzotto, C., Borino, G., 1998. A thermodynamics-based formulation of gradient-dependent plasticity. *Eur. J. Mech. A/Solids* 17, 741–761.
- Polizzotto, C., Borino, G., Fuschi, P., 1998. A thermodynamically consistent formulation of nonlocal and gradient plasticity. *Mech. Res. Comm.* 25, 75–82.
- Rice, J.R. and Rosengren, G., 1968a. Plane strain deformation near a crack tip in a power-law hardening material. *J. Mech. Phys. Solids* 16, 1–16.
- Rice, J., 1968b. A path independent integral and the approximate analysis of strain concentration by notches and cracks. *Journal of Applied Mechanics* 35, 379–386.
- Rice, J., 1976. The Localization of Plastic Deformation. *Theoretical and Applied Mechanics*. Ed. W.T. Koiter, North Holland, Amsterdam etc.
- Rizzi, E., Carol, I., Willam, K., 1994. Localization analysis of elastic degradation with application to scalar damage. *ASCE, J. Eng. Mech.* 121, 541–554.
- Runesson, K., Ottosen, N., Peric, D., 1991. Discontinuous bifurcations of elastic-plastic solutions at plane stress and plane strain. *Int. J. Plasticity* 7, 99–121.
- Seeger, A., 1955. Neuere mathematische Methoden und physikalische Ergebnisse zur Kristallplastizität. *Pro. Iutam Colloq. on Deformation and Flow of Solids (Madrid)*, Springer, Berlin.
- Shield, R., 1967. Inverse deformation results in finite elasticity. *ZAMP* 18, 490–500.
- Shizawa, K., Zbib, H., 1999. A thermodynamical theory of gradient elastoplasticity with dislocation density tensor. I: Fundamentals. *Int. J. Plasticity* 15, 899–938.
- Shu, J., Barlow, C., 2000. Strain gradient effects on microscopic strain field in a metal matrix composite. *Int. J. Plasticity* 16, 563–591.
- Shu, J., Fleck, N., Van der Giessen, E., Needleman, A., 2001. Boundary layers in constrained plastic flow: comparison of nonlocal and discrete dislocation plasticity. *J. Mech. Phys. Solids* 49, 1361–1395.
- Simo, J., 1992. Algorithms for static and dynamic multiplicative plasticity that preserve the classical return mapping schemes of the infinitesimal theory. *Comput. Methods Appl. Mech. Engrg.* 99, 61–112.
- Simo, J., Ju, J., 1987. Strain- and stress-based continuum damage models: I. formulation. *Int. J. Solids Struct.* 23, 821–840.
- Simo, J., Kennedy, J., Taylor, R., 1989. Complementary mixed finite element formulations for elastoplasticity. *CMAME* 74, 177–206.

- Simo, J., Miehe, C., 1992. Associated coupled thermoplasticity at finite strains: Formulation, numerical analysis and implementation. *Comput. Methods Appl. Mech. Engrg.* 98, 41–104.
- Sluys, L., 1992. Wave propagation, localization and dispersion in softening solids. Ph.d. dissertation, Delft University of Technology, Delft.
- Sluys, L., de Borst, R., Mühlhaus, H., 1993. Wave propagation, localization and dispersion in a gradient-dependent medium. *Int. J. Solids Struct.* 30, 1153–1171.
- Sluys, L., Estrin, Y., 2000. The analysis of shear banding with a dislocation based gradient plasticity model. *Int. J. Solids Struct.* 37, 7127–7142.
- Steinmann, P., 1996. Views on multiplicative elastoplasticity and the continuum theory of dislocations. *Int. J. Engrg. Science* 34, 1717–1735.
- Steinmann, P., 1997. Modellierung und numerik duktiler kristalliner werkstoffe. Ph.D. thesis, Institut für Baumechanik und Numerische Mechanik, Universität Hannover, habilitationsschrift.
- Steinmann, P., 1999. Formulation and computation of geometrically non-linear gradient damage. *Int. J. Num. Meth. Eng.* 46, 757–779.
- Steinmann, P., 2000. Application of material forces to hyperelastostatic fracture mechanics. Part I: continuum mechanical setting. *Int. J. Solids Struct.* 37, 7371–7391.
- Steinmann, P., 2002. On spatial and material settings of hyperelastodynamics. *Acta Mechanica* 156, 193–218.
- Steinmann, P., 2003. On spatial and material settings of thermo-hyperelastodynamics. *J. Elasticity* 66, 109–157.
- Steinmann, P., Ackermann, D., Barth, F., 2001. Application of material forces to hyperelastostatic fracture mechanics. Part II: computational setting. *Int. J. Solids Struct.* 38, 5509–5526.
- Steinmann, P., Stein, E., 1996. On the numerical treatment and analysis of finite deformation ductile single crystal plasticity. *Comput. Methods Appl. Mech. Engrg.* 129, 235–254.
- Steinmann, P., Willam, K., 1994. Finite element analysis of elastoplastic discontinuities. *ASCE J. Eng. Mech.* 120, 2428–2442.
- Stelmashenko, A., Walls, A., Brown, L., Milman, Y., 1993. Microindentation on w and mo oriented single crystals: An stm study. *Acta Metallurgy Mater.* 41, 2855–2865.
- Stolken, J., Evans, A., 1998. A microbend test method for measuring the plasticity length scale. *Acta Mater.* 46, 5109–5115.
- Svedberg, T., 1999. On the modeling and numerics of gradient-regularized plasticity coupled to damage. Ph.D. thesis, Chalmers University of Technology, Göteborg, Sweden.
- Svedberg, T., Runesson, K., 1998. An algorithm for gradient-regularized plasticity coupled to damage based on a dual mixed FE-formulation. *Comput. Methods Appl. Mech. Engrg.* 161, 49–65.
- Svendsen, B., 1996. A fibre bundle model for structured continua. *ZAMM* 76, 209–210.

- Svendsen, B., 1999. On the thermodynamics of thermoelastic materials with additional scalar degrees of freedom. *Cont. Mech. Thermodyn.* 4, 247–262.
- Svendsen, B., 2002. Continuum thermodynamic models for crystal plasticity including the effects of geometrically–necessary dislocations. *J. Mech. Phys. Solids* 50, 1297–1329.
- Svendsen, B., Reese, S., 2003. Continuum thermodynamic modeling and simulation of additional hardening due to deformation incompatibility. In: Miehe, C. (Ed.), *IUTAM Symposium on the Computational Mechanics of Solid Materials at Large Strains*. Kluwer Publishers, Stuttgart, Germany.
- Taylor, G., 1938. Plastic strain in metals. *J. Institute Metals* 62, 307–328.
- Toupin, R., 1962. Elastic materials with couple–stresses. *Arch. Ration. Mech. Anal.* 11, 385–414.
- Truesdell, C., Noll, W., 1992. *The Non–Linear Field Theories of Mechanics*, 2nd Edition. Springer.
- Truesdell, C., Toupin, R., 1960. *Handbuch der Physik*. Vol. III/I. Springer-Verlag, Berlin, Ch. Classical field theories of mechanics.
- Tvergaard, V., Hutchinson, J. W., 1992. The relation between crack growth resistance and fracture process parameters in elastic-plastic solids. *JMPS* 40, 1377–1397.
- Tymiak, N., Kramer, D., Bahr, D., Wyrobek, T., Gerberich, W., 2001. Plastic strain and stain gradients at very small indentation depths. *Acta Mater.* 49, 149–160.
- Vardoulakis, I., Exadaktylos, G., Aifantis, E., 1995. Gradient elasticity with surface energy. mode iii crack problem. *IJSS* 33, 4531–4559.
- Weber, G., Anand, L., 1990. Finite deformation constitutive equations and a time integration procedure for isotropic hyperelastic- viscoplastic solids. *Comput. Methods Appl. Mech. Engrg.* 79, 173–202.
- Williams, M., 1957. On the stress distribution at the base of a stationary crack. *J. Appl. Mech.* 24, 109–114.
- Zbib, H., Aifantis, E., 1992. On the gradient-dependent theory of plasticity and shear banding. *Acta Mecanica* 92, 209–225.



## Curriculum Vitae

Name	Tina Liebe
Nationality	German
Date of birth	13.05.1975, Magdeburg
09/1981 – 06/1990	Polytechnische Oberschule „Salvador Allende“, Magdeburg
09/1990 – 06/1993	Gymnasium „Otto von Guericke“, Magdeburg
06/1993	General qualification for university entrance („Abitur“)
10/1993 – 12/1998	Civil Engineering, University of Hanover
01/1999 onwards	Research Associate, University of Kaiserslautern Chair of Applied Mechanics (Prof. Dr.-Ing. P. Steinmann)

